

Photovoltaic stimulation of retinal microcircuit for vision restoration

Présentée le 13 avril 2021

Faculté des sciences et techniques de l'ingénieur
Chaire Medtronic en Neuroingénierie
Programme doctoral en neurosciences

pour l'obtention du grade de Docteur ès Sciences

par

Naïg Aurelia Ludmilla CHENAIS

Acceptée sur proposition du jury

Prof. D. N. A. Van De Ville, président du jury
Prof. D. Ghezzi, directeur de thèse
Prof. S. Fried, rapporteur
Prof. E. Zrenner, rapporteur
Prof. G. Rainer, rapporteur

Abstract

Sight restoration through retinal prostheses was still a mere dream a century ago. Current challenges are even greater: providing a quantitatively and qualitatively useful artificial vision to late blind patients eligible for retinal stimulators. Existing approaches all face engineering and biological questions which directly threaten the quality of the restored vision. The engineering design and the intrinsic information encoding in the retina must be factored together when designing prosthetic visual interfaces. Compromises made on wired designs, stiff materials, external powering and implant location drastically restrain the restored visual field and the stimulation resolution. Epiretinal implants can cover a large visual field but with limited resolution, and stimulate retinal ganglion cell non-specifically through multiple compartments, including distal axons of the retinal nerve fiber bundles. Subretinal and suprachoroidal implants are limited in size but rely on inner retina activation, that allows to preserve most of spatial and temporal properties of the sighted retinal response, for better or worse; the retinal circuits behind spatial segregation and parallel feature encoding can be recruited, but neurons' responsivity rapidly wanes. Axonal activation and desensitisation hamper the spatio-temporal properties of the perceived phosphenes, as they distort the high spatial frequencies perceptions, and cause them to fade in less than a second. High-level perceptual mechanisms in the visual associative cortices such as grouping or multisensory causal inference can resolve the missing piece of information resulting from poor spatio-temporal prosthetic resolution, but require a high cognitive load: a too high price to pay for implants recipients to adapt and use artificial vision on day to day life. Consequently, current visual prostheses do not rescue vision as a primary sense in implanted patients. A 20/200 visual acuity, together with a 30 to 40° visual field, and qualitative properties as close as possible to patients' early visual experience are the minimal requirements for a potentially useful prosthetic approach.

The introduction of light-powered electronics represents a step forward in biomimetic retinal activation, but it is not fully emancipated from power supply and limited coverage concerns. The use of organic semiconductors allows to fabricate flexible discrete *p-n* junctions that can be embedded into a large hemispherical photovoltaic epiretinal implant. Such an organic photovoltaic array can cover 45° of visual angle, and total up to 10'498 pixels, spaced out by 120 μm. Complementary to this high-density and wide-field epiretinal implant engineering, investigations on retinal network activation allow to design network-oriented photovoltaic stimulation paradigms. Strategies that factor the intrinsic connectivity and properties of retinal neurons – convergence, lateral inhibition, and adaptation mechanisms – permit to take advantage of the retinal microcircuit organization rather than letting it defeat the technical efforts towards high-resolution stimulation.

A wide-field photovoltaic epiretinal approach could restore peripheral vision with native visual acuity in *Retinitis Pigmentosa* patients, as well as a theoretical 20/480 foveal visual acuity. The restoration of a very large visual field is made possible by the flexibility of the active materials and substrate, as well as by the epiretinal placement of the implant. The high resolution of the stimulation has been electrophysiologically evaluated *in-vitro*; photovoltaic stimulation of degenerating mouse retinas revealed that the non-rectangular photovoltage delivered under 560 nm light illumination was prone to recruit inner excitatory and inhibitory retinal circuits from the epiretinal side. This allows first to avoid uncontrolled axonal stimulation, second to preserve the intrinsic retinal processing, and third to specifically activate the amacrine cells network and benefit from natural lateral response segregation. These effects are reinforced using 10-ms long light stimulation pulses. In addition, delivering light stimuli in a non-stationary manner that mimics fixational saccades allows to reduce the Retinal Ganglion cells' desensitisation, by alternating the sub-excitatory circuits recruitment.

Altogether, this work emphasizes the relevance of considering intrinsic retinal processing in the development of artificial vision. The proposed approach, that combines withstanding organic photovoltaic prosthesis, and naturalistic epiretinal stimulation paradigm, could allow to stimulate human parasol cells with a natural spatial resolution and limit the need of head scanning. Both points are critical for motion perception, self-orientation and ambulation in late blind patients. Combined with a low vision foveal acuity, such visual functions may allow implant receivers to rely again on their sense of sight.

Keywords

Retinal prosthesis · Organic photovoltaics · Epiretinal implant · Retinal processing · Network-mediated stimulation · Electrophysiology · Retinal ganglion cells · Retinal neural network · Retinal degeneration · Artificial vision

Résumé

Restaurer la vue grâce à une prothèse rétinienne aurait semblé un rêve fantasque il y a encore un siècle. Les défis d'aujourd'hui sont plus grands encore : offrir une vision artificielle qui soit quantitativement et qualitativement profitable au quotidien pour les patients aveugles ou malvoyants tardifs. Les approches existantes se heurtent à des difficultés tant ingénieriques que biologiques qui impactent directement la qualité de vision qui peut être restaurée. Les compromis qui ont été faits jusqu'à présent sur la conception technologique, les cellules ciblées, la rigidité des matériaux et l'alimentation restreignent à la fois la résolution et le champ visuel. Les implants épirétiens couvrent un large champ visuel mais avec une faible résolution, et stimulent de manière indifférenciée les différents compartiments cellulaires des cellules ganglionnaires, y compris les axones des faisceaux des fibres maculaires et périphériques. Les implants subrétiens sont limités en taille, mais activent les circuits rétiens en amont des cellules ganglionnaires, ce qui préserve en grande partie les propriétés spatio-temporelles de la réponse visuelle – notamment sa ségrégation spatiale et le mode de traitement parallèle des informations – mais avec une excitabilité très limitée dans le temps. L'activation des axones et la désensibilisation des neurones nuisent directement aux phosphènes perçus par les patients : le premier les déforme et le second les rend imperceptibles au-delà d'une seconde. Les mécanismes perceptuels de haut niveau des aires visuelles associatives, comme la formation de groupes perceptuels ou l'inférence causale, sont à même de compléter les informations partielles apportées par la vision prothétique ; mais au prix d'un tel effort cognitif que les patients ne peuvent ou ne souhaitent pas utiliser cette forme de vision dans leurs actions quotidiennes. Pour une approche prothétique qui soit profitable dans une situation réelle de handicap, une acuité visuelle de 20/200, un champ visuel de 30 à 40°, et une vision qualitativement proche de l'expérience visuelle passée des patients malvoyants sont conjointement nécessaires.

Le développement de dispositifs électriques photosensibles a constitué un progrès certain vers une stimulation biomimétique de la rétine, mais sans être totalement affranchi des problématiques de l'alimentation ou de la limite de taille. L'utilisation de semi-conducteurs organiques en revanche permet la fabrication de jonctions *p-n* miniaturisées et flexibles qui peuvent être intégrées dans un large dispositif photovoltaïque implantable. Ce dispositif photovoltaïque hémisphérique peut couvrir un champ visuel de 45° et totaliser jusqu'à 10'498 pixels, espacés de 120 µm. En complément de cette approche à large champ de vision et haute résolution, l'étude des mécanismes d'activation photovoltaïque des réseaux rétiens permet de concevoir des stratégies de stimulations biologiquement pertinentes. La prise en compte de la connectivité intrinsèque de réseaux rétiens – convergence, inhibition latérale, adaptation – permet de tirer profit des microcircuits locaux, plutôt qu'ils n'annihilent les efforts technologiques pour offrir une haute résolution.

Un implant épirétien photovoltaïque pourrait permettre de restaurer une acuité visuelle constitutive dans le champ de vision périphérique des patients atteints de rétinopathie pigmentaire, ainsi qu'une acuité visuelle de 20/480 au niveau de la fovée. La restauration d'un large champ de vision est rendue possible par la flexibilité des matériaux actifs et du substrat, ainsi que par le placement épirétien du dispositif. La résolution de la stimulation a elle été évaluée *in-vitro* au moyen de mesures électrophysiologiques. La stimulation photovoltaïque de rétines murines dégénérantes a montré la capacité particulière du potentiel non-rectangulaire généré par les pixels photovoltaïques à recruter les circuits interne de la rétine, en dépit de leur placement épirétien. Le recrutement épirétien des circuits excitateurs et inhibiteurs permet tout d'abord d'éviter la stimulation axonale des cellules ganglionnaires ; mais aussi de préserver les mécanismes intrinsèques de traitement de l'information ; et enfin d'activer le réseau de cellules amacrines et de bénéficier de la ségrégation spatiale constitutive de la rétine. Ces trois effets sont renforcés par l'utilisation d'impulsions de stimulation supérieures ou égales à 10 ms. En outre, une stimulation lumineuse non-stationnaire qui reproduit les microsaccades oculaires et alterne les zones excitatrices recrutées permet de réduire la désensibilisation des cellules ganglionnaires.

Cette étude met l'accent sur l'importance du dialogue entre l'ingénierie technique et la connectivité des réseaux rétiens lors de la conception de dispositifs de stimulation rétinienne. L'approche proposée à l'issue de ce travail conjugue la photovoltaïque organique et des paradigmes de stimulation naturaliste. Elle pourrait notamment permettre de stimuler les cellules ganglionnaires humaines parasol avec une résolution spatiale constitutive, et de réduire les mouvements de balayage du champ visuel que doivent effectuer les patients, deux aspects critiques pour la perception du mouvement et l'orientation des patients aveugles ou malvoyants. En association avec une vision centrale minimale, la restauration de cette fonction visuelle pourrait permettre aux patients implantés de se baser de nouveau sur leur vue pour se déplacer et effectuer des activités quotidiennes.

Mots-clés

Prothèse rétinienne · Photovoltaïque organique · Implant épirétien · Traitement rétinien de l'information · Stimulation des réseaux rétiens · Electrophysiologie · Cellules ganglionnaires · Réseaux de neurones rétiens · Dégénérescence rétinienne · Vision artificielle

Contents

Abstract	- 1 -
Keywords	- 1 -
Résumé	- 2 -
Mots-clés	- 2 -
Contents	- 3 -
List of Figures	- 6 -
List of Tables	- 7 -
List of Equations	- 7 -
Chapter 1 Introduction: Retinal prostheses for vision restoration	- 8 -
1.1 Blindness and visual impairment due to retinal degenerative diseases.....	- 8 -
1.1.1 Late blindness.....	- 8 -
1.1.2 Retinal degenerative diseases	- 8 -
1.1.3 Visual field and visual acuity loss	- 9 -
1.1.4 Treatments' availability.....	- 11 -
1.2 Visual prostheses: historical perspective and current approaches.....	- 11 -
1.2.1 Principle and target cells	- 11 -
1.2.2 Electrical stimulation for the restoration of sight	- 14 -
1.2.3 Current retinal prosthetic approaches.....	- 15 -
1.2.3.1 Epiretinal approach.....	- 15 -
1.2.3.2. Subretinal approach.....	- 17 -
1.2.3.3. Suprachoroidal approach	- 19 -
1.2.4 Other retinal approaches to sight restoration	- 20 -
1.3 Outcomes and performance of retinal prostheses.....	- 21 -
1.3.1 Phosphenes characteristics	- 21 -
1.3.2 Visual restoration	- 23 -
1.3.3 Biocompatibility.....	- 24 -
1.3.4 Challenges for next generation implants: summary and prospects	- 25 -
Chapter 2 Design and validation of a foldable and photovoltaic wide-field epiretinal prosthesis	- 27 -
2.1 Abstract.....	- 27 -
2.2 Introduction.....	- 28 -
2.3 Results.....	- 29 -
2.3.1 Design and fabrication	- 29 -
2.3.2 Optimization of the photovoltaic pixel.....	- 30 -
2.3.3 Validation <i>ex-vivo</i> with explanted retinas from blind mice	- 34 -
2.3.4 Spatial selectivity.....	- 35 -
2.3.5 Cytotoxicity and long-term functioning.....	- 36 -
2.3.6 Thermal and optical safety	- 37 -
2.4 Discussion.....	- 40 -
2.5 Methods.....	- 42 -
2.5.1 Prosthesis micro-fabrication.....	- 42 -
2.5.2 Chips micro-fabrication.....	- 42 -
2.5.3 Kelvin Probe Force Microscopy	- 42 -
2.5.4 Accelerated ageing tests	- 42 -
2.5.5 Measure of photo-voltage and photo-current.....	- 43 -
2.5.6 Electrophysiology	- 43 -
2.5.7 pH measurements	- 43 -
2.5.8 Spatial selectivity measures and modeling.....	- 43 -
2.5.9 Optical safety	- 44 -
2.5.10 Thermal measurements	- 44 -
2.5.11 Thermal modeling.....	- 44 -
2.5.12 <i>In-vitro</i> cytotoxicity test	- 44 -
2.5.13 Surgical implantation	- 45 -

2.5.14 Statistical analysis and graphical representation.....	45 -
2.6 Acknowledgment	45 -
2.7 Supplementary material.....	46 -
Chapter 3 Capacitive-like photovoltaic epiretinal stimulation enhances the network-mediated activity of retinal ganglion cells by recruiting the lateral inhibitory network	52 -
3.1 Abstract.....	52 -
3.2 Introduction.....	53 -
3.3 Methods.....	54 -
3.3.1 Statistical analysis and graphical representation.....	54 -
3.3.2 Animal handling and preparation of retinal explants.....	54 -
3.3.3 Light stimulation.....	54 -
3.3.4 Photovoltaic and electrical stimulation.....	54 -
3.3.5 Computational model.....	55 -
3.4 Results.....	57 -
3.4.1 Light responsivity of <i>Rd10</i> retinas to high irradiance levels.....	57 -
3.4.2 Photovoltaic stimulation of the inner retinal network.....	58 -
3.4.3 Capacitive-like versus rectangular electrical stimulation of the inner retinal network	60 -
3.4.4 Computational model	64 -
3.4.5 Spatial selectivity of rectangular and capacitive-like voltage pulses	71 -
3.4.6 Modelling sustained α -RGCs.....	73 -
3.5 Discussion.....	75 -
3.6 Conclusion.....	76 -
3.7 Acknowledgements.....	76 -
Chapter 4 POLYRETINA restores high-resolution responses to single-pixel stimulation in blind retinas	77 -
4.1 Abstract.....	77 -
4.2 Introduction.....	78 -
4.3 Results.....	79 -
4.3.1 High-density retinal prosthesis.....	79 -
4.3.2 Single-pixel stimulation efficiency of titanium nitride photovoltaic pixels	82 -
4.3.3 Photovoltaic receptive fields	83 -
4.3.4 Spatial resolution of single-pixel stimulation.....	85 -
4.3.5 Design constraints for thermal safety	88 -
4.4 Discussion.....	89 -
4.5 Methods.....	91 -
4.5.1 Mechanical simulations.....	91 -
4.5.2 Thermal model	91 -
4.5.3 Chips micro-fabrication.....	91 -
4.5.4 Measure of photo-voltage and photo-current.....	92 -
4.5.5 POLYRETINA micro-fabrication	92 -
4.5.6 Atomic force microscopy.....	92 -
4.5.7 Kelvin Probe Force Microscopy	92 -
4.5.8 Spatial selectivity measures	93 -
4.5.9 Electrophysiology	93 -
4.5.10 Optical safety	94 -
4.5.11 Statistical analysis and graphical representation.....	94 -
4.6 Acknowledgment	94 -
Chapter 5 Naturalistic spatiotemporal modulation of epiretinal stimulation increases the response persistence of retinal ganglion cell	95 -
5.1 Abstract.....	95 -
5.2 Introduction.....	96 -
5.3 Materials and methods.....	97 -
5.3.1 POLYRETINA micro-fabrication	97 -
5.3.2 Preparation of retinal explants.....	97 -
5.3.3 Electrophysiological recordings.....	97 -
5.3.4 Retina stimulation	97 -
5.3.5 Experimental Design and statistical analyses	98 -

5.4 Results.....	- 99 -
5.4.1 Frequency dependent desensitisations of RGCs.....	- 99 -
5.4.2 Temporal modulation of epiretinal stimulation with irregular pulse trains.....	- 101 -
5.4.3 Spatial modulation of epiretinal stimulation with non-stationary pulse trains.....	- 102 -
5.4.4 Temporal modulation of epiretinal stimulation with interrupted pulse trains	- 104 -
5.4.5 Spatiotemporal modulation of epiretinal stimulation.....	- 105 -
5.5 Discussion.....	- 107 -
5.5.1 The cognitive burden of transient percepts	- 107 -
5.5.2 Spatial and temporal modulations reduce the rapid desensitisation.....	- 107 -
5.5.3 Artificial microsaccades.....	- 107 -
5.6 Acknowledgement	- 108 -
Chapter 6 Conclusion	- 109 -
6.1 Achieved results.....	- 109 -
6.2 Future development.....	- 111 -
6.2.1 Foveal resolution and selectivity	- 111 -
6.2.2 Assessing the functional usefulness of network-based strategies	- 112 -
6.2.3 Interaction of prosthetic stimulation with the plastic visual system.....	- 113 -
References.....	- 116 -
Appendix.....	- 130 -
Acknowledgement.....	- 131 -
Curriculum Vitae.....	- 132 -

List of Figures

Ch.1 Figure 1 - Visual field loss in Age-related Macular Degeneration and <i>Retinitis Pigmentosa</i>	10 -
Ch.1 Figure 2 - The human visual system	12 -
Ch.1 Figure 3 - Extracellular stimulation mechanism	13 -
Ch.1 Figure 4 - The first patented retinal stimulator	14 -
Ch.1 Figure 5 - Retinal stimulation sites	15 -
Ch.1 Figure 6 - Examples of epiretinal prostheses	17 -
Ch.1 Figure 7 - Examples of subretinal prostheses	19 -
Ch.1 Figure 8 - Spatial and temporal properties of the percepts elicited by retinal implants	22 -
Ch.2 Figure 1 - Foldable and photovoltaic wide-field retinal prosthesis	29 -
Ch.2 Figure 2 - Simulated surgical implantation	30 -
Ch.2 Figure 3 - Optimization of the photovoltaic pixel	31 -
Ch.2 Figure 4 - Characterization of the photo-current and photo-voltage	32 -
Ch.2 Figure 5 - High-frequency train stimulation	33 -
Ch.2 Figure 6 - Evaluation <i>ex-vivo</i> with retinal explants	34 -
Ch.2 Figure 7 - Spatial confinement of the prosthetic stimulation	36 -
Ch.2 Figure 8 - Lifetime of the retinal prosthesis	37 -
Ch.2 Figure 9 - Temperature variation during operation	38 -
Ch.2 Figure 10 - FEA simulation of thermal effects with POLYRETINA	39 -
Ch.2 Supplementary Figure 1 - Design of POLYRETINA	46 -
Ch.2 Supplementary Figure 2 - pH measurements upon prosthetic stimulation	46 -
Ch.2 Supplementary Figure 3 - Evaluation <i>ex-vivo</i> with retinal explants	47 -
Ch.2 Supplementary Figure 4 - Recording of <i>Rd10</i> retinas <i>ex-vivo</i>	48 -
Ch.2 Supplementary Figure 5 - Pharmacological blockage of network activity	49 -
Ch.2 Supplementary Figure 6 - Optical absorption	49 -
Ch.2 Supplementary Figure 7 - FEA simulation of thermal effects	50 -
Ch.2 Supplementary Figure 8 - FEA simulation of thermal effects with POLYRETINA	50 -
Ch.2 Supplementary Figure 9 - Aggregated model of POLYRETINA	51 -
Ch.3 Figure 1 - Light responsivity decay in <i>Rd10</i> retinas over the degeneration process	57 -
Ch.3 Figure 2 - Photovoltaic stimulation elicits exposure-dependant activity in <i>Rd10</i> retinas	58 -
Ch.3 Figure 3 - Characterisation of the direct and the indirect activities evoked by photovoltaic stimulation ..	59 -
Ch.3 Figure 4 - Classification of RGCs exhibiting or not LL activity	60 -
Ch.3 Figure 5 - Electrical stimulation of <i>Rd10</i> retinas with rectangular and non-rectangular capacitive-like voltage pulses	61 -
Ch.3 Figure 6 - Characterisation of the RGC response to rectangular and non-rectangular capacitive-like voltage pulses	63 -
Ch.3 Figure 7 - Biophysical model of the retinal layers under epiretinal stimulation	65 -
Ch.3 Figure 8 - Spike latency and contribution of amacrine cells	66 -
Ch.3 Figure 9 - Characterisation of the <i>in-silico</i> RGC response	67 -
Ch.3 Figure 10 - Modelling of the retinal network activity upon repetitive sub-threshold stimulation	68 -
Ch.3 Figure 11 - Comparison of ML indirect activity elicited by capacitive-like pulses with increasing falling time constants	69 -
Ch.3 Figure 12 - Comparison of epiretinal and subretinal stimulations <i>in-silico</i>	70 -
Ch.3 Figure 13 - Modelling of the spatial extent of the retinal circuit response	71 -
Ch.3 Figure 14 - Electrical receptive fields of RGCs upon rectangular and non-rectangular capacitive-like stimulation	73 -
Ch.3 Figure 15 - Sustained RGC modelling	74 -
Ch.4 Figure 1 - High-density POLYRETINA device	79 -
Ch.4 Figure 2 - Stimulation selectivity of the photovoltaic pixel	80 -
Ch.4 Figure 3 - Optoelectronic characterisation of the photovoltaic pixel	81 -
Ch.4 Figure 4 - Single-pixel stimulation of retinal ganglion cells	83 -

Ch.4 Figure 5 - Photovoltaic receptive fields.....	84 -
Ch.4 Figure 6 - Two-points discrimination pattern reversal test with single-pixel stimulation.....	85 -
Ch.4 Figure 7 - Grating pattern reversal with a fixed bar width.....	86 -
Ch.4 Figure 8 - Spatial resolution limit.....	87 -
Ch.4 Figure 9 - Modulation of stimulus contrast without spatial content.....	87 -
Ch.4 Figure 10 - Thermal simulations at the iris plane.....	88 -
Ch.5 Figure 1 - Detection and sorting of RGC network-mediated activity.....	98 -
Ch.5 Figure 2 - RGC responses to repeated indirect photovoltaic stimulation.....	99 -
Ch.5 Figure 3 - Double exponential decay of network-mediated ML RGC activity.....	100 -
Ch.5 Figure 4 - Randomised time-varied stationary pulse trains reduced RGC desensitisation.....	101 -
Ch.5 Figure 5 - Non-stationary pulse trains reduced RGC desensitisation.....	102 -
Ch.5 Figure 6 - Quantification of the RGC response preservation with non-stationary pulse trains.....	103 -
Ch.5 Figure 7 - Interrupted pulse trains reduced RGC desensitisation.....	104 -
Ch.5 Figure 8 - Quantification of the RGC response preservation with interrupted pulses.....	105 -
Ch.5 Figure 9 - Combined spatiotemporal modulation reduced RGC desensitisation.....	106 -

List of Tables

Ch.2 Supplementary Table 1 - FEA simulation of thermal effects.....	51 -
Ch.2 Supplementary Table 2 - FEA model of POLYRETINA.....	51 -
Ch.3 Table 1 - Retinal layers' parameters.....	55 -
Ch.3 Table 2 - Biophysical parameters of the retinal layers.....	56 -
Ch.4 Table 1 - Mechanical simulations.....	91 -
Ch.4 Table 2 - Eye parameters used for the eye model.....	91 -
Ch.4 Table 3 - Animal groups.....	93 -
Ch.5 Table 1 - Animals and experimental conditions.....	98 -
Appendix Supplementary Table 1 - Retinal prostheses systems.....	130 -

List of Equations

Ch.2 Equation 1.....	44 -
Ch.2 Equation 2.....	44 -
Ch.3 Equation 1.....	55 -
Ch.3 Equation 2.....	55 -
Ch.3 Equation 3.....	55 -
Ch.3 Equation 4.....	55 -
Ch.3 Equation 5.....	55 -
Ch.3 Equation 6.....	55 -
Ch.3 Equation 7.....	56 -
Ch.4 Equation 1.....	94 -
Ch.4 Equation 2.....	94 -
Ch.4 Equation 3.....	94 -
Ch.4 Equation 4.....	94 -

Chapter 1 Introduction: Retinal prostheses for vision restoration

1.1 Blindness and visual impairment due to retinal degenerative diseases

1.1.1 Late blindness

Blindness or severe visual impairment can be congenital or, more frequently, acquired during the course of life. Acquired blindness or late blindness can be the consequence of traumas to the ocular structure or to the retina, but is also – in near to 1/10 of the cases – the effect of a degenerative retinal disease that progressively impairs the retina structure and leads to retinal cell death and vision loss¹. Such progressively acquired blindness is very much different from congenital blindness, from both physiological and psychological perspectives. In patients that have had visual experience, the visual cortical areas and networks have been shaped according to the presence of visual primary sensory inputs^{2,3}. In humans, vision is a cross-modal and dominant sensory modality⁴⁻⁶, and visual experience not only leads the early development of visual processing, but also of a variety of more complex processes, as mental representation and self-referencing⁷, visuo-tactile association⁸ or language development^{9,10}.

This early shaping of the brain processes leads to two major consequences at the time the visual senses are severally impaired. First, in spite of their total or partial visual modality deprivation, late visually impaired or blind people seek for navigation cues, allocentric orientation strategies and multisensory associations close to those of sighted people¹¹. When a visual input is partially restored, this allows the late blind brain to integrate the restored source of information in more complex sensory processings¹². Second, late visually impaired people are more prone to experience practical and psychological stress related to visual disabilities, with seldom resilience and high depression incidence¹³⁻¹⁵. Precisely because of their sighted sensory processings, late blind patients might need but also benefit from vision restoration strategies.

1.1.2 Retinal degenerative diseases

Amongst retinal diseases that cause progressive degeneration of the retina, the most prevalent pathology is Age-related Macular Degeneration (AMD), which accounts for 8 to 9 % of the blindness worldwide, and is characterised by its late onset (after 60 years of age)¹. Diabetic retinopathy is the second most prevalent retinal degeneration condition, accounting for 5 % of world blindness¹⁶; in 72 % of diabetics, the disease progresses towards advanced proliferative states where retinal detachment and degeneration of the neural retina are unavoidable¹⁷. The global prevalence of both diseases is expected to raise by 50 % between 2040 and 2045, due to the ageing of the population in industrialized countries and the progression of diabetes worldwide^{1,18}. A third and heterogenous cause of retinal degeneration are inherited retinopathies, of which *Retinitis Pigmentosa* is one of the most common and well-studied. It is estimated to affect 1:3500 to 1:7000 people in Europe and USA¹⁹⁻²². Unlike diabetic retinopathy that can be screened and prevented with disease control strategies or minimal laser intervention^{23,24}, no preventive treatments can be proposed to *Retinitis Pigmentosa* nor AMD patients.

At the cellular level, AMD is characterized by the inflammation, apoptosis and necrosis of the retinal pigment epithelium (RPE) and the retinal photoreceptors (PRs), and more especially of the cones in the macula²⁵⁻²⁷ (**Figure 1a,b**). The deterioration of the RPE forms cellular debris, called drusen, that obstructs the nutrient exchange with choroid vessels. Eventually, this nutrient stress induces the death of the photoreceptors located above, typically in the macula. In a less frequent form of AMD, known as wet form, the macula is altered by neovascularization from choroidal vessels. Both forms results in the progressive loss of central vision and the apparition of a central scotoma, typically from 3 to 10° of visual field and extending with the progression of the disease^{28,29} (**Figure 1c**). Patients' peripheral vision is typically preserved^{30,31}, but the loss of central vision prevents them to identify faces, read or perform high-visual acuity tasks^{32,33}. Indeed, the loss of 10° of central visual field roughly corresponds to the loss of approximately 50 % of the primary visual cortex sensory input^{34,35}.

Retinitis Pigmentosa is a class of inherited disorders, characterized by the apoptosis of photoreceptors and a periphery to center disease progression^{19,20}. *Retinitis Pigmentosa* can be inherited in an autosomal dominant, autosomal recessive or X-linked manner, and occurs in some cases as part of the Usher syndrome or the Bardet-Biedl syndrome²². In spite of heterogenous causes, *Retinitis Pigmentosa* phenotype is characterized by a retinal hyperpigmentation and the progressive death of photoreceptors, typically starting from the

mid-peripheral retina and extending towards the periphery (**Figure 1d,e**). Early death of rod photoreceptors leads to night blindness, then to tunnel vision – characterized by a progressive reduction of the visual field, which is narrowed to some 3 to 10° in diameter in average cases³⁶ (**Figure 1f**). The macula and the central vision are generally spared in *Retinitis Pigmentosa*³⁷; as in most of its forms, rods are affected more severely than cones (rod-cone form)^{38,19}. Indeed, *Retinitis Pigmentosa* is associated with more than 60 genes³⁹, but the majority of them are expressed either in the pigmented epithelium cells (PECs) or in the photoreceptors, and in most of the *Retinitis Pigmentosa* forms, the mutated genes are specifically expressed in rods⁴⁰. Yet, in late-stage patients, both rods and cone photoreceptors are nearly completely degenerated; it is assumed that in rod-cone forms, cone are affected by the progressive impairment of retinal homeostasis – what eventually causes complete blindness^{41–43}. In such patients, the visual acuity can fall to 20/200 (25 %) or even to no light sensitivity (0.5 %)⁴⁴.

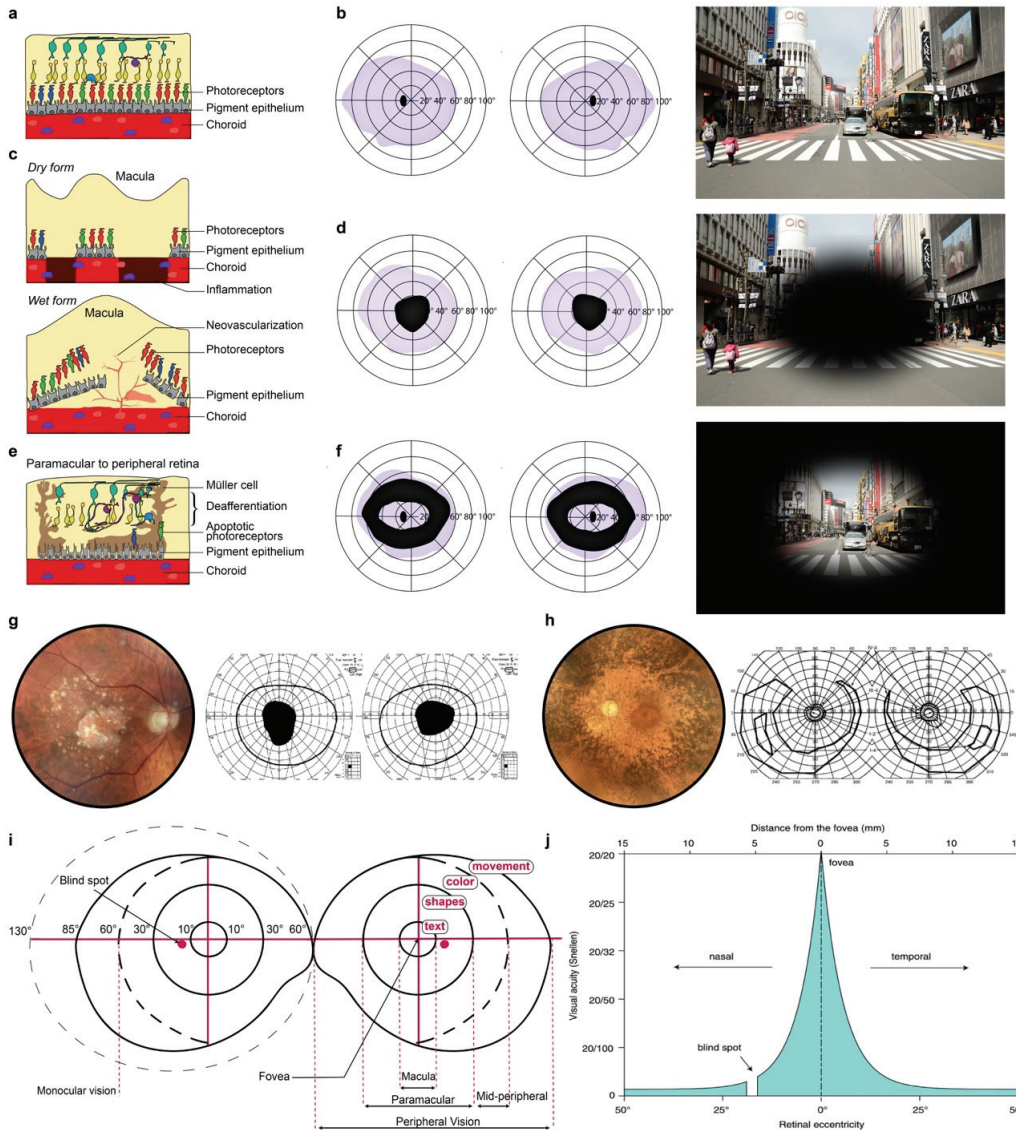
1.1.3 Visual field and visual acuity loss

Both *Retinitis Pigmentosa* and AMD are characterized by a significant loss in visual field or visual acuity that class patients as legally blind.

The reference point to estimate sight resolution is a visual acuity of 20/20 (or 6/6 in metric notation). This corresponds to the ability to discriminate lines 3.5 cm apart when the observer is at a distance of 6 meters, or to a 5 μm distance on the retina²⁹. Visual acuity in severe AMD typically ranges from 20/100 (6/30) to 20/800 (less than 2/60)⁴⁵. People with a visual acuity of less than 20/400 (3/60) are considered legally blind in most European countries^{46–48}, while in North America, the threshold is set at 20/200 (6/60)⁴⁹. In *Retinitis Pigmentosa* patients, visual acuity ranges from mild visual impairment (20/40 or 6/12, 52 %) to no light sensitivity (0.5 %), but the majority obtain a low vision score (20/70 or 6/21) due to the relative preservation of the macula⁴⁴. However, the narrowness of the visual field is also recognized as a major sight impairment^{46–48}. Lateral and vertical visual angles in human range between 130° and 145° (**Figure 1g**). Areas of photoreceptor cells' death can vary a lot between patients, disease forms, or upper and lower visual field, but the average ring scotoma is estimated to leave a tunnel visual field below 10°³⁶ (**Figure 1b**). According to the visual standards, a visual field restricted to 20°, or 16° in case of lower and upper field disparity, is considered as a severe visual impairment⁵⁰. In most European countries and North America, people whose visual field is under 20° in the better seeing eye are considered legally blind⁴⁹.

Legal blindness thresholds are based on the severity of functional vision loss a condition generates, as that sets its psychosocial and economic consequences⁵⁰. The functional abilities that are most impaired with visual field loss are orientation and mobility abilities. It is estimated that with a visual field of 20°, visual mobility is slower, but still possible with the adjunction of aids like canes. When restricted to 10°, visual mobility is only marginally possible: obstacles cannot be visually detected and people mostly need to rely on other sensory aids, vision only serving as an adjunct. When the central visual field is most affected as in AMD patients, the reading ability is used as a functional ability estimation. With a visual acuity of 20/200 (6/60), patients need high power magnifying aids to be able to decipher prints. Below 20/400 (3/60), visual reading is highly limited and patients must shift towards substitution aids such as Braille reading or talking books. In near-blind patients (a visual field lower than 4° or a visual acuity of 20/1000) substitution devices are required for both reading and mobility⁵⁰.

Ideally, to restore a functional form of vision in which visual sense can be used as the primarily reliable sense, therapeutical strategies should restore a visual field from 20 to 40° and a minimum visual acuity of 20/100 (6/30)^{29,50}.



Ch.1 Figure 1 – Visual field loss in Age-related Macular Degeneration and *Retinitis Pigmentosa*

a, Schematic representation of a healthy retina. **b**, Standard visual field. **c**, Schematic representation of the mechanisms causing gradual loss of central vision in AMD patients. Aging induces changes in the immune system that can generate pro-inflammatory environments and eventually chronic tissue inflammation, resulting in PECs and photoreceptors death. Inflammatory response can also promote neovascularization. Outgrowth of the choroid vasculature towards the outer retina and leakings speed up the epithelium and photoreceptors cells death. **d**, Central scotoma alters vision in AMD patients. **e**, Schematic representation of a retina with advanced *Retinitis Pigmentosa*: gene defects cause photoreceptors dysfunction and death, followed by reactive change in RPE and Müller glia cells, and eventually retinal remodeling. **f**, Ring scotoma and loss of peripheral light-sensitivity alters *Retinitis Pigmentosa* patients' vision. **g**, Representative fundus and Goldmann perimetry from AMD patients. The retinal fundus image lets see the drusen aggregates containing cellular debris that are characteristic from dry AMD form. From Horton & Guly, 2017⁵¹. The Goldmann perimetry shows central scotomas of approximately 10°. From Han, Kwon, Han *et al.*, 2009⁵². **h**, Representative fundus and Goldmann perimetry from *Retinitis Pigmentosa* patients. The Goldmann perimetry of a 27 years-old patient with *Retinitis Pigmentosa* shows important ring scotomas: the retinal sensitivity is overall decreased in mid periphery and far periphery (40° to 80°) with an asymmetry between upper and lower visual fields. From D. J. Creel, Moran Eye Center⁵³ and Weleber & Gregory-Evams, 2005⁵⁴. **i**, The standard visual angle under healthy conditions covers 130°. The central macular vision accounts for high acuity tasks: reading, examining, executing fine visually guided movements. The fovea is the retina area with the higher photoreceptors' density. Peripheral vision, from the paramacular retina to the far periphery, allows to identify objects, detect motion and is accountable for night vision. **j**, The visual acuity decreases with retinal eccentricity. As a result, patients with central scotomas dramatically loose visual acuity, while it can be to some extent preserved in *Retinitis Pigmentosa*. From Lambertus *et al.*, 2017⁵⁵.

1.1.4 Treatments' availability

Various gene therapies or pharmacological strategies have been investigated to slow down or prevent the progression of the retinal degenerative diseases.

Several teams worldwide are developing bioengineering tools for *Retinitis Pigmentosa* therapies, such as autologous stem cell transplants^{56,57}, CRISPR-Cas9 technology⁵⁸⁻⁶¹, or biallelic RPE65 retinal dystrophy gene therapy. The latter has recently been approved by the FDA and shows a transient but inconsistent ability to improve visual functions^{62,63}. Due to its genetic heterogeneity, addressing *Retinitis Pigmentosa* from a gene therapy point of view is incredibly complex and might require highly personalized bioengineered tools. Moreover, the development of genetic tools first relies on suitable translational disease models; if retinal degeneration mice are an established non-human mammalian model, the retinal cell types, the cell-type specific gene expression, and the macroscopic organization of the retinal circuit differ between the human and the mouse retina, and weaken the translatability of cell therapies⁶⁴.

Regarding AMD, commercially available anti-angiogenic drugs like Lucentis® (Novartis) or Avastin® (Roche) can block Vascular Endothelial Growth Factor (VEGF) signaling pathway, therefore preventing choroidal neovascularization and the development of the wet form. These anti-angiogenic drugs have shown some ability to slow down the disease progression in roughly 50 % of the patients⁶⁵⁻⁶⁷, but needs to be delivered monthly through intravitreal injection to be efficient, and are in any case not an option for patients having already lost a significant portion of photoreceptors.

However, the common thread behind AMD and the various *Retinitis Pigmentosa* phenotypes is, in spite of the death of photoreceptors, the relatively good preservation of the retinal circuit downstream^{68,69}. Despite patients locally or entirely lost light sensitivity, their visual pathway – from the inner retina to the visual cortex – remains functional (under the condition, no trauma nor retinal detachment has occurred). The integrity of the most of the retinal and visual sensory neurons enables to deliver effective and meaningful visual information to the brain via electrical, optogenetical or pharmacological stimulation of the afferent system. The prosthetic and bioengineered approaches for visual neurons stimulation are detailed in the following section.

1.2 Visual prostheses: historical perspective and current approaches

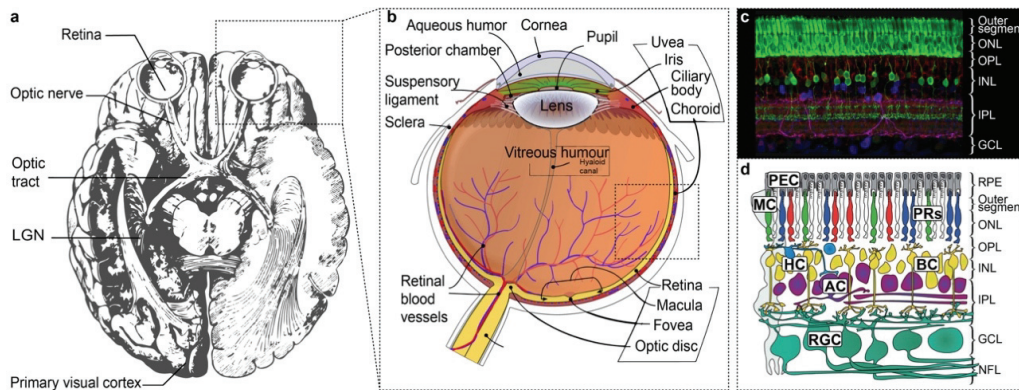
1.2.1 Principle and target cells

Visual information projected onto the eye needs between 13 to 100 ms to reach the cortical areas that will allow its identification^{70,71}. This relatively fast processing is possible because the information transmission along the visual pathway is highly spatially and sequentially organized (**Figure 2a**). In a healthy visual pathway, visual information is conveyed by photons that enter the eye through the iris aperture and are converted into neural signals in the retina (**Figure 2b,c**). The incident light projected by the cornea and the lens to the retina is absorbed by the photosensitive retinal cells located in the outermost side of the retina that forms tight contacts with the RPE. Incident light is photoconverted to membrane potential change by means of light-sensitive opsin proteins located on the photoreceptors' discs membranes^{72,73}. The change in cell membrane potential leads in turn to changes in the photoreceptors' chemical synaptic output. Chemical signaling is then relayed through a vertical excitatory pathway (**Figure 2c,d**). bipolar cells (BCs) interneurons relay the photoreceptors information to the retinal ganglion cells (RGCs), themselves directly connecting to the thalamic Lateral Geniculate Nucleus (LGN) by means of the optic nerve formed by their axons (**Figure 2a**). Signals then propagate along the optic radiation to the primary visual cortex (V1), from where it is further processed into dorsal and ventral streams, branching into various pathways involved in visuospatial processing, working memory, navigation and visuo-tactile or visuo-haptic multimodal interactions, among others⁷⁴⁻⁷⁷.

The retina is organized into three cell layers: the photoreceptor layer or outer nuclear layer (ONL), the inner nuclear layer (INL) and the ganglion cell layer (GCL) (**Figure 2c,d**). In the human retina, the photoreceptor layer contains about 120 million cells of different spectral sensitivities (rods, S, M, and L-cones). The inner nuclear layer contains two major cell types, bipolar cells (BCs) and horizontal cells (HCs), both non-spiking interneurons, *i.e.* that do not generate action potential but graded voltage change as a function of synaptic activation⁷⁸. In mammals, the GCL contains about 20 to 30 classes of RGC types, anatomically and functionally distinct⁷⁹. In both INL and GCL, 30 types of inhibitory non-spiking amacrine cells (ACs) can be found, that are involved in specific modulation and spatial segregation functions^{80,81}.

Given this straightforward laminar organization, it is tempting to describe the retinal network as a simple convergent system: photoreceptor cells sample the retinal image and transduce light into chemical signals, that are then transmitted to interneurons and finally to output RGCs, whose axon projects into the brain. Yet, the functional connectivity and the functional diversity of the retina makes it a highly complex image processing network. The anatomical cells' diversity and the lateral inhibition draws distinct and parallel visual pathways, each of them originating from a distinct RGC population and its associated circuitry⁸². In addition, the functional connectivity between retinal neurons draws spatiotopic organization (**Figure 2d**). Each RGC responds to a specific area of the retina, called its receptive field. Receptive fields are organized in mosaics that cover the retinal surface⁸³⁻⁸⁶ and may overlap, due to the parallel processing of the various RGCs population. Both horizontal and amacrine cells participate in shaping the RGCs'

receptive field, most presumably at the photoreceptors to Bipolar and Bipolar to RGC synapses^{87–90}. Lateral inhibition from these two inhibitory interneuron classes notably defines an antagonistic center-surround effect^{91–93}. In summary, the retina is a unitary neural structure that gives rise to diverse parallel visual pathways that all encode for distinct visual response properties in a spatiotopic fashion.



Ch.1 Figure 2 – The human visual system

a, The afferent visual pathway. The visual information is conveyed from the retina – where light is transduced into chemical and electrical signals – to the primary visual brain area. The retina originates from an outgrowth of the neural tube and is therefore part of the central nervous system (CNS). The most inner retinal cells – retinal ganglion cells (RGCs) – are monosynaptically projecting to the LGN. The axons of those cells form the optic nerve fibers that connects the neural retina to the higher visual system. From the optic chiasm the optic fibers continue as the optic tract and terminate in the LGN of the thalamus. Consequently, each LGN predominantly receives input from the contralateral visual field. The LGN neurons are organized according to their response feature and retinotopy. The LGN neurons connect through optic radiation to the primary visual cortex, located in the posterior occipital lobe. The pathway segregation and the retinotopy is maintained from the LGN to the visual cortex, with cortical magnification of the foveal input. Adapted from Mirochnik & Pezaris, 2019⁹⁴. **b**, Schematic diagram of the human eye anatomy showing the intrinsic eye optics and the retina. The incident light is projected through the pupil onto the phototransducing retina by the cornea and crystalline lens which forms a convex lens. The size of the pupil is controlled by the iris diaphragm to adapt to brightness levels. Most of the intraocular space is filled with vitreous humor produced by the ciliary body. This transparent viscous fluid not only shapes the eye but helps maintaining the contact between the retina and the underlying tissue layers. The retinal tissue is supplied with nutrients by the retinal vasculature but to a larger extent by the choroid coat. **c**, The retina is a thin tissue organized into successive cell layers that allows the phototransduction and the processing of the visual information. It is composed of three cell layers – the outer nuclear layer (ONL), the inner nuclear layer (INL) and the ganglion cell layer (GCL) – and two synapses layers – the outer plexiform layer (OPL) and the inner plexiform layer (IPL). The phototransduction occurs in the photosensitive cells of the ONL – rods and cones photoreceptors – whose outer segments contain light-sensitive membranous proteins, opsins. The processing of visual information starts in the neural retina. Adapted from Wei Li, National Eye Institute, National Institutes of Health, USA. **d**, The retinal layers are cell-specific and organized in a convergent circuitry. The main cell types involved in the visual signal processing are the photoreceptors (PRs), the bipolar cells (BCs), the retinal ganglion cells (RGCs), the horizontal cells (HCs), and the amacrine cells (ACs). The incident photons are absorbed in the PRs' outer segments. The PRs form chemical synapse with the BCs at the OPL level. The BCs form excitatory synapses with the RGCs in the IPL. The axons of RGCs converge towards the optic head over the GCL, forming the nerve fiber layer (NFL). HCs and ACs are inhibitory cells involved in the response boundary, respectively intervening at the PR-BC and BC-RGC synapse terminals. Glial Müller cells (MCs) and pigment epithelial cells (PECs) are respectively involved in neural cells homeostatic and metabolic support.

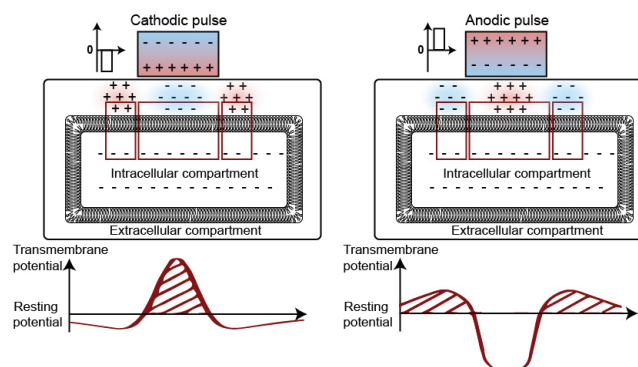
In AMD and *Retinitis Pigmentosa* patients, the inner nuclear layer and retinal ganglion cell layer remain preserved even at later stages of the diseases^{68,20,69}. Post-mortem retina analysis of patients with late-stage *Retinitis Pigmentosa* has revealed that 78 % of BCs cells and 30 % of RGCs are spared at advanced stages of the disease, while it was the case for only 5 % of photoreceptors^{68,95}. In AMD patients, 93 % of RGCs were spared and the INL cell number was found to either be stable or to have increased^{96,97}. Thus, the retinal cells, either RGCs or inner retinal cells, are an ideal target to be stimulated to substitute for rods or foveal cones input. Besides, prosthetic stimulation at the very early stages of the visual process allows to preserve as much as possible the downstream visual processing, *i.e.* the complex spatial and features parallel processing occurring at the INL level, the LGN and the V1 level. A common paradigm is that preserving such processes increases the chances to elicit meaningful perception in late blind patients with previous visual experience^{98–100}.

Yet, there are diverging views about the retinal circuits' integrity in retinal degenerative diseases: while some studies reported the anatomical and functional preservation of the GCL in both humans and animal models^{68,69,101,102}, some others underlies the remodeling and reorganization of the synapses in the INL, particularly in *Retinitis Pigmentosa* patients and in advanced dry forms of AMD^{43,103–105}. The preservation of the GCL in humans is undeniable until very late stages of degeneration, although the total number

of RGCs does decline over the disease, with up to a 30 % decline in advanced *Retinitis Pigmentosa* patients⁶⁸. The preservation of bipolar cells and amacrine cells in human *Retinitis Pigmentosa* has been established too⁶⁸. Unfortunately, negative plastic remodeling of the neural retina has been reported by multiple studies in both human and animal models^{106,107,103,108,109,43}. The apoptotic loss of rod and cones triggers plastic reorganization in the neural retina that has been deafferented, as it has been observed in other regions of the central nervous system^{110–112}. Reprogramming events, including collateral sprouting, have been observed in surviving cells at the cellular and molecular levels^{113,114,106,108,115,116,43}. The retinal remodeling can be characterized by three phases: the first one corresponds to the BCs dendrites retraction from the synaptic endings of photoreceptors^{114,117,43}, the second reflects the pathological cascade resulting from the inner retinal cells' deafferentation, and is characterized by the engagement of morphological signaling pathways and Müller cells^{106,118}, and the third and most problematic one is characterized by the cell's migration and aberrant rewiring, with complex synapse formation between bipolar cells, amacrine cells and eventually RGCs^{119,120}. Such shortings, known as microneuromas, are suspected to generate the intrinsic excitation events at the source of RGCs spontaneous activity, and to threaten stimulation strategies^{120,121}. Contrariwise, others works have enhanced the intact aspect of the IPL in rodents models of retinal degeneration: the morphology, arborization and presynaptic connectivity of the RGCs and the three major types of amacrine cells (starburst ACs, dopaminergic ACs, and All ACs) were preserved even at the very advanced stages of degeneration^{122,101,102}. Additionally, functional studies have shown that RGCs maintained their glutamate excitability in spite of altered bipolar cells morphology¹²³. These contradictory evidences, together with the difficulty to statistically interpret the human-based studies – the occurrence of phase three remodeling in the multiple human *Retinitis Pigmentosa* genotypes is not yet established – leaves some hope for the prosthetic stimulation of remaining neurons.

However, because of the high variability of disease progression in retinal degenerative diseases, the evaluation of prosthetic candidates is crucial to determine the benefits of a prosthetic implant. Candidates are often evaluated using a corneal stimulation electrode that can induce electrically-evoked response in RGCs, which gives a good indicator of RGCs' functional preservation^{124–126}. Most of the patients that currently benefit from retinal prosthetic implants are thus late-stage *Retinitis Pigmentosa* patients with functionally preserved retinas.

The preserved cells can be stimulated electrically by mimicking a change in their membrane potential. Membrane potential changes in neurons for clinical applications, either in the central or peripheral nervous system^{127–133}, are typically elicited with one or several extracellular electrodes that interface with the neural tissue. The current path from the electrode-tissue interface across the neural tissue goes through a parallel resistive and highly-conductive element, which respective components are primarily bilayer membrane-insulated cells and extracellular electrolyte. While the current can rapidly polarize the extracellular medium, charges transfer across the lipid bilayer are limited¹³⁴. This polarization discrepancy induces local variations of charges equilibrium around the cell's surface (**Figure 3**). As a result, the cell's transmembrane potential is locally modified, and the cell is either hyperpolarized or depolarized, according to the polarity of the delivered electric pulse^{135,136}. In spiking neurons as RGCs, if the transmembrane potential change exceeds the spiking threshold, an action potential can be generated. In non-spiking interneurons, the graded potentials are enough to trigger synaptic release⁷⁸. In the case of bipolar cells, it causes the glutamatergic excitation of RGCs, that are then indirectly stimulated by the mean of the presynaptic network.



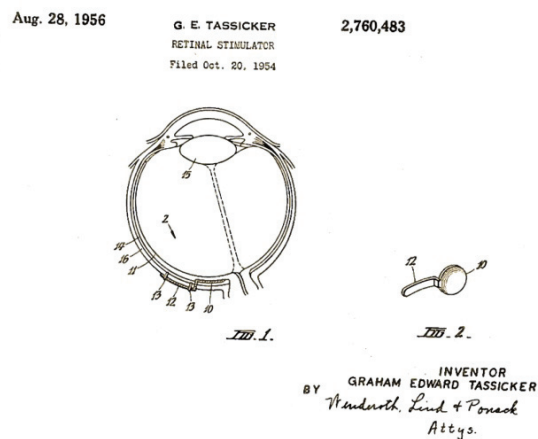
Ch.1 Figure 3 – Extracellular stimulation mechanism

Neural retina cells can be stimulated through close electrodes polarizing their extracellular medium. The voltage pulse delivered by the electrode induces charge redistribution in the highly conductive extracellular medium, but not in the intracellular compartment isolated by the double bilayer membrane. Consequently, the polarity between the extracellular and intracellular cells' compartments, *i.e.* the transmembrane potential, is locally modified from its resting potential. This leads to cells' depolarization in the case of cathodic pulses, or to cell hyperpolarization with anodic pulses. Because hyperpolarized areas are flanked by compensatory depolarized areas, both configurations can lead to cell depolarization and action potential generation in spiking neurons. This mechanism is exploited in retinal stimulation, either to depolarize inner retinal cells or to directly generate action potential in RGCs. Other – optogenetic – strategies to artificially polarize cells are further mentioned in section 1.2.4.

1.2.2 Electrical stimulation for the restoration of sight

The first experimentations that lead to phosphene perception, *i.e.* perception of transient flashes of bright light without natural vision being involved, took place in the early 1900s. Phosphenes are visual qualia that can occur spontaneously, for example during migraine auras, visual deprivation or mechanical strains, as the result of visual neurons aberrant activity – aberrant intended to be understood here as non-related to any activation of the upstream visual path. The medical community discovered in the early 20th century that they can also be produced and controlled by magnetic or electrical stimulation of visual neurons. In the aftermath of the first world war, surgeons were facing projectile-wounded patients with occipital lesions and cortical blindness. By applying local electrical stimulation or electrical field around their patients' head, Lowenstein and Borchardt (1918)¹³⁷, then Krause (1924)¹³⁸, and Foerster (1929)¹³⁹ could induce small evoked flickering visual percept – phosphenes.

The source and the nature of the evoked phosphenes was only identified in 1952, thanks to Hodgkin and Huxley's work on neuronal signal propagation. The discovery of the ionic flux mechanism and action potential generation also widened the possibilities for medical neural stimulation, identifying retinal and cortical neurons as potential targets¹⁴⁰. The first concept of retinal stimulator was introduced few years later by G. E. Tassicker (Figure 4). This first stimulator interestingly had much in common with the latest implant prototypes: he proposed to use a supporting base conforming to the curvature of the retina and to coat it with photosensitive material such as selenium crystal¹⁴¹.



Ch.1 Figure 4 – The first patented retinal stimulator

The left scheme shows a plan view of the stimulator implanted into an eye, while the right figure is a sectional plan taken from the direction indicated by the arrow 2. The stimulator consists of a tantalum, platinum or gold disc of 5 mm in diameter coated with photoactive selenium crystal. The disc is intended to be inserted between the retina and the choroid or between the choroid and the sclera. 10: disc, 11: retina, 12: lug, 13: sutures, 14: choroid, 15: lens, 16: sclera. From Tassicker, 1954¹⁴¹.

However, till the late 1980s, most of the effort in visual prosthetics was placed towards cortical stimulation. In 1962, Button and Putnam raised the hope for functional cortical stimulation when they demonstrated it was possible to elicit independent perceptual responses through different stimulation channels (*i.e.* two pairs of stainless-steel wires) in a blind patient with an 18-year history of blindness¹⁴². In 1968, Brindly and Lewin implanted a cortical array connected to radio receiver in a 52-year old-blind patient: despite the roughness of the device, this was a pioneering experiment and showed not only the retinotopy of the stimulation but also the possibility to generate patterned percepts, and thus a meaningful form of vision.

A few groups have more recently investigated stimulating the visual path at the level of the optic nerve, either with cuff electrodes or penetrating arrays^{143–147}. Yet, though necessary in case of damage to the retinal structure, this approach is delicate for several reasons. First, the surgical implantation is almost as invasive as for a cortical implant: it requires dissection of the dura matter and presents high ischemia risks^{145,148}. Second, the optic nerve is a dense neural structure with approximately 1.2 million axons in a 2-mm diameter cylinder, and relatively poor known fiber organization. Moreover, the macular fibers are located in the inside of the nerve and less easily stimulated by cuff electrodes. Patients with advanced *Retinitis Pigmentosa* and no-light sensitivity have been implanted by two different groups, and both studies revealed the difficulties to obtain focused stimulation in the optic nerve^{145,149}.

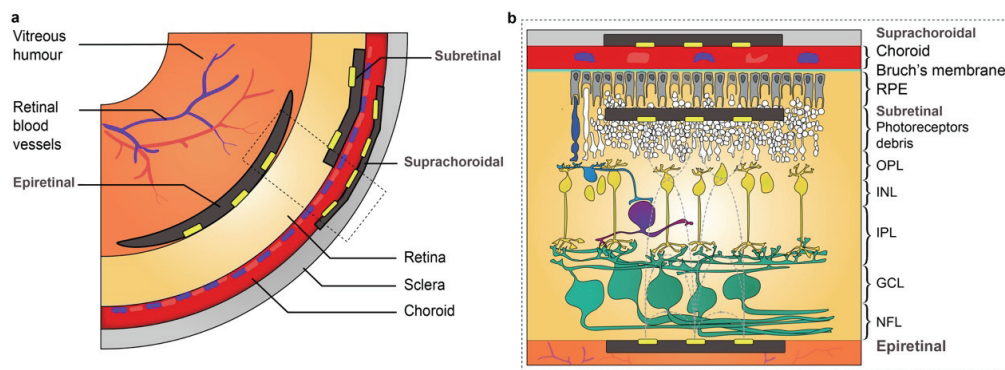
The identification of the retina as a leading prosthesis target came about 20 years later, to a large extent motivated by the success of cochlear implants in hearing restoration^{150,151}. A common current paradigm for vision restoration is that, depending on the etiology of the visual impairment, the stimulating arrays can be placed at different positions along the visual pathway: at the retinal level, the optic nerve level, in the LGN, or at the visual cortex level, according to their functional integrity. The retinal approach then appears especially convenient in diseases that only affect the more upstream portions of the visual path, *i.e.* the photoreceptors. In addition, the retina is a convenient visual prosthesis target for practical reasons: it has relatively easy extracranial surgical access, and a single

implanted eye can theoretically cover up to the 60° monocular visual field. Consequently, from the late 1980's and till today, the retina continues to be a major focus for visual prostheses, with more than 20 groups and companies working on retinal stimulation worldwide and three devices approved in the USA or in Europe (**Appendix Supplementary Table 1**).

Various structures of the retina can be electrically stimulated: from the outer nuclear layer if preserved, the inner nuclear layer, the retinal ganglion cell layer, to the axons bundle of the nerve fiber layer.

1.2.3 Current retinal prosthetic approaches

While this may be open to debate, distinction of retinal implants are generally done according to their implantation site: epiretinal devices, that are implanted directly into the vitreous body and whose electrodes are facing the ganglion cell and nerve fiber layers; subretinal devices, that are implanted below the choroid and directed towards the eventually remaining photoreceptors layer or the INL; suprachoroidal devices, that are implanted below the sclera; and, more rarely, intra-scleral prosthesis (**Figure 5**). This surgery-based classification corresponds to a partial extend to a functional classification: subretinal and suprachoroidal implants facing the internal part of the retina are primarily stimulating the INL bipolar cells; while epiretinal facing the GCL are primarily stimulating RGCs through direct depolarization of their cell body or axon initial segment. Nonetheless, this presumptive matching between stimulation site and targeted cells is not exhaustive; this will be further discussed in section 1.3.1 and in Chapter 2.



Ch.1 Figure 5 – Retinal stimulation sites

a, Epiretinal, subretinal and suprachoroidal placement of retinal implants. **b**, Cellular targets of the various approaches. Epiretinal implants face the ganglion cell layer and nerve fiber layer. Their primary cellular targets are RGCs but they may also indirectly stimulate them through the retinal network. Subretinal implants are placed below the choroid, in place of or penetrating into the degenerating photoreceptor layers¹⁵². This placement permits to stimulate the bipolar cells, that in turn excites RGCs. The network-mediated activation of RGCs allows to preserve the intrinsic processing of the INL. Suprachoroidal implants are placed below or in the sclera and face the choroid coat. They also aim at network-mediated RGC, but the choroid, the PECs, the photoreceptors debris and the distance to bipolar cells can elevate the inner retinal cells' stimulation thresholds.

1.2.3.1 Epiretinal approach

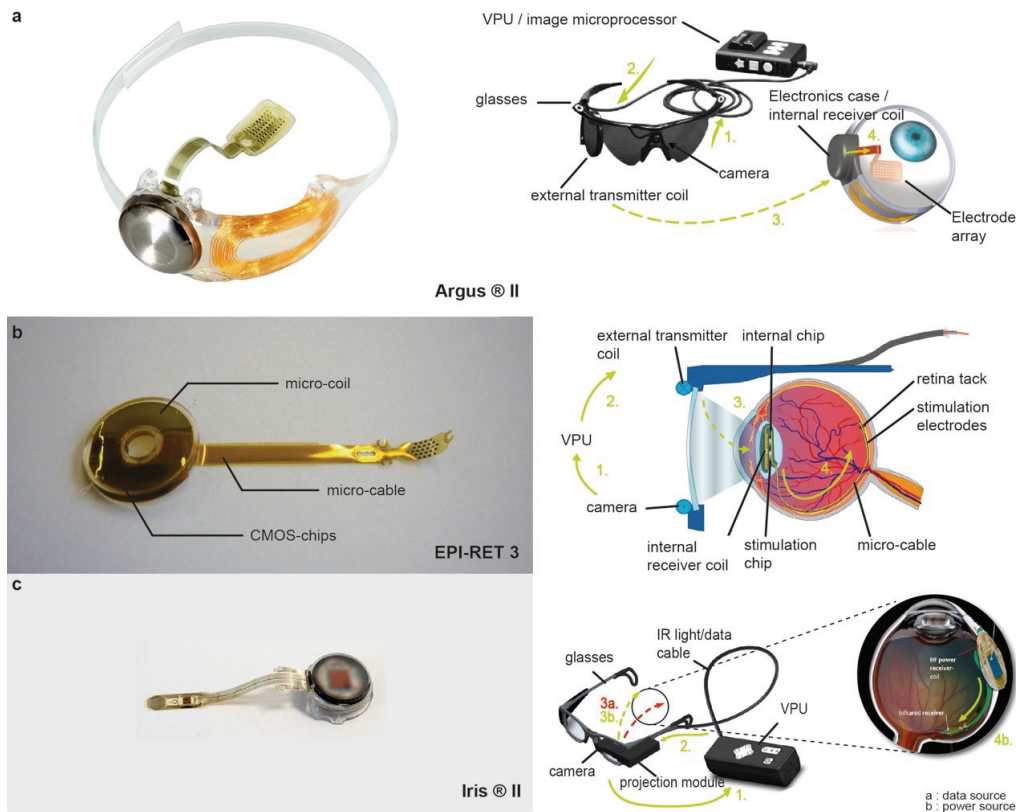
Epiretinal prostheses are placed on the surface of the retina, adjacent to the nerve fiber layer. The implantation is usually done through transvitreal delivery, an approach that ophthalmic surgeons carrying out vitreo-retinal surgery are familiar with. The implant then needs to be secured to the retinal surface with one or several tacks. The epiretinal placement presents some technical advantages: for the implantation first, but also for heat dissipation as the vitreous space facilitates it. Epiretinal prosthesis frequently consist of an intraocular electrode array and an external imaging source, typically a goggles-mounted camera driving the electrode array via a wearable visual processing unit. In the present section we will focus on the devices that have successfully completed implantations in human patients. Detailed characteristics and outcomes of devices currently undergoing clinical or preclinical testing can be found in **Appendix Supplementary Table 1**.

The development of epiretinal implants was pioneered by Humayun, Greenberg, Liu and Clements in the 1990s^{153–155}. Their efforts would lead to the first Argus® implant (Argus® I, Second Sight LLC, Sylmar, CA, USA) to be implanted into six *Retinitis Pigmentosa* patients between 2002 and 2004. The implant consisted of an extraocular camera, a wireless transmitter, and a 16-electrode array. The patients that previously had no light perception were able to see discrete phosphenes and simple shapes. This first trial mostly enhanced the need for smaller, denser electrode array for evoking finer percepts^{156,157}. As a result, the 60-electrode array implant Argus® II was developed few years later (Argus® II, Second Sight LLC, Sylmar, CA, USA, 2006). It received the CE mark in 2011, together with the FDA approval in 2013¹⁵⁸. The Argus® II system is to this day the most widely used retinal prosthesis worldwide, with over 400 implanted patients. The Argus® II system consists of an external part and an internal part, the latter split between suprascleral and intraocular locations. The external part consists of a pair of glasses with a mounted camera, connected to an image

microprocessor (**Figure 6a**, arrow 1.) sending command signal to the glass-mounted external coil (**Figure 6a**, arrow 2.). The external coil sends the command data to an internal coil embedded in an electronic case attached to the sclera (**Figure 6a**, arrow 3.), connected to the intraocular stimulator (**Figure 6a**, arrow 4.). The external coil provides both power induction and command data through wireless radiofrequency (RF) telemetry (**Figure 6a**, arrow 3.), but the internal coil is wire connected to the electrode array with a transcleral cable (**Figure 6a**, arrow 4.). The presence of a transcleral cable limits the number of electrodes that can be placed in the microelectrode array, as the sclerotomy is typically limited to 5.2 mm^{159,160}. The array itself comprises 60 electrodes of 200 µm in diameter, organized in a 6 by 10 grid covering 20 ° of visual field diagonally. The Argus® II could allow *Retinitis Pigmentosa* patients to recognize letters, detect faces and perform mobility tasks^{161–164}. Functional outcomes and drawbacks are further described in section 1.3.

At the same period, the German government founded a research group consortium for retinal implants. The EPI-RET device resulting from that collaboration is shown in **Figure 6b**. The device, like the Argus® II, consists of an external pair of goggles mounted with a photosensor array, connected to a visual processing unit (**Figure 6b**, arrow 1.), sending commands to an emitter coil (**Figure 6b**, arrow 2.), powering and transmitting signal to a receiver coil (**Figure 6b**, arrow 3.), connected to an intraocular stimulator implanted adjacent to the GCL (**Figure 6b**, arrow 4.). The singularity of the EPI-RET device is the absence of transcleral cable: as the internal receiver coil is placed on the lens, the internal part of the device is entirely intraocular, which reduces the risk of an opening or infection. Yet, the internal receiver coil and the stimulating array are connected through an intraocular micro-cable (**Figure 6b**, arrow 4.). The power and data are transmitted wirelessly between the receiver and emitter coils via induction with electromagnets (**Figure 6b**, arrow 3.)¹⁶⁵. The EPI-RET 3 device has been successfully implanted for a four week period into six blind *Retinitis Pigmentosa* patients¹⁶⁶. EPI-RET 3 embeds 25 electrodes arranged in a hexagonal grid on a 3 mm diameter chip on the edge of a 45 mm long implant¹⁶⁶. A larger version of the chip (12 mm) has also been developed in order to cover a greater visual field (37°)^{167,168}. The adhesion difficulties encountered during preclinical trials¹⁶⁹ and the room for improvement in the stimulation resolution and coverage have put a damper to further human testing of the device.

The most recent epiretinal device undergoing human implantation trials is the Pixium Vision S.A. Intelligent Retinal Implant System (IRIS®) II device, that obtained CE approval in 2016. The IRIS® II system is based on the Intelligent Medical Implants Learning Device (IMI), that demonstrated the ability to elicit phosphenes and patterned phosphenes in acutely implanted patients and up to 12 months later^{170–172}. As the Argus® II device, IRIS® II comprises a goggles-mounted image sensor, connected to a wearable microprocessor (**Figure 6c**, arrow 1.), sending stimulation commands to an external element (**Figure 6c**, arrow 2.). However, the power supply and the stimulation data are transmitted separately from that stage. The stimulation commands are directly sent to the intraocular microelectrode array via IR light (**Figure 6c**, arrow 3a.), allowing high data transfer rates and thus high refresh rates of the stimulating pattern¹⁷³. The power is supplied to the array via a transmitter-receiver coil system using RF telemetry, in which the suprascleral receiver coil is connected to the array through a transcleral cable (**Figure 6c**, arrows 3b. and 4b.). The stimulating array is a microfabricated polyimide structure which embeds 150 microelectrodes. Additionally, the system includes several image preprocessing stages¹⁷⁴: the visual scene is filtered according to the spatio-temporal properties of the retina in order to provide an optimized stimulation of the retinal ganglion cells. The learning retinal encoder can notably partition the signal into two temporal components (sustained and transient) that match the temporal resolution of the retina processing; and spatially partition the signal into excitatory and inhibitory channels, that mimic the retinal ON/OFF pathways^{175–177}. This strategy has been conceived to counterbalance the absence of inner retinal processing in epiretinal stimulation. The 10 *Retinitis Pigmentosa* patients implanted during the IRIS® II clinical study showed ability to localize objects, detect direction of motion, and could recognize real-word objects¹⁷⁸. However, both the materials and the surgical methods were found to threaten the lifespan of the device, and current investigations are focusing on that aspect^{178,179}.



Ch.1 Figure 6 – Examples of epiretinal prostheses

a, The Argus® II system is the most implanted and used retinal stimulation device worldwide. Visual data are externally processed; data and power are transmitted via RF telemetry to an internal electronic case; itself connected to an electrode array. Adapted from Second Sight Medical Products, Sylmar, CA, USA. b, The EPI-RET 3 implant is a fully intraocular implant whose internal electronics is integrated to an artificial lens. Adapted from Koch et al., 2008¹⁶⁶. c, The IRIS® II system has recently received the CE mark. It allows high data transmission rate thanks to infrared data encoding. Adapted from Pixium Vision, Paris, F.

1.2.3.2 Subretinal approach

Subretinal prostheses are placed between the RPE and degenerated or degenerating photoreceptor layer. It is assumed to be a more delicate surgery, both due to epithelium-retina adhesive junctions and the typical little practice of ophthalmic surgeons^{100,180}. Subretinal placements do not require mechanical fixation of the implant to the tissue, but it limits the size of the array that can be fitted, mainly due to thermal increase leading to retinal detachment.

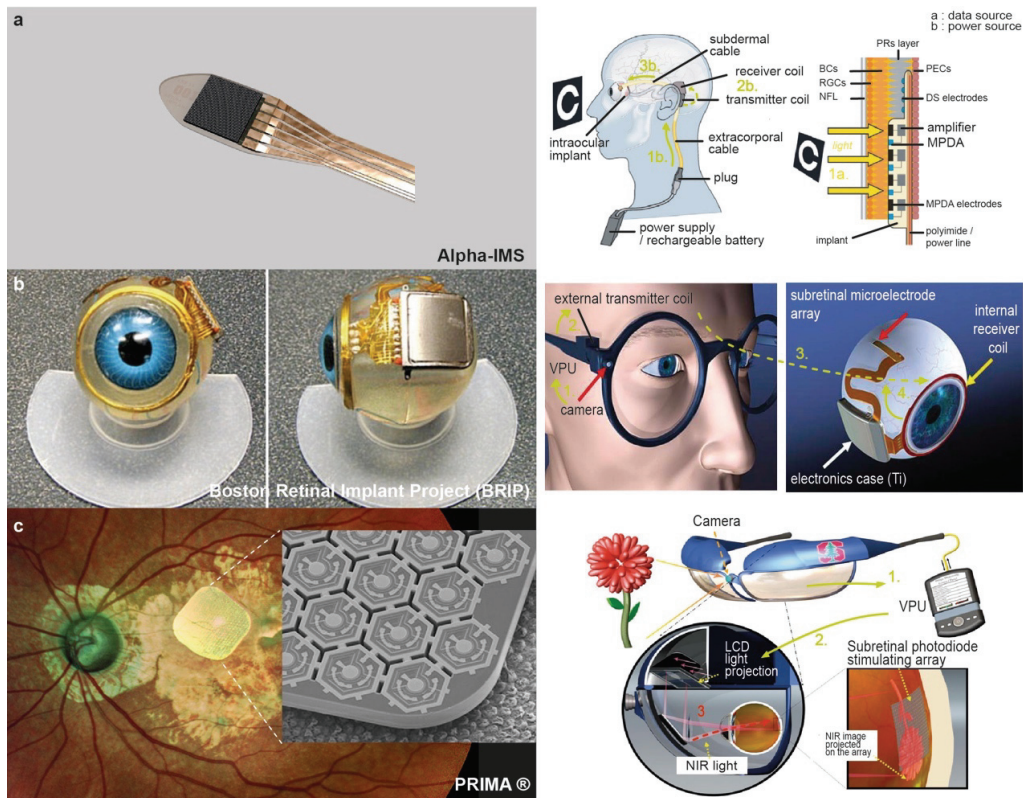
Yet, a major biological argument in favor of subretinal positioning is that, by placing the electrodes at the level of the degenerated photoreceptors, the early intrinsic signal processing of the retinal interneurons is preserved, so presumably do the spatial and feature processing of the visual input. The desire of physiological mimicry has been pushed forward with the subretinal approach, and several groups took the occasion to create intrinsically photosensitive implants that can act as a replacement for lost photoreceptors^{181,182}. Indeed, retinal prostheses frequently follow two formats: an internal electrode array driven by an external camera via a visual processing unit, or an internal photosensitive array converting light energy into electrical signals. The requirement for a wireless and sustainable power supply for electrical stimulating chips is undoubtedly an additional source of constraints and possible surgical complications. The use of photosensitive elements such as microphotodiodes (MPDA) enables to bypass the problem, as the light becomes the powering mechanism as well as the data transmission medium. However, the energy efficiency of most photodiode arrays is too low to stimulate retinal cells at safe irradiances and requires ad hoc amplification.

This is the case for the Alpha-IMS/AMS implant (Retina Implant AG, Reutlingen, Germany), the only subretinal implant that obtained CE marking to date. The Alpha-IMS implant consists of an intraocular multiphotodiode array, an external transmitter coil and a subdermal receiver coil. The intraocular photodiode array is a 3 mm² microchip encased in 70 µm thick polyimide structure¹. It embeds 1500 independent photodiode-amplifier pairs, each of them being connected to an electrode adjacent to the retinal cells. Contrary to most other stimulation devices, the Alpha-IMS and AMS implants do not require image acquisition and processing from an external camera. Each photodiode converts ambient light into an electrical signal (Figure 7a, arrow 1a.). However, such signals

needs to be amplified to reach bipolar cells' stimulation thresholds^{183,184}. Thus, although the photodiodes use light as a powering source, the amplifiers paired to each of them require an extrinsic power source. The extrinsic power is supplied through transmitter-receiver RF coils and a subdermal cable connected to the stimulating chip, similar to a cochlear implant¹⁸⁵ (**Figure 7a**, arrows 1b., 2b. and 3b.). The power cable connects subdermally to the post-auricular receiver coil loops in the orbit, and attaches to the subretinal implant as shown in **Figure 7a**, arrow 3b. The external coil is magnetically attached to its subdermal counterpart, and provides power induction and control of contrast sensitivity via a control unit. The Alpha-IMS device has been implanted in blind patients who reported significant visual improvement: not only the restoration of a crude visual acuity but also the recovery of visual functions^{181,183,186}. Patients' outcomes are further discussed in section 1.3. It is worth to mention that the presence of a subdermal and intraorbital cable impaired the long-term use of the device, and led to device repositioning, replacement surgery, and early device failure^{181,187}. Corrosion was another source of early failure, both due to the physical coupling between the photodiode and active electronics as well as the stimulating electrode interfacing with the tissue, meaning the chip could not be hermetically housed¹⁸⁸. Alpha-AMS, the upgraded version of the Alpha-IMS was also CE approved in 2016. The Alpha-AMS incorporates 1600 photodiode-amplifiers pairs in a 3.2 x 4mm array, and showed similar functional benefits to its IMS precursor¹⁸⁹. Improvements on the design and conformal coating of the stimulating chip could extend the Alpha device lifespan up to 3.3 years¹⁸⁸.

The Boston Retinal Implant Project (BRIP) was the second subretinal implant to be tested in human patients with end-stage *Retinitis Pigmentosa* for acute surgical trials¹⁹⁰. The BRIP device is similar to the Argus®II in many aspects: a goggles-mounted camera connected to a visual processing unit (**Figure 7b**, arrow 1.) sending stimulation commands to a goggles-mounted external coil (**Figure 7b**, arrow 2.), emitting via RF telemetry (**Figure 7b**, arrow 3.) to an internal receiver coil placed on top of the sclera – here placed in the front of the eye all around the cornea but under the conjunctiva. The electronic circuitry is enclosed into a hermetic case, that is wire connected to the 256-channel stimulating chip with a serpentine electrode array. The curvature of both the receiving coil and the serpentine are designed to facilitate the surgical placement of the array through the sclera into the subretinal space^{191,192} (**Figure 7b**, arrow 4.).

The recent PRIMA implant from Pixium Vision S.A. has integrated many aspects of the above-mentioned designs to create a promising photovoltaic model of subretinal stimulation. The device consists of a pair of goggles comprising a camera and a LCD screen projecting near-infrared (NIR) light. The image from the camera is sent to and processed by a visual microprocessor (**Figure 7c**, arrow 1.), but contrary to electrical stimulation devices, the command output is also conveyed as an image (**Figure 7c**, arrow 2.). The output image is projected through the pupil by the goggles-mounted light projection system and directly provides information and power sources to the photovoltaic array in the back of the eye (**Figure 7c**, arrow 3.). The stimulating chip is a 1mm-wide and 30-µm-thick hexagonal chip, that contains 142 pixels or photovoltaic cells, each of them formed of a stimulating electrode, a return electrode, and multiple photodiodes in series. When hit by the NIR beam, the photodiodes generate an electrical current in the adjacent tissue. Contrary to the Alpha-IMS system, the serial arrangement of photodiodes allows to generate enough current to reach bipolar cells' stimulation thresholds, thus to avoid the need of an extrinsic power source^{193–196}. Preclinical studies showed that the PRIMA implant could elicit visual-evoked potentials (VEPs) with irradiances far below the ocular safety limit for near-infrared light, as well as visually evoked behaviors in non-human primates^{12,197,182}. A first feasibility study has been run in France and a second is currently running in the USA^{198,199}. Among the five patients with dry AMD that have been implanted with the PRIMA implant in France, all showed satisfying acute tolerance to the implant and the majority of them could identify patterns and prints²⁰⁰.



Ch.1 Figure 7 – Examples of subretinal prostheses

a, The Alpha-IMS subretinal prosthesis relies on the ambient light to pattern activate microphotodiodes (MPDA) according to the visual scene. Though, the replacement of photoreceptors by MPDA requires external power supply. Adapted from Zrenner et al., 2010²⁰¹. **b**, The Boston Retinal Implant relies on external image processing and suprascleral wiring to the electrode array that is places subretinally. Adapted from Rizzo, 2011²⁰². **c**, The PRIMA[®] photovoltaic implant is intended to provide high-resolution stimulation in the macula. Adapted from Pixium Vision, Paris, F.

1.2.3.3 Suprachoroidal approach

A third position that has been exploited for retinal prosthesis placement is the suprachoroidal space, either between the choroid and the sclera or on the sclera. Suprachoroidal implantation presents some surgical specificities: it does not require a transvitreal surgery, so that the implantation procedure could be repeated for repair or replacement; but the presence of choroid vasculature increases the risk of haemorrhage. At the cellular level, typical suprachoroidal prostheses are, as subretinal ones, targeting the inner retinal neurons, though further from the INL. This increased distance to the retina limits the performance of suprachoroidal prosthesis, preventing fine spatiotopic discrimination and requiring high stimulation thresholds⁷⁹.

A series of suprachoroidal prototypes have been and are developed by the Bionic Vision Australia (BVA) group, from the early 24-channels device clinically tested to the most recent 99-channels Phoenix device ongoing *in-vivo* testing²⁰³. Late-stage *Retinitis Pigmentosa* patients have been implanted with the 24-channels implant in a pilot study in 2014²⁰⁴. The implanted device from the BVA group consisted of 20 stimulating electrodes array, controlled by a head-mounted camera, a visual processing unit, and a transmitter-receiver coil system as previously described. The pilot study confirmed the high risk of subretinal and suprachoroidal hemorrhage. However, implanted patients were able to localize static objects, light, or trajectories, despite a poor visual acuity restoration^{205,206} (see section 1.3).

Japan's Artificial Vision Project also developed a suprachoroidal-transretinal stimulation (STS) system. The device is composed of a goggles-mounted camera and processed by a goggles-mounted microprocessor, and relay via external-internal coil wire connected to the device. Its specificity lies in its 49 protruding electrodes that penetrate 0.3 mm through the sclera²⁰⁷. Phosphenes could be successfully elicited in patients suffering for Stargard disease and *Retinitis Pigmentosa*, but functional testing did not show any improvement with respect to natural residual vision^{207,208}.

1.2.4 Other retinal approaches to sight restoration

Besides the electric and photovoltaic approaches described in the sections above, several bioengineered approaches exist to restore vision in patients suffering from retinal degenerative diseases.

Gene therapy strictly speaking should be considered as a preventive approach, *i.e.* it aims at preventing the loss of photosensitive cells and related remodeling. However, transfection of a wild-type gene, even in the case of loss of function mutations and intervention at an early stage of the disease, do not fully translate in a non-degenerative phenotype, but rather offer a partial functional restoration of vision. Yet, as mentioned earlier, the genetic heterogeneity of retinal degenerative diseases makes the development of gene therapies a long, costly, and complex process. Moreover, gene therapy is – currently – limited to recessive mutations²⁰⁹.

An alternative bioengineering approach is to introduce an extrinsic gene that renders the preserved cells photosensitive, in default of photoreceptors. This optogenetic approach requires the transfection of cells with viral carriers that express a light-sensitive cell-membrane protein. A large variety of optoproteins exhibiting various kinetics and wavelength responsivities are currently being evaluated. Most of them are either ion channels (*e.g.* channelrhodopsins (ChRs), blue-light activated depolarizing cation channels), ion pumps (*e.g.* halorhodopsin, a yellow-light activated hyperpolarizing chloride pump) or G-protein-coupled receptors (*e.g.* melanopsin, blue-light activated transmembrane G-protein-coupled receptor). The first optoprotein to be transduced in a retinal cell was ChR-2 (Channelrhodopsin-2), after it was identified in *Chlamydomonas reinhardtii algae* and demonstrated its photomodulation ability^{210–212}. ChR-2 can be transduced via an adeno-associated virus (AAV) vector construct into bipolar cells or RGCs and restore a form of light sensitivity^{213–215}. Because gene therapy is a disease independent therapeutic protocol, it could benefit to a great number of *Retinitis Pigmentosa* patients, regardless of their genetic background. Optogenetic therapies offer a major technical advantage over current prosthetic approaches: the optogenetic stimulation can be delivered with a cellular resolution. Though activating the retina at the bipolar cell level rather than at the photoreceptor level reduces the theoretical resolution from a factor of 30 to 50^{216,217}, single bipolar cell resolution is approximately 200 times finer than what could be achieved by the PRIMA subretinal implant²¹⁸. Similarly, RGCs transfection would provide a limited resolution due to the neural convergence, but still 4300 to 6400 times better than what is achieved by Argus® II epiretinal implant in the fovea²¹⁹. Also, the transfection area and thus the potentially restored visual field are not limited, except by the AAV transfection efficiency. It must be mentioned that, without the signal amplification provided by the neural convergence, the light-driven depolarization of RGCs requires high irradiance levels. The intensity of blue light necessary to activate ChR-2 in RGCs typically exceeds the safety threshold of retinal illumination, forcing the use of channelrhodopsins that respond to low-energy light²²⁰. A goggles-mounted camera system converting the ambient light to a light beam of adequate wavelength – similar to those implemented for photovoltaic implants – must also be envisaged²²¹.

A feasibility clinical trial for a ChR gene therapy is ongoing in the USA, and a clinical trial for *Retinitis Pigmentosa* patients is running in Europe that uses ChrimsonR, a red-shifted channelrhodopsin²²². Nevertheless, the poor transduction efficacy in primates threatens the success of optogenetic therapies^{223,224}.

Finally, combined pharmacoprostheses may offer interesting therapeutic opportunities. The Microfluidic Retinal Prosthesis Implant project developed at the Kresge Eye Institute (Detroit, USA) and the Artificial Synapse Chip project from Stanford (USA) share the idea to create a visual prosthesis mimicking the chemical synaptic transmission between neurons^{225,226}. Although at very preliminary stages, the concept of pharmacoprosthetic implants is to convert images into an array of neurochemical signals through an implanted microfluidic chip. Glutamate has been identified as the best candidate for such signals, as it is the major excitatory neurotransmitter at the photoreceptor-to-bipolar-cell synapse. A glutamate releasing chip placed subretinally could in theory simultaneously depolarize OFF-bipolar cells and hyperpolarize ON-bipolar cells²²⁷. Little is known at this stage about the uptake and recycling of the delivered neurotransmitter in the degenerating retinal circuit.

The combinatory potential of all the different stimulation approaches is much unknown. A high-density prosthesis could be an interesting complement to the spatially limited transfection in the human retina with optogenetic approach²²⁸. Chronic electrical stimulation also shows neurotrophic effects²²⁹ that are hardly dispensable. The complementarity of pharmacological and electrical approaches for prosthetic application has been demonstrated²³⁰ too. However, the translatability of such findings in the retinal feedforward processing that only involves a few classes of protagonists is uncertain. In the following section and chapters, we will only focus on the electrical and photovoltaic stimulation approaches.

1.3 Outcomes and performance of retinal prostheses

1.3.1 Phosphenes characteristics

Most of the patients implanted with retinal prosthesis were able to perceive visual sensations called phosphenes. Phosphenes brightness, shape, and duration exhibits tremendous variability amongst subjects, implants, and stimulation methods.

Argus® II subjects reported phosphenes as blobs or, more often, as curved lines (**Figure 8a**) whose thickness could vary between 1 to 10° and length up to 15°^{231,232}. In most patients, the locations of the phosphenes within the visual field roughly corresponded to the retinotopic position of the stimulating electrodes, but with curved distortion. In epiretinal stimulation, the compartments closer to the stimulating electrodes are the arcuate nerve fiber bundles, *i.e.* the distal axons of RGCs converging towards the optic disc (**Figure 8b**). Although the most excitable compartment of a RGC is its axon initial segment (AIS), the distal portions of its axon can be electrically stimulated, and the elicited action potential propagate orthodromically or antidromically²³³. The orientation of the phosphenes can indeed be predicted according to the subjects retinal curvature and more importantly, according the stereotypic organization of nerve fiber bundle²³⁴ (**Figure 8c,d**). It has been proposed to avoid RGCs axonal activation by adjusting the delivered voltage to an intermediate value between AIS and distal axon respective stimulation thresholds²³⁵. However, the distal RGCs axons lack myelination up to the optic disc and exhibit relatively high excitability potential compared to most central nervous system axons – what on another note allows to preserve the tissue optical properties²³⁶. Axonal and somatic stimulation thresholds are in practice hardly distinguishable²³⁵. Better focalization of the phosphenes could be obtained by lengthening the duration of the delivered pulses up to 10 to 20 ms, instead of the typical sub-millisecond stimulus pulses used with the Argus® II device²³⁷. Yet, the reasons behind this duration-selective stimulation are poorly understood. Patients acutely implanted with the EPI-RET 3 device also reported elongated and arched phosphenes presumably originating from distal axons depolarization¹⁶⁶. These arched comet-like phosphenes can drastically impair the perception of complex images (**Figure 8d**).

Axonal activation is less of a problem in subretinal or suprachoroidal stimulation. Patients implanted with the BVA suprachoroidal device reported retinotopically organized phosphenes of various complex shapes, that they described as blobs rather than lines. Adjacent electrodes were found to generate overlapping phosphenes, presumably due to the increased stimulation thresholds and increased distance to the inner retinal cells that may favor cross-talk²³⁸. Patients implanted with subretinal devices also reported reproducible phosphenes described as round dots but occasionally as elongated lines^{183,201}.

In addition to potential distortion, phosphene legibility can be hampered by a poor temporal resolution (**Figure 8e,f**). Prostheses preferentially targeting the inner retinal neurons (BCs), *i.e.* subretinal and suprachoroidal prostheses, could only elicit transient phosphenes. Patients using the BVA suprachoroidal device at a 50 Hz stimulation rate described phosphenes as a very brief flash of light quickly disappearing after the stimulation onset²³⁸. Alpha-IMS patients also reported percepts that faded out within 15 s at 0.3 Hz and 0.5 s at 10 Hz stimulation rate²⁰¹.

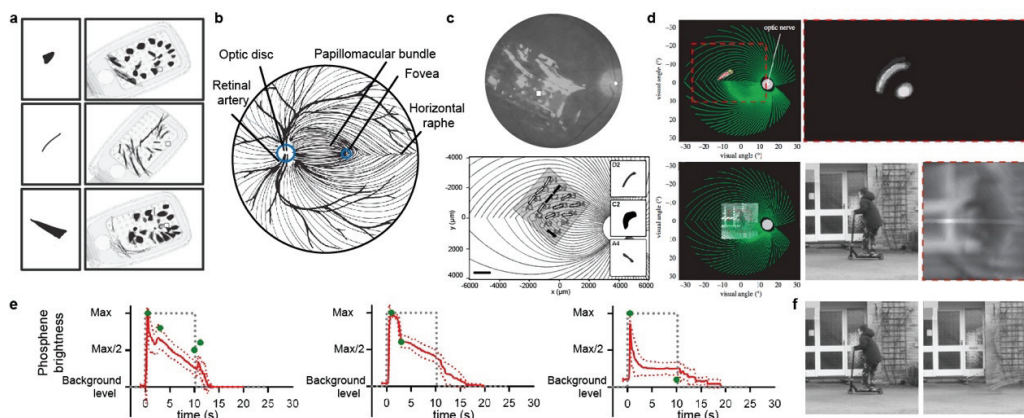
The fading of the phosphenes elicited by electrical stimulation is assumed to be a Troxler effect, *i.e.* an optical illusion of disappearance caused by the prolonged fixation of a stimulus. At the retinal level, Troxler effect can be explained by a neural adaptation phenomenon. Under healthy conditions, the retina does not respond to steady illumination but to spatial and temporal contrast, due to the chemical nature of the neural signaling, that requires homeostasis regulation^{239,240}. Without changes in the stimulus pattern (*i.e.* without temporal contrast), RGCs' response gradually declines from the initial contrast onset. This sensory adaptation phenomenon is highly conserved over species and senses^{241,242}. In the mammalian retina, the bipolar cell pathway has been identified as the site of several forms of contrast adaptation^{243–246}. The contrast adaptation phenomenon occurs in two phases^{246,247}. Immediately after a strong contrast stimulation, the glutamate released from bipolar cells decreases – given its decreased availability – which leads to a prolonged RGC hyperpolarization. A second long-range (tens of milliseconds) adaptation comes from inhibitory amacrine cells. Amacrine cells can either directly inhibit RGCs or presynaptic bipolar terminals, depending on their functional type and partners²⁴⁶. As a consequence of RGC hyperpolarization, the postsynaptic LGN and cortical neurons are no longer excited; and the visual percepts fade out in a few tens of milliseconds if no further contrast occurs – *e.g.* when the image is stabilized with extrinsic optics^{248–250}. In a similar fashion, under steady repeated electrical stimulation, bipolar cells rapidly desensitize²⁵¹, causing RGCs response to decline^{252,253} and percepts to fade. Because network-mediated stimulation shares most of the retinal processing with natural light stimulation, and RGC desensitisation under electrical stimulation can also be decomposed into two phases, one might also expect the inhibitory amacrine cells to be involved in RGCs response decay over repeated stimulation²⁵³. However, their involvement has not been demonstrated yet.

In natural vision, besides under Troxler illusion conditions, temporal contrast adaptation cannot be perceived: the visual scene is never stationary, intrinsically at first, but also because the eyes are constantly moving, even during conscious fixation. Fixational eye movements – drifts, microtremors and microsaccades – are therefore necessary to allow for a continuous perception of brightness. The involuntary oculomotor commands drag (drifts) or vibrate (tremors and saccades) the image across the retinal receptive fields, preventing the stationary stimulation of the retina. These eye movements, notably microsaccades, represent a form of adjusted image motion, necessary for optimal visual processing. Indeed, although controlled by the superior colliculus, saccadic

eye movements (typically 0.01° to 1° of visual angle at 1 to 8 Hz^{254,255}) are task and attention dependant^{256–258}. They have been shown to play a critical role in preventing peripheral fading, in low contrast perception, hyperacuity, or attentional shifts^{259–262}

In artificial vision systems that allow freely moving gaze and provide sufficient electrode density, the effects of eye movements may limit the Troxler fading effect, just as in natural vision. Indeed, Alpha-IMS patients experienced fading under single-electrode stimulation but some of them could perceive complex objects like grating patterns or letters almost continuously. The Alpha-IMS team estimated that subjects' microsaccades could shift the input image 1 to 3 pixels aside, and thus prevent its fading²⁰¹. However, severe visual impairment is frequently associated with aberrant oculomotor functions, such as nystagmus and reduced saccade amplitude^{263–266}, possibly by reason of visual field loss²⁶⁷, and not all patients were able to benefit from this strategy. In fact, little is known on the actual contribution of subjects' involuntary and voluntary eye movements on the stability of their percepts.

The rapid perceptual fading of the phosphenes has also been reported by most of Argus® II subjects. The phosphenes evoked by single-electrode and multiple electrodes stimulation were reported to fade out in a few seconds, in most cases in less than 0.5s²⁶⁸. The primary targets of Argus® II prostheses are RGCs, however RGCs can be electrically stimulated with short pulses in a repetitive fashion and briefly depolarize at each pulse without desensitisation²⁶⁹. One can assume that the reported fading then originates from the inner retinal cells, and that the Argus® II epiretinal electrodes activates RGCs both directly and through their inner retinal network, especially during prolonged stimuli (**Figure 8c**). The fading of phosphenes is a more delicate problem in Argus® II patients: contrarily to Alpha-IMS, Argus® II electrodes are too spaced out ($575\ \mu\text{m}$ pitch) to allow the image to switch to the adjacent pixel with a 1° saccadic movement ($\sim 300\ \mu\text{m}$ of retinal distance). The subject is therefore required to perform a large voluntary movement to refresh the electrical stimulation pattern on the retina. As a result, patients constantly have to head scan their environment to study objects of interest or identify obstacles^{268,270}.



Ch.1 Figure 8 – Spatial and temporal properties of the percepts elicited by retinal implants

a, Phosphene drawings from three different patients implanted with the Argus® II device. The right image shows the averaging of drawings obtained from individual stimulation trials of each electrode. Mean drawings were then aligned over the electrode layout. Most of the patients implanted with Argus® II and EPI-RET 3 devices reported arched phosphenes as the second and third drawings, while patients with Alpha-IMS and BVA devices reported phosphenes as blobs in most cases. Adapted from Beyeler et al., 2019²³⁴. **b**, Nerve fiber bundle trajectories. The organization of the nerve fibers converging towards the optic disk is stereotypic in the human retina. The nerve fiber bundle is especially dense around the macula, due to the high density of RGCs in the fovea. **c**, Electrode array orientation on the nerve fiber bundle allows to predict the perceived phosphenes. The top picture is a fundus image of an eye implanted with Argus® II. The bottom graph shows the simulated map of nerve fibers bundles, the electrode overlay and the phosphenes prediction. The orientation of predicted phosphenes matches patients' drawings (bottom, left sidebars). This evidence suggests that elongated phosphene shapes observed in epiretinal stimulation originates from the stimulation of the nerve fibers running over the GCL. Adapted from Beyeler et al., 2019²³⁴. **d**, Mathematical modeling of the nerve fibers bundle organization allows to predict phosphenes shapes (top) and complex percepts (bottom). The simulated percept enhances the qualitative issue of axonal stimulation. The density of the papillomacular bundle distorts and blurs the restored central vision. Adapted from Fine et al., 2015²⁷¹. **e**, Phosphenes brightness decay over stimulation time. The red line indicates the phosphene brightness level indicated by three Argus® II subjects during a 10 s stimulation (grey dotted line) at 20 Hz. The brightness was reported thanks to a joystick: the resting position corresponded to background level, the uppermost position to the highest brightness level, and the other positions were mapped on a ± 10 scale. The green dots correspond to the verbal appreciation of the decay by the patients. Similar brightness has been qualitatively reported by BVA and Alpha-IMS patients, respectively under 50 Hz and 1 Hz stimulation. Adapted from Fornos et al., 2012²⁶⁸. **f**, Possible effects of response kinetics on perception. Adapted from Fine et al., 2015²⁷¹.

Despite these spatial and temporal constraints, the form of vision provided by retinal prostheses allows patients to recover part of their visual functions.

1.3.2 Visual restoration

Parameters to be considered when evaluating a sensory prosthesis are visual functions restoration and biocompatibility. Visual restoration strictly speaking refers to the device's ability to improve visual acuity, visual field and functional vision with respect to patients' impaired condition. Biocompatibility and safety issues can be evaluated through a series of pre-implantation tests and post-implantation analysis of the severe adverse events (SAEs) experienced by patients. This is further discussed in section 1.3.3.

Visual restoration is typically assessed by a series of psychophysical tests where high-contrast objects (bars, gratings, squares, letters) are projected onto a screen in a controlled environment. As previously mentioned, the epiretinal placement of an implant may restrict the spatial focalization and distort the evoked phosphenes, but, when several electrodes are activated together to form geometrical objects, patients are able to distinguish orientation and shapes. During the acute clinical testing of the EPI-RET 3 implants, late-stage *Retinitis Pigmentosa* patients could discriminate between several high-contrast bar orientations¹⁶⁶. After 6-months of training all IRIS® II patients had significantly improved their performance in localizing high-contrast squares, and in bar direction of motion test¹⁷⁸. Amongst the 8 patients implanted that reached the secondary endpoint of clinical trials so far, 5 had measurable grating visual acuity, and a 20/2000 average visual acuity score. The highest visual acuity recorded was 20/400. The Goldmann visual field of 9 participants was also assessed: 5 of them had a measurable visual field (in contrast to none of them before implantation), of 119° on average¹⁷⁸. Finally, most of the Argus® II subjects exhibited similar localization performance 3 years post implantation²⁷²: 89 %, 56 % and 33 % of patients showed increased performance in high-contrast square localization test, high-contrast bar direction of motion test, and black and white grating visual acuity test, respectively. The grating visual acuity of subjects for those it was measurable was on average of 20/6324. Interestingly, while the early rehabilitation phase shows drastic patient performance increases with training, both in term of speed and accuracy of identification, the visual acuity and localization performances showed no evolution between one and three years post-implantation²⁷².

Similar geometric shape localization tasks, visual acuity and if applicable perimetric tests were conducted in subretinal prosthesis patients. 86 % of Alpha-IMS patients could perceive phosphenes with the implant, and exhibited significant improvement in light localization task, while 20 % of them could also detect motion. Visual acuity was measured with Landolt C-ring test with an average of 20/1280. The best acuity reported was 20/546¹⁸⁶. As observed in Argus® II patients, the performance in object recognition tasks significantly improved during the early rehabilitation phase, *i.e.* the initial 3 months training, after which it stagnates and could eventually fall below significance level^{183,186}. 13 of the 15 *Retinitis Pigmentosa* patients implanted with Alpha-AMS also demonstrated the ability to localize visual targets. Measurable visual acuities ranged from 20/1111 to 20/546. The subjects' performances were stable during the 12-month follow-up study¹⁸⁴. Clinical trials of the PRIMA subretinal implant are currently ongoing, but the first follow-up results from Pixium Vision revealed that all the implanted AMD patients could perceive light in their central visual field; and that the majority of them could identify high-contrast patterns, letters and objects²⁰⁰. According to the spatial resolution of the implant and *in-vivo* receptive field measurements, it is estimated that the PRIMA implant might provide a 20/250 visual acuity in humans¹⁹⁴, which would be the best among current retinal prosthetic technologies.

Performances reported with suprachoroidal prostheses are more variable. Patients implanted with the BVA implant were able to localize light with results higher than chance level, but only one subject had a measurable visual acuity of 20/8397. 2 of 3 subjects were able to recognize and localize static objects, while one could detect direction of motion²⁰⁴⁻²⁰⁶. The pilot study of the STS implant on two patients showed that suprachoroidal stimulation could elicit phosphenes in the visual field corresponding to the implant area. Both patients could use these phosphenes to identify high-contrast objects, and 1 of 2 patients could detect motion and perform grasping task²⁷³. However, a second study led to poorly reproducible results, though functionally encouraging (patients were able to localize a high-contrast line and walk along). It has been suggested that such gain of function resulted of a combination of artificial vision and natural residual vision²⁰⁸.

Psychophysical and localization tests are expected to reflect daily living needs: localizing high-contrast openings such as doors and windows, navigate between obstacles in a path, finding and grasping daily objects, etc. Indeed, a retinal prosthesis must not only improve visual acuity or visual field *per se*, but also improve visual performance in real-world uncontrolled environment. Understanding the impact of a device on patients' quality of life and Activities of Daily Living (ADLs) is of prime importance to judge its qualitative benefits and provide a meaningful comparison of the available technologies.

In this perspective, real-world functional assessment studies – based on participant-reported outcomes – have been conducted for Argus® II and Alpha-IMS devices. The functional benefit of Argus® II was evaluated with the Functional Low-vision Observer Rated Assessment (or FLORA assay). This qualitative assay developed by the Argus® II group is based on both assessors' and patients' opinions of benefit; it involves patient's self-report, interview and observation in its daily environment at home²⁷⁴. According to the FLORA results, 80 % of the patients experienced benefit in their functional vision and quality of life at 1-year post implantation, and none experienced negative effects. This result is maintained at 3-years post implantation²⁷². However, the absence of negative effect and the presence of some visual improvement do not seem to be sufficient for patients to keep using their prosthetic device as anything other than an occasional aid or for a contemplative use^{126,270}.

The improvement in Activities of Daily Living (ADLs) in Alpha-IMS and AMS patients was assessed with a series of tests consisting of table top object localisation, clock hand angle discrimination, Turano Independent Mobility Questionnaire and self-reports of

improvement in quality of life. Overall, 72 % of the patients exhibited a statistically significant improvement in ADLs, but only 45 % of them self-reported a satisfying improvement of daily life experiences. Patients reporting benefits were able to recognize unknown objects such as cars, houses, dinner plates, but also to better localize doorways, people and objects and avoid bumpings^{183,275}. 28 % of the subjects reported no benefit at all¹⁸³.

The visual acuity, the visual field and the functional vision that can be restored by a retinal implant are influenced by multiple factors: the patients' cognition, the integrity of its retina, the site of stimulation (epi-, subretinal, or suprachoroidal), the mode of stimulation (direct or network-mediated) – in the second case the intrinsic retinal processing – the positioning and attachment of the implant, and the design of the stimulating array (electrodes number, array size and electrodes density). Regarding the latter, simulation studies estimate that a prosthetic resolution of approximately 0.33° can permit handling, pointing, and recognition activities with a reasonable success rate^{276–278}, what corresponds to a 100 µm electrode spacing. To perform visually guided tasks such as pouring water or cutting food, subjects preferred larger visual fields (21°), even without resolution improvement²⁷⁶. Recent evidence also enhanced the role of restored visual field in ADLs and recognition tasks²⁷⁹. Though successful navigation seems possible with 60 phosphenes²⁸⁰, a visual field of 30° to 40° was estimated to be required for safe mobility in an unpredictable environment^{281,282}.

Given these estimations, it is striking to note that Argus® II and Alpha-IMS exhibit relatively similar benefits in real-world situations. Despite diverging in design and thus in restored visual acuity and visual field, both are overtaken by their respective functional drawbacks. The Alpha-IMS has 1500 electrodes and covers a relatively small visual field of 11° × 11°. Its high electrode density gives a resolution advantage: the Alpha-IMS has a theoretical resolution of 0.5° (under the estimation that 300 µm on the retina corresponds to 1° visual angle). Indeed, the best visual acuity to date (20/546), even if far away from theoretical resolution, has been reported with the Alpha-IMS/AMS^{181,201}. However, the narrowness of the restored visual field does not allow for independent mobility nor daily localization tasks. Additionally, the fading of the phosphenes, though partially compensated by freely moving gaze, forces users to set the stimulation rate to relatively low values (1-20 Hz)¹⁸⁶. By contrast, the Argus® II system counts 60 electrodes in a 6 × 10 design, what corresponds to 11° × 19° in the visual field (~ 20° diagonally). Argus® II electrodes are 200 µm in diameter and separated by 575 µm, which only allows a theoretical resolution of 4°. As a consequence, visual grating acuity in patients is in most cases lower than 20/1000; and this poor resolution makes patients lose the benefit of a larger visual field, as they have to perform large head movements to refresh the stimulation pattern on the retina^{280,283}. Patients are indeed instructed during rehabilitation training to screen the visual scene with head rather than eye movements to avoid phosphenes fading. This need for scanning and constant space decomposition is the major qualitative obstacle to Argus® II usage in daily life, as it leads to a very unnatural and cognitively demanding way of seeing²⁷⁰.

1.3.3 Biocompatibility

The safety profile of a retinal prosthesis is typically evaluated upstream from the clinical trials from its compliance to medical biocompatibility standards and downstream, judging from the significant adverse effects (SAEs) encountered during implantation and mid-term use.

Most prostheses that underwent clinical trials or acute implantation trials demonstrated a relatively low frequency of SAEs (**Appendix Supplementary Table 1**), which attests for a good mechanical and molecular compliance of the devices, as well as for safe implantation procedure. 60 % of patients implanted with Argus® II did not encounter any significant adverse effect within 5-year post-implantation. The surgery and device-related adverse effects were mostly conjunctival erosion, hypotony and endophthalmitis. 2 patients had to undergo a retacking surgery. Most of the SAE occurred within 3 years of implantation, except a case of retinal detachment^{283,284}. Over nine subjects, Alpha-IMS team reported 2 SAEs and 75 adverse effects within 1-year post implantation. The SAEs comprised increase ocular pressure and retinal detachment during explantation both treated without sequelae²⁸⁵. 4 of 15 Patients with Alpha-AMS experienced SAEs, among which implant drift requiring readjustment surgery, conjunctival erosion, and suprascleral coil related pain¹⁸⁹. After 24 months post implantation, one patient additionally experienced retinal detachment²⁷⁵. Patients that underwent acute implantation of EPI-RET 3 faced spontaneous dislocation of the electrodes, although they were well tolerated^{169,166}. Despite the careful follow-up of adverse effects at the macroscopic level, few studies are available on the effects of chronic implantation on the retinal tissue.

Long-term and daily use of retinal prostheses indeed exposes the retinal tissue to chronic electrical or photovoltaic stimulation. Excessive electrical stimulation can cause cell electroporation, cell death, tissue inflammation and swelling²⁸⁶. In case of photovoltaic retinal prosthesis, an excessive light stimulation can additionally damage the retina through photothermal, photomechanical and photochemical mechanisms²⁸⁷; and ophthalmic devices must respect the maximum permissible exposure (ANSI Z136.1 / ISO 60825 / ISO 15004) and maximum thermal increase (ISO 14708-1:2014 / EN 45502-1:1997) defined by international standards. Indeed, the use of photic energy either from the ambient light or from a light beam of specific wavelength allows to stimulate retinal cells at a high rate of information and/or to avoid the need of extrinsic power supply, but the transfer of photic energy to the retinal tissue can be toxic under excessive conditions. First, when photons are absorbed by a semi-conducting material, it increases the mean kinetic energy of the material's molecules, that collide and make temperature locally increase. The temperature rise may denature cellular membranes and proteins and trigger cells' apoptosis^{288–290}. The ability of a light beam to cause an increase

in kinetic energy and thus in temperature is inversely proportional to its wavelength: for a given exposure time, shorter wavelengths close to the UV spectrum have a greater risk to cause photothermal tissue damage than near-infrared light. The retinal tissue is irreversibly damaged when temperature rises by at least 10° C, but safety standards limits the chronic temperature rise to 2° C²⁹¹. Second, the light beam can induce photomechanical damage by thermoelastic expansion of the cells it hits. Tensile forces exerted on the cells lead to permanent damage and cell death. Third, the prolonged retinal tissue exposure to high energy light risks to generate reactive oxygen species, presumed to be the source of photochemical damage. Reactive oxygen species are produced when a cell directly absorbs light, and are susceptible to induce protein oxidation and trigger apoptotic mechanisms. PECs and photoreceptors, that have an inherent ability to absorb light, are especially vulnerable to this mechanism^{292–295}. Safe irradiance levels thus can be calculated according to the wavelength, exposure time, stimulation frequency and implant materials (*cf.* Section 2.5.9). It is worth to mention that the safety standards for ophthalmic devices are based on photochemical damage risk, that primarily threaten photoreceptors and PECs. Higher irradiances might be tolerated in end-stage degenerative diseases²⁹⁶.

Another point to be considered for biocompatibility are the residual photosensitive cells that survive in late blind patients. A typical symptom of *Retinitis Pigmentosa* is a marked photophobia, especially under short-wavelength light^{297–299}. It is hypothesized to originate from surviving cells S-cones and intrinsically photosensitive retinal ganglion cells (ipRGCs), that both respond to short-middle wavelengths^{300,301}. While residual and prosthetic vision seem to be complementary when they are spatially mutually exclusive¹², there is no data to date on the outcome of their overlap. Moreover, repeated stimulation is expected to generate some changes in the retinal physiology. Increases in surviving cells have been reported after retinal stimulation *in-vivo*, related to growth factor production^{180,302}. Retinal remodeling is also likely to be affected by the restoration of a form of sensory input, as *in-vitro* experimental results revealed the potential of electrical stimulation to guide neurite outgrowth^{303–305}.

In general, the interaction of prosthetic stimulation with remaining vision is a major biocompatibility challenge, for which no answers can be currently provided, either in term of photophobia, remodeling, or stimuli integration.

1.3.4 Challenges for next generation implants: summary and prospects

The restoration of sight with visual prostheses was a mere dream a century ago. Early patients' trials have demonstrated the undeniable potential of retinal prosthesis approaches to generate visual perception in late blind patients with no light perception. Yet, the retinal approaches have several disadvantages which are question marks hanging over the future of the field. It is only with research efforts on those points that blind patients may have a chance to draw satisfactory benefits from retinal prostheses in the long run and on a wider scale.

The first question mark is the cell survival and retinal remodeling in retinal degenerative diseases. There is strong evidence of synaptic reorganization in the animal models of retinal degeneration but also in human *Retinitis Pigmentosa* patients, sometimes even prior to photoreceptors death^{106,107,119,115}. Reorganization of the INL connectivity and formation of synaptic loops in microneuromas risks to compromise the efficacy of network-mediated stimulation, modify known stimulation parameters, or distort evoked percepts. The necessity of considering retinal reorganization has been raised by multiple authors^{119,306,98,180,136,43,307,64}. Yet, how systematic is such remodeling and to what extent it varies across genotypes and across the retina in humans are still question marks. The differences between murine models of retinal degeneration and the primate retina are considerable: presence of a macula, Bruch's membrane thickness, receptive field sizes, and unknown translatability of animal homologous diseases genotypes^{308,309}. In-depth knowledge of the remodeling in human retinal degenerative diseases – including the role of genotype and the consequences of joined remodeling and electrical stimulation – are necessary to determine if, in which cases, and during which time window prosthetic therapies can be used to their full potential.

Furthermore, the success and the resolution of retinal implants depend on the number of surviving RGCs to be stimulated. Epiretinal approaches relying on direct RGCs stimulation might to some extent avoid remodeling issues, but not the cell survival question. The preservation of significant numbers of RGCs and bipolar cells in both late stage *Retinitis Pigmentosa* and AMD patients has been documented^{95,97}. Still, the minimum requirements – number, location, connectivity – for successful prosthetic stimulation are not known. At present, candidate patients for retinal implants are primarily selected based on their absence of residual vision and their ocular structural integrity¹²⁶. Pre-operative OCT scans may be the first indicators of the degree of retinal degeneration, but RGC counts and fine retinal imaging might be necessary to predict the stimulability of the retinal tissue. Several groups are developing *in-vivo* microscopy approaches to image the neural retina^{310,311}.

Beyond the issue of patients' selection criteria, all prosthesis approaches evoked so far face technical engineering challenges that directly hamper patients' experiences. Those challenges can be of two natures: the design approach of the prosthesis (the form of image capture, processing, powering, the materials used, the number of electrodes that can be fitted, the implant size, etc.), and how it interacts with the intrinsic retinal processing (the target cells, and the processing mechanisms triggered). The most frequently encountered issues at the design levels are the wired data transmission (limiting the number of electrodes and increasing the inflammatory risk), the need for extrinsic powering, the presence of extraocular cases (at the source of conjunctival erosion), and the limited size of the array (due to limited scleral incision during surgery and poor conformability). These issues can be partially addressed and overcome: photovoltaic devices encode the command pattern with light beams, that bypasses the data transmission

and electrode limitations, the PRIMA implant additionally avoids extrinsic powering thanks to amplifying photodiodes in series^{196,194}, EPI-RET 3 implant solved the problem of extraocular cases by embedding its inductive receiver and stimulation unit in an intraocular lens¹⁶⁶, and implantation of multiple stimulating modules has been proposed to cover a larger retinal surface via a unique incision^{312,313}. There is thus far no technical solution concurrently addressing all these issues.

The compromises that were made in existing implants' designs have direct consequences on the visual restoration they can offer. Epiretinal implants can cover a large visual field but with limited resolution and reduced biocompatibility, as most of them rely on extrinsic powering and data processing, thus on several implanted elements and limiting cables (**Appendix Supplementary Table 1**). Alpha-AMS and PRIMA subretinal photovoltaic implants can restore a high visual acuity (20/546 and 20/460), but with a restricted visual field, which might be useful for AMD patients but not to rod-cones dystrophy ones. The accessibility of the suprachoroidal space makes it feasible to implant several arrays to cover a larger visual field, but can only offer a poor resolution due to the electrode distance to the INL.

In fact, both visual acuity and visual field are necessary to offer day-to-day visual functioning. Self-reporting questionnaires and simulated prosthetic vision studies demonstrated the importance of both visual parameters in daily tasks performances^{314-316,14,317,279}. As things currently stand, the cognitive load required from implant recipients to adapt to artificial vision is not balanced by the restored visual functions. Although retinal implants provide some quantified help in object recognition, motion detection, or deciphering ability, it is qualitatively not sufficient for patients to use them in a long-term basis²⁷⁰. To meet the visually impaired patients' needs, the next generation of retinal implants must be able to address visual field and visual resolution challenges together in their design.

In addition, the engineering of retinal prosthesis must factor the intrinsic electrical and networking properties of the tissue it interfaces. There are two major drawbacks related to the intrinsic retinal cells' properties. The first issues lies in the excitability of RGCs axons running towards the optic disk. Involuntary axonal stimulation leads to distorted phosphenes and impair the vision resolution, especially in the peripheral visual field, but also in the macula, due to the papillomacular bundle^{234,271}. Second, the desensitisation of the inner retinal cells in response to repeated stimulation makes phosphenes fade in less than few hundreds of milliseconds, which forces implanted users to constantly head scan their environment. Implants aiming at direct depolarization of RGCs from the epiretinal side are limited by the former, while implants aiming at network-mediated stimulation of RGCs by the latter. In practice, both issues can be encountered with epiretinal stimulation, possibly stimulating RGCs through both direct and indirect mechanisms^{232,268}. Adequate stimulation paradigms are thus necessary to limit both drawbacks. Stimulation site, stimulation thresholds or pulses durations have been identified as available tools to do so – in an exploratory fashion^{318,237,235}. Complementing frontier research and a better understanding of the mechanisms behind retinal network activation could allow to design better network-oriented stimulation paradigms.

The current thesis presents a novel approach for retinal stimulation that can address some of the key challenges of visual restoration: visual field, visual acuity, compliance and compatibility, and functional usability. Such approach is based on organic photovoltaics, flexible materials' use, and indirect RGCs stimulation from the epiretinal side (**Appendix Supplementary Table 1**).

In order to resolve the conflict between resolution and visual angle, an innovative epiretinal photovoltaic prosthesis has been developed, based on the ability of organic polymers to generate light-induced activity in neurons^{319,320}. The design approach that allows to address such quantitative aspect of vision restoration are explored in Chapter 2.

This work also strives to develop a network-oriented approach, *i.e.* to factor the intrinsic properties of vision and retina on a basis of stimulation paradigms. In this perspective, Chapter 3 explores the role of photovoltage waveform on the retinal network activation, including the overlooked inhibitory network.

It emerges that improving a prosthesis' resolution can be done in two complementary ways: ensuring a design with a high density of independent stimulating channels, and taking advantage of the intrinsic spatial processing in the retina. Further improvement of the stimulation resolution is presented in Chapter 4, that details the design of a high-resolution epiretinal photovoltaic prosthesis and the activation resolution it can provide *in-vitro*.

Finally, Chapter 5 addresses the desensitisation issue and proposes network-oriented tools to reduce RGCs' response fading.

Chapter 2 Design and validation of a foldable and photovoltaic wide-field epiretinal prosthesis

Postprint version of the article published in Nature Communications vol. 9, 2018 (DOI: 10.1038/s41467-018-03386-7).

Authors: Laura Ferlauto^{a, ‡}, Marta J. I. Airaghi Leccardi^{a, ‡}, Naïg A. L. Chenais^{a, ‡}, Samuel G.A. Gillérion^a, Paola Vagni^a, Michele Bevilacqua^a, Thomas J. Wolfensberger^b, Kevin Sivula^c and Diego Ghezzi^a.

^a Medtronic Chair in Neuroengineering, Center for Neuroprosthetics, Institute of Bioengineering, School of Engineering, École Polytechnique Fédérale de Lausanne, Switzerland

^b Hôpital Ophtalmique Jules Gonin, Université de Lausanne, Switzerland

^c Laboratory for Molecular Engineering of Optoelectronic Nanomaterials, Institute of Chemical Sciences and Engineering, School of Basic Science, École Polytechnique Fédérale de Lausanne, Switzerland

[‡] These authors contributed equally to this work.

Authors contributions: L.F. fabricated the devices and performed/analysed KPFM, PV/PC, temperature, and accelerated ageing tests. M.J.I.A.L. designed, fabricated, and characterized the devices and the retinal prostheses; she performed/analysed PV/PC measures and electrical simulations. N.A.L.C. performed/analysed pH, voltage spreading, and electrophysiological experiments. M.B. performed/analysed PV and PC measures. S.C.A.G. performed thermal simulations. T.J.W. performed the simulated surgeries. P.V. performed the simulated surgeries. K.S. participated in the fabrication and characterization of the prostheses. D.G. designed and led the entire study, validate the data analysis, and wrote the manuscript. All the authors read and accepted the manuscript.

2.1 Abstract

Retinal prostheses have been developed to fight blindness in people affected by outer retinal layer dystrophies. To date, few hundred patients have received a retinal implant. Inspired by intraocular lenses, we have designed a foldable and photovoltaic wide-field epiretinal prosthesis (named POLYRETINA) capable of stimulating wireless retinal ganglion cells. Here we show that within a visual angle of 46.3 degrees, POLYRETINA embeds 2215 stimulating pixels, of which 967 are in the central area of 5 mm, it is foldable to allow implantation through a small scleral incision, and it has a hemispherical shape to match the curvature of the eye. We demonstrate that it is not cytotoxic and respects optical and thermal safety standards; accelerated ageing shows a lifetime of at least 2 years. POLYRETINA represents a significant progress towards the improvement of both visual acuity and visual field with the same device, a current challenging issue in the field.

2.2 Introduction

Blindness affects more than 30 million people worldwide³²¹, and it is defined as visual acuity of less than 20/400 or a corresponding visual field loss to less than 10 degrees, in the better eye with the best possible correction¹⁶. In North America and most of European countries, legal blindness is defined as visual acuity of 20/200 or visual field no greater than 20 degrees. In the last decade, various visual prostheses have been developed to fight blindness in case of retinal dystrophies, such as *Retinitis Pigmentosa*⁹⁹ and more recently Age-related Macular Degeneration (Clinical Trial NCT02227498). Several multi-center clinical trials showed the feasibility of restoring a coarse form of vision with retinal implants, such as single letters discrimination and simple objects recognition^{158,186}. However, several challenges remain open, such as the improvement of visual acuity and the enlargement of the visual field above the thresholds of blindness¹⁹³. An agreed upon strategy to improve visual acuity is to increase the electrode density, while a large visual field could be attained by enlarging the retinal coverage with a larger prosthesis.

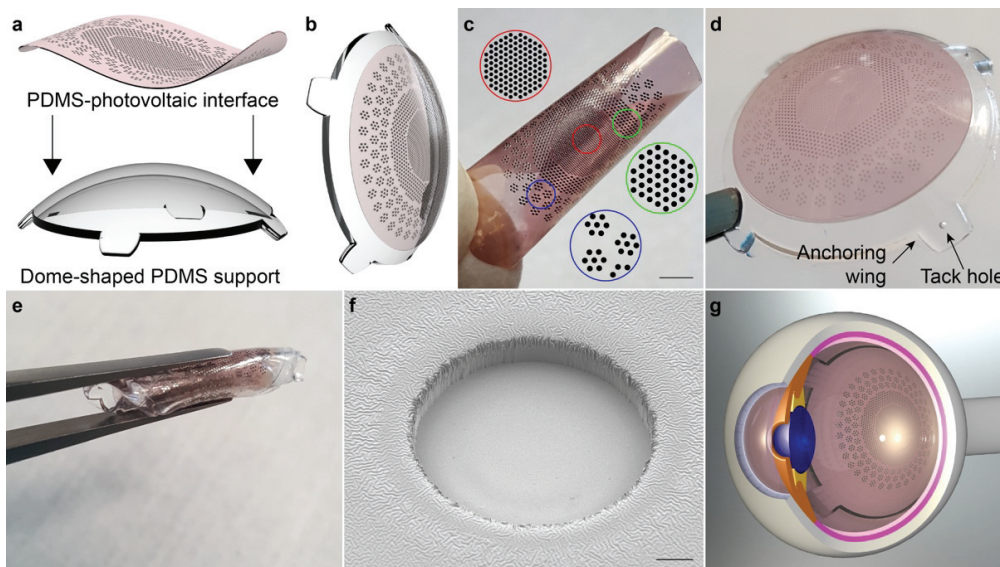
Concerning the visual field, tests on healthy subjects under pixelated vision indicated that an array of 25 × 25 pixels and 30 degrees of visual angle (about 8.5 mm in diameter) could provide adequate mobility skills^{281,322}. However, the size of the prosthesis is typically limited by the maximal allowed sclerotomy, which is about 6 to 7 mm long; available prostheses are therefore in the range of 1 to 5 mm. Argus® II, the largest implanted electrode array in humans, is a 6 × 10 array with a 575 μm electrode pitch¹⁵⁸ and a theoretical field of view of 10 × 18 degrees. Increasing the size of the array is associated with two main challenges: it requires a large scleral incision and it may not conform to the eye curvature. In a flat prosthesis placed over the retina, central and peripheral electrodes may not be at the same distance from the retina. A large distance will inevitably increase the stimulation threshold and the cross-talk between adjacent electrodes³²³. Preliminary attempts in designing wide-field retinal prosthesis have been proposed^{167,323}. However, these approaches are based on materials (*i.e.* polyimide) with high elastic modulus (GPa), very thin substrates (*i* 10 μm), and complex shapes (*e.g.* star) that could create challenges in manipulation, implantation, and fixation.

Concerning visual acuity, previous researches estimated that, to be useful in daily life, a retinal prosthesis should have 500 pixels distributed in the central area of approximately 5 mm in diameter^{324,325}. More recently, a trial on healthy subjects showed that the number of pixels required to recognize common objects is on the order of 3,000 to 5,000³²⁶. Despite microfabrication techniques allow such electrode density, a limitation remains due to the routing of the connection tracks in the active area and the size of the flat cable connection to the implantable electronics/stimulator. To overcome these issues, in photovoltaic stimulation¹⁹⁶, the light projected into the pupil is wirelessly converted into electrical stimuli delivered to the retina. After the first demonstration of vision restoration in blind rats with a silicon photovoltaic subretinal prosthesis¹⁹⁴, a second major step was achieved with the exploitation of conjugated polymers and organic semiconductors (*i.e.* poly(3,4-ethylenedioxythiophene)-poly(styrenesulfonate), PEDOT:PSS; regioregular poly(3-hexylthiophene-2,5-diyl), P3HT; [6,6]-phenyl-C61-butyric acid methyl ester, PCBM) to build an organic photovoltaic subretinal interface^{319,327,328}. In the latter, despite the capability of improving visual acuity in dystrophic rats after 1 month of implantation³²⁰, several issues remain unsolved. Conjugated polymers are well tolerated when exposed to the subretinal space³²⁹, but they start to delaminate a few months after placement leading to an unavoidable degradation of the organic materials. Moreover, in the cases of both silicon and organic photovoltaic subretinal prostheses, the limited size of the devices (1 to 2 millimetres) will not allow the recovery of a large visual field, unless implanting multiple devices³¹². Some concerns remain about the risks associated with the implantation of multiple devices in the subretinal space (*e.g.* retinal detachment, movements of the devices, and device overlaps). Thus, increasing both visual acuity and visual field size with a single retinal prosthesis remains one of the main unsolved challenges in the field³²⁴.

2.3 Results

2.3.1 Design and fabrication

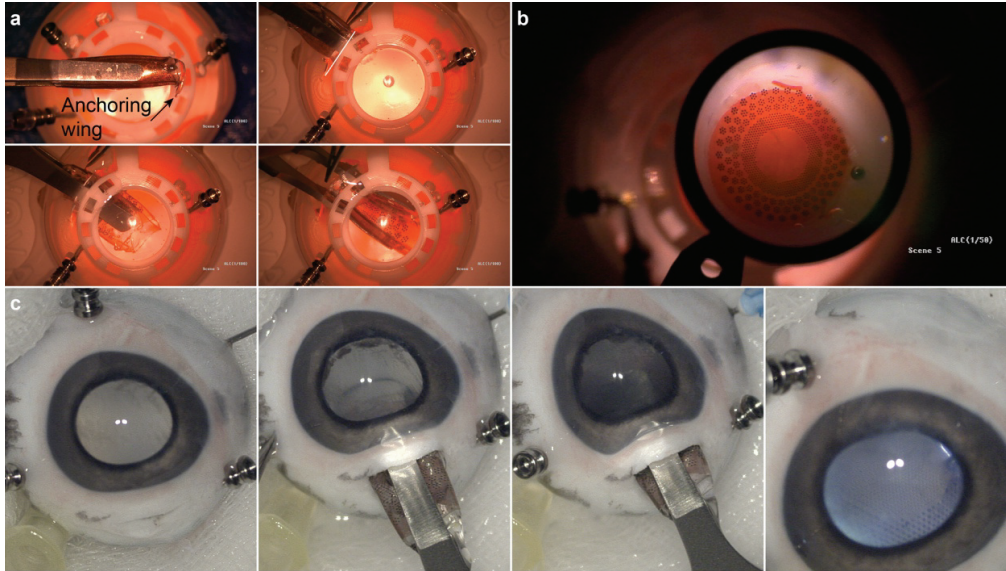
POLYRETINA is a novel foldable and photovoltaic wide-field epiretinal prosthesis based on poly(dimethylsiloxane) (PDMS) as substrate material, because of its transparency, elasticity, low Young's modulus, and high strain to failure^{330,331}. Moreover, PDMS is available as medical grade elastomer already in use in medical device applications. The device consists in a PDMS-photovoltaic interface (**Figure 1a,c**), embedding 2215 stimulating pixels (80 μm and 130 μm in diameter) distributed on an active area of 12.7 mm (**Supplementary Figure 1a**). Each pixel is composed by a PEDOT:PSS bottom anode, a P3HT:PCBM (referred also as Blend) semiconductor layer, and a top cathode in titanium (Ti). Another PDMS layer encapsulates the prosthesis, avoiding the delamination and degradation of the organic materials and extending its lifetime (**Supplementary Figure 1b**). Openings of 67 and 120 μm in diameter have been made in the encapsulation layer to expose the cathodes (**Figure 1f**). Titanium is a mechanically and electrochemically stable metal, it is widely used in implantable devices, it has an appropriate work function for the photovoltaic mechanism, and it is a capacitive charge-injection material (also due to the thin layer of titanium oxide formed at the surface). The latter is desirable with mono-phasic pulses, as in this photovoltaic approach, because no chemical species are created or consumed during a stimulation pulse³³², thus avoiding undesired tissue reactions. Under this condition, the electrode/electrolyte interface can be modelled as pure electrical capacitor without electron transfer from the metal to the solution³³³. To verify this hypothesis, we measured the pH with a microelectrode positioned above the titanium electrode of the PDMS-photovoltaic interface (**Supplementary Figure 2**) upon 1 hr of pulsed illumination (20 Hz, 10 ms, 3.4 mW mm^{-2} ; $N = 3$ devices). The irradiance has been set to a value above the maximum allowed for prosthetic application (see Optical and thermal safety). During illumination, a negligible pH shift of about 0.002 pH units has been detected, which could be explained by a recording artefact due to the local temperature increase induced by the prosthesis (see Optical and thermal safety). Local heating could reduce the resistivity of the solution and decrease the voltage difference between the pH microelectrode and the local reference. The hemispherical shape of POLYRETINA (**Figure 1b,d**) is obtained by bonding the PDMS-photovoltaic interface on a dome-shaped PDMS support (**Figure 1a**) with a radius of curvature of 12 mm, corresponding to the standard human eye. The bonding induces a radial elongation in the PDMS-photovoltaic interface of about 3% (in diameter), which has been considered to determine the covered retinal surface (**Supplementary Figure 1c**). Four anchoring wings, with holes for tacks, have been included for the fixation of the prosthesis (**Figure 1d**).



Ch.2 Figure 1 - Foldable and photovoltaic wide-field retinal prosthesis

a, 3D model of the fabricated PDMS-interface and of the dome-shaped PDMS support. **b**, 3D model of the retinal prosthesis after bonding the PDMS-photovoltaic interface to the PDMS support. **c**, Fabricated PDMS-photovoltaic interface with pixels arranged in 3 areas of different sizes and densities: central area (red), diameter of 5 mm, 967 electrodes in hexagonal arrangement, electrode diameter 80 μm and pitch 150 μm , density 49.25 px mm^{-2} ; first ring (green), diameter of 8 mm, 559 electrodes in hexagonal arrangement, electrode diameter 130 μm and pitch 250 μm , density 17.43 px mm^{-2} ; second ring (blue), diameter 12.7 mm, 719 electrodes, electrode diameter 130 μm , density 9.34 px mm^{-2} . Circles show an enlarged view of the pixels distribution. Scale bar is 2.5 mm. **d**, Picture of POLYRETINA. Four anchoring wings with holes are present for attaching the prosthesis with retinal tacks. **e**, POLYRETINA folded before injection. **f**, Scanning electron microscope image (40° tilted view) of a photovoltaic pixel. Scale bar is 10 μm . **g**, 3D model after epiretinal placement.

The folding of POLYRETINA, its insertion, and covering of the retinal surface have been evaluated in simulated surgeries with plastic models of the human eye (**Figure 2a**). The prosthesis can be folded prior implantation (**Figure 1e** and **Figure 2a**, top-left), inserted through an aperture of 6.5 mm (**Figure 2a**, top-right), released within the posterior chamber (**Figure 1g** and **Figure 2b**, bottom-right and bottom-left), and attached in epiretinal configuration (**Figure 2b**). The same surgical approach has been also validated in enucleated pig eyes (**Figure 2c**).

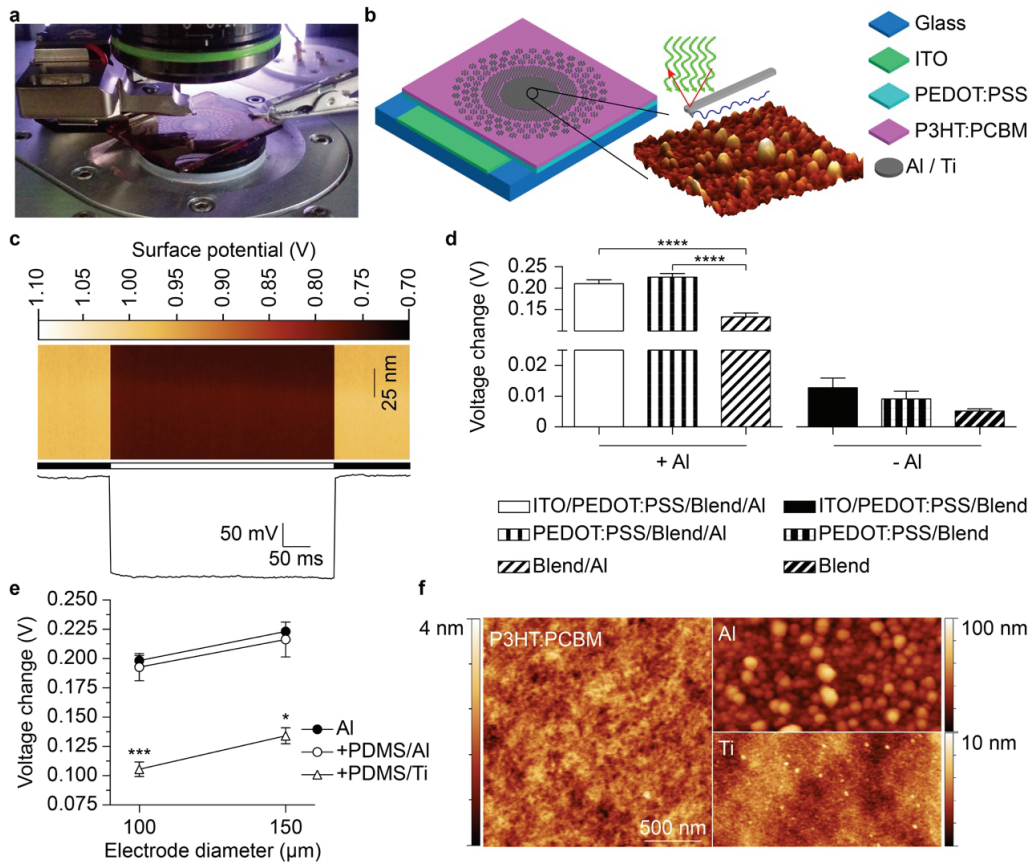


Ch.2 Figure 2 - Simulated surgical implantation

a, Picture sequence of the implantation in a human eye plastic model. The white line in top-right panel shows the incision of 6.5 mm. b, Picture of POLYRETINA placed in epiretinal configuration. c, Picture sequence of the implantation in a pig eye.

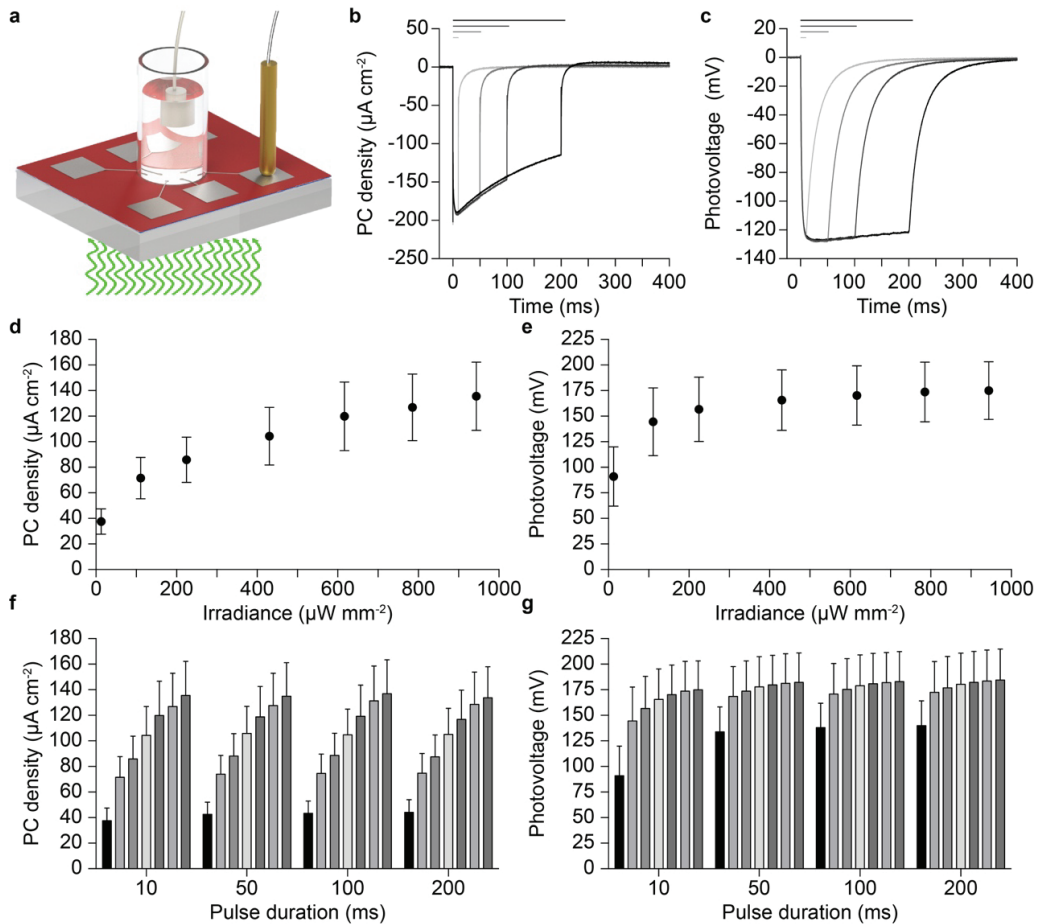
2.3.2 Optimization of the photovoltaic pixel

First, using Kelvin Probe Force Microscopy (KPFM), we evaluated the changes in the surface potential generated at the cathode upon illumination for different conditions of fabrication (**Figure 3a,b**). To assess the role of the bottom anode, we fabricated photovoltaic interfaces onto glass substrates including a bottom anode made of Indium Tin Oxide (ITO), an injection layer of PEDOT:PSS, a semiconductor layer of P3HT:PCBM, and aluminum (Al) top cathodes. We initially used aluminum since it is one of the most common cathode material in organic photovoltaics. KPFM measures (**Figure 3c**) across several devices showed that the variation of the surface potential upon illumination (white LED, light from the top, 0.4 mW mm^{-2}) is about 15 folds higher (**Figure 3d**) with aluminum cathodes with respect to P3HT:PCBM only. When aluminum is present (**Figure 3d**, left), the absence of any anode (ITO or ITO/PEDOT:PSS) significantly reduces the surface potential variation upon illumination (ITO/PEDOT:PSS/Blend/Al versus Blend/Al, $p < 0.0001$; PEDOT:PSS/Blend/Al versus Blend/Al, $p < 0.0001$; One Way ANOVA, Tukey's multiple comparison test). No significant difference has been found with or without the ITO anode if the PEDOT:PSS injection layer is present (ITO/PEDOT:PSS/Blend/Al versus PEDOT:PSS/Blend/Al, $p = 0.6219$; One Way ANOVA, Tukey's multiple comparison test). In the absence of aluminum cathodes (**Figure 3d**, right), the architectures with different bottom anodes do not induce any significant difference (ITO/PEDOT:PSS/Blend versus PEDOT:PSS/Blend, $p = 0.9997$; ITO/PEDOT:PSS/Blend versus Blend, $p = 0.9890$; PEDOT:PSS/Blend versus Blend, $p = 0.9995$; One Way ANOVA, Tukey's multiple comparison test). The maximization of the surface potential variation has been obtained with aluminum cathodes and both ITO/PEDOT:PSS or only PEDOT:PSS anodes. Therefore, to simplify the fabrication process, we implemented PEDOT:PSS alone as bottom layer. We also verified that the surface potential variation was not altered (**Figure 3e**) when the interface was built over a PDMS substrate instead of bare glass with aluminium cathode diameters of both $100 \mu\text{m}$ and $150 \mu\text{m}$ (● PEDOT:PSS/Blend/Al and ○ PDMS/PEDOT:PSS/Blend/Al); no statistical differences have been found among the groups (Two Way ANOVA, Tukey's multiple comparison test, interaction $p = 0.9633$; factor 1, diameter, $p = 0.0887$; factor 2, substrate, $p = 0.6385$). When titanium replaces aluminium (Δ PDMS/PEDOT:PSS/Blend/Ti), the surface potential is slightly reduced (for $100 \mu\text{m}$: One Way ANOVA, $F = 25.43$, $p < 0.001$; PDMS/PEDOT:PSS/Blend/Ti versus both PEDOT:PSS/Blend/Al and PDMS/PEDOT:PSS/Blend/Al, $p < 0.001$, Tukey's multiple comparison test; for $150 \mu\text{m}$: One Way ANOVA, $F = 9.266$, $p < 0.01$; PDMS/PEDOT:PSS/Blend/Ti versus both PEDOT:PSS/Blend/Al and PDMS/PEDOT:PSS/Blend/Al, $p < 0.05$, Tukey's multiple comparison test).



KPFM measurements have been performed in air in non-contact mode; therefore, the measured variations in the surface potential may be slightly different with respect to the electric potential generated by the double layer capacitive charging occurring at an electrode-electrolyte interface, as in the case of an implanted retinal prosthesis. Therefore, we measured the photo-current (PC) and the photo-voltage (PV) generated in the presence of electrolyte solution upon illumination. We fabricated chips embedding 6 electrodes, each of them connected to a contact pad for measuring the signal with respect to an Ag/AgCl reference electrode immersed in solution (Figure 4a). Both PC and PV have been measured with illumination (565 nm) at increasing light intensities (12.75, 111.11, 225.00, 430.56, 616.67, 785.65, and 943.98 $\mu\text{W mm}^{-2}$) and pulse duration (10, 50, 100, and 200 ms). The PC (Figure 4b) generated by pulsed illumination (943.98 $\mu\text{W mm}^{-2}$) has a typical capacitive profile, peaking in about 10 ms and then decreasing with an exponential decay, while the PV (Figure 4c) reaches a steady-state value and remains constant. This is in agreement with the capacitive nature of the electrode/electrolyte interface. Moreover, the PV generated (about 180 mV) is largely below the redox potential of titanium (or titanium oxide), thus ensuring that no irreversible reactions occur at the interface. The PC density increases with irradiance, with a mean (\pm s.e.m.) peak value of 135.51 ± 26.74 $\mu\text{A cm}^{-2}$ (10 ms) for 943.98 $\mu\text{W mm}^{-2}$ (Figure 4d,f). According to

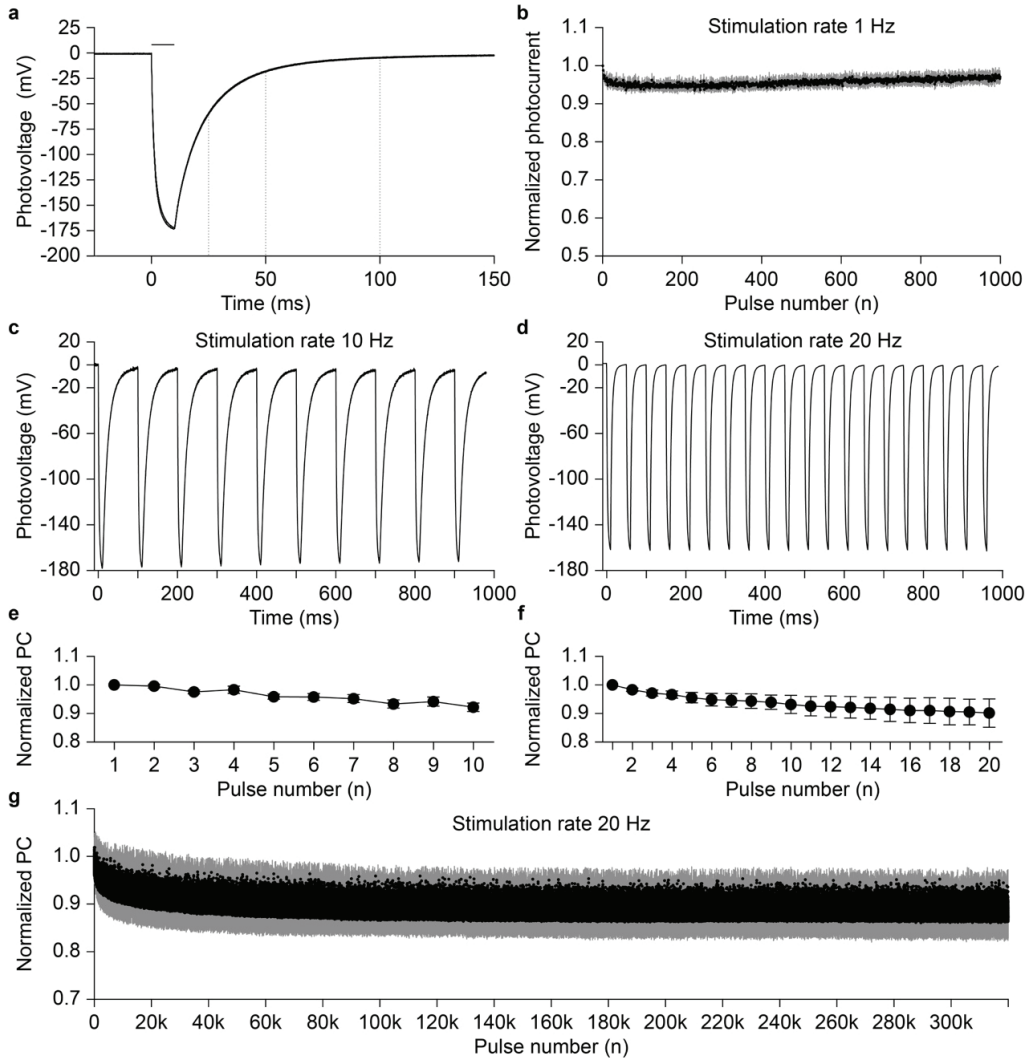
the literature in the field²², these current values should be able to induce epiretinal stimulation of retinal ganglion cells (RGCs). The slope of the PC density profile is decreasing while increasing irradiance, and a saturation of the response could be expected for irradiance higher than 1-2 mW mm⁻². We also measured the PC density (10 ms, 943.98 μW mm⁻²) after 48 hrs of immersion in physiological solution (stored in dark). The mean (± s.e.m.) ratio before/after has been measured in 94.44 ± 12.28 %, 95.11 ± 13.07 %, 93.36 ± 13.26 %, 94.99 ± 12.48 % respectively for 10 ms, 50 ms, 100 ms, and 200 ms pulses; no significant differences have been found (10 ms: p = 0.4423; 50 ms: p = 0.5798; 100 ms: p = 0.5798; 200 ms: p = 0.5526; N = 3 devices, n = 6 electrodes per device; Wilcoxon matched-pairs signed rank test).



a, Drawing of the experimental setup for the measure of PC and PV; the light pulse comes from the bottom. **b,c**, Examples of PC density (**b**) and PV (**c**) measures obtained from 1 electrode (diameter 100 μm) at maximal light intensity (565 nm, 943.98 μW mm⁻²) and for increasing pulse durations (10, 50, 100, and 200 ms). Horizontal bars represent the light pulses. **d,e**, Mean (± s.e.m.) PC density (**d**) and PV (**e**) measured upon illumination with 10 ms pulses at increasing light intensities. **f,g**, Mean (± s.e.m.) PC density (**f**) and PV (**g**) measured for increasing light intensities (12.75, 111.11, 225.00, 430.56, 616.67, 785.65, and 943.98 μW mm⁻²) and pulse durations (10, 50, 100, and 200 ms). In panels **d** to **g**, the PC density and PV on every device (N = 3) has been measured for all electrodes (n = 6) and data have been averaged.

Ti-based photovoltaic electrodes show a full discharge (97.7 %) after 100 ms (**Figure 5a**) when illuminated with 10 ms pulses (943.98 μW mm⁻²); while they are discharged of 65.4 % and of 89.9 % after 25 ms and 50 ms respectively. This suggests that POLYRETINA could operate in the 1-20 Hz range without the need of an external shunting resistor^{33,4}. To characterize the stimulation efficiency over repetitive stimuli, we measured the PC over 1,000 stimuli (**Figure 5b**) delivered at 1 Hz (10 ms, 943.98 μW mm⁻²). The mean (± s.e.m.) steady state response (average of the last 20 pulses / first response) is almost unchanged (96.99 ± 1.51 %). At a higher stimulation frequency, such as 10 Hz, the electrodes are entirely discharged between pulses (**Figure 5c**), therefore the PC density is not largely affected by repetitive stimulations; in a train of 10 pulses at 10 Hz, the mean (± s.e.m.) ratio last/first responses is 92.20 ± 1.52 % (**Figure 5e**). Also, in a train of 20 pulses at 20 Hz, the mean (± s.e.m.) ratio last/first responses is 90.21 ± 4.96 % (**Figure 5f**). Given the possibility to stimulate at 20 Hz, we tested Ti-based photovoltaic electrodes over a long operation period (**Figure 5g**). Upon

320,000 stimuli (20 Hz, 10 ms, $943.98 \mu\text{W mm}^{-2}$), the stable steady state response (average of the last 1000 pulses / first response) is only slightly affected (88.6 %).

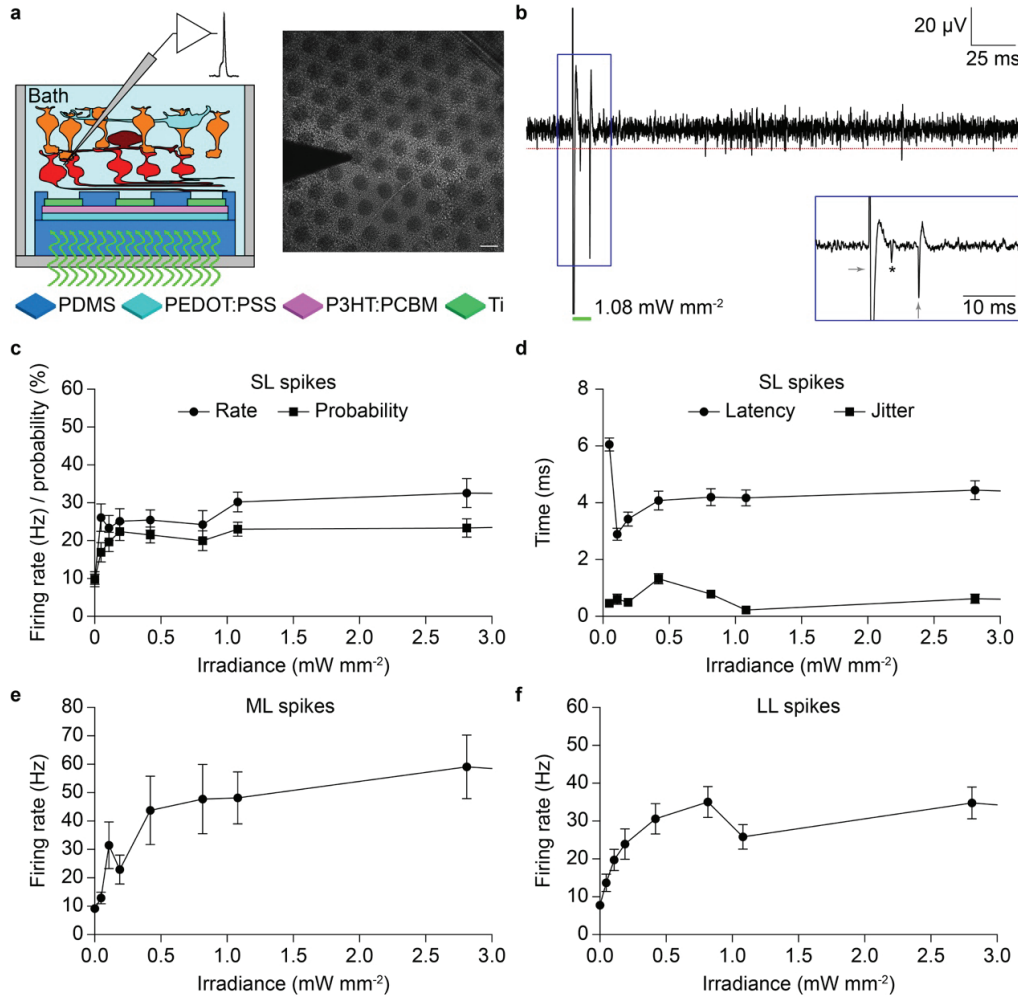


Ch.2 Figure 5 - High-frequency train stimulation

a, Mean PV trace obtained at maximal light intensity (565 nm, 10 ms, $943.98 \mu\text{W mm}^{-2}$). The trace is the mean of $N = 6$ devices; in which $n = 6$ electrodes have been measured and averaged. The horizontal bars represent the light pulse. The dotted lines highlight the discharging rate of the electrode. **b**, Evolution of the PC density peaks during 1,000 stimuli delivered at 1 Hz (10 ms, $943.98 \mu\text{W mm}^{-2}$). Each point is the mean (\pm s.e.m.) of $N = 3$ devices, in which $n = 6$ electrodes have been measured and averaged. **c**, Representative PV recording upon 10 pulses at 10 Hz (565 nm, 10 ms, $943.98 \mu\text{W/mm}^2$). **d**, Representative PV recording upon 20 pulses at 20 Hz (565 nm, 10 ms, $943.98 \mu\text{W mm}^{-2}$). **e**, Evolution of the PC density peaks normalized to the first pulse. Each point is the mean \pm s.e.m. of $N = 10$ devices, in which $n = 6$ electrodes have been measured and averaged. **f**, Evolution of the PC density peaks normalized to the first pulse. Each point is the mean \pm s.e.m. of $N = 8$ devices, in which $n = 6$ electrodes have been measured and averaged. **g**, PC generated with 320,000 stimuli delivered at 20 Hz (565 nm, 10 ms, $943.98 \mu\text{W mm}^{-2}$). Each point is the mean \pm s.d. of $n = 2$ electrodes from $N = 1$ device.

2.3.3 Validation *ex-vivo* with explanted retinas from blind mice

Next, we tested the *ex-vivo* efficacy of the PDMS-photovoltaic interface in stimulating RGCs. For this purpose, we used the *Retinal degeneration 10 (Rd10)* mouse model³³⁵, that is recognized as an excellent model for *Retinitis Pigmentosa*³³⁶. Extracellular recordings of prosthetic-evoked spiking activity of RGCs have been collected from retinas explanted from old mice to avoid as much as possible the natural responses from surviving photoreceptors ($n = 39$ cells, $N = 15$ mice; mean \pm s.d. age 140.87 ± 20.35 days). Retinas have been layered on the central 5 mm area of the PDMS-photovoltaic interface mimicking the epiretinal configuration (Figure 6a).



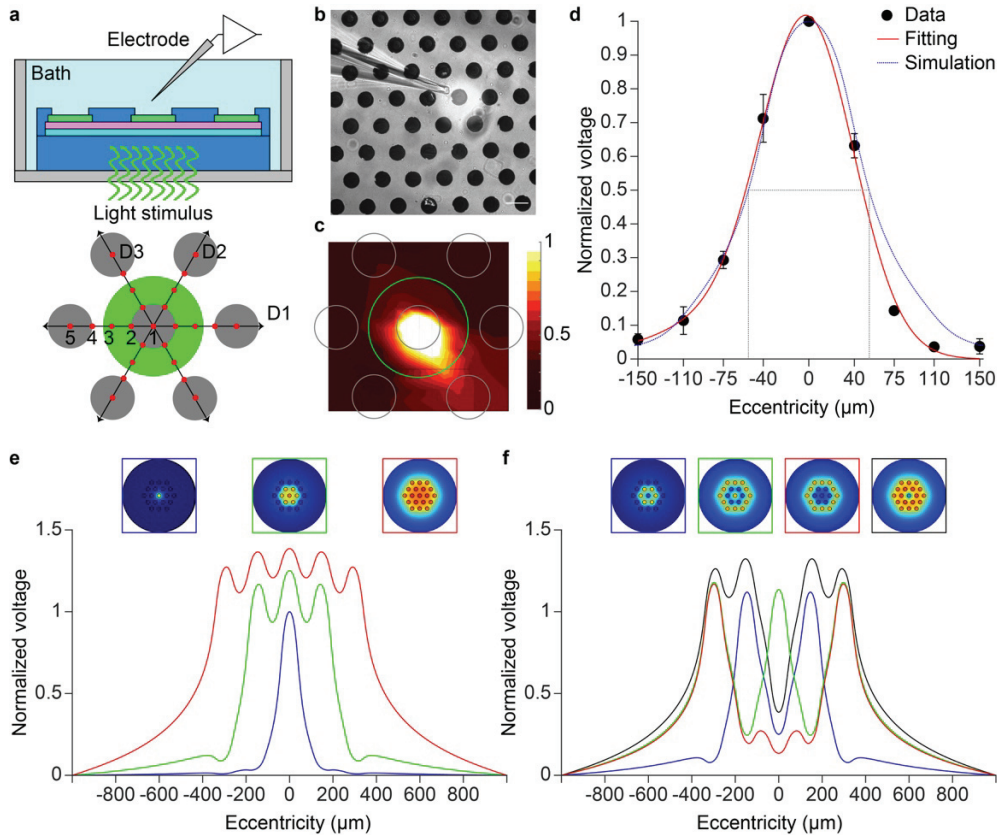
Ch.2 Figure 6 - Evaluation *ex-vivo* with retinal explants

a, Sketch of the recording set-up together with a picture of a retinal explant over the PDMS-photovoltaic interface with the metal electrode used for recordings. Scale bar is $100 \mu\text{m}$. b, Representative single-sweep recording from a retinal ganglion cell over PDMS-photovoltaic interface upon 10 ms illumination at $1081.7 \mu\text{W mm}^{-2}$. The red dotted line is the threshold set for spike detection. The green bar represents the light pulse. The blue insert shows a magnification of the period around the light pulse. The asterisk (*) indicates the over-threshold spike detected, while the grey arrows are the on-set and off-set stimulation artefacts. c, Mean (\pm s.e.m.) firing rate (\bullet) and firing probability (\blacksquare) of SL spikes, computed across all the recorded cells ($n = 39$, 10 sweeps each) on the PDMS-photovoltaic interface. For each cell, the probability has been defined as the percentage of sweeps with at least a SL spike over the 10 consecutive trials. d, Mean (\pm s.e.m.) latency (\bullet) and jitter (\blacksquare) of the first spike occurring in the 10 ms window after the light onset, computed across all the recorded cells ($n = 39$, 10 sweeps each) on the PDMS-photovoltaic interface. For each cell, the mean latency and jitter has been computed over the 10 consecutive trials. e, f Mean (\pm s.e.m.) firing rate of medium (e) and long (f) latency spikes, computed across all the recorded cells ($n = 39$, 10 sweeps each) on the PDMS-photovoltaic interface. In panels c-f values have been plotted up to 3 mW mm^{-2} , while the full profiles are shown in Supplementary Figure 3c-f.

According to the PC density measures, we tested only 10 ms pulses (peak of the PC response) with a broad range of irradiance (from $47.35 \mu\text{W mm}^{-2}$ to 29.07mW mm^{-2}). Light pulses induced a prosthetic-evoked spiking activity in the recorded RGC (**Supplementary Figure 3a** and **Figure 6b**). Spikes have been detected with a threshold algorithm (red lines in **Figure 6b** and **Supplementary Figure 3a**), converted into a raster plot (**Supplementary Figure 3a**, middle), and presented as peri-stimulus time histogram (PSTH; **Supplementary Figure 3a**, bottom). As previously reported³³⁷, we observed three types of responses, classified as short, medium, and long latency (SL, ML, and LL). The presence of SL spikes (elicited in the 10 ms window after the light onset, 1 bin) indicates a direct electrical stimulation of RGCs; while the presence of ML and LL spikes indicates a network-mediated activation. We have found that SL spikes can be evoked starting from the first irradiance tested ($47.35 \mu\text{W mm}^{-2}$), then the firing rate slowly increases and it remains stable above 1.08mW mm^{-2} till the highest irradiance tested (**Figure 6c** and **Supplementary Figure 3c**). However, the mean (\pm s.e.m.) latency (**Figure 6d**) at this first irradiance is relatively long (6.05 ± 0.23 ms); it decreases with the increase of the irradiance, and it stabilizes at 4.12 ± 0.07 ms for irradiance higher than 1.08mW mm^{-2} (**Figure 6d** and **Supplementary Figure 3d**). In this range (higher than 1.08), the mean (\pm s.e.m.) jitter of the first SL spike is 0.39 ± 0.05 ms. This suggests that the SL response is saturated for irradiance higher than 1.08mW mm^{-2} , as predicted by the measure of the PC densities. For irradiance lower than 1.08mW/mm^2 the mean latency appears shorter but the jitter is more variable, indicating a more instable response (**Figure 6d**). The firing rate of ML (**Figure 6e** and **Supplementary Figure 3e**) and LL (**Figure 6f** and **Supplementary Figure 3f**) spikes growth more progressively, but they also become stable after 1.08mW mm^{-2} . As a control, when retinas have been layered on bare PDMS substrates ($n = 34$, $N = 13$; 143.08 ± 32.09 days), no light-evoked responses have been detected for all the irradiance tested (**Supplementary Figure 3b** and **Supplementary Figure 4b**). As already demonstrated by others³³⁸, we also verified in a second subset of cells ($n = 6$, $N = 5$; 209.4 ± 37.14 days) that the prosthetic activation of both ML and LL spikes is abolished by using synaptic blockers (**Supplementary Figure 5**). This confirms the hypothesis that ML and LL are induced by the activation of the internal retinal circuit.

2.3.4 Spatial selectivity

We then addressed the spatial selectivity by using an experimental/computation hybrid approach. First, using a glass microelectrode (**Figure 7a,b**) we measured the radial voltage spreading in 3 directions (D1, D2, and D3) upon illumination of a single pixel (**Figure 7c**). For each illuminated pixel ($n = 4$ pixels), the normalized voltage spreading in the 3 principal directions have been averaged. The mean (\pm s.e.m.) voltage distribution across all the pixel tested has been plotted and interpolated with a Gaussian function (**Figure 7d**). Experimental data match with the normalized voltage profile obtained by a Finite Element Analysis (FEA) model (**Figure 7d**, dotted blue line). The Full Width at Half Maximum (FWHM) of the simulated curve (**Figure 7d**, dotted grey line) has been taken as the effective activation area, which is about $100 \mu\text{m}$. FEA simulations have been used to characterize the normalized voltage profile induced by illumination of increasing diameters (**Figure 7e**). Increasing the spot size from 1 pixel to 7 and 19 pixels increases the potential. Last, we simulate the effect of different patterns of activation (**Figure 7f**). In all cases, a spatially selective potential profile corresponding to light pattern is shown.



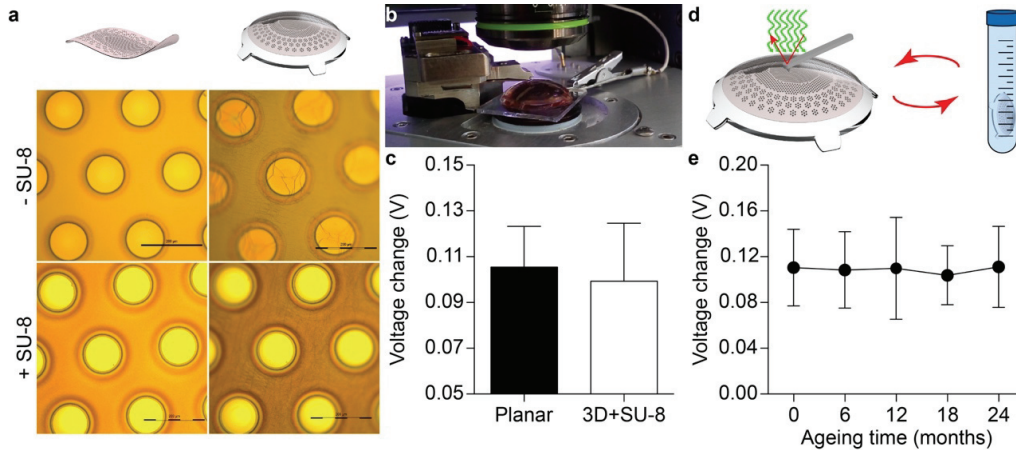
Ch.2 Figure 7 - Spatial confinement of the prosthetic stimulation

a, Sketch of the experimental setting. The green circle corresponds to the area illuminated around the central pixel. Grey circles represent the illuminated pixel and the 6 surrounding ones. The voltage has been measured in 9 positions (red dots) for each direction (D1, D2, and D3), all centered in the centre of the illuminated pixel. **b**, Picture during recordings. The light spot is visible (brighter area). The scale bar is 100 μm . **c**, Voltage spreading colour map generated by interpolating the experimental measures with a triangulation-based linear interpolation. At each point 10 consecutive recordings have been averaged and the voltage peaks have been normalized with respect to the value obtained in the central pixel (position 1 in **a**). The green circle is the illuminated area, while the grey circles represent the pixels. **d**, Mean (\pm s.e.m.) normalized PV peaks from $n = 4$ pixels. For each pixel, the data from the 3 directions have been averaged. The red line shows a Gaussian fitting, while the blue dotted line represents the normalized voltage profile obtained by FEA simulations. The grey dotted lines show the FWHM value for the simulated profile. **e**, FEA simulations for 3 beam sizes, normalized to the potential corresponding to the illumination of the single central pixel. **f**, FEA simulations for various patterns of activation normalized to the potential corresponding to the illumination of the single central pixel.

2.3.5 Cytotoxicity and long-term functioning

To validate the long-term functioning of POLYRETINA, we tested the mechanical impact of the hemispherical shape. For this purpose, the PDMS-photovoltaic interface has been bonded on the dome-shaped PDMS support. The bonding procedure induces tensile stresses in the PDMS-photovoltaic interface leading to the formation of cracks in the polymers and the titanium cathodes (**Figure 8a**, top row). To avoid cracks in the titanium cathodes, SU-8 rigid platforms³³⁹ have been integrated below each cathode in the substrate of the interface (**Supplementary Figure 1b**). With this precaution, the pixel above the SU-8 rigid platforms is protected from cracks (**Figure 8a**, bottom row); images correspond to the green area in **Figure 1c**. Cracks are still formed within the blend film in the area between SU-8 rigid platforms, however this is less critical since that area is encapsulated in PDMS to prevent delamination and the carriers photo-generated outside of the area defined by the cathode do not significantly contribute to the photo-potential/current generated at the electrode/electrolyte interface. Then, we measured the changes in the surface potential by using KPFM (**Figure 8b**). Due to the hemispherical shape, only the electrodes at the top of the prosthesis (80 μm in diameter / 67 μm openings) can be reached by the AFM tip. The surface potential change induced by illumination (white LED, light from the top, 0.4 mW mm^{-2}) is not statistically different (Mann-Whitney test, $p = 0.8182$) with respect to the planar PDMS-interface (**Figure 8c**). To simulate the lifetime of POLYRETINA once implanted, we performed a functional accelerating ageing test by immersion in physiological saline solution hold at 87 $^{\circ}\text{C}$ (**Figure 8d**). The changes of the surface potential upon illumination have been measured with KPFM before starting the ageing and at several time points during the protocol (**Figure 8e**). No statistically significant changes

in the mean (\pm s.d.) surface potential have been detected till 24 months of accelerated ageing (One Way ANOVA, $F = 0.1252$, $p = 0.9731$). Last, according to ISO 10993-5: Biological Evaluation of Medical Devices, *in-vitro* cytotoxicity has been evaluated via an extraction test on the murine fibroblastic L929 cells. Cell viability has been estimated via an XTT cell viability assay. Results on the prosthesis showed a 100 % viability, while positive control has 0.3 % viability and negative control has 100 % viability (averages of 3 repetitions; see Certificate in **Supplementary Information**).



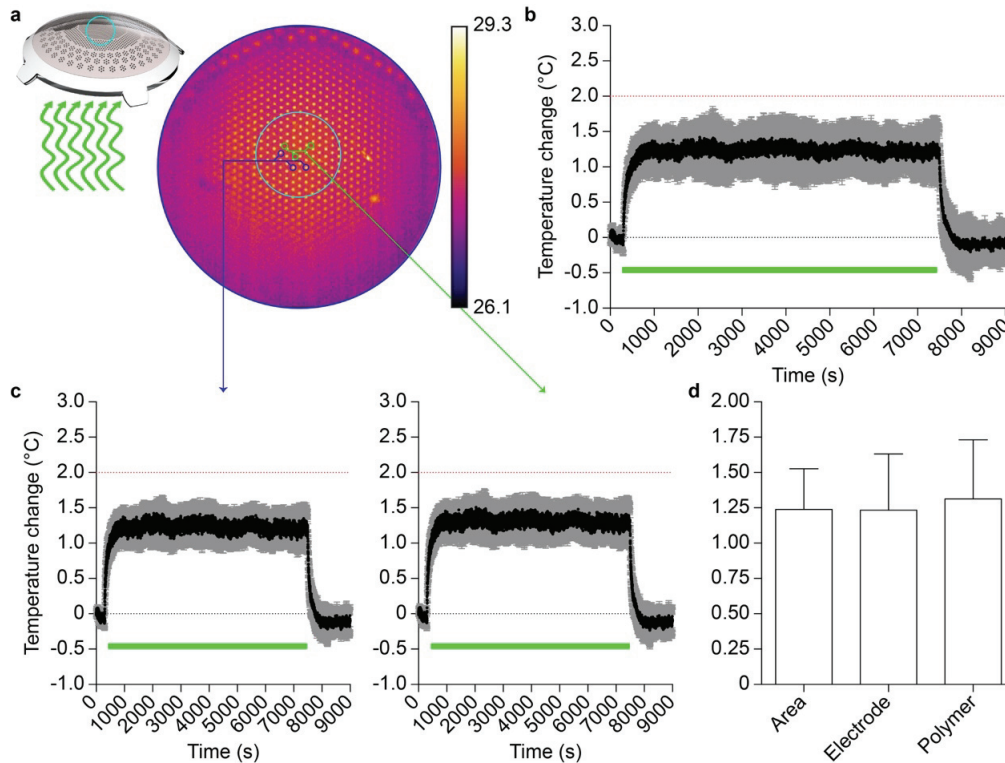
Ch.2 Figure 8 - Lifetime of the retinal prosthesis

a, Pictures of the titanium cathodes before (left column) and after (right column) bonding on the dome-shaped PDMS support. The top row is without SU-8 rigid platforms, while the bottom row is with SU-8 rigid platforms. **b**, Picture of a KPFM measure on bonded prostheses integrating SU-8 rigid platforms. **c**, Comparison of KPFM measures on bonded prostheses integrating SU-8 rigid platforms (99.35 ± 25.26 mV, mean \pm s.d., $n = 15$; electrode diameter $80 \mu\text{m}$) with respect to measures on PDMS-interface bonded to a planar glass substrate (105.50 ± 17.79 mV, mean \pm s.d., $n = 36$; electrode diameter $100 \mu\text{m}$). **d**, Sketch of the accelerated ageing tests. KPFM measures have been performed at the beginning of the experiment, then prostheses have been immersed in saline solution at 87°C and 100 % humidity for 135 hr, after that KPFM has been repeated, and on for four cycles. **e**, Quantification (mean \pm s.d., $N = 4$ prostheses, $n = 4$ electrodes per prosthesis) of the surface potential changes (voltage in light – voltage in dark) during accelerated ageing tests over a simulated period of 24 months (months: 0, 110.5 ± 33.53 mV; 6, 108.5 ± 33.37 mV; 12, 109.8 ± 44.59 mV; 18, 103.8 ± 25.73 mV; 24, 111.1 ± 35.48 mV).

2.3.6 Thermal and optical safety

According to the thermal safety standard for active implantable medical devices (ISO 14708-1 / EN 45502-1), the maximum temperature on the surface of the implant should not exceed 2°C above the normal surrounding body temperature of 37°C ³⁴⁰. We measured in air the increase in temperature on the POLYRETINA surface (**Figure 9a,b**) due to continuous operation for 2 hrs under full-field pulsed illumination (20 Hz , 10 ms , 1.22 mW mm^{-2}). The irradiance has been set to the maximal allowed by the LED. The mean (\pm s.d., $N = 4$ prostheses) thermal increase at steady state is $1.24 \pm 0.29^\circ\text{C}$, which is below the standard limit of 2°C . We verified also that the temperature increases on the electrodes and on the polymer surface are not different (**Figure 9c,d**). This experiment corresponds to the extreme case of projecting a constant full white frame, which is not realistic in daily operation when images will be presented as black and white. Under this condition, the average light dose is lower and therefore the related increase in temperature will be lower. In addition, the eye vitreous has a thermal conductivity about 30 times higher than air, therefore heat sinking is more efficient.

Regarding optical safety, photovoltaic prostheses are limited by retinal damage upon light exposure²⁹¹ (ANSI Z136.1 / ISO 60825 / ISO 15004). According to the standards, the maximum permissible exposure (MPE) during chronic illumination of the full POLYRETINA (equivalent to a full white frame) is controlled by the photothermal damage and equal to $328.75 \mu\text{W mm}^{-2}$ (see Methods). However, photovoltaic prostheses operate with pulsed illumination. With pulses of 10 ms and duty cycle of 5, 10, or 20 % (respectively for 5, 10, or 20 Hz), the MPE is increased to 6.58, 3.29, or 1.64 mW mm^{-2} respectively. These values are higher than the saturation value measured with retinal explants (1.08 mW mm^{-2}).

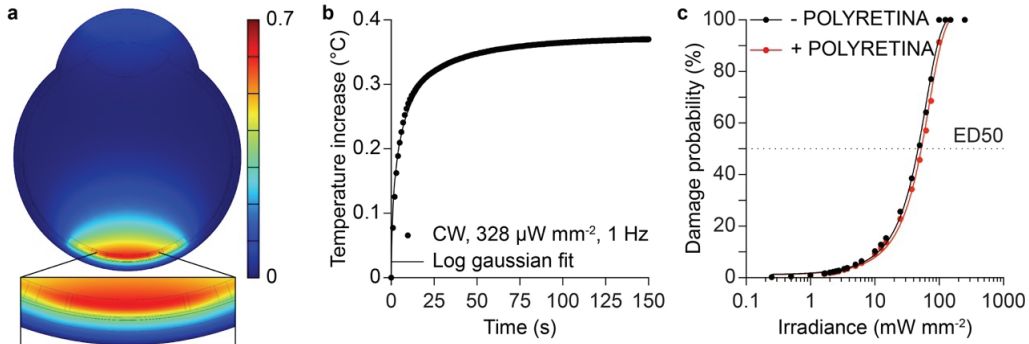


Ch.2 Figure 9 - Temperature variation during operation

a, The top surface of POLYRETINA has been imaged with a thermal camera while pulsed illumination has been provided from the bottom, as in the epiretinal configuration. The camera has been focused on the top electrodes and a ROI has been selected to measure the changes in surface temperature (cyan circle). Electrodes show higher value of baseline temperature because the metallic surface reflects part of the IR light used for the measurement. **b**, Mean (\pm s.d.) changes in surface temperature measured in $N = 4$ prostheses. Data have been plotted with difference with respect to the baseline temperature measured for 5 min before pulsed illumination. The green bar represents the period of 2 hrs when light pulses have been applied (10 ms pulses, 20 Hz repetition rate, 1.22 mW mm^{-2}). The dotted red line represents the maximal allowed temperature increase. **c**, Mean (\pm s.e.m.) changes in surface temperature measured on the electrodes (left, $N = 4$ prostheses) or on the polymer area (right, $N = 4$ prostheses). For each prosthesis, $n = 3$ electrodes/areas have been sampled and averaged. **d**, Mean (\pm s.d.) changes in surface temperature in the average surface, the electrode area or the polymer area are not significantly different (1.24 ± 0.29 , 1.23 ± 0.20 , 1.31 ± 0.21 respectively; One Way ANOVA, $F = 0.0569$, $p = 0.9451$).

In case of POLYRETINA, the incident light is first absorbed by the P3HT:PCBM layer. The mean (\pm s.d., $N = 4$ prostheses) transmittance of POLYRETINA has been experimentally measured as $49.07 \pm 5.25 \%$ (**Supplementary Figure 6**). Therefore, only part of the incident light reaches the retina and the retinal pigmented epithelium (RPE), thus reducing the effect of retinal heating due to light absorption in the RPE. However, the light absorbed by P3HT:PCBM generates heat, that should be taken into account when evaluating the MPE. We performed FEA simulations to estimate the temperature increase in the retina upon illumination of POLYRETINA. First, we verified the temperature increase at the RPE-retina interface using the MPE obtained without POLYRETINA ($328 \mu\text{W mm}^{-2}$ and 1.64 mW mm^{-2}) respectively for continuous and pulsed (10 ms pulses at 20 Hz) illumination. After 150 s of continuous illumination (560 nm , $328 \mu\text{W mm}^{-2}$), the temperature increase is stable at $0.42 \text{ }^\circ\text{C}$ (**Supplementary Figure 7a,b**). Pulsed illumination (10 ms pulses at 20 Hz, 1.64 mW mm^{-2}) generates temperature spikes of about 0.04°C , oscillating around the profile corresponding to the continuous illumination (**Supplementary Figure 7c,d**). This demonstrate that the scaling factor of 5 to estimate the MPE during pulsed stimulation (20 % duty cycle) is correct. Continuous illumination has been used in the following simulations to reduce the computational cost. With POLYRETINA the temperature increase after 150 s of continuous illumination (560 nm , $328 \mu\text{W mm}^{-2}$) is slightly reduced to $0.37 \text{ }^\circ\text{C}$ (**Figure 10a,b**). In this case, the critical interface is the one between the retina and the prosthesis (**Supplementary Figure 8a,b**) giving a slightly higher temperature increase with respect to the RPE-retina interface (0.37 versus $0.35 \text{ }^\circ\text{C}$). POLYRETINA has been simulated in direct contact with the retina because this represents the worst-case scenario. A thin space of vitreous ($100 \mu\text{m}$) between the retina and POLYRETINA reduces the temperature increase by $0.009 \text{ }^\circ\text{C}$, which is negligible. Thermal damage of the retina requires a local rise in temperature higher than $10 \text{ }^\circ\text{C}^{341}$; the 50 % of probability of retinal damage (ED50) has been previously defined for a temperature rise of $12.5 \text{ }^\circ\text{C}^{340}$. In our model, we estimated the ED50 with (red) and without (black) POLYRETINA (**Figure 10c**). As expected the ED50 for continuous illumination is slightly higher when POLYRETINA is present (10.6 versus 9.4 mW mm^{-2}), which correspond to 53 mW mm^{-2} for pulsed illumination. A comparison with and without POLYRETINA showed that over the broad range

of irradiances the temperature increase in the retina is reduced by 11 % with POLYRETINA. Therefore, the MPE could be slightly increased to 1.84 mW mm^{-2} and POLYRETINA can safely operates at 1 mW mm^{-2} .



Ch.2 Figure 10 - FEA simulation of thermal effects with POLYRETINA

a, Temperature increase in the modelled eye with POLYRETINA after 150 s of continuous illumination (CW, 560 nm, $328 \mu\text{W mm}^{-2}$). The insert shows a larger view of the modelled retina and POLYRETINA. **b**, Time course of the temperature increase in the modelled retina during 150 s of continuous illumination (CW, 560 nm, $328 \mu\text{W mm}^{-2}$). The simulation frequency has been set to 1 Hz. The solid line is the log Gaussian fit ($R^2 = 0.9934$). **c**, Probability of retinal damage as a function of irradiance with (red) and without (black) POLYRETINA. ED50 corresponds to a temperature increase of 12.5°C . The irradiance has been expressed for pulsed illumination (20 % of duty cycle). The solid lines are the Sigmoidal fits ($R^2 = 0.9971$ for black and $R^2 = 0.9977$ for red).

2.4 Discussion

One of the most important open questions in the field of retinal prostheses concerns how to increase both visual acuity and visual field size together. From the engineering point of view this implies to increase the density of the stimulating electrodes and enlarge the size of the prosthesis. POLYRETINA is a novel foldable and photovoltaic wide-field epiretinal prosthesis with a remarkable increase in its size (46.3 degrees) and in the number of stimulating pixels (2215) compared to other epiretinal prostheses^{158,342}.

Concerning visual field, POLYRETINA has the potential to cover a retinal surface corresponding to a visual angle of 46.3 degrees, which is larger than the threshold for both legal blindness (20 degrees) and adequate mobility skills (30 degrees).

Concerning spatial resolution, the presence of a continuous semiconductor layer does not represent a limitation. In organic photovoltaics, the low carrier mobility and lifetime limit the carrier-transport length to tens of nm for holes and few hundreds of nm for electrons³⁴³. It has been shown by another group that the PC detected at the cathode is reduced to about 10 % of the maximum if the illumination spot (size 1 μm) is moved laterally by about 12 μm from the electrode edge³⁴⁴. This large decay length, beyond the simple diffusion processes, has been explained by a steady state nonlocal electric field inducing a lateral flow of the separated carriers. For this reason, an internal cross-talk between electrodes due to charge carriers generated under one electrode traveling laterally towards an adjacent electrode can be excluded (at least down to an edge-to-edge distance of about 20 μm). By measuring the voltage spread in solution together with FEA simulations we showed that the area of activation (about 100 μm) of one pixel is comparable to the pixel size.

Concerning visual acuity, with a pitch of 150 μm the theoretical visual acuity restored by POLYRETINA is in the order of 20/600¹⁹³; which is better than the current epiretinal prostheses (e.g. Argus® II) but still below the threshold of legal blindness. However, the technology of POLYRETINA is highly scalable. Based on mechanical simulations (not shown), the pitch can be reduced down to a value of 110 μm , keeping the same electrode size (80 μm), thus approaching the theoretical value of 20/400. A further improvement consists in reducing the size of the electrode (i.e. 60 μm) with a pitch of 80 μm , thus approaching a theoretical visual acuity of 20/300, similar to the silicon photovoltaic subretinal prosthesis¹⁹⁴. However, these values come from theoretical computation, and therefore must be validated with proper *in-vivo* experiments in animals and later in humans. Moreover, the reduction of the pixel size will reduce the PC generated by the interface, therefore the efficiency in stimulating RGCs should be validated again.

To be used as retinal prosthesis, POLYRETINA must operate with a stimulation rate higher than 1 Hz. The subretinal prosthesis Alpha-IMS operates in a frequency range of 1 to 20 Hz (variable from patient to patient) with a pulse duration of 1 to 4 ms²⁰¹. Available pulse rates in the Argus® II are in the range of 3 to 60 Hz³⁴⁵; however, also in this case the effect of pulse rate have been reported to be very variable among subjects²⁶⁸. This suggests that, even if overall the variation in the pulse rate does not have a significant effect, an optimal pulse rate can be defined for each subject. Moreover, the recent identification of an optimal pulse duration of 25 ms per phase²³⁷ may limit the operating range of Argus® II to a theoretical limit of 20 Hz. For the silicon photovoltaic subretinal prosthesis, the stimulation frequency is mainly limited by the discharge rate of the electrode, therefore a shunt resistor has been included to allow faster stimulations (20 to 40 Hz)³³⁴ up to flicker fusion¹⁹⁴. POLYRETINA shows a fast discharge of the Ti-based photovoltaic electrodes (probably due to the high shunting capacity of the P3HT:PCBM layer), and we demonstrated its functioning up to 20 Hz of stimulation rate without an additional shunting resistor. This is within the operation range of other epiretinal (e.g. Argus® II) and subretinal (e.g. Alpha-IMS) prostheses.

The activation of RGCs has been obtained already at 47.35 $\mu\text{W mm}^{-2}$ with a response saturation above 1.08 mW/mm². However, recording *ex-vivo* with retinal explants may not be representative of the complexity of retinal stimulation *in-vivo* in humans, where the electrode-to-cell distance could be larger and increase during years of implantation³⁴⁶, thus increasing the perceptual threshold. The hemispherical design is a solution to reduce the electrode-cell distance over the area of the prosthesis. Moreover, the capability of activating retinal ganglion cells at low irradiance is promising in perspective of an *in-vivo* application. In a future development, titanium / titanium nitride electrodes can be fabricated in order to improve the stimulation efficiency (because of their higher charge injection capacity).

The presence of SL spikes is an evidence in support of a direct activation of retinal ganglion cells. On the contrary, ML and LL spikes are due to the activation of the internal retinal circuit. In literature, SL spikes are reported to be very close (i.e. 0.5 to 4 ms) to the stimulus³³⁷, which is typically a sharp squared pulse. The photo voltage/current generated by POLYRETINA have a less shaped transition from 0 to the peak (in about 10 ms). This may explain why the average latency is 4.12 ± 0.07 ms and we considered as SL spikes those with a latency in the 0-10 ms window. It is known that brief (hundreds of μs) cathodic epiretinal stimulation preferentially excite RGCs, while pulses longer than 1 ms excite both RGCs and bipolar cells^{347,348}. It has been recently demonstrated that the use of pulses shorter than 8 ms results in the activation of axons of passage that causes streak responses, while longer pulses results in a more focal activation²³⁷. Using calcium imaging techniques, authors explained this result via a shift from direct to indirect activation of RGCs. We showed by electrophysiological recordings and pharmacological experiments that the cathodic stimulation provided by POLYRETINA is also indirectly activating RGCs. This represents a promising result for the *in-vivo* translation of POLYRETINA in order to obtain a focal activation. Further experiments aiming at dissecting the circuit activated by POLYRETINA will help in defining the appropriate stimulation parameters to obtain a more focal stimulation. Taking advantage of accelerated ageing experiments, we demonstrated that POLYRETINA preserves its optoelectronic functions unaltered for at least 2 years. More experiments and

additional time points will be added to investigate the entire lifetime of the prosthesis. Last, POLYRETINA fulfils the requirements for *in-vitro* cytotoxicity according to ISO 10993-5 and for thermal safety (ISO 14708-1 / EN 45502-1).

POLYRETINA is foldable to allow implantation through a small scleral incision and it self-opens once released into the eye. Although it could operate in both epiretinal and subretinal conditions, it has been designed as an epiretinal prosthesis, since the implantation of a large retinal prosthesis in the subretinal space may result in an excessive damage to the remaining retinal tissue. Moreover, an epiretinal placement may allow an easier replacement in case of malfunction (*e.g.* due to ageing or detachment). The hemispherical shape has been obtained by bonding the PDMS-photovoltaic interface on a dome-shaped PDMS support with a radius of curvature of 12 mm. However, the flexibility in the fabrication process of the dome-shaped PDMS support (PDMS molding) allows the fabrication of prostheses designed to fit the real eye curvature/shape of a patient³⁴⁹. This opens up the possibility to an optimized retinal prosthesis according to personal needs. Last, the shape of the prosthesis and the insertion strategy have been inspired by the widely use intra ocular lenses. With further investigations, a similar 'injection' approach could also be envisaged for POLYRETINA, simplifying even more the surgical approach. A future improvement for human use may include the removal of electrodes in correspondence of the optic nerve head and the creation of small holes within the substrate to allow metabolic exchange between the vitreous and the retina. On the functional point of view, the next step is the electrophysiological validation *in-vivo* with large animal models, such as swine models.

2.5 Methods

2.5.1 Prosthesis micro-fabrication

PDMS-photovoltaic interfaces were fabricated on silicon wafers. A thin sacrificial layer of poly(4-styrenesulfonic acid) solution (561223, Sigma-Aldrich) was spin-coated on the wafers (1000 rpm, 40 s) and baked (120 °C, 15 min). Degassed PDMS pre-polymer (10:1 ratio base-to-curing agent, Sylgard 184, Dow-Corning) was then spin-coated (1000 rpm, 60 s) and cured in oven (80 °C, 2 hr). After surface treatment with oxygen plasma (30 W, 30 s), a 6 µm thick SU-8 (GM1060, Gersteltec) layer was spin-coated (3800 rpm, 45 s), soft-baked (130 °C, 300 s), exposed (140 mJ cm⁻², 365 nm), post-baked (90 °C, 1800 s; 60 °C, 2700 s), developed in propylene glycol monomethyl ether acetate (48443, Sigma-Aldrich) for 2 min, rinsed in isopropyl alcohol, and dried with nitrogen. After surface treatment with oxygen plasma (30 W, 30 s), a second layer of degassed PDMS pre-polymer (10:1) was spin-coated (3700 rpm, 60 s) and cured in oven (80 °C, 2 hr). PEDOT:PSS (HTL Solar, Ossila) was filtered (1 µm PTFE filters) and then spin-coated (3000 rpm, 60 s) onto the O₂-plasma treated (30 W, 30 s) PDMS surface. Subsequent annealing (120 °C, 30 min) was performed. The preparation of the organic semiconductor blend was performed in a glovebox under argon atmosphere. 20 mg of P3HT (698997, Sigma Aldrich) and 20 mg of PCBM (M111, Ossila) were dissolved in 1 mL of anhydrous chlorobenzene each and left stirring overnight at 70 °C. The solutions were then filtered (0.45 µm PTFE filters) and blended [1:1 v:v]. The P3HT:PCBM blend was then spin-coated at 1000 rpm for 60 seconds. Titanium cathodes were deposited by DC sputtering through a shadow mask aligned with the SU-8 pattern. After surface treatment with oxygen plasma (30 W, 15 s), the encapsulation layer of degassed PDMS pre-polymer (5:1 ratio) was spin-coated (4000 rpm, 60 s) and cured in oven (80 °C, 2 hr). To expose the cathodes, photolithography and PDMS dry etching were performed. The wafers were then placed in deionized water to allow dissolution of the sacrificial layer and the release of the PDMS-photovoltaic interfaces. The floating membranes were finally collected and dried in air. The dome-shaped PDMS supports were fabricated using a milled PMMA mold, filled with PDMS pre-polymer (10:1), which was then degassed and cured in oven (80 °C, 2 hr). The supports were released from the molding parts and perforated with a hole-puncher (330 µm in diameter) at the locations dedicated to the insertion of retinal tacks. The released PDMS-photovoltaic interfaces were clamped between two O-rings and, together with the PDMS supports, were exposed to oxygen plasma (30 W, 30 s). The activated PDMS surfaces were put in contact and allowed to uniformly bond thanks to radial stretching of the fixed membrane. The excessive PDMS used to clamp the array was removed by laser cutting.

2.5.2 Chips micro-fabrication

Chips for KPFM and PC/PV measurements were fabricated on 20 x 24 mm² glass substrates (2947-75X50, Corning Incorporated). Before micro-fabrication, glass chips were cleaned by ultra-sonication in deionized water, acetone and isopropyl alcohol for 15 min each and then dried with nitrogen. ITO (200 nm) was deposited on glass chips by RF sputtering. PEDOT:PSS (HTL Solar, Ossila) was filtered (1 µm PTFE filters) then spin-coated at 3000 rpm for 60 seconds on each chip. Subsequent annealing at 120 °C for 30 minutes was performed. The preparation of the organic semiconductor blend was performed as described before. The P3HT:PCBM blend was then spin-coated at 1000 rpm for 60 seconds on each chip. Aluminum cathodes were deposited by thermal evaporation using a shadow mask; titanium cathodes were deposited by DC sputtering using a shadow mask. When present, degassed PDMS pre-polymer (10:1) was deposited on the glass substrate by spin-coating (1000 rpm, 60 s) and then cured in oven (80 °C, 2 hr).

2.5.3 Kelvin Probe Force Microscopy

KPFM characterization was performed in ambient conditions with an Asylum Research Cypher S microscope using PtIr coated tips (AC240TM, Asylum Research, Oxford Instrument) in surface potential imaging mode. To measure the surface potential variation, KPFM images were collected by repetitively scanning a single line of 100 nm under dark and illumination conditions. The white led of the microscope positioned above the tip and sample was acting as light source and it was manually turned 100 % off and 100 % on to reach the desired conditions. KPFM images were analyzed using Gwyddion 2.36 software. For each image, the average surface potential variation value was obtained by subtracting the surface potential under illumination to the one under dark (voltage in light – voltage in dark).

2.5.4 Accelerated ageing tests

Accelerated ageing was performed in a dry oven set to 87 °C. Samples were immersed in physiological saline solution (0.9 % NaCl, pH 7.4) within a sealed 50-ml falcon tube. Under this condition, the acceleration factor was 32^{350,351}. KPFM measures were obtained before starting the ageing protocol and at several time points during ageing. Each accelerated ageing session between KPFM measures lasted for 135 hr, corresponding to 6 months. Before KPFM, samples were removed from the sealed falcon tube, rinsed with deionized water, and dried under nitrogen flow.

2.5.5 Measure of photo-voltage and photo-current

In this experiment, the photovoltaic interface has been fabricated directly on glass (without PDMS) to avoid breaking the connecting lines from the electrode to the pad when contacted. The titanium electrodes have been fabricated with a diameter of 100 μm ; however, when evaluating the PC density generated by the interface, also the area of the connecting line exposed to light has been considered. A plastic reservoir was attached to the chip using PDMS as adhesive. Chips were placed on a holder, and each pad was sequentially contacted. Silver paste was used to improve the electrical contact. An Ag/AgCl pellet immersed in physiological saline solution (NaCl 0.9 %) was used as reference electrode. Light pulses were delivered by a 565-nm Green LED (Thorlabs, M565L3-C5) focused at the sample level. Photo-voltage was measured using a voltage amplifier (DL-Instruments, 1201; gain 20, band DC-3000 Hz) and photo-current using a current amplifier (DL-Instruments, 1212; gain 10^{-6} A/V). Data sampling (16 kHz) and instrument synchronization were obtained via a DAQ board (PCIe-6321, National Instruments) and a custom-made software. Data analysis was performed in Matlab (Mathworks). Due to a limitation in the acquisition system, long pulse trains (**Figure 5e**) have been delivered in packages of 20 pulses at 20 Hz (total of 1 second), while each package was separated by 1 second needed by the system to save data before starting the next package.

2.5.6 Electrophysiology

Experiments were conducted under the animal authorizations VD3055 and GE3717. Retinas were explanted in normal light conditions from mice sacrificed by injection of Sodium Pentobarbital (150 mg kg^{-1}). After eye enucleation, retinas were dissected in carboxygenated (95 % O_2 and 5 % CO_2) Ames' medium (A1420, Sigma-Aldrich) and transferred to the microscope stage for recordings. In the experiment with synaptic blockers, Ames' medium was supplemented with DL-AP4 (250 μM l^{-1} , No. 0101, Tocris Bioscience), DL-AP5 (50 μM l^{-1} , No. 0105, Tocris Bioscience), DNQX (10 μM l^{-1} , No. 0189, Tocris Bioscience), Carbenoxolone (100 μM l^{-1} , No. 3096, Tocris Bioscience). Retinas were placed mimicking an epiretinal configuration, therefore with retinal ganglion cells facing the substrate (bare PDMS or prosthesis). On the prosthesis, retinas were layered in the central part of the array with electrodes of 80 μm in diameter and 150 μm pitch. Recordings were performed in dim light at 32 °C with a sharp metal electrode (PTM23B05KT, World Precision Instruments), amplified (Model 3000, A-M System), filtered (300-3000 Hz), and digitalized at 30 kHz (Micro1401-3, CED Ltd.). Illumination was carried out on a Nikon Ti-E inverted microscope (Nikon Instruments) by the Spectra X system (Emission filter 560/32, Lumencor). The microscope was equipped with a dichroic filter (FF875-Di01-25x36, Semrock) and a 10x (diameter of the illumination spot 2.2 mm; CFI Plan Apochromat Lambda) objective. The stimulation protocol consisted in a repetition of 10 pulses at 1 Hz for each irradiance; irradiance was increased sequentially: LED at 0 % (0 μW mm^{-2}), 2 % + ND4 (47.38 μW mm^{-2}), 3 % + ND4 (107.91 μW mm^{-2}), 2 % (189.50 μW mm^{-2}), 3 % (421.12 μW mm^{-2}), 3 % (815.92 μW mm^{-2}), 5 % (1081.75 μW mm^{-2}), 10 % (2.81 mW mm^{-2}), 20 % (5.89 mW mm^{-2}), 40 % (11.98 mW mm^{-2}), 60 % (17.92 mW mm^{-2}), 80 % (23.56 mW mm^{-2}), and 100 % (29.08 mW mm^{-2}). Spike detection and sorting were performed by threshold detection using the Matlab-based algorithm Wave_clus³⁵² and further data processed in Matlab (Mathworks). The threshold for spike detection has been defined as 3.7 times the standard deviation of the background noise. The minimum refractory period between spikes of the same class was set to 1.4 ms. To ensure the rejection of artifacts, an exclusion period of ± 1 ms around light onset and offset was applied. However, the spikes in the first 10 ms after the light onset (SL) have been manually verified. Peri-stimulus time histograms for each condition of illumination were computed discretizing and averaging spike raster obtained over 10 stimulations repetitions into bins of 10 ms. Spikes were sorted from individual PSTHs and classified according to their timing after light onset (cyan bars in **Supplementary Figure 3a**) in SL (< 10 ms), ML (from 40 to 120 ms), and LL (from 150 to 350 ms)³³⁷. Firing rates in the three groups were measured as follow. For SL spikes the first bin (10 ms) after the pulse was used. For ML spikes 3 bins (30 ms) in the defined time range, centred in the highest bin, were used. For LL spikes 5 bins (50 ms) in the defined time range, centered in the highest bin, were used.

2.5.7 pH measurements

Experiments have been performed in phosphate-buffered saline at room temperature. Illumination was carried out on a Nikon Ti-E inverted microscope (Nikon Instruments) by the Spectra X system (Emission filter 560/32, Lumencor). The microscope was equipped with a dichroic filter (FF875-Di01-25x36, Semrock) and a 10x (diameter of the illumination spot 2.2 mm; CFI Plan Apochromat Lambda) objective. Light pulses of 10 ms were delivered at 20 Hz for 1 hr with an irradiance of 3.4 mW mm^{-2} . pH was measured with a microelectrode (tip diameter of 200 μm) with internal reference (pH-200C, Unisense). Data were sampled at 1 H.

2.5.8 Spatial selectivity measures and modeling

Measures of the voltage spread have been performed in Ames' medium (A1420, Sigma-Aldrich) at 32°C with a glass micropipette (tip diameter about 15 μm). Data were amplified (Model 3000, A-M System), filtered (DC-1000 Hz), and digitalized at 30 kHz (Micro1401-3, CED Ltd.). Illumination was carried out on a Nikon Ti-E inverted microscope (Nikon Instruments) by the Spectra X system (Emission filter 560/32, Lumencor). The microscope was equipped with a dichroic filter (FF875-Di01-25x36, Semrock) and a 10x objective. A pin-hole was used to limit the spot diameter to about 150 to 170 μm . After alignment of the illumination spot on a target pixel of the central area of POLYRETINA, 10 pulses of 10 ms were delivered at 1 Hz with an irradiance of 29.07 mW mm^{-2} . The

resulting voltage has been measured at 9 positions in 3 directions around the illuminated pixel. Data analysis was conducted in Matlab (Mathworks). Voltage peaks above noise level (mean noise threshold 6.2 μV) have been detected and their amplitude normalized respect to the central pixel value. Simulations were performed in COMSOL Multiphysics 5.2, with a stationary electric currents study. The titanium cathodes were set at 0.1 V, while PEDOT:PSS was put at 0 V. The ground was situated at the bath top and lateral walls that were placed 2 mm and 1 mm away from the central pixel respectively (cylindrical geometry). Line plots shown in the results were taken at a distance of 20 μm from the titanium surface. For each material, the conductivity (S m^{-1}) and relative permittivity is listed: titanium ($2.6 \times 10^6 / 1$), P3HT:PCBM (0.1 / 3.4), PEDOT:PSS (30 / 3), Saline (1 / 80), PDMS ($2 \times 10^{-14} / 2.75$).

2.5.9 Optical safety

Retinal damage upon light exposure can occur because of three main factors: photo-thermal damage, photo-chemical damage, and thermo-acoustic damage³⁴⁰. The first one is related to retinal heating upon light absorption by the melanin in the RPE. The second one occurs at short wavelengths (less than 600 nm) and for exposures longer than 1 s. The latter occurs for short pulses (less than 1 ns) and is associated with nonlinear photo-mechanical effects. POLYRETINA functions with 10 ms green light pulses; therefore, this limit could be controlled by the photo-thermal or photo-chemical damage. According to the ANSI Z136.1 Standard²⁹¹, the MPE allowed for ophthalmic applications can be calculated (in W) according to **Equation 1** for photo-thermal damage (MPE_T) and **Equation 2** for photo-chemical damage (MPE_C). Those equations are valid for $\lambda = 560 \text{ nm}$ and $\alpha = 808.12 \text{ mrad}$ (**Supplementary Figure 1c**).

$$\text{MPE}_T = 6.93 \times 10^{-5} C_E C_T \frac{1}{P} \text{ with } \begin{cases} C_E = 6.67 \times 10^{-3} \alpha^2 \text{ for } \alpha > 100 \text{ mrad} \\ C_T = 1 \text{ for } 400 < \lambda < 700 \\ P = 5.44 \text{ for } 400 < \lambda < 600 \text{ and } t \geq 0.7 \text{ s} \end{cases}$$

Ch.2 Equation 1

$$\text{MPE}_C = 5.56 \times 10^{-10} C_B \alpha^2 \text{ with } C_B = 10^{0.02(\lambda-450)}$$

Ch.2 Equation 2

MPE_T results in 47.41 mW, which corresponds to 328.75 $\mu\text{W mm}^{-2}$ for an exposed area of 144.22 mm^2 . MPE_C results in 57.55 mW, which corresponds to 399.02 $\mu\text{W mm}^{-2}$.

2.5.10 Thermal measurements

Measures have been performed with a thermal camera (FLIR A325sc Infrared Camera, FLIR Systems, Inc.) focused on the top surface of the POLYRETINA prosthesis. Images have been acquired at 1 frame per second. Light pulses (10ms, 20 Hz, 1.22 mW mm^{-2}) were delivered by a 565-nm Green LED (Thorlabs, M565L3-C5) focused at the sample level.

2.5.11 Thermal modeling

Simulations were performed in COMSOL Multiphysics 5.2 with the Bioheat module for the heat transfer equation and the General PDE module for the Beer-Lambert light propagation. Illumination has been modelled as a uniform beam with a diameter of 13 mm. The eye is a 2D axi-symmetric model composed of several spheres representing each domain (**Supplementary Figure 9**). A total of 8 domains (Cornea, Aqueous Humor, Lens, Vitreous Humor, Retina, RPE, Choroid and Sclera) are defined in the model, with the parameters listed in **Supplementary Table 2**. POLYRETINA was modelled as a single composite material, with volume averaged properties of PDMS, Pedot:PSS, P3HT:PCBM and Titanium (**Supplementary Table 3**). It was simplified into 5 domains with homogeneous properties: the center, the first ring, the second ring, the domains where no titanium is present, and PDMS only (**Supplementary Figure 9**). A volume average has been performed on each of this domain, to obtain the parameters for the aggregated material. To account for the non-uniform distribution of titanium, the fraction area of titanium was considered. To validate the parameters of the aggregated model, a simulation has been performed with POLYRETINA in air exposed to continuous illumination (560 nm, 244 $\mu\text{W mm}^{-2}$) corresponding to pulsed illumination of 1.22 mW mm^{-2} . The heat losses at the prosthesis interface-air were radiative (emissivity = 0.9) and convective (heat transfer coefficient = 38.5 $\text{W m}^{-2} \text{K}^{-1}$). In agreement with our experimental results, the average transmittance was measured to be 51.67 % (49.07 % in **Supplementary Figure 6**) and the steady-state temperature increase was 1.25 $^\circ\text{C}$ (1.24 $^\circ\text{C}$ in **Figure 9**).

2.5.12 *In-vitro* cytotoxicity test

The study validation was performed by an accredited company (Medistri SA). The test was conducted according to the requirement of ISO 10993-5: Biological Evaluation of Medical Devices, *in-vitro* cytotoxicity test; ISO 10993-12: Test article preparation and reference materials; USP 35-NF30 (87): Biological Reactivity test, *in-vitro*; Medistri internal procedure WI 47 and WI 56. Prostheses were sterilized with EtO prior the test. The test on extraction was performed with 2 retinal prostheses for a total surface

area of 3.54 cm², with a ratio of the product to extraction vehicle of 3 cm² ml⁻¹. Extraction vehicle was Eagle's Minimum Essential Medium supplemented with foetal bovine serum, penicillin-streptomycin, amphotericin B, and L-glutamine. The extraction was performed for 24 hr at 37 °C. The extract was added on triplicate cultures wells containing a sub-confluent L929 cell monolayer (1:1 dilution). The test samples and the control wells were incubated at 37 °C in 5 % CO₂ for 24 hours. Following incubation, the cell cultures were examined for quantitative cytotoxic evaluation. 50 µl per well of XTT reagent was added to the cells then incubated at 37 °C in 5 % CO₂ for further 3 to 5 hr. An aliquot of 100 µl was then transferred from each well into the corresponding wells of a new plate and the optical density (OD) was measured at 450nm.

2.5.13 Surgical implantation

Plastic eye models (Eyelabinnovations, Austria) and enucleated pig eyes were used. First three 23-gauge transconjunctival valved canulas (DORC, Zuidland, The Netherlands) were inserted into the eye at 4 mm from the limbus at the following positions: nasal superior, temporal superior and temporal inferior. A balanced salt solution infusion was hooked up to the eye to maintain a constant intraocular pressure through one of the cannulas. A 6.5 mm long incision was then performed using a 15 ° scalpel. The implant was folded using special forceps and then inserted through the incision into the posterior cavity. Once inside the eye the forceps grip was released and the implant could unfold. Using a light pipe and an intraocular 23-gauge forceps inserted through the other two cannulas the implant was then manipulated and fixed in epiretinal configurations.

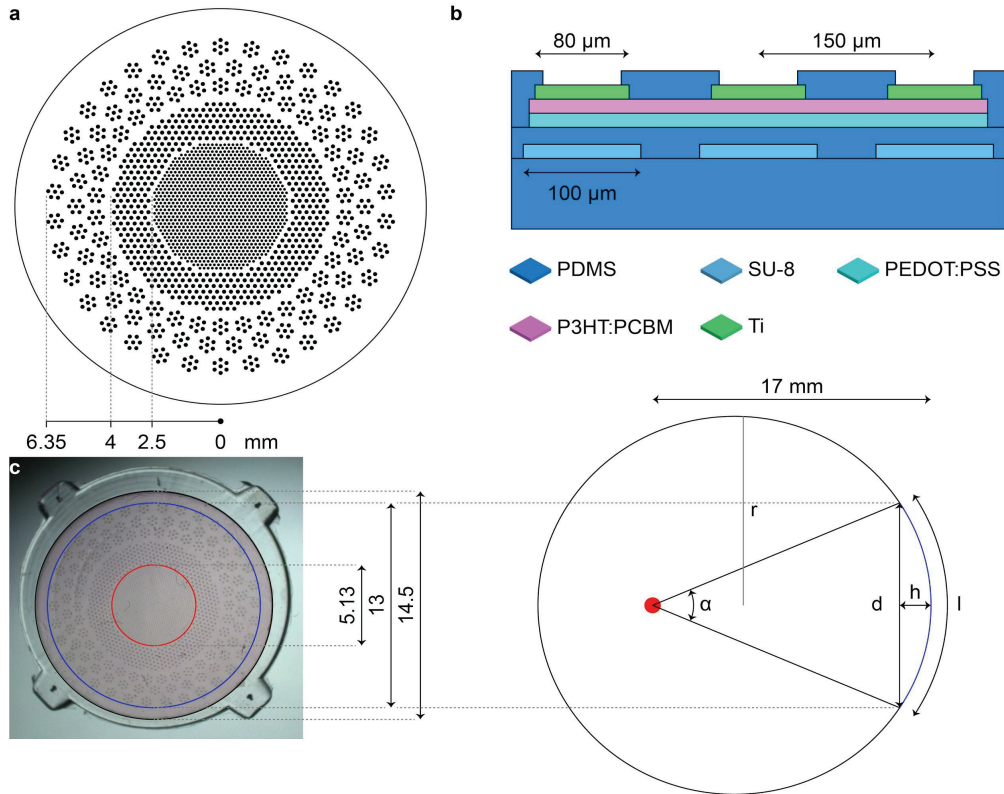
2.5.14 Statistical analysis and graphical representation

Statistical analysis and graphical representation were performed with Prism (GraphPad Software Inc.). The normality test (D'Agostino & Pearson omnibus normality test) was performed in each dataset to justify the use of a parametric or non-parametric test. In each figure p-values were represented as: * p < 0.05, ** p < 0.01, *** p < 0.001, and **** p < 0.0001. Data are reported as mean ± s.e.m. or mean ± s.d., *n* is used to identify the number of electrodes or cells used; *N* is used to identify the number of devices or animals.

2.6 Acknowledgment

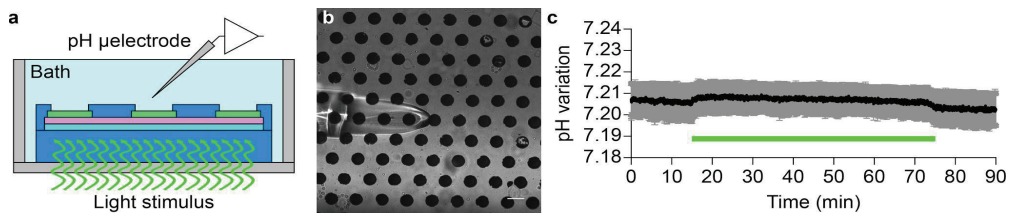
We would like to acknowledge the EPFL center of micronanotechnology for the support. Prof. Matthias Lütolf for having reviewed our manuscript and Prof. Stéphanie Lacour for her advices. This work has been supported by École polytechnique fédérale de Lausanne, Medtronic, European Commission (EU project 701632), Fondation Pierre Mercier pour la science, and Velux Stiftung (Project 1102).

2.7 Supplementary material



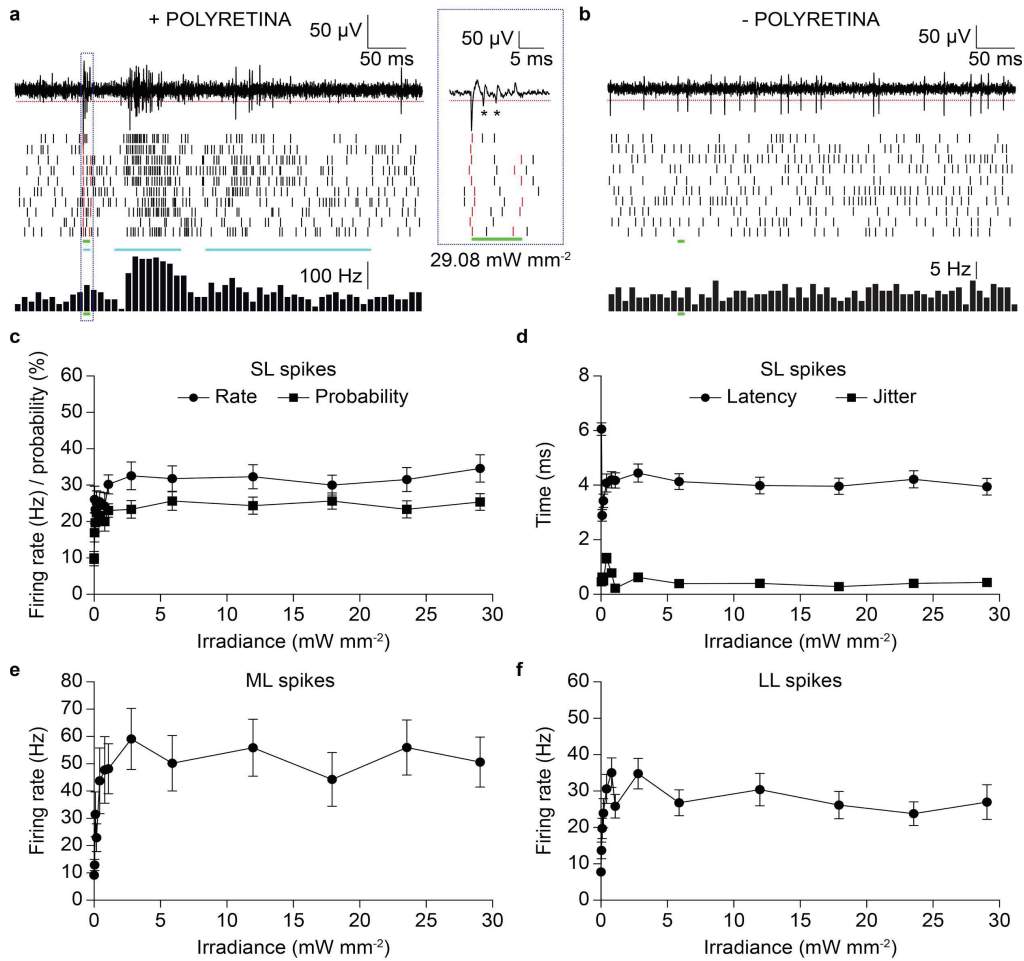
Ch.2 Supplementary Figure 1 - Design of POLYRETINA

a, Distribution of the photovoltaic pixels. **b**, Cross section of the PDMS-photovoltaic interface, including: PDMS (50 μm), a second layer of PDMS (10 μm) embedding SU-8 rigid platforms (6 μm), a layer of PEDOT:PSS (50 nm), a layer of P3HT:PCBM (100 nm), titanium cathodes (150 nm), and a final layer of PDMS (4 μm). Thicknesses are not in scale. **c**, Picture of the prosthesis after bonding. Due to the radial elongation, the central area (red) is slightly stretched from 5 to 5.13 mm, while the active area (blue) is increased from 12.7 to 13 mm. On the right, the visual angle is calculated. The human eye is modelled as a sphere of 12 mm radius (r). The blue arc corresponds to the active area, where d is the chord length of 13 mm, l is the arc length of 13.738 mm, and h is the height of 1.9128 mm. The nodal point is represented in red, with a distance of 17 mm. Under these conditions, the area covered by the active area can be calculated as $S = 2\pi rh = 144.2217 \text{ mm}^2$, and it corresponds to a visual angle α of 46.3° (or 808.12 mrad).



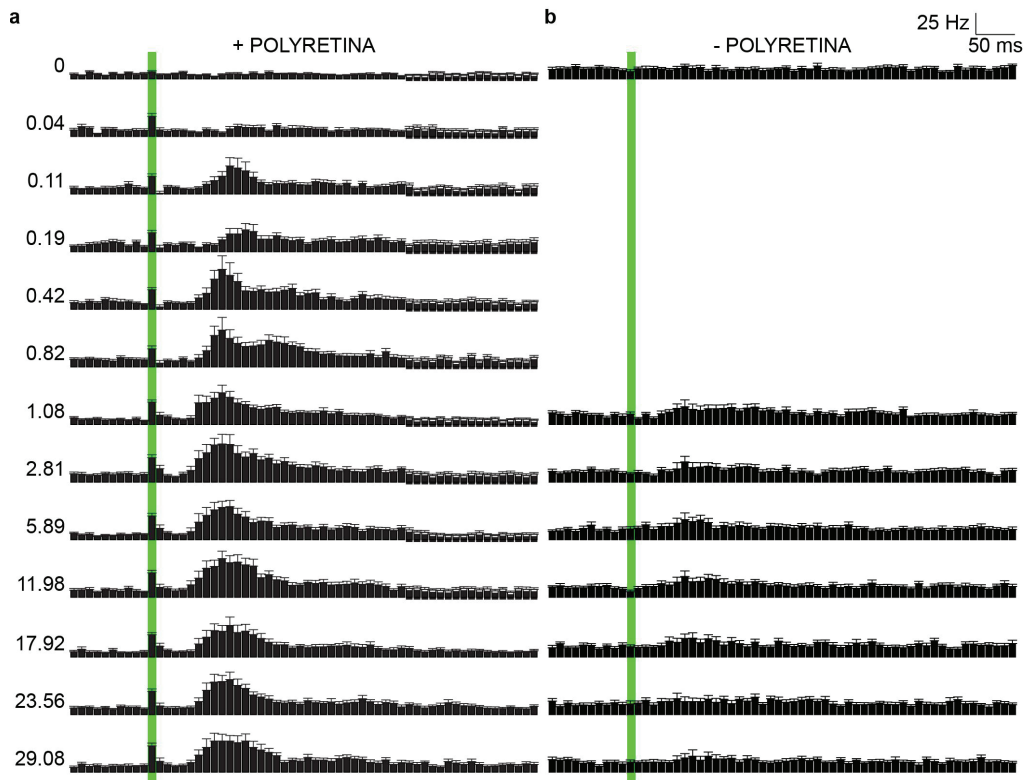
Ch.2 Supplementary Figure 2 – pH measurements upon prosthetic stimulation

a, Sketch of the recording set-up. **b**, Picture of the pH microelectrode located on top of the PDMS-photovoltaic interface. The scale bar is 100 μm. **c**, Mean (\pm s.d., $N = 3$ devices) pH measurements upon 1 hr of full field pulsed illumination (10 ms, 20 Hz, 3.4 mW mm⁻², 560 nm, illumination spot 2.2 mm).



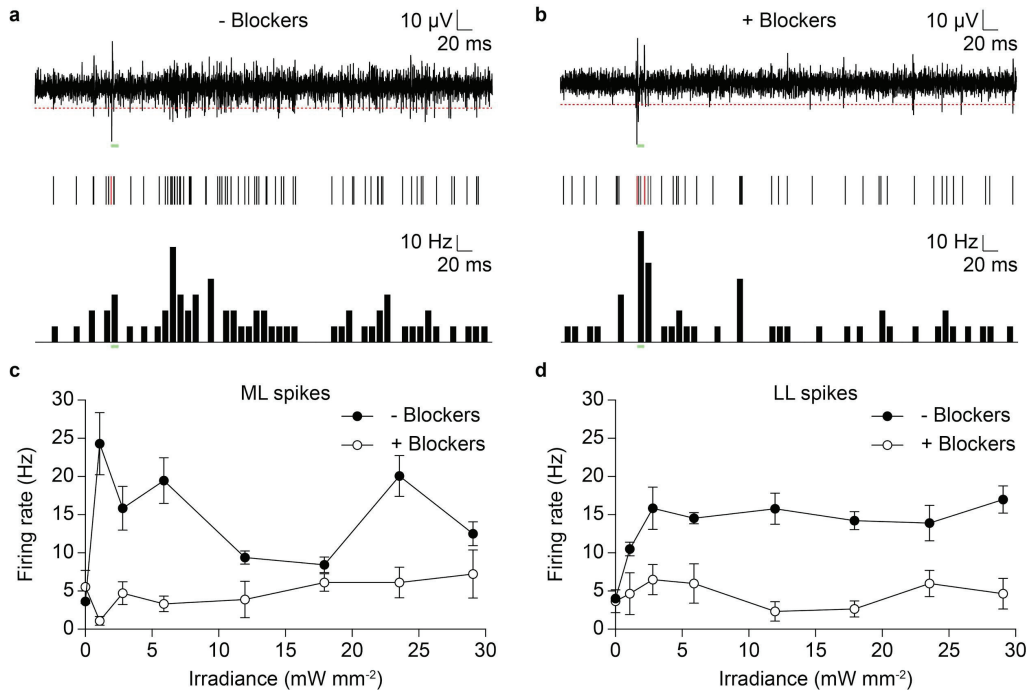
Ch.2 Supplementary Figure 3 – Evaluation *ex-vivo* with retinal explants

a, The top panel shows a representative single-sweep recording from a retinal ganglion cell over the PDMS-photovoltaic interface upon maximal illumination (10 ms, 29.08 mW mm⁻²). The red dotted line is the threshold set for spike detection. The middle panel shows the raster plot based on the over-threshold events detected and classified as spikes upon 10 consecutive sweeps in the same cell. The green bars represent the light illumination. The cyan bars represent the regions where SL, ML, and LL spikes have been identified. The red bars correspond to the detection of the stimulation artefacts at the onset and offset of illumination. Artefacts have been excluded in subsequent analysis. The bottom panel shows the PSTH of the cell computed over 10 consecutive sweeps. The blue box shows an enlarged view of the light onset. The asterisks (*) indicate the over-threshold events detected and classified as spikes. **b**, Example from a retinal ganglion cell over bare PDMS. **c**, Mean (\pm s.e.m.) firing rate (●) and firing probability (■) of SL spikes, computed across all the recorded cells ($n = 39$) on the PDMS-photovoltaic interface. For each cell, the probability has been defined as the percentage of sweeps with at least a SL spike over the 10 consecutive trials. **d**, Mean (\pm s.e.m.) latency (●) and jitter (■) of the first spike occurring in the 10 ms window after the light onset, computed across all the recorded cells ($n = 39$, 10 sweeps each) on the PDMS-photovoltaic interface. **e,f** Mean (\pm s.e.m.) firing rate of medium (e) and long (f) latency spikes, computed across all the recorded cells ($n = 39$, 10 sweeps each) on the PDMS-photovoltaic interface.



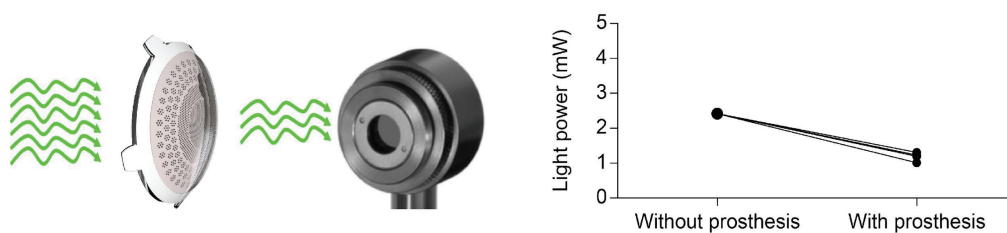
Ch.2 Supplementary Figure 4 – Recording of *Rd10* retinas *ex-vivo*

PSTHs (bin 10 ms, mean \pm s.e.m.) obtained from $n = 39$ and $n = 34$ retinal ganglion cells, respectively for the PDMS-photovoltaic interface (a) and the bare PDMS substrate (b). Each row corresponds to a different light intensity expressed on the left in mW mm⁻². Green bars represent the light pulses. On bare PDMS substrate, cells have been tested only for the high range of irradiance.



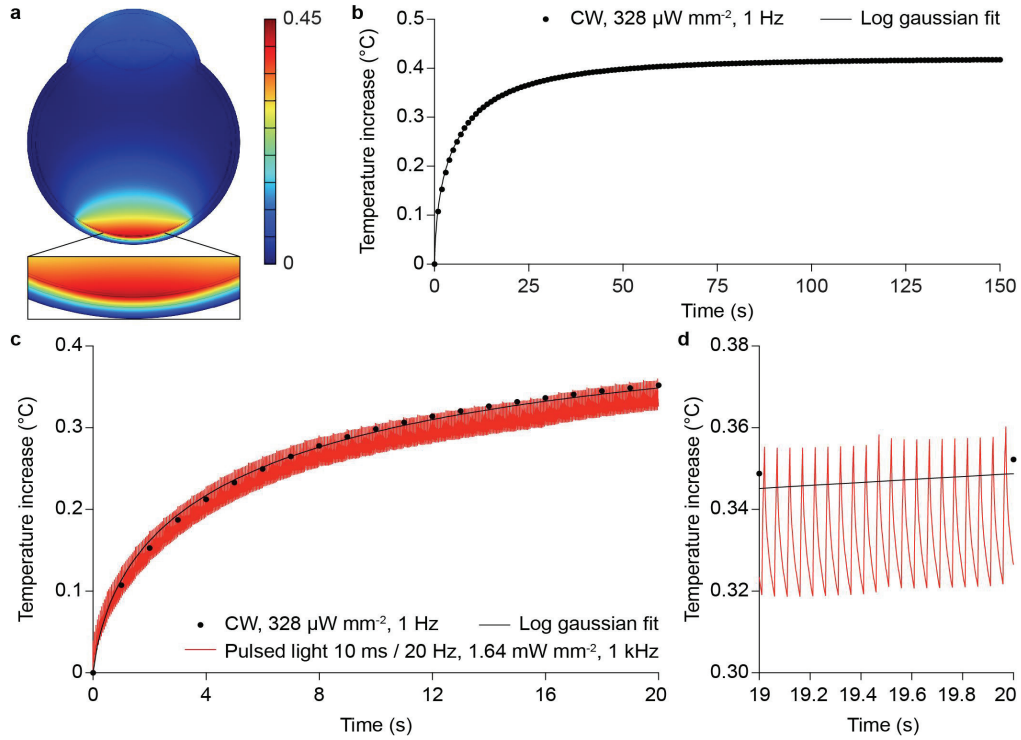
Ch.2 Supplementary Figure 5 – Pharmacological blockage of network activity

a, The top panel shows a representative single-sweep recording from a retinal ganglion cell over the PDMS-photovoltaic interface upon illumination (10 ms, 23.56 mW mm^{-2}). The red dotted line is the threshold set for spike detection. The green bars represent the light pulse. The middle panel shows the raster plot based on the over-threshold events detected and classified as spikes upon 10 consecutive sweeps (overlay) in the same cell. The red bars correspond to the detection of the stimulation artefacts at the onset and offset of illumination. Artefacts have been excluded. The bottom panel is the PSTH (bin 10 ms) of the cell computed over 10 consecutive sweeps. **b**, Response upon illumination (10 ms, 23.56 mW mm^{-2}) of the same retinal ganglion cell shown in **a**, after inclusion of synaptic blockers. Panels **c/d** respectively show the mean (\pm s.e.m.) firing rate of medium/long latency spikes, computed across all the recorded cells ($n = 6$, 10 sweeps each) on the PDMS-photovoltaic interface before (\bullet) and after (\circ) the inclusion of synaptic blockers.



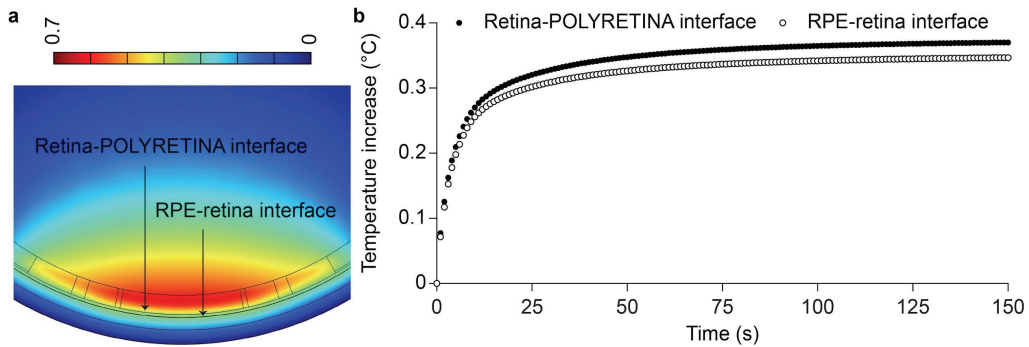
Ch.2 Supplementary Figure 6 – Optical absorption

Light absorbance/transmittance of POLYRETINA has been evaluated by using a green LED (565 nm, 2.42 mW). Light has been measured with a power meter (PD300-R Juno, Ophir Optronics Solutions Ltd.). The retinal prostheses ($N = 4$) have been inserted in the light path and the light power has been compared with respect of the condition without the prostheses.



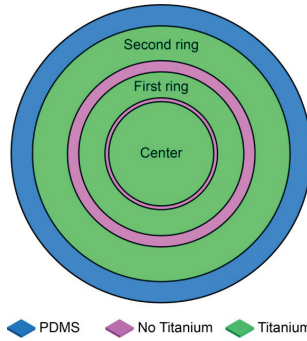
Ch.2 Supplementary Figure 7 – FEA simulation of thermal effects

a, Temperature increase in the modelled eye after 150 s of continuous illumination (CW, 560 nm, 328 $\mu\text{W}/\text{mm}^2$). The insert shows a larger view of the modelled retina. **b**, Time course of the temperature increase in the modelled retina during 150 s of continuous illumination (CW, 560 nm, 328 $\mu\text{W}/\text{mm}^2$). The simulation frequency has been set to 1 Hz. The line is the log gaussian fit ($R^2 = 0.9958$). **c**, Comparison of the temperature time course during continuous illumination at 328 $\mu\text{W}/\text{mm}^2$ (black dots) and pulsed illumination with 10 ms pulses at 20 Hz and 1.64 mW/mm^2 (red line) for 20 s of simulation. The simulation frequency for the pulsed illumination has been set to 1 kHz. **d**, Magnification of the last 1 s of the simulation in c.



Ch.2 Supplementary Figure 8 – FEA simulation of thermal effects with POLYRETINA

a, Enlarged view of the temperature increase in the modelled eye with POLYRETINA after 150 s of continuous illumination (CW, 560 nm, 328 $\mu\text{W}/\text{mm}^2$). **b**, Time course of the temperature increase at the RPE-retina (\circ) and retina-POLYRETINA (\bullet) interfaces during 150 s of continuous illumination (CW, 560 nm, 328 $\mu\text{W}/\text{mm}^2$).



Ch.2 Supplementary Figure 9 – Aggregated model of POLYRETINA

Drawing of the simplified model of POLYRETINA.

	Thickness	Heat Capacity	Thermal Conductivity	Density	Absorption (at λ in nm)	Perfusion rate	Self Heat
	μm	$\text{J kg}^{-1} \text{K}^{-1}$	$\text{W m}^{-1} \text{K}^{-1}$	Kg m^{-3}	1 cm^{-1}	1 s^{-1}	W m^{-3}
Eye	ϕ 24000						
Aqueous Humor	3100	3997	0.58	1000	0.00025 (500)	0	0
Blood	/	3840	0.53	1050	0	0	0
Choroid	430	3840	0.53	1050	150 (500)	0.0091	10000
Cornea	500	4178	0.58	1050	0.51 (514.5)	0	0
Lens	3600	3000	0.4	1000	0.025 (514.5)	0	0
Retina	100	3680	0.565	1000	4 (500)	0	0
RPE	10	4178	0.603	1050	1100 (500)	0	0
Sclera	500	4178	0.58	1000	5.9 (550)	0	0
Vitreous Humor	/	3997	0.595	1050	0.00025 (500)	0	0
PDMS	669	1460	0.15	970	3.58 (514.5)	0	0
PEDOT:PSS	0.15	1978	0.29	1011	1700 (500)	0	0
P3HT:PCBM	0.1	1400	0.2	1100	40000 (530)	0	0
Titanium	0.05	5263	6.7	4430	120000 (500)	0	0

Ch.2 Supplementary Table 1- FEA simulation of thermal effects

Parameters used in the thermal model obtained from³⁵³⁻³⁶⁶.

Domain	Heat Capacity	Thermal Conductivity	Density	Absorption (at λ in nm)	Fraction of Titanium
	$\text{J kg}^{-1} \text{K}^{-1}$	$\text{W m}^{-1} \text{K}^{-1}$	Kg m^{-3}	1 cm^{-1}	%
Center	1460.89	0.15	970.07	16.91	27
First ring	1460.89	0.15	969.90	12.30	10
No titanium	1459.70	0.15	969.80	9.73	0
Second ring	1460.89	0.15	969.85	11.09	0.5
PDMS	1460.00	0.15	970.00	3.58	0

Ch.2 Supplementary Table 2 - FEA model of POLYRETINA

Parameters used to generate the aggregated model of POLYRETINA used in the thermal simulations. Parameters can be obtained from³⁵³⁻³⁶⁶.

Supplementary Certificate

The original document with official signatures can be shared upon request.

Chapter 3 Capacitive-like photovoltaic epiretinal stimulation enhances the network-mediated activity of retinal ganglion cells by recruiting the lateral inhibitory network

Postprint version of the article published in Journal of Neural Engineering, 2019 (DOI: 10.1088/1741-2552/ab3913).

Authors: Naïg A. L. Chenais^a, Marta J. I. Airaghi Leccardi^a, and Diego Ghezzi^a.

^a Medtronic Chair in Neuroengineering, Center for Neuroprosthetics, Institute of Bioengineering, School of Engineering, École Polytechnique Fédérale de Lausanne, Switzerland

Authors contribution: N.A.L.C. designed the study, performed all the experiments and simulations, and wrote the manuscript. M.J.I.A.L. fabricated the photovoltaic array, fabricated the custom MEA for electrical stimulation, and designed FEA simulations. D.G. led the study and wrote the manuscript. All the authors edited and accepted the manuscript.

3.1 Abstract

Photovoltaic retinal prostheses theoretically offer the possibility of a standalone high-resolution electrical stimulation of the retina. However, achieving focused epiretinal stimulation is particularly challenging, because of axonal activation and electrical cell coupling. Recent evidence shows that long electric pulses allow for a more focal activation of retinal ganglion cells, and non-rectangular waveforms induce higher network-mediated indirect activity. The role of the pulse shape in focusing the retinal ganglion cell activation and the underlying mechanisms are not yet fully understood. To address this question, we implemented a hybrid *ex-vivo* and *in-silico* approach. We recorded the evoked activity of retinas explanted from *Retinal degeneration 10* mice upon photovoltaic and electrical stimulation with rectangular or non-rectangular capacitive-like voltage pulses. Moreover, we used a biophysical model to investigate the role of the pulse shape and the pulse duration on the genesis and the extent of the network-mediated activity in retinal ganglion cells. Altogether our results suggest that non-rectangular capacitive-like voltage pulses activate stronger the inner excitatory and inhibitory layers of the retina when compared to a rectangular stimulation with paired pulse amplitude and duration. This feature leads to an increase of the network-mediated activity and a decrease in the network-mediated electrical receptive field of the stimulated retinal ganglion cell. These results demonstrate that recruiting the inner retinal cells with epiretinal stimulation enables not only to bypass axonal stimulation but also to obtain a more focal activation thanks to the natural lateral inhibition. The involvement of the inhibitory feedback from amacrine cells in the genesis of the network-mediated activity represents a novel biological tool to confine the response of the retinal ganglion cells. These results support future waveform engineering strategies and offer new perspectives to epiretinal devices to better shape prosthetic perception.

3.2 Introduction

Retinal dystrophies, such as age-related macular degeneration and *Retinitis Pigmentosa*, are amongst the leading causes of visual impairment worldwide (together with cataract and glaucoma) and are the primary cause of visual deficit in middle income and industrialised countries, with prevalence above 15 %^{1,321}. Although the dystrophy induces the progressive loss of photoreceptors (PRs), the inner retinal cells and the retinal ganglion cells (RGCs) are temporarily preserved and can be electrically excited to produce artificial vision^{68,69,157,367}. Several retinal prostheses, developed in the past decades, enabled the restoration of an elementary form of vision in humans, including the discrimination of high-contrast gratings, reading of large prints, and spatial orientation^{158,186,205,367}. Nevertheless, they provide limited visual field and visual acuity, so that the recovered sight quality is still far away from being adequate in daily life³²⁵. Following these results, several new devices are currently under development, and among them, photovoltaic prostheses offer the possibility of a wireless high-resolution electrical stimulation of the retina^{194,320,368,99,329,369,370}.

With epiretinal prostheses, the low visual acuity reported in patients is often associated with the perception of amplitude-dependent elongated phosphenes^{232,318}, attributed to the direct depolarisation of several axons of passage located between the epiretinal device and the RGC layer^{235,367,371}. The perception of these elongated phosphenes hampers the capability of the patient to perceive complex shapes^{136,233,372}. Although the axon initial segment is the cellular compartment with the lowest activation threshold²³³, in practice, its activation threshold is barely discriminable from the ones of more distal axonal segments²³⁵, making the selective stimulation of a single axon a challenge. Various complementary approaches were proposed to improve the stimulation resolution of epiretinal prostheses: minimizing the spread of the electric field generated by single electrodes to avoid stimulation cross-talk³⁷³, using penetrating electrode arrays to reduce the stimulation distance^{152,374,375}, increasing the charge injection capacity of microelectrodes with coatings to reduce their size^{369,376,377}, tuning the stimulation parameters to selectively activate only cells close the electrode^{237,348}, or selecting the optimal cluster of electrodes curtailing the activation of distal axon segments^{235,371}.

Besides, a large share of effort has been directed towards the understanding and exploitation of network-mediated indirect stimulation of RGCs, which arises from the direct activation of presynaptic neurons, such as bipolar cells (BCs), which in turn lead to a secondary indirect excitation of RGCs^{251,269,337,338,378–381}. During epiretinal stimulation, the direct activation of RGCs typically results in only one or two short latency (SL) spikes³⁸², occurring within a few milliseconds from the stimulus onset. Conversely, the indirect activity arising through network-mediated activation is delayed and can be composed of multiple types of responses. Usually, a first indirect activation burst, defined as medium latency (ML), occurs within 10 to 70 ms after the stimulus onset, with considerable variability between reports^{251,269,337,338,378,379,381–383}. After, a second indirect activation burst, defined as long latency (LL), occurs with longer latencies (e.g. longer than 150 ms). Notably, the indirect activation pattern is specific for each RGC type^{382,383} and, for a given RGC, it shows a remarkable timing^{337,338,381} closely matching with the temporal complex light-evoked responses³⁸³.

It was reported that short pulses (e.g. μ s long) preferentially activate the axons of RGCs^{29,237,269,378}, generating one or two SL action potentials with high temporal precision^{269,378,382}, but causing streak responses²³⁷. Pulses of longer duration lead to both direct and indirect excitation of RGCs^{251,337,338,378,382}. Recent evidence suggests a clinical relevance of indirect activity to improve the resolution of retinal responses upon electrical stimulation. A study with the Argus® II retinal prosthesis, the epiretinal system currently approved by regulatory bodies, notably pointed out the relationship between the inner retina activation elicited by long electric pulses (i.e. 25 ms) and the increased spatial resolution, observed both *ex-vivo* and in patients implanted with the Argus® II²³⁷. However, the mechanisms behind the epiretinal indirect activation pattern of RGCs are not yet fully understood. Converging evidence suggests the activation of the inner retinal layer as the primary factor causing indirect activity^{251,337,384,385}. It is in addition likely that the generation of an indirect response involves the coordinate activation of several cell types, including the retinal inhibitory network.

Our previous work with POLYRETINA, a photovoltaic epiretinal prosthesis, showed that light sensitivity could be restored by photovoltaic stimulation in *Retinal degeneration 10 (Rd10)* mice retinas at advanced stages of degeneration³⁶⁹. Consistently with other group findings, we reported both direct and indirect activation of RGCs, upon 10-ms light pulses. Conventionally, retinal prostheses employ electrical pulses with a rectangular shape; however, POLYRETINA intrinsically generates non-rectangular capacitive-like voltage pulses³⁶⁹. Growing insights suggest that non-rectangular pulses, with slow increase rates, elicit a stronger activation of the inner retinal presynaptic neurons than rectangular pulses, leading to an enhanced indirect firing activity of RGCs^{386,387}. Moreover, low-pass filtering inner retinal cells are less activated by high-frequency signals such as rectangular pulses, more favourable to the direct depolarisation of RGCs^{386,387}. Given the importance of indirect activation of RGCs and the role played by the shape of the electric pulses, we explored whether and how the non-rectangular capacitive-like voltage pulses generated by POLYRETINA lead to robust indirect activation of RGCs. Beyond the investigation on the effect of non-rectangular capacitive-like voltage pulses, we documented the underlying biophysical principles that relate the stimulus waveform with the indirect activation and the focusing of the evoked response.

3.3 Methods

3.3.1 Statistical analysis and graphical representation

Statistical analysis and graphical representation were performed with MATLAB (MathWorks) and Python. The normality test (D'Agostino & Pearson omnibus normality test) was performed in each dataset to verify the use of a parametric or non-parametric test. In each figure, p-values were reported as: * $p < 0.05$, ** $p < 0.01$, *** $p < 0.001$, and **** $p < 0.0001$. Data are reported as mean \pm s.e.m. or mean \pm s.d.; n identifies the number of electrodes or cells and N identifies the number of retinas.

3.3.2 Animal handling and preparation of retinal explants

Experiments were conducted according to the ethical authorisation GE3717 approved by the Département de l'emploi, des affaires sociales et de la santé (DEAS), Direction générale de la santé of the République et Canton de Genève, Switzerland. Male and female *Rd10* mice from a homozygous colony of B6.CXB1-Pde6b^{rd10}/J mice (The Jackson Laboratory) were used for the experiments. All animals were kept in a 12 h day/night cycle with access to food and water ad libitum. All the experiments were carried out during the day cycle. Eyes were enucleated from euthanised mice (sodium pentobarbital, 150 mg kg⁻¹) and dissected in carboxygenated (95 % O₂ and 5 % CO₂) Ames' medium (A1420, Sigma-Aldrich) under dim red light. Retinas were placed ganglion cells down and maintained in contact with a microelectrode array (MEA) or a POLYRETINA prosthesis using a 1 mm nylon mesh. Retinas were continuously superfused with carboxygenated Ames' medium at 32 °C and maintained under dim red light during all the experiments.

3.3.3 Light stimulation

In order to assess the natural light responsivity in *Rd10* mice, retinas explanted at various postnatal days (P16, P30 \pm 3, P45, P60, P96, P115 \pm 3, P130 \pm 1, and P155 \pm 1) were mounted on filter paper and placed with RGCs down on a transparent MEA with 256 electrodes (256MEA200/30iR-ITO, Multi Channel Systems). Retinal explants were illuminated with an inverted microscope (Ti-E, Nikon Instruments) and a LED illuminator (Spectra X, emission filter 560/32 nm, Lumencor). The microscope was equipped with a dichroic filter (FF875-Di01-25x36, Semrock) and 4x / 10x / 20x objectives (diameter of the illumination spot: 5.5, 2.2, and 1.1 mm respectively; CFI Plan Apochromat Lambda). The signal from the 256 recording electrodes was amplified, filtered (300 – 3000 Hz), and digitalised at 10 kHz (USB-MEA256-System, Multi Channel Systems). Spike detection was performed with the MC_rack software (Multi Channel Systems), and the results were further processed with Neuroexplorer (Neuronexus) and MATLAB. For each retina, data from all the electrodes presenting spontaneous or light-evoked spikes were averaged. The number of detected RGCs varied between preparations as follows: P16 ($n = 7$, $N = 2$), P30 ($n = 10$, $N = 4$), P45 ($n = 10$, $N = 3$), P60 ($n = 8$, $N = 2$), P96 ($n = 8$, $N = 2$), P115 ($n = 13$, $N = 4$), P130 ($n = 10$, $N = 2$), and P155 ($n = 25$, $N = 6$).

3.3.4 Photovoltaic and electrical stimulation

Photovoltaic and electrical stimulations were performed in *Rd10* mice at P144 \pm 18.5 (mean \pm s.d). Photovoltaic stimulation was carried out with the central part of the POLYRETINA prosthesis, embedding 80- μ m diameter titanium electrodes with a 150- μ m pitch³⁶⁹. Illumination was performed as described above. Electrical stimulation was carried out with a custom-made MEA, embedding a grid of 16 x 16 (256) titanium electrodes (80- μ m diameter) with a 150- μ m pitch. All the recorded RGCs were stimulated with both rectangular and non-rectangular capacitive-like voltage pulses.

In both photovoltaic and electrical stimulation, the stimulation protocol consisted of a repetition of 10 pulses at 1 Hz for each condition. Irradiance, pulse amplitude, pulse duration, and stimulus shape were increased sequentially up to the condition eliciting the highest RGC activity. The activity of RGCs was recorded extracellularly with a sharp metal electrode (PTM23B05KT, World Precision Instruments), amplified (Model 3000, A-M System), filtered (300 - 3000 Hz), and digitalised at 30 kHz (Micro1401-3, CED Ltd.). Spike detection and sorting were performed by threshold detection using the MATLAB-based algorithm Wave_clus³⁵²; the results were further processed with MATLAB. Voltage transients detected within \pm 1 ms around the stimulus onset and offset were automatically classified as stimulus artefacts and the timestamps removed for subsequent calculations. In addition, neural spikes detected from 1 to 10 ms after the stimulus onset were manually verified to ensure a proper detection and artefact rejection. The spike raster from 10 consecutive sweeps was averaged and discretised to compute 10-ms bins PSTHs. To be consistent with our previous study³⁶⁹, spikes occurring within 1 to 10 ms from the stimulus onset were classified as SL, spikes occurring between 40 and 120 ms as ML, and spikes occurring between 150 and 350 ms as LL. Supra-threshold SL, ML, and LL activities were determined as the minimal condition leading to responses whose firing rates were significantly higher ($p < 0.05$) than RGC spontaneous activity, assessed from control trials or pre-stimulus recordings.

3.3.5 Computational model

The biophysical retinal layers were modelled using the python-based NEST 2.14.0 simulator tool³⁸⁸. For the RGC layer, a grid of 10 x 10 transient α -RGCs (without any ON-OFF specification) was modelled as Hodgkin–Huxley neurons¹⁴⁰, in which the resting potential (V_{rest}) was set to -70 mV^{389,390} and the threshold potential (V_T) to -55 mV³⁸⁹. RGCs were connected with local gap junctions as formalized in **Equation 1**, where j is the neuron coupled to the cell i by gap junctions, V is the membrane potential and g the junction weight³⁹¹.

$$I_{gap\ i}(t) = \sum_j g_{ij}(V_j(t) - V_i(t))$$

Ch.3 Equation 1

In order to model sustained α -RGCs, the Hodgkin–Huxley model was substituted by an adaptive exponential integrate-and-fire model³⁹², whose membrane potential is described by **Equations 2** and **3**.

$$C \times \frac{dV}{dt} = -w + I + g \times (V - V_{rest}) + g \times \Delta_T \times e^{\frac{V - V_T}{\Delta_T}}$$

Ch.3 Equation 2

$$\tau_w \times \frac{dw}{dt} = a(V - V_{rest}) - w$$

Ch.3 Equation 3

In these equations, V_{rest} was set to -70 mV, V_T was set to -55 mV^{389,390}, C is the membrane capacitance (281 pF), g is the leak conductance (30 nS), Δ_T is the voltage slope factor (2 mV), a is the subthreshold adaptation level (0.75 nS), τ_w the adaptation time constant (144 ms), and w the internal adaptation current^{392,393}. After a spike has been triggered, w is decremented of a spike-triggered adaptation constant of 50 pA and **Equation 2** is reintegrated from a reset value $V_{reset} = -67.5$ mV, as previously described^{392,393}. For both models, the RGC layer was placed 10 μ m above an 80- μ m diameter titanium epiretinal electrode delivering voltage-controlled pulses. As a result, the dynamics of the RGCs depend on the external delivered voltage, their presynaptic inputs, and the membrane potential of neighbouring RGCs.

The inner retinal layer was modelled with non-spiking leaky integrating neurons (whose resting potential V_{rest} was set to -70 mV^{389,390}). In these neurons, a membrane potential change induces in the post-synaptic cells a current linearly proportional to the membrane potential variation of the presynaptic cell. The dynamics of the membrane potentials were conductance-based modelled. The resulting response model can be defined according to **Equation 4** and **5**, where i represents the presynaptic cell, j the postsynaptic cell, V the cell membrane potential, V_{rest} the resting potential, τ its membrane time constant, J the external input, and I the synaptic input³⁹⁴:

$$\frac{dV_j}{dt} = -\frac{V_j - V_{j,rest}}{\tau_j} + \sum_i I_i(t) + J(t)$$

Ch.3 Equation 4

$$I_i(t) = w_{ij} \times \frac{dV_i > 0}{dt}$$

Ch.3 Equation 5

	Neuronal layer				Reference
	RGC	AC	BC	HC	
Cell ratio to RGC	1	5	4	1	395,396
Distance to the electrode	10 μ m	30 μ m	49 μ m	64 μ m	397
Cell diameter	10 μ m	5 μ m	5 μ m	10 μ m	396

Ch.3 Table 1 - Retinal layers' parameters

The model parameters for the retinal layers are summarised in **Table 1**. According to previous studies^{395,398,399}, the connectivity between layers was designed as follows: the horizontal cell (HC) to bipolar cells (BC) convergence was 1:16; the BC to amacrine cell (AC) convergence 1:5; the AC to RGC convergence 1:4; the RGC to BC divergence 1:4.

For each layer, the filter time constant was calculated according to **Equation 6**.

$$RC = \left(R_{ex} \times d + A \times \frac{1}{g_{mb}} \right) \cdot \frac{1}{\frac{1}{C_{ex} \cdot d} + \frac{1}{A \cdot C_{mb}}}$$

Ch.3 Equation 6

where R_{ex} is the extracellular resistivity, C_{ex} is the extracellular capacitance, C_{mb} is the passive membrane capacitance, g_{mb} is the bilayer membrane conductance, d is the cell distance to the electrode surface, and A is the area of the bilayer membrane in the ascending column between the targeted cell and the electrode, as in **Equation 7**:

$$A = a \times \rho \times \frac{d}{D}$$

Ch.3 Equation 7

in which α is the single cell surface, ρ is the number of cells in a theoretical receptive field per each layer, and D is the average retinal cell diameter. These parameters are provided in **Table 2**.

	R_{ex}	C_{ex}	C_{mb}	g_{mb}	α	ρ	D
	[$\Omega \cdot m$]	[$F \cdot m^{-1}$]	[$F \cdot m^{-2}$]	[$\mu\Omega^{-1} \cdot m^{-2}$]	[μm^2]		[μm]
	10	0.1	0.01	5	300,000	42.8	7
Reference	400,401	400,401	371	402	403	396,404	396

Ch.3 Table 2 - Biophysical parameters of the retinal layers

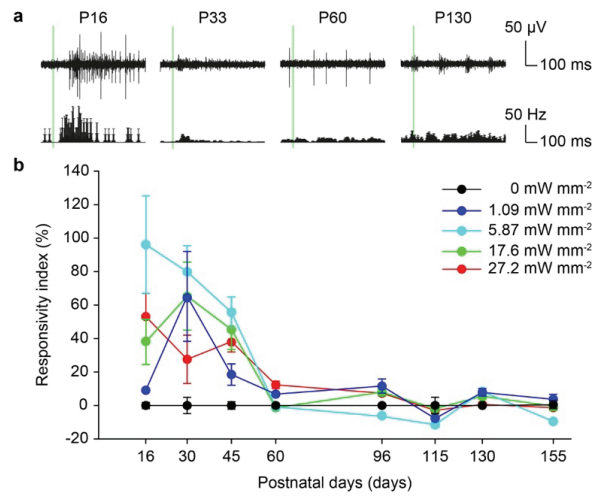
The voltage density above the epiretinal electrode was simulated with a finite element analysis (FEA) method with a stationary electric current study (COMSOL Multiphysics® v. 5.2.). The ground was located at the bath top and lateral walls, respectively 2 mm and 1 mm away from the electrode. The retinal tissue was placed from 10 to 110 μm above the electrode surface. The distribution of the voltage densities in the retina was evaluated every 5 μm from the retinal surface. For each material, the conductivity ($S \cdot m^{-1}$) and relative permittivity values were set to: titanium ($2.6 \times 10^6 / 1$)⁴⁰⁵, P3HT:PCBM (0.1 / 3.4)^{406,407}, PEDOT:PSS (30 / 3)^{408,409}, Saline (1 / 80)^{410,411}, PDMS ($2 \times 10^{-14} / 2.75$)³⁵⁷, and retinal tissue (0.1 / 0.01)⁴¹². The voltage density was spatially approximated as a Gaussian probability distribution and temporally fitted as a first-degree exponential peaking at the FEA output values. The membrane potential of the cells located in the centre of the stimulated electrode and the two-dimensional firing activity were directly assessed using the multimeter tool. The membrane potentials were sampled at 1 kHz and the network updated with 1-ms time steps. Spikes occurring within 10 ms after stimulus onset were classified as SL, spikes occurring between 20 and 150 ms were classified as ML, and for sustained α -RGCs, spikes occurring between 150 and 400 ms were classified as LL. The time intervals for ML and LL responses have been slightly adapted from *ex-vivo* ones accordingly to the output of the model. Supra-threshold SL, ML, and LL activities were determined as the voltage leading to responses whose firing rates were higher than zero.

3.4 Results

3.4.1 Light responsivity of *Rd10* retinas to high irradiance levels

All the experiments were performed with explanted retinas from *Rd10* mice, which is an established model for *Retinitis Pigmentosa*^{101,121,413}. However, in order to formally exclude any intrinsic light responsivity to high irradiance levels from possible surviving PRs, we first assessed the time course of the light responsivity decay at the wavelength and irradiance used for prosthetic stimulation with POLYRETINA: full-field 10-ms light pulses at 560 nm with irradiance levels from 0.39 to 27.2 mW mm⁻² (Figure 1a). For each time point and irradiance, we computed a light responsivity index as the relative percent change in firing rate during the 0- to 180-ms time window after the light onset (\bar{R}) compared to a 100-ms pre-stimulus time window (R), as $\frac{\bar{R}-R}{R}$ (Figure 1b). In this manner, the index accounts for both ON and OFF transient and sustained responses.

After the formation of functional PRs at P16, a rapid decay in the light responsivity index was observed up to P60, where it reaches its minimum value and remains constant around a baseline value of 0 regardless of the irradiance. This time course is in agreement with the reported anatomical changes in the outer nuclear layer of *Rd10* retinas^{413,414}. In young retinas (from P16 to P45), mostly transient ON responses could be detected (Figure 1a), with a mean (\pm s.e.m.) latency of 67.08 \pm 3.61 ms. The light responsivity to green light increases with the irradiance up to 5.87 mW mm⁻², after which further increase of the irradiance weakens the response of the retina. This weakening is most probably due to PR saturation and eventually bleaching for higher irradiance levels. In retinas over P60, we could not record any significant light responsive RGC, nor at low or high irradiance levels. On the other hand, in line with previous reports^{121,414,415}, the majority of RGCs from retinas explanted at those advanced stages of degeneration exhibits a robust light-independent spontaneous activity, with a peak frequency of about 10 to 15 Hz. The more advanced the degeneration process, the higher the number of cells presenting strong spontaneous activity is observed. In order to ensure a proper exclusion of intrinsic light-responses together with proper detection of spontaneously active RGCs, further experiments were performed in *Rd10* retinas at late stages of degeneration (> P120).

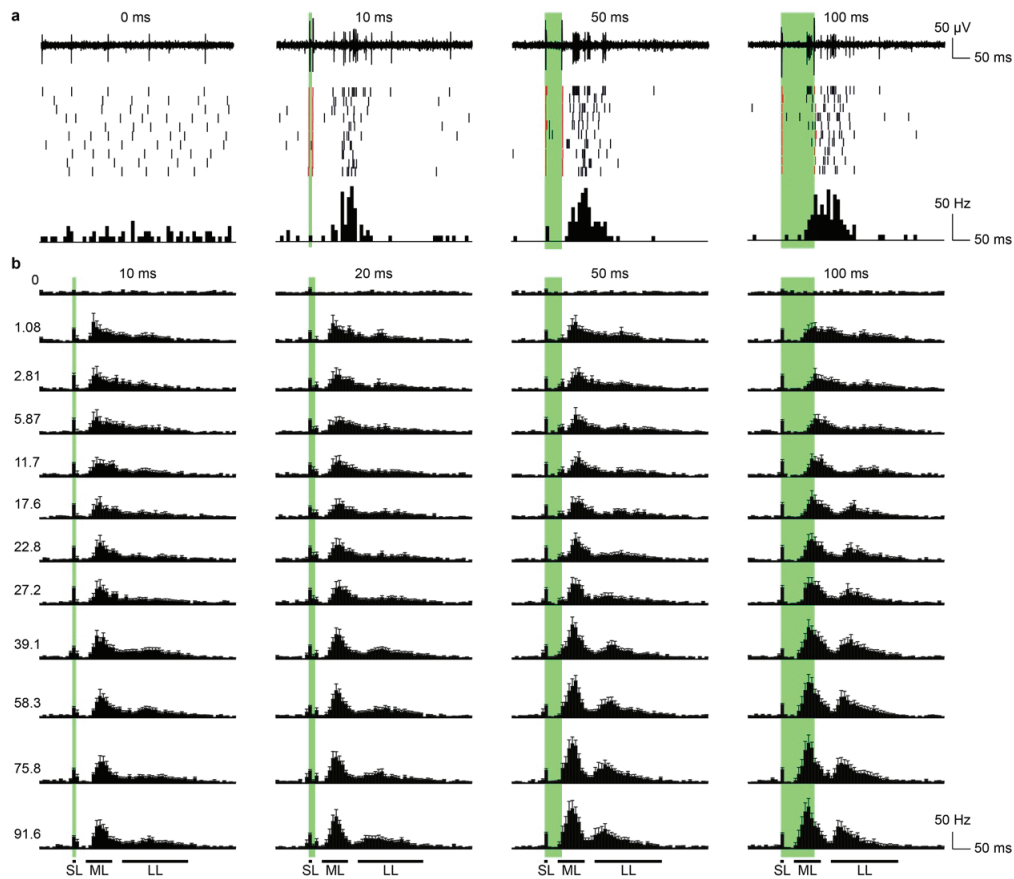


Ch.3 Figure 1 - Light responsivity decay in *Rd10* retinas over the degeneration process

a, Extracellular spiking activity from *Rd10* retinas explanted at P16, P33, P60, and P130 in response to a light pulse (10 ms, 560 nm, 1.08 mW mm⁻²). The top row shows the electrophysiological recordings from one electrode upon illumination. The bottom row shows the corresponding mean (\pm s.e.m.) PSTH (bins of 10 ms). The green bars show the duration of the light pulse. b, Mean (\pm s.e.m.) light responsivity index upon illumination (10 ms, 560 nm) of *Rd10* retinas recorded at P16, P30 \pm 3, P45, P60, P96, P115 \pm 3, P130 \pm 1, and P155 \pm 1. For each RGC, ten consecutive sweeps were averaged. Data are shown for five irradiance levels only: 0, 1.08, 5.87, 17.6, and 27.2 mW mm⁻².

3.4.2 Photovoltaic stimulation of the inner retinal network

Next, we investigated whether, with a photovoltaic approach, the duration of the light pulse alters the response pattern of RGCs, as previously reported for electric stimuli^{337,381}. Retinas were explanted in epiretinal configuration over the POLYRETINA prosthesis and the activity of RGCs ($n = 16$, $N = 9$) was recorded upon 10-, 20-, 50-, and 100-ms light pulses (560 nm), with irradiance levels ranging from 1.08 to 91.59 mW mm⁻² (**Figure 2**).



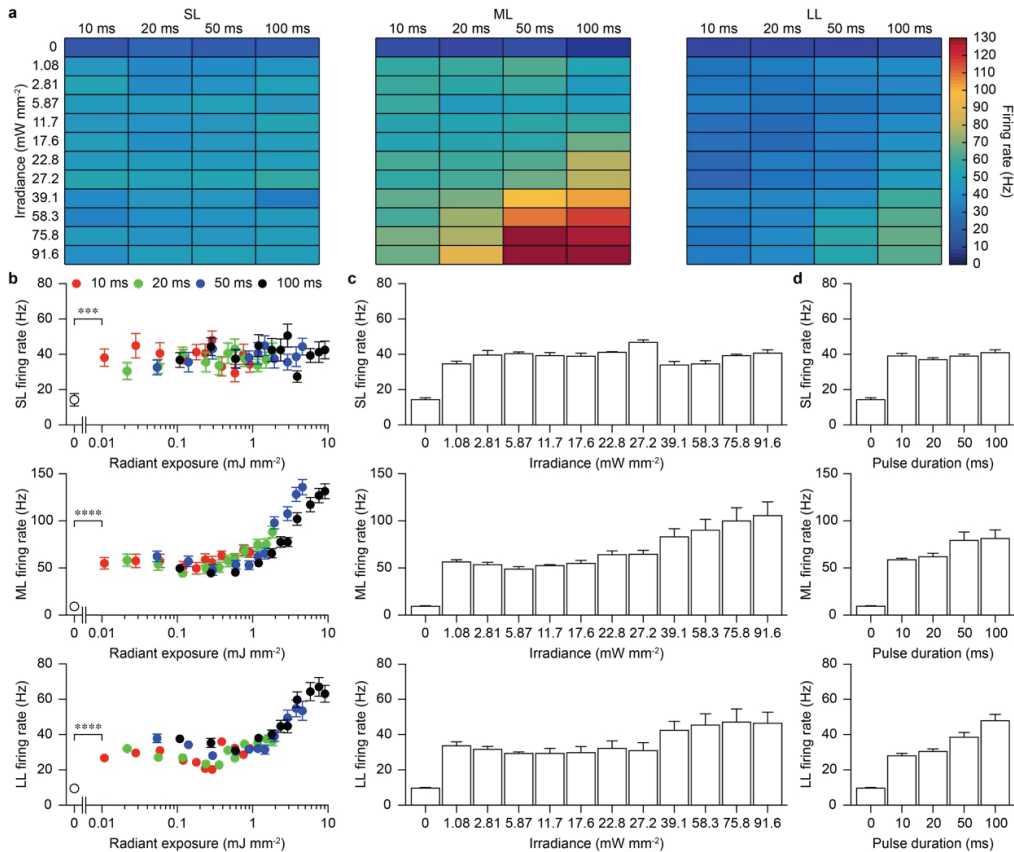
Ch.3 Figure 2 - Photovoltaic stimulation elicits exposure-dependant activity in *Rd10* retinas

a, Extracellular spiking activity of one RGC in response to a 0-, 10-, 50-, and 100-ms photovoltaic stimulation (560 nm, 2.81 mW mm⁻²) with POLYRETINA. The top row shows the electrophysiological recordings upon illumination. The middle row shows the raster plot of 10 consecutive sweeps. The bottom row shows the corresponding PSTH (bins of 10 ms). The red lines in the raster correspond to the events classified as stimulus artefacts. **b**, Mean (\pm s.e.m.; $n = 16$, $N = 9$) PSTH (bins of 10 ms) of RGC activity upon 10-, 20-, 50-, and 100-ms photovoltaic stimulation. For each RGC, ten consecutive sweeps were averaged. Light pulses were delivered with increasing irradiance levels: 1.08, 2.81, 5.87, 11.68, 17.60, 22.76, 27.17, 39.06, 58.32, 75.80, and 91.59 mW mm⁻². The horizontal bars at the bottom of the PSTHs show the time windows used for the discrimination of SL, ML, and LL responses. In both panels, the green bars show the duration of the light pulse.

Extracellular recordings under photovoltaic stimulation revealed a spiking pattern made of two to three waves of activation (SL, ML, and LL). Within the tested range of irradiance levels (from 1.08 to 91.59 mW mm⁻²) and pulse durations (from 10 to 100 ms), SL responses are exposure independent while ML and LL responses strongly depend on light exposure (**Figure 3a**). Supra-threshold activities can be recorded (**Figure 3b**); $p < 0.001$, $p < 0.0001$, and $p < 0.0001$, respectively for SL, ML, and LL; one-tailed t-test) from the lowest exposure tested (10 ms and 1.08 mW mm⁻²). SL spikes are elicited at an average (\pm s.e.m.) steady frequency of 36.9 ± 8.25 Hz (**Figure 3(b-d)**, top panels). Instead, the indirect activity (ML and LL) strongly depends on both irradiance and pulse duration (**Figure 3b-d**, respectively middle and bottom panels).

A two-way ANOVA analysis revealed that both the main effects of irradiance and pulse duration on ML and LL responses are significant, while their interaction is not ($p = 0.81$ and $p = 0.96$, respectively for ML and LL). For ML response, irradiance has a stronger effect than pulse duration (irradiance: $F = 10.36$ and $p < 0.0001$; duration: $F = 5.08$ and $p < 0.01$), while the opposite occurs for LL

response (irradiance: $F = 7.24$ and $p < 0.0001$; duration: $F = 13.52$ and $p < 0.0001$). The ML indirect activity reaches $187 \pm 26\%$ (mean \pm s.e.m) of its initial values when increasing the irradiance from 1.08 to 91.59 mW mm^{-2} (average of all the pulse durations tested; **Figure 3c**, middle) and $139 \pm 16\%$ (mean \pm s.e.m) of its initial values when lengthening the pulse duration from 10 to 100 ms (average of all the irradiance levels tested; **Figure 3d**, middle). The LL indirect activity reaches $138 \pm 31\%$ (mean \pm s.e.m) of its initial values when increasing the irradiance (**Figure 3c**, bottom) and $171 \pm 19\%$ (mean \pm s.e.m) of its initial values when lengthening the pulse duration (**Figure 3d**, bottom) as computed above.

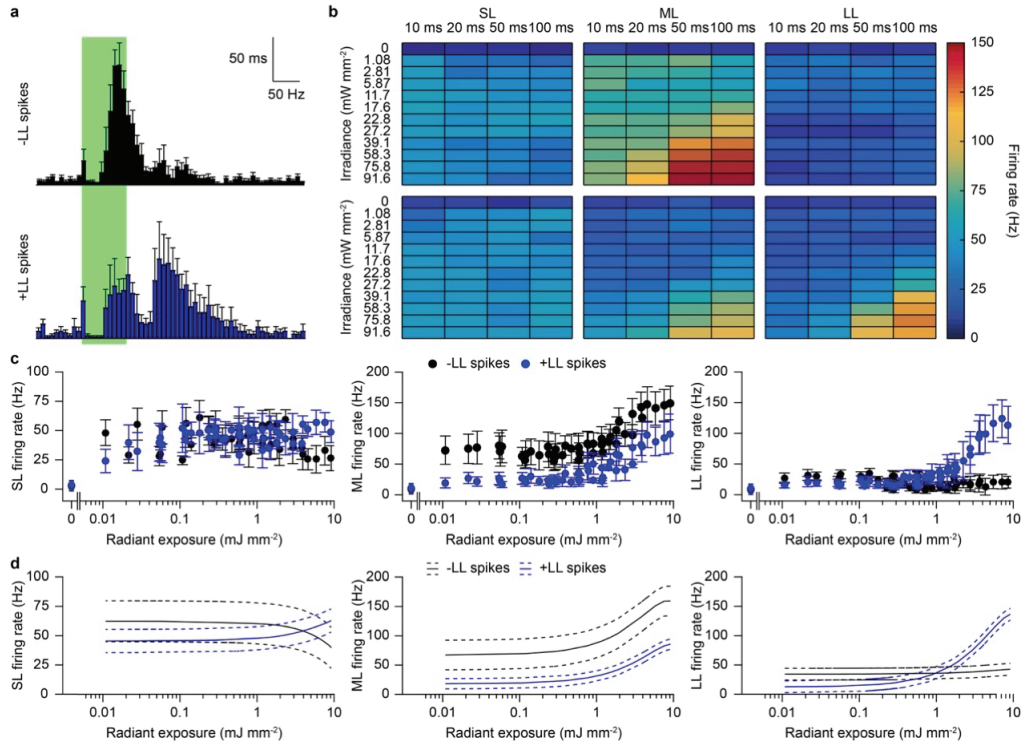


Ch.3 Figure 3 - Characterisation of the direct and the indirect activities evoked by photovoltaic stimulation

a, Heatmaps of SL (left), ML (middle), and LL (right) mean firing rates upon 10-, 20-, 50-, and 100-ms photovoltaic stimulation. The irradiance is indicated on the left of each row. **b**, Mean (\pm s.e.m; $n = 16$, $N = 9$) firing rates of SL (top), ML (middle), and LL (bottom) responses as function of the radiant exposure (mJ mm^{-2}), obtained by multiplying the irradiance (mW mm^{-2}) per the pulse duration (s). For each RGC, ten consecutive sweeps were averaged. **c,d**, Grand averages of the mean (\pm s.e.m, $n = 16$, $N = 9$) firing rates of SL (top), ML (middle), and LL (bottom) responses over all the pulse durations (**c**) and irradiance levels (**d**).

Noteworthy, only 5 out of 16 (31.25 %) of the recorded RGCs showed significant LL activity, independently of the animal age and retina quadrant recorded (**Figure 4**). The two groups of RGCs, exhibiting or not LL spikes (**Figure 4a,b**), showed a similar evolution in the SL and ML spiking activity to increasing radiant exposures (**Figure 4c,d**, left and middle respectively), despite exhibiting a different behaviour for the LL one (**Figure 4c,d**, right). The fitting of the two responses over exposure with quadratic (second order polynomial) functions revealed a significant difference in the second-degree term coefficient for LL response ($p < 0.0001$; two-tailed t-test) but not for SL ($p = 0.12$; two-tailed t-test) and ML ($p = 0.08$; two-tailed t-test) responses. The first-degree term coefficients were not significantly different between the two populations in none of the cases ($p = 0.49$, $p = 0.40$, and $p = 0.18$ respectively for SL, ML, and LL responses; two-tailed t-test). ML responses showed also a significant difference in the offset regression coefficient ($p < 0.0001$; two-tailed t-test). Such difference might arise from diverging intrinsic firing properties of the two RGCs types. SL and LL offset firing rates were not significantly different between the two populations ($p = 0.08$ and $p = 0.06$ for SL and LL, respectively; two-tailed t-test). Taking into account the RGCs exhibiting LL activity only ($n = 5$), the LL indirect activity reaches $374 \pm 64\%$ (mean \pm s.e.m) of its initial values when increasing the irradiance and $367 \pm 191\%$ (mean \pm s.e.m) of its initial values when lengthening the pulse duration as computed above. The generation of significant LL indirect responses in only a portion of the overall cell population might be related

to the functional characteristics of RGCs. Indeed, sustained cells could respond up to hundreds of milliseconds after a single electrical stimulation while transient RGCs exhibited shorter indirect responses³⁸².



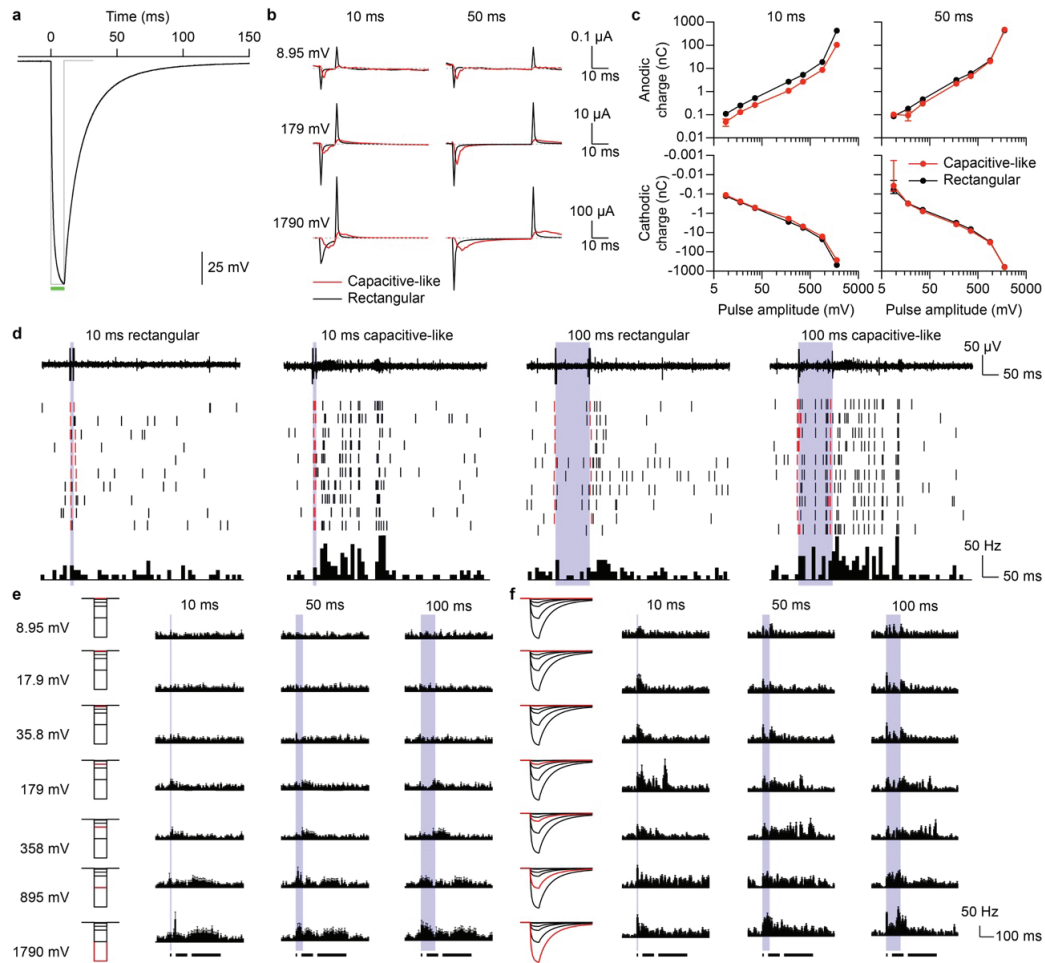
Ch.3 Figure 4 - Classification of RGCs exhibiting or not LL activity

a, Mean (\pm s.e.m) PSTH (bins of 10 ms) upon 100-ms photovoltaic stimulation (560 nm, 91.6 mW mm⁻²) of RGC activity with (blue, $n = 5$) or without (black, $n = 11$) LL activity. For each RGC, ten consecutive sweeps were averaged. The green bar shows the duration of the light pulse. **b**, Heatmaps of SL (left), ML (middle), and LL (right) mean firing rates upon 10-, 20-, 50-, and 100-ms photovoltaic stimulation of RGCs with (bottom, $n = 5$) or without (top, $n = 11$) LL activity. The irradiance is indicated on the left of each row. **c**, Mean (\pm s.e.m) firing rates of SL (left), ML (middle), and LL (right) responses of RGCs with (blue, $n = 5$) or without (black, $n = 11$) LL activity. **d**, Quadratic regression (\pm s.d.) of SL (left), ML (middle), and LL (right) responses with (blue) or without (black) LL activity.

3.4.3 Capacitive-like versus rectangular electrical stimulation of the inner retinal network

Photovoltaic stimulation with POLYRETINA was triggered by rectangular light pulses; however, POLYRETINA intrinsically generates non-rectangular capacitive-like voltage pulses³⁶⁹. Therefore, we investigated whether the capacitive-like shape of the voltage delivered by POLYRETINA would play a role in the activation of the inner retinal network.

To compare photovoltaic capacitive-like versus rectangular pulses, explanted retinas were stimulated through a custom-made MEA with 256 80- μ m titanium electrodes. Stimulation consisted in paired rectangular and non-rectangular capacitive-like voltage pulses of increasing pulse amplitudes (8.5, 17.9, 35.8, 179, 358, 895, and 1790 mV) and pulse durations (10, 50, and 100 ms). Non-rectangular capacitive-like voltage pulses of various peak amplitudes were generated by scaling the mean voltage profiles measured on top of the photovoltaic pixels under 10-, 50-, and 100- light pulses at 0.94 mW mm⁻² (data profiles obtained from³⁶⁹). As a consequence, the nominal duration of non-rectangular capacitive-like voltage pulses (defined by the duration of the light pulse) does not correspond to the total duration of the voltage stimulus, since the latter has a slow voltage decrease (**Figure 5a**).



Ch.3 Figure 5 - Electrical stimulation of *Rd10* retinas with rectangular and non-rectangular capacitive-like voltage pulses
a, Photovoltage profile (black line) generated by POLYRETINA pixels upon a 10-ms light pulse (green bar) at 0.94 mW mm^{-2} . Data profile from³⁶⁹. The grey line shows a 10-ms rectangular voltage pulse of identical peak amplitude. **b**, Current delivered by 80- μm titanium electrodes upon 10- (left) and 50-ms (right) rectangular (black) and non-rectangular capacitive-like (red) voltage pulses with various peak amplitudes (8.95, 179, and 1790 mV). **c**, Mean (\pm s.d., $n = 3$) anodic (top) and cathodic (bottom) charge delivered upon 10- (left) and 50-ms (right) rectangular (black) and non-rectangular capacitive-like (red) voltage pulses with various peak amplitudes (8.95, 17.9, 35.8, 179, 358, 895 and 1790 mV). **d**, Extracellular recordings of one RGC in response to a 179-mV electrical stimulation with a 10-ms rectangular pulse (left), a 10-ms non-rectangular capacitive-like pulse (middle left), a 100-ms rectangular pulse (middle right), and a 100-ms non-rectangular capacitive-like pulse (right). The top row shows the electrophysiological recordings upon electrical stimulation. The middle row shows the raster plots of 10 consecutive sweeps. The bottom row shows the corresponding PSTHs (bins of 10 ms). The red lines in the raster correspond to the events classified as stimulus artefacts. **e**, **f**, Mean (\pm s.e.m; $n = 13$, $N = 11$) PSTHs (bins of 10 ms) of RGC activity upon 10-, 50-, and 100-ms stimulation with rectangular (**e**) and non-rectangular capacitive-like (**f**) voltage pulses. For each RGC, ten consecutive sweeps were averaged. The pulse shapes corresponding to each amplitude are highlighted in red (8.95, 17.9, 35.8, 179, 358, 895 and 1790 mV). The horizontal bars at the bottom of the PSTHs show the time windows used for the discrimination of SL, ML, and LL responses. In all the panels, the blue bar shows the electric pulse.

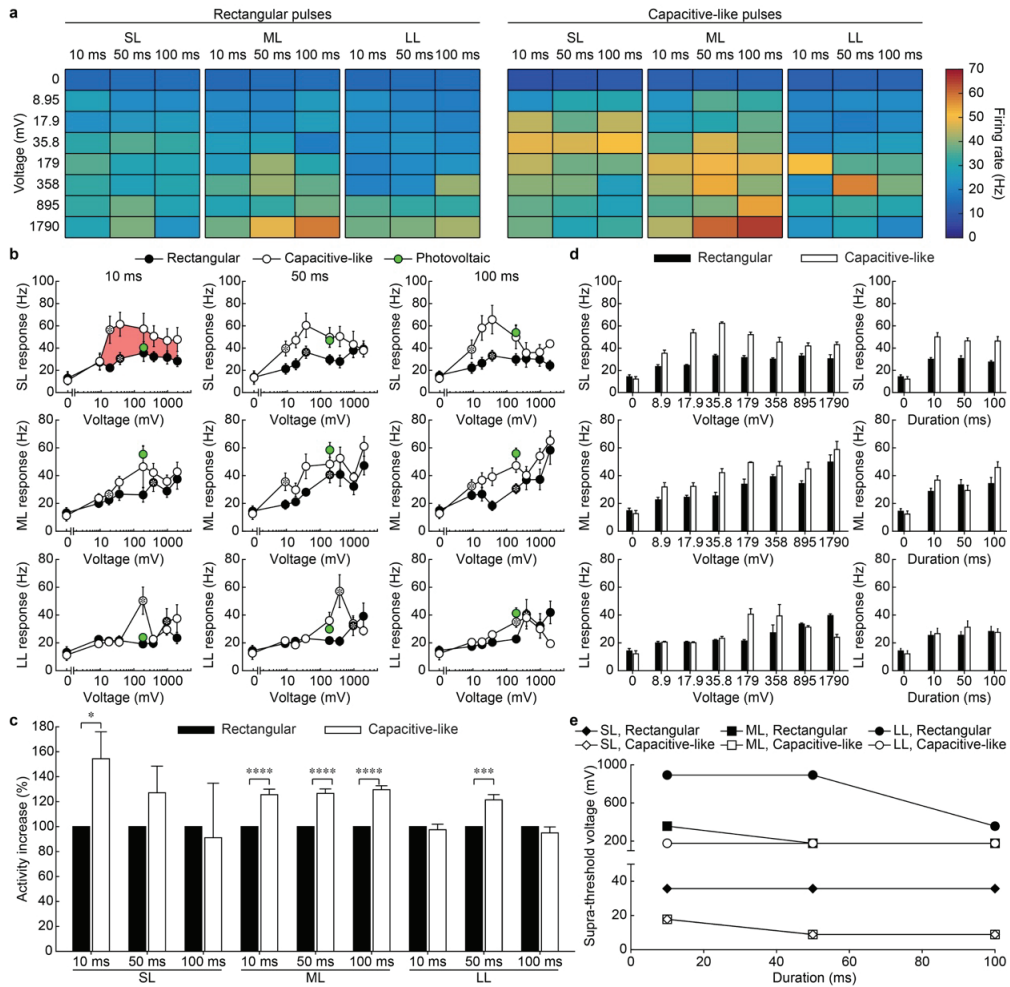
To ensure that the total charge delivered by the two voltage profiles is comparable, we measured the cathodic and anodic charges injected during 10- and 50-ms voltage pulses with both rectangular and non-rectangular capacitive-like voltage pulses at various peak amplitudes (**Figure 5b**). Measures were performed with a three-electrode (Ag / AgCl reference electrode, Pt counter electrode) potentiostat (Compact Stat, Ivium) in PBS (pH 7.4) at room temperature. Cathodic and anodic charge was respectively calculated as the integral of the current waveform over its negative and positive peaks. Because titanium is a capacitive material³³², during a cathodic rectangular voltage pulse the current peaks at the onset (cathodic current) and at the offset of the stimulus (anodic current), and it is nil during the pulse (**Figure 5b**, black). For non-rectangular capacitive-like voltage pulses, the cathodic and anodic current peaks are widened by the slow voltage increase and decrease (**Figure 5b**, red). However, the average (\pm s.d., $n = 3$ electrodes) charge

delivered by rectangular (black) and non-rectangular capacitive-like (red) voltage pulses under paired condition of pulse amplitude and duration are not significantly different (**Figure 5c**). A three-way mixed ANOVA (waveform is a between-subject variable; amplitude and duration are within-subject variables; Mauchly's sphericity test $p < 0.0001$) revealed that the pulse waveform had no statistically significant effect on the cathodic nor anodic charge (cathodic phase: $F = 0.55$ and $p = 0.46$; anodic phase: $F = 1.23$ and $p = 0.27$; repeated measures ANOVA), neither did the pulse duration (cathodic phase: $F < 0.0001$ and $p = 0.99$; anodic phase: $F = 0.29$ and $p = 0.59$; repeated measures ANOVA), while the pulse amplitude did for both phases (cathodic phase: $F = 10.8$ and $p < 0.05$; anodic phase: $F = 23.0$ and $p < 0.05$; repeated measures ANOVA). The interaction between the pulse amplitude and the pulse duration was not statistically significant for any of the phases (cathodic phase: $F = 0.03$ and $p = 0.87$; anodic phase: $F = 4.42$ and $p = 0.054$; repeated measures ANOVA). Such results prevent any difference between rectangular and non-rectangular capacitive-like voltage pulses effects on the retinal network activation to be attributed to the amount of charge they deliver.

Retinas were then explanted in epiretinal configuration over the custom-made MEA, and electrically stimulated with voltage-controlled pulses. The evoked spiking activity in RGCs ($n = 13$, $N = 11$) was recorded with an extracellular metal electrode (**Figure 5d**). SL, ML, and LL responses were present with both rectangular (**Figure 5e**) and non-rectangular capacitive-like (**Figure 5f**) voltage pulses, but the latter appears to induce stronger ML and LL indirect activities. Consistently with the previous set of experiments, the ML and LL indirect responses showed a behaviour dependent on both amplitude and duration (**Figure 6a**). Besides, the SL and ML activities evoked by non-rectangular capacitive-like voltage pulses (179 mV) are not significantly different (SL 10 ms: $p = 0.060$; ML 10 ms: $p = 0.296$; SL 50 ms: $p = 0.054$; ML 50 ms: $p = 0.174$; SL 100 ms: $p = 0.08$; ML 100 ms: $p = 0.066$; two-tailed t-test) to the activities evoked by the corresponding photovoltaic pulse (560 nm, 1.08 mW mm⁻²), as shown in **Figure 6b**. Only LL activities showed a significant difference for 10-ms and 50-ms pulses (LL 10 ms: $p < 0.01$; LL 50 ms: $p < 0.05$; two-tailed t-test) but this difference is abolished for 100-ms pulses (LL 100 ms: $p = 0.132$; two-tailed t-test). Considering RGCs showing significant LL activity only ($n = 5$ out of 16 for photovoltaic pulses and $n = 4$ out of 13 for electrical pulses), LL responses were not significantly different between electrical and photovoltaic stimulations for any of the tested durations (LL 10 ms: $p = 0.163$; LL 50ms: $p = 0.439m$; LL 100ms: $p = 0.402$; two-tailed t-test). In agreement with the previous dataset, the percentage of RGCs showing LL activity was 30.77 %.

In order to quantify the efficacy of the non-rectangular capacitive-like voltage pulses to evoke direct (SL) and indirect (ML and LL) activities with respect to rectangular voltage pulses, we integrated both response curves over the range of pulse amplitudes (from 8.5 to 1790 mV, see the red area in **Figure 6b**) and computed the percental increase of the activity evoked by non-rectangular capacitive-like voltage pulses in comparison to the rectangular ones (**Figure 6c**). SL activity is significantly increased with the use of capacitive-like pulses with respect to the use of rectangular ones, for 10-ms pulses only ($p < 0.05$, two-tailed paired t-test). ML activities are significantly increased with capacitive-like pulses for all the three pulse durations ($p < 0.0001$, two-tailed paired t-test). ML activity is therefore consistently strengthened by non-rectangular capacitive-like voltage pulses. LL activity is significantly increased for 50-ms pulses only ($p < 0.001$, two-tailed paired t-test), regardless whether we considered the whole dataset of RGCs or only the subset exhibiting significant LL activity. This might be due to the decrease in LL activity with non-rectangular capacitive-like voltage pulses at high voltage amplitudes (> 200 - 300 mV), as visible in **Figure 6b**.

Whereas growing evidence shows that non-rectangular pulse shapes preferentially trigger indirect activity^{386,387}, it is yet not evident from scientific literature whether non-rectangular pulse shapes should be more or less prone to elicit SL direct activity, and results supporting both hypotheses were provided^{384,387,416,417}. In our dataset, non-rectangular capacitive-like voltage pulses elicited a stronger SL activity than rectangular ones. However, SL spikes elicited by rectangular pulses could be underestimated. Upon non-rectangular capacitive-like voltage pulses, SL spikes appears with a longer delay from the pulse onset^{369,386} making their detection more accurate, since they appear after the recording period affected by the stimulation artefact. For rectangular pulses, the SL direct spikes occur with shorter delays³³⁷ and therefore they may be masked by the stimulation artefact and may remain undetected.



Ch.3 Figure 6 - Characterisation of the RGC response to rectangular and non-rectangular capacitive-like voltage pulses

a, Heatmaps of SL (left), ML (middle), and LL (right) mean firing rates upon 10-, 50-, and 100-ms rectangular and non-rectangular capacitive-like voltage pulses. The voltage amplitudes are indicated on the left of each row. **b**, Mean (\pm s.e.m.; $n = 13$, $N = 11$) firing rate of SL (top), ML (middle), and LL (bottom) spikes upon electrical stimulation with 10- (left), 50- (middle), and 100-ms (right) rectangular and non-rectangular capacitive-like voltage pulses. The green circles correspond to the mean (\pm s.e.m.; $n = 16$, $N = 9$) SL, ML, and LL firing rates obtained upon photovoltaic stimulation at 1.08 mW mm⁻². For each RGC, ten consecutive sweeps were averaged. The asterisk within a symbol highlights the beginning of supra-threshold activity. **c**, Percentual increase in the RGC activity induced by non-rectangular capacitive-like voltage pulses compared to paired rectangular voltage pulses. The activity difference calculation is illustrated in panel (b) by the red area. **d**, Grand average (\pm s.e.m.; $n = 13$, $N = 11$) of the mean firing rates of SL (top), ML (middle), and LL (bottom) responses over the tested pulse durations (left) and over the tested pulse amplitudes (right). **e**, Pulse amplitudes required to induce SL, ML, and LL supra-threshold activities upon 10-, 50-, and 100-ms rectangular and non-rectangular capacitive-like voltage pulses. The y-axis represents the first voltage condition eliciting a supra-threshold activity.

A three-way ANOVA (shape, amplitude, and duration) revealed that the pulse shape (rectangular versus non-rectangular capacitive-like) was the main critical parameter responsible for the difference in direct and indirect RGC responses. It had the greatest significant effect on ML response ($F = 28.36$, $p < 0.0001$). The main effects of pulse amplitude and pulse duration on ML response were also both significant (amplitude: $F = 11.95$ and $p < 0.0001$; duration: $F = 5.42$ and $p < 0.01$). The pulse amplitude has also a significant effect on LL responses for the whole dataset of RGCs ($F = 7.16$, $p < 0.0001$) and on the subset of RGCs exhibiting significant LL activity ($F = 11.15$, $p < 0.0001$). No interaction between pulse duration, amplitude, and shape was significant. When increasing the pulse amplitude from 8.9 to 1790 mV, the ML indirect activity could reach $199 \pm 94\%$ (mean \pm s.e.m) of its initial values (average of all the pulse durations tested; **Figure 6d**, middle left) and $139 \pm 16\%$ (mean \pm s.e.m) of its initial values when lengthening the pulse duration from 10 to 100 ms (average of all the pulse amplitudes tested; **Figure 6d**, middle right). The LL indirect activity reaches $157 \pm 108\%$ (mean \pm s.e.m) of its initial values when increasing the pulse amplitude (**Figure 6d**, bottom left) and $108 \pm 65\%$ (mean \pm s.e.m) of its initial values

when lengthening the pulse duration (**Figure 6d**, bottom right) as computed above. Taking into account the RGC exhibiting LL activity only ($n = 4$ out of 13), the LL indirect activity reaches 269 ± 107 % (mean \pm s.e.m) of its initial values when increasing the exposure and 125 ± 76 % (mean \pm s.e.m) of its initial values when lengthening the pulse duration.

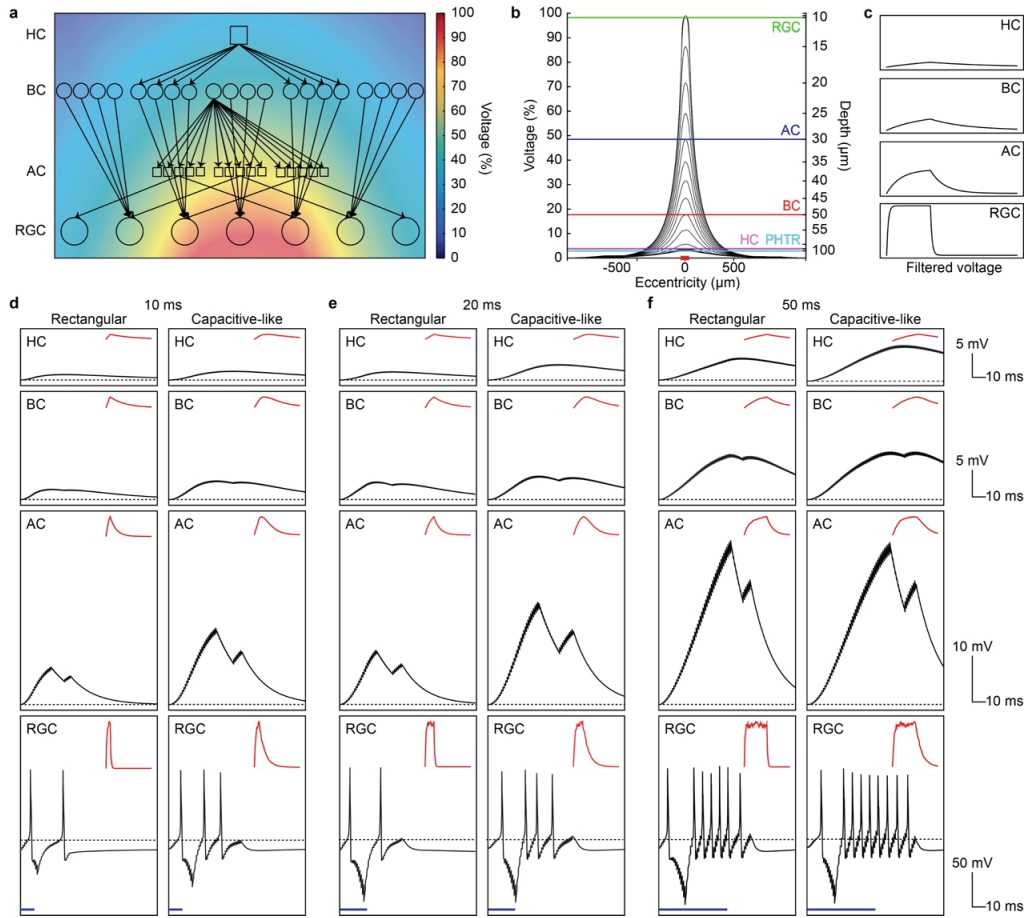
The efficacy of non-rectangular capacitive-like voltage pulses to strengthen indirect activity was also reflected in the amplitude required to induce supra-threshold activity (**Figure 6e**). SL, ML, and LL supra-threshold responses required lower voltage amplitudes when evoked by non-rectangular capacitive-like pulses in contrast to rectangular pulses. Nonetheless, as previously suggested, the decrease in the voltage required to elicit SL supra-threshold responses might be attributed to the underestimation of SL spikes elicited by rectangular pulses.

These results demonstrate that non-rectangular capacitive-like voltage pulses can elicit stronger ML indirect activation of RGCs than rectangular ones. The statistical independence of the pulse shape and duration, together with the evidence that both shapes deliver the same effective charge, reinforce the hypothesis that the voltage delivery rate is a key parameter to control indirect activation of RGCs. This is also consistent with the integrative nature of interneurons.

3.4.4 Computational model

To provide a biophysical interpretation of the effect of the stimulus features (*i.e.* amplitude, duration, and shape) on the indirect activity, we simulated the response of a three dimensional stratified and interconnected *in-silico* retina upon epiretinal stimulation (**Figure 7a**). The voltage pulse was modelled with a FEA simulation as a local Gaussian-shaped voltage increase, whose amplitude decreases with depth within the retinal-like tissue (**Figure 7b**). The rising and falling phases of the capacitive-like voltage pulse were fitted with a one-term exponential function. Given the high electrical resistivity of the neural retina, when stimulating in epiretinal configuration less than 5 % of the electric field reaches a distance of 100 μm from the electrode (where the PR layer is located), while only less than 20 % reaches a distance of 50 μm from the electrode (where the BC layer is located). A previous report also showed that in *Rd10* mice, at this stage of degeneration ($> P120$), only apoptotic PRs remain, and the dendrites of BCs retract as early as P25. On the other hand, BCs remain relatively preserved: only 23 % are lost at a very late stage of degeneration ($> P180$)¹⁰¹. Taking into account the minor voltage changes in the PR layer, together with the advanced degree of degeneration of the retinas in our experimental dataset, only four layers of retinal cells were modelled: RGCs, ACs, BCs, and HCs, as sketched in **Figure 7a**. Considering both the resistance and the capacitance properties of the neural retina, each layer was modelled as a low-pass filter, whose impulse response varies according to its distance from the stimulating electrode. The electric field generated by the electrode is hence low-pass filtered by each retinal layer, as shown in **Figure 7c**.

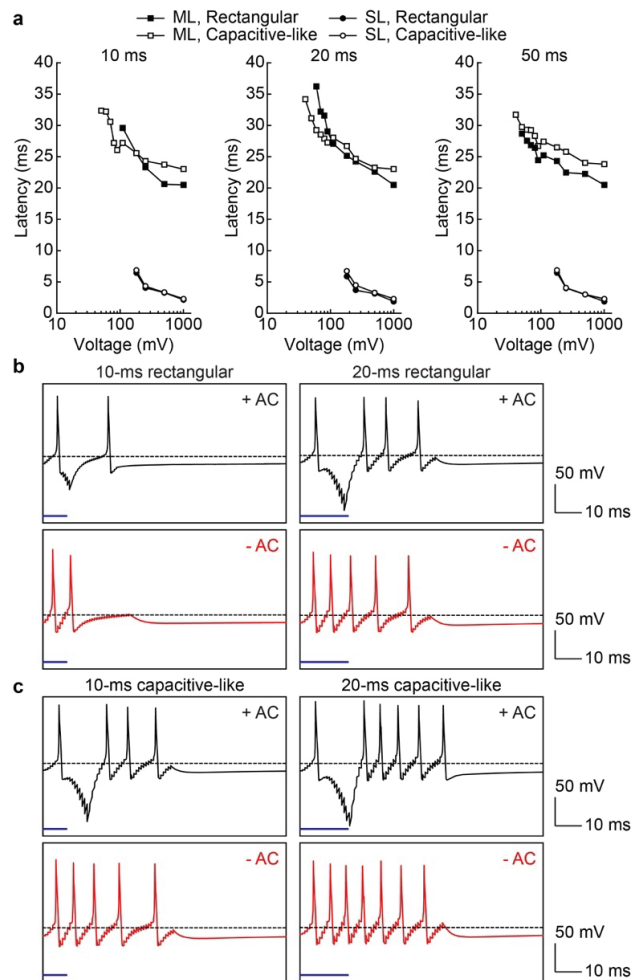
Upon voltage injection, *in-silico* stimulations of the retina lead to a typical RGC spiking pattern including SL and ML activities (**Figure 7d-f**). First, we observed an action potential within a few milliseconds after the stimulus onset (SL). Then, the stimulus propagates to the neighbouring retinal columns, including the close inhibitory surround. As a result, the excitability of the directly stimulated RGCs is decreased by their surrounding ACs. Meanwhile, granted that the input voltage is sufficient, upstream BCs are also depolarised and, in turn, they activate downstream RGCs. Voltage reduction and low-pass filtering together induce a slow trade-off phase between excitatory and inhibitory backward inputs to the RGCs. Specifically, non-rectangular capacitive-like voltage pulses induce higher depolarisation of ACs, BCs, and HCs compared to rectangular ones of paired pulse duration and amplitude. This behaviour leads to a stronger ML response in downstream RGCs (**Figure 7d-f**). Importantly, this *in-silico* model of retinal-like tissue embedding transient α -RGCs does not reproduce LL responses. The generation of indirect response patterns with latencies higher than 100 ms might indeed be related to the functional characteristics of RGCs: sustained cells could respond up to 150 ms after single electrical stimulation while ON and brisk-transient RGCs exhibited shorter indirect responses³⁸². In the absence of any functional ON-OFF nor sustained local circuits, the biophysical retinal-like model is hence unable to reproduce LL responses. However, the implementation of sustained α -RGCs exhibiting tonic responses to isolated stimulation allows the reproduction of both ML and LL responses (**Figure 15**).



Ch.3 Figure 7 - Biophysical model of the retinal layers under epiretinal stimulation

a, Simplified topology of the model. Circles represent the excitatory cells (BCs, RGCs), while squares represent the inhibitory cells (HCs, ACs). The background image shows a FEA simulation of the potential generated by an electrode placed in the centre of the sketched network. **b**, FEA simulation of the potential generated by the electrode (red bar) when it is facing the retinal tissue. Each potential line is separated from the previous one by a 5- μ m step. The green line shows the potential at 10- μ m depth from the electrode surface, the blue line at 30- μ m depth, the red line at 49- μ m depth, the magenta line at 64- μ m depth, and the cyan line at 100- μ m depth, respectively corresponding to the location of RGC, AC, BC, HC, PR cell bodies. **c**, Filtered 50-ms 180-mV rectangular voltage pulse effective at the level of the HC, BC, AC, and RGC layers. **d**, **e**, **f**, Characterisation of the biophysical retinal circuit response upon stimulation with rectangular and non-rectangular capacitive-like voltage pulses. The membrane potentials of an HC, BC, AC, and RGC located at the centre of the epiretinal electrode are shown upon a 180-mV rectangular (left) and non-rectangular capacitive-like (right) stimulations lasting for 10 (**d**), 20 (**e**), and 50 ms (**f**). In all panels, the red traces show the filtered voltage pulse effective at each layer. The horizontal blue bars represent the duration of the voltage pulse.

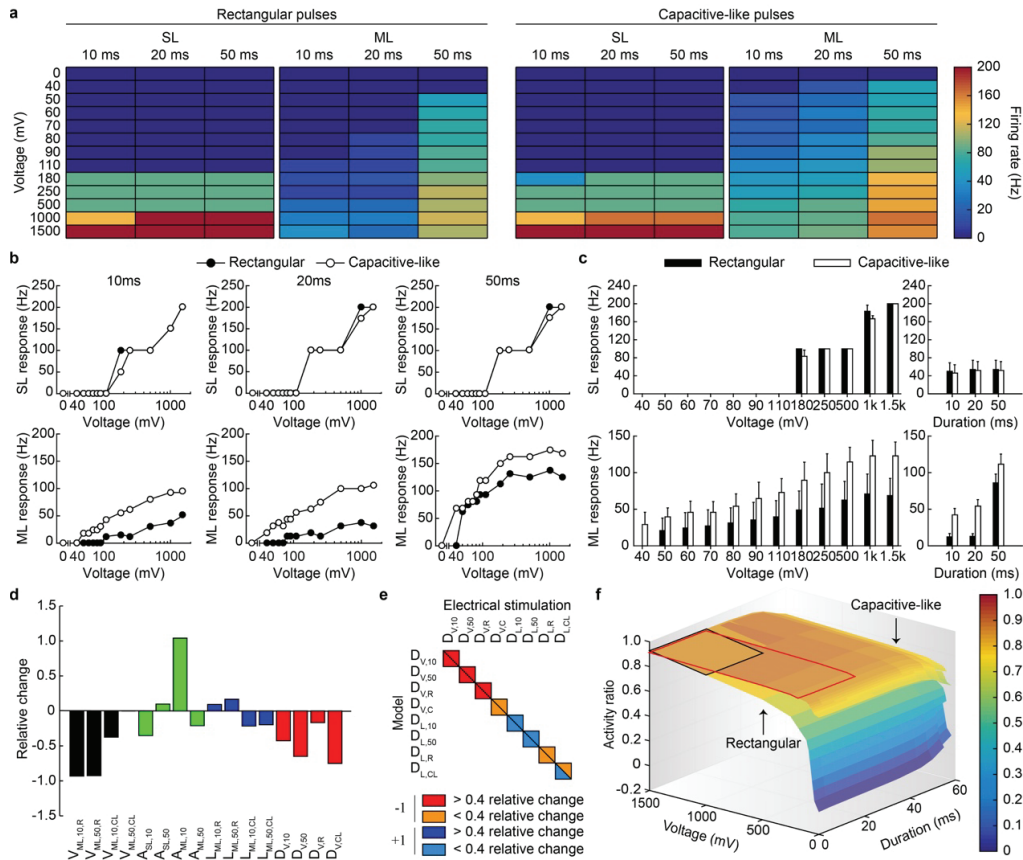
The ML indirect activation of RGCs occurs within 20 to 35 ms after the stimulus onset, with a latency decreasing with the pulse amplitude (**Figure 8a**). The latency of ML spikes is related to the increase of the membrane potential in inner retinal cells. Under sufficient voltage delivery, the BC input to the RGC induces a spike burst; however, the increase in the membrane potential in ACs induces an inhibition of RGCs, which delays the onset of the indirect response (**Figure 8b,c**). Shutting off ACs in the biophysical model cancels out the time interval between SL and ML spikes, thus leading to a continuous firing of RGCs (**Figure 8b,c**). These results show that BCs and ACs are both necessary to produce a secondary activity pattern with a latency in the order of few tens of milliseconds as observed *ex-vivo*.



Ch.3 Figure 8 - Spike latency and contribution of amacrine cells

a, Latency of SL and ML activity induced by 10-, 20-, and 50-ms rectangular and non-rectangular capacitive-like voltage pulses.
b, c, Membrane potential of the RGC located at the centre of the electrode, upon 10- and 20-ms rectangular (**b**) and non-rectangular capacitive-like (**c**) stimulation at 250 mV, with (black) and without (red) presynaptic inhibition from the ACs.

RGCs stimulated *in-silico* also exhibited a voltage-dependent SL direct activity and a voltage- and duration-dependent ML indirect activity (**Figure 9a-c**). In agreement with our *ex-vivo* results, non-rectangular capacitive-like voltage pulses elicited stronger ML indirect activity compared to the rectangular ones of paired pulse amplitude and duration (**Figure 9b,c**). The firing rate (**Figure 9b,c**) and latency (**Figure 8a**) of SL responses were not different between rectangular and non-rectangular capacitive-like stimulations. Nonetheless, the network modelling does not take into account the compartmental complexity and the dynamics of ion channels at the RGC level, according to which the pulse shape might alter SL activity³⁸².



Ch.3 Figure 9 - Characterisation of the *in-silico* RGC response

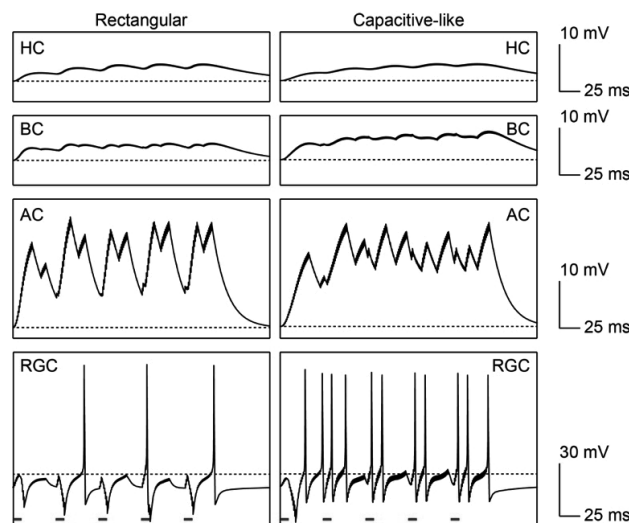
a, Heatmaps of SL (left) and ML (middle) mean firing rates upon 10-, 20-, and 50-ms rectangular and non-rectangular capacitive-like voltage pulses. The voltage amplitudes are indicated on the left of each row. **b**, SL (top) and ML (bottom) spiking activity generated in the RGC located at the centre of the electrode by 10-, 20-, and 50-ms stimuli for both rectangular and non-rectangular capacitive-like voltage pulses. **c**, Grand average (\pm s.e.m) of the mean firing rates of SL (top) and ML (bottom) responses over the tested durations (left) and pulse amplitudes (right). **d**, Relative changes observed between the model outputs and the *ex-vivo* measurements ($n = 13$, $N = 11$). **e**, Normalised strategy-dependant changes observed *ex-vivo* and from the model outputs when lengthening the pulse duration or changing the stimulating shape from rectangular to non-rectangular capacitive-like. **f**, The ML over SL activity ratio as a function of the pulse amplitude and duration. The activity ratio has been computed as the difference in firing rates between ML and SL activities divided by their sum. The red and black squares respectively highlight the optimal parameters found for rectangular and non-rectangular capacitive-like voltage pulses to elicit indirect activity (duration < 20 ms; activity ratio > 0.8).

To further validate the model predictions and discriminate the changes due to this point-like reduction of the neurons, we compared the relative changes observed between the model outputs and the *ex-vivo* measurements ($n = 13$, $N = 11$). For such need, we evaluated: (i) the voltage required for supra-threshold ML responses upon 10- and 50-ms, rectangular and non-rectangular capacitive-like stimulations ($V_{ML,10,R}$, $V_{ML,50,R}$, $V_{ML,10,CL}$ and $V_{ML,50,CL}$), (ii) the SL ($A_{SL,10}$, $A_{SL,50}$) and ML ($A_{ML,10}$, $A_{ML,50}$) activity increase between 10- and 50-ms, rectangular and non-rectangular capacitive-like pulses, (iii) the mean latencies of the first indirect spike upon 10- and 50-ms, rectangular and non-rectangular capacitive-like stimulations ($L_{ML,10,R}$, $L_{ML,50,R}$, $L_{ML,10,CL}$, $L_{ML,50,CL}$), (iv) the ML voltage threshold difference induced by increasing the pulse duration from 10- to 50-ms ($D_{V,10}$, $D_{V,50}$), and by substituting the stimulating waveform from rectangular to non-rectangular capacitive-like ($D_{V,R}$, $D_{V,CL}$) (Figure 9d). For each parameter, the relative change was computed as $\frac{\hat{\beta} - \beta}{\beta}$, where β is the mean *ex-vivo* observation and $\hat{\beta}$ the model output. The effects of stimulation strategies enhancing network-mediated activity (*i.e.* pulse lengthening and non-rectangular capacitive-like waveform use) on ML voltage thresholds and latencies were represented for both *in-silico* and *ex-vivo* datasets in Figure 9e. The model generally underestimates these parameters. The voltages required to induce supra-threshold ML activity are underestimated for rectangular pulses and 10-ms non-rectangular capacitive-like pulses. As a consequence, the activity increase between rectangular and non-rectangular capacitive-like 10-ms voltage pulses ($A_{ML,10}$) shows the largest relative change. The latencies of the ML activity are accurately fitted by the model, exhibiting relative changes lower than 0.2. However, because this computational framework is a biophysical reduction of the retinal tissue properties,

it does not take into account the distribution of ion channels along the cell somas, axons, and axon hillock, nor it mimics functional retinal pathways properties, such as centre-surround organisation and the ON-OFF transient-sustained behaviours. Because of this reduction in complexity, the model accuracy decreases for conditions involving one (SL) or few cells (low rates ML response). In fact, without those features, the behaviour of SL spikes cannot be sharply reproduced⁴¹⁸. However, the relative changes for stimulation paradigms involving a larger portion of the tissue (long or non-rectangular pulses leading to higher ML responses) are substantially smaller: the activity increase between rectangular and non-rectangular capacitive-like 50-ms voltage pulses ($A_{ML,50}$) notably being lower than 0.2. This discrepancy suggests an excessively linear modelling over the tested conditions. The effect of lengthening the pulses and the substitution of rectangular pulse by non-rectangular capacitive-like one are adequately fitted by the model (**Figure 9e**). Despite the retinal complexity reduction, the connection pattern between stratified inhibitory and excitatory layers is sufficient to reproduce the main features and strategy-dependant changes observed in *ex-vivo* electrophysiological recordings. Both *ex-vivo* and *in-silico* approaches show the following strategy-dependant features: lengthening of the stimulation pulse reduces the ML voltage required to induce supra-threshold activity, increases the ML activity, and decreases the ML response latency. Likewise, the use of non-rectangular capacitive-like pulses reduces the ML voltage required to induce supra-threshold activity, increases the ML activity, but increases the ML response latency. This last point is not reproduced by the model, presumably because the relative changes of ML response latencies between the *ex-vivo* data and the model outputs are both very small (lower than 0.2).

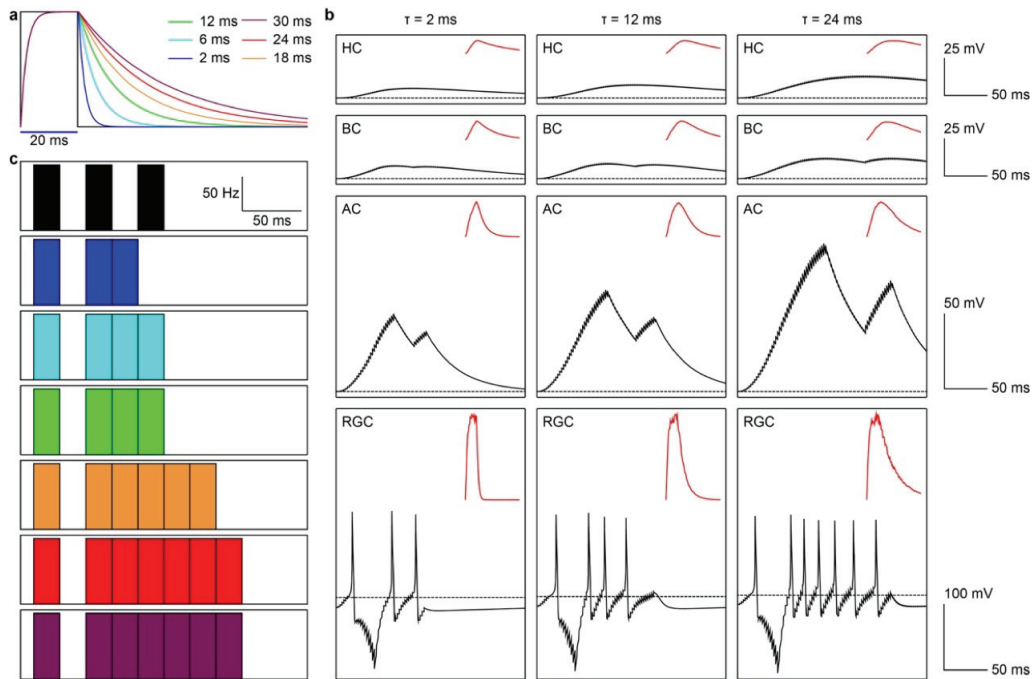
Figure 9f shows a linear assumption of the indirect-to-direct activity ratio for various pulse amplitudes and durations, either rectangular or non-rectangular capacitive-like shaped. While rectangular stimuli require high voltages (higher than 1 V) or very long durations (longer than 60 ms) to maximise the indirect-to-direct activity ratio, non-rectangular capacitive-like pulses maximise the indirect-to-direct activity ratio at amplitudes one order of magnitude lower or with shorter pulses. The range of pulse amplitudes maximising the indirect-to-direct activity ratio (> 0.8) for rectangular and capacitive-like pulses (< 20 ms in order to ensure a stimulation frequency of about 20 Hz) are highlighted respectively by the black and red contours.

Furthermore, since capacitive-like pulses induce longer depolarisation in inner retinal cells, they might facilitate the temporal summation of repetitive stimuli (**Figure 10**). This feature has to be considered in the context of clinical use since the conventional stimulation frequencies used in retinal prostheses range from 5 to 20 Hz^{158,186,232,237,318}. Recent evidence suggests 4 to 10 Hz as an optimal stimulation frequency range for epiretinal prostheses, in order to maximise the RGC excitation, in particular ON RGCs^{387,419}. However, the possibility to reproduce flicker fusion with prosthetic vision at high frequencies is a remarkable advantage towards a more physiological-like artificial vision¹⁹⁴. A trade-off between the stimulation frequency and stimulus duration becomes especially important when dealing with photovoltaic electrodes. A compromise has to be found between maintaining the light pulse short enough to ensure high stimulation frequencies and avoid photothermal damage to the retina, but still enabling indirect activity and eventually temporal summation. The control of the falling phase of the voltage stimulus (independent from the duration of the light pulse) can be a solution to increase the ML activity elicited by a pulse of given duration and amplitude (**Figure 11**). For identical supra-threshold single 20-ms pulses, increasing the decay phase time constant from 6 ms (time constant obtained from an exponential fit of the voltage measured in³⁶⁹) to 18 ms enables to increase the ML activity by 166%. No comparable modulation could be found when varying the rising phase time constant.



Ch.3 Figure 10 - Modelling of the retinal network activity upon repetitive sub-threshold stimulation

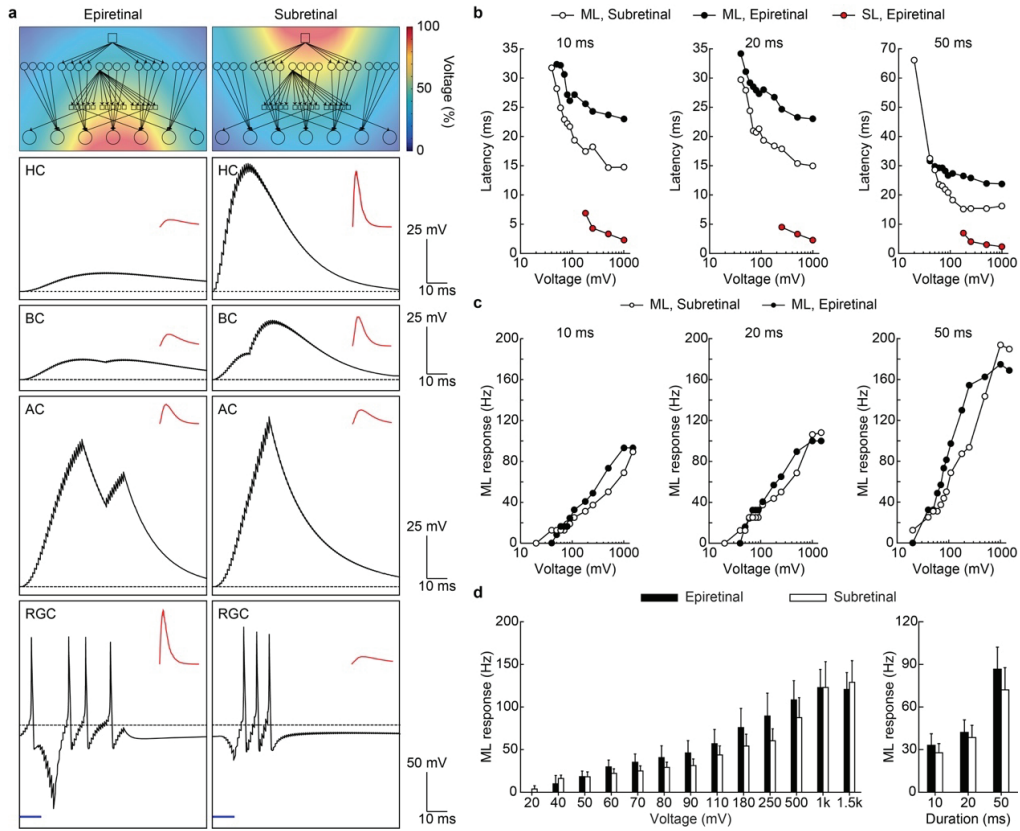
Membrane potentials of an HC, BC, AC, and RGC located at the centre of the electrode, upon repetitive rectangular (left) and non-rectangular capacitive-like (right) sub-threshold stimulations (five 10-ms and 20-mV voltage pulses at 20 Hz).



Ch.3 Figure 11 - Comparison of ML indirect activity elicited by capacitive-like pulses with increasing falling time constants

a, Normalised photovoltage curves with various discharge time constants. The photovoltage measured on top of photovoltaic pixels³⁶⁹ is fitted by the green curve. **b**, Membrane potentials of an HC, BP, AC, and RGC located at the centre of the electrode, upon 20-ms non-rectangular capacitive-like stimulation at 250 mV, with falling time constants of 2, 12, and 24 ms. The red traces show the filtered voltage pulse effective at each layer. **c**, PSTHs of the RGC located at the centre of the electrode, upon 20-ms capacitive-like stimulations at 250 mV with increasing falling time constants. In all panels the horizontal blue bars show the pulse duration.

Last, the biophysical model indicates that shuffling the stimulating electrode from the epiretinal to the subretinal side allowed to shorten the onset of the ML indirect activity upon non-rectangular capacitive-like voltage pulses (**Figure 12a,b**), in agreement to what was previously shown *ex-vivo*³³⁷. The subretinal stimulation induced a balanced contribution of excitation (from BCs) and inhibition (from ACs), as shown in the right column of **Figure 12a**, while epiretinal stimulation induces a stronger contribution from ACs compared to that from BCs (**Figure 12a**, left), due to the vicinity of the electrode to the AC layer. In this manner, epiretinal stimulation can be characterised as inhibition-driven, while subretinal stimulation is excitation and inhibition-driven. This difference in presynaptic regime leads to shorter latencies for ML activity upon subretinal stimulation compared to epiretinal stimulation (**Figure 12b**). However, no difference was found between the ML firing rates induced by subretinal or epiretinal stimulation (**Figure 12c,d**); although the voltage required to induce supra-threshold ML indirect activity in subretinal stimulation was consistently 20 to 30 mV lower than that required upon epiretinal stimulation, due to the higher contribution of BCs respect to ACs inhibition (**Figure 12a,c**). In conclusion, these data suggest that epiretinal stimulation can induce ML indirect activation of RGCs comparable to subretinal stimulation.

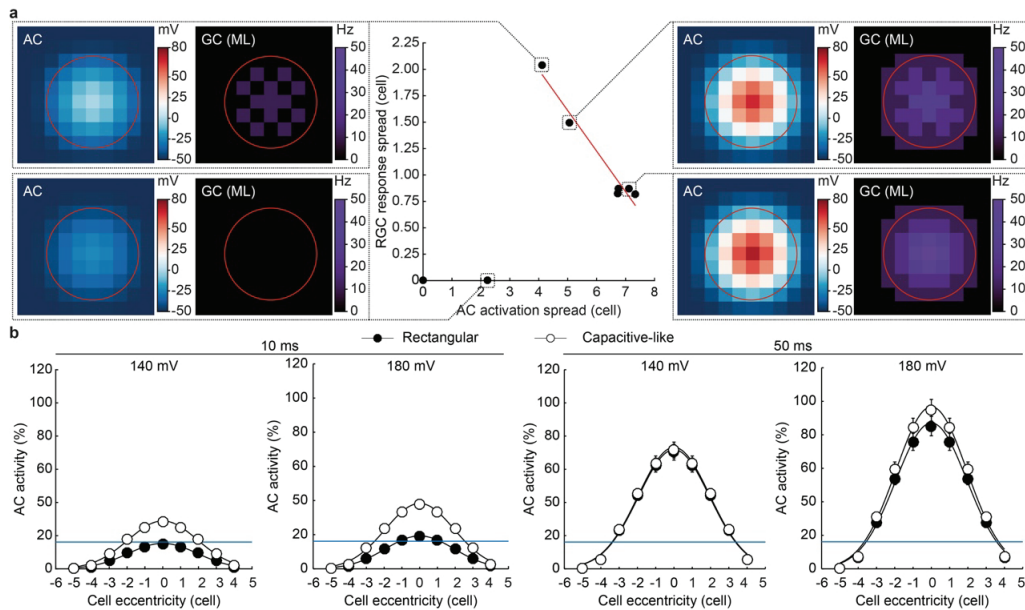


Ch.3 Figure 12 - Comparison of epiretinal and subretinal stimulations *in-silico*

a, The top panels show the probability distribution of the electrical potential in the retinal tissue under epiretinal (left) or subretinal (right) stimulation. The other panels show the membrane potentials of an HC, BC, AC, and RGC located at the centre of the electrode, upon 10-ms non-rectangular capacitive-like stimulation at 250 mV from an epiretinal (left) or a subretinal (right) electrode. The red traces show the filtered voltage pulse effective at each layer. For subretinal stimulation, the electrode was placed 10 μm away from the horizontal cell layer. **b**, First SL direct and ML indirect spikes latencies measured from the RGC located at the centre of the electrode upon 10-ms, 20-ms, and 50-ms non-rectangular capacitive-like voltage pulses of amplitudes ranging from 20 to 1000 mV delivered from the epiretinal or subretinal side. **c**, ML indirect spiking activity generated in the RGC located at the centre of the electrode upon 10-, 20-, and 50-ms non-rectangular capacitive-like voltage pulses of amplitudes ranging from 20 to 1000 mV delivered from the epiretinal or subretinal side. **d**, Grand average (\pm s.e.m) of the mean firing rates of ML response over the tested durations (left) and voltage amplitudes (right).

3.4.5 Spatial selectivity of rectangular and capacitive-like voltage pulses

Next, we evaluated the spatial extent of RGCs responses to epiretinal voltage-controlled stimulation using a computational and experimental hybrid approach. From two-dimensional activation plots of the simulated RGCs, ACs, BCs, and HCs, we estimated the spatial extent of the response in the AC and RGC layers upon 10- and 50-ms rectangular and non-rectangular capacitive-like voltage pulses (**Figure 13**).



Ch.3 Figure 13 - Modelling of the spatial extent of the retinal circuit response

a, Spatial extent of the ML indirect response of RGCs compared to the extent of ACs activity. A 10 x 10 grid of RGCs and upstream network were simulated upon 10- and 50-ms rectangular or non-rectangular capacitive-like voltage pulses at 140 mV and 180 mV. RGCs indirect activity (right) and ACs activation (left) colormaps are shown for four representative conditions: 10-ms and 140-mV rectangular pulse (bottom left); 10-ms and 140-mV non-rectangular capacitive-like pulse (top left); 50-ms and 140-mV rectangular pulse (top right); 50-ms and 140-mV non-rectangular capacitive-like pulse (bottom right). On the ACs activity colormaps, each pixel represents the cell membrane potential difference compared to the membrane potential threshold required for the appearance of the ML activity. Positive differences are represented in white to red colours, while negative (sub-threshold) differences are represented in blue. The red circle indicates the electrode location. The spatial extent of the RGCs response has been calculated as the full width at half maximum of its activation profile fit, while the spatial extent of the ACs activation has been calculated as the full width at the threshold for ML indirect activity. **b**, Mean normalised activation profile and Gaussian fit of the activity of ACs upon 10-ms and 50-ms rectangular or non-rectangular capacitive-like voltage pulses with amplitudes of 140 mV and 180 mV. 10 x 10 cells have been averaged over four directions. The blue line indicates the AC membrane potential threshold for ML indirect activity.

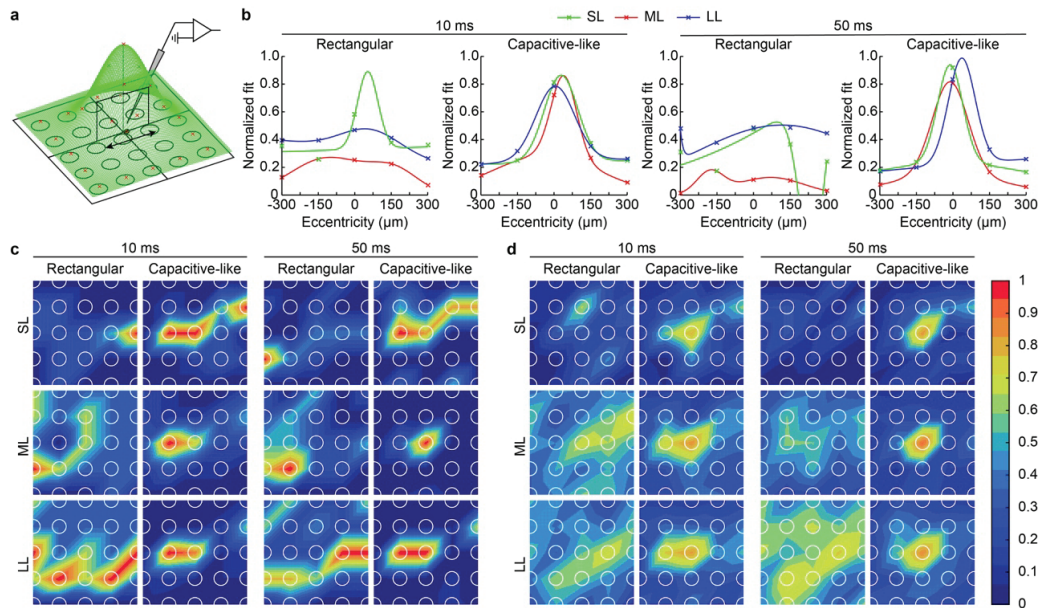
In order to assess the spatial extent of the responses to *in-silico* stimulation, the RGC and AC population activities were fitted with a Gaussian function. To quantify the activation of non-spiking ACs, we determined a threshold of relevant membrane potential rise. The AC activation was evaluated compared to the minimum AC membrane potential allowing indirect activity (-21.53 mV). This value represents the voltage threshold leading to the first indirect spike with the less efficient condition to generate indirect activity (10-ms rectangular pulses). Below this value, ACs are slightly depolarised by the epiretinal stimulus, but not enough to contribute to the formation of the indirect activity pattern. In the representative maps of **Figure 13a**, we presented the AC membrane potential rise with respect to this threshold, in order to graphically display only the relevantly active ACs. Above the indirect activation threshold, the spreading of the AC activation and the RGC indirect response (estimated from a Gaussian fit of the membrane potentials of the 10 x 10 cell population) can be linearly anticorrelated (**Figure 13a**): the spatial activation of RGC layer inversely varied with that of the AC layer. With 10-ms, 140-mV rectangular pulse (**Figure 13a**, bottom left), any RGC is indirectly activated, and any AC is significantly activated. With 10-ms, 140-mV non-rectangular capacitive-like pulse (**Figure 13a**, top left), the ACs nearest to the electrode centre are moderately activated, and several of the RGCs located over the electrode present spikes with a uniform 10 Hz firing rate. When lengthening the applied pulse (**Figure 13a**, top and bottom right, respectively 50-ms, 140-mV rectangular and non-rectangular capacitive-like pulses), the AC layer is activated strongly and widely, and the RGC response is consequently not uniform anymore. For 50-ms, 140-mV non-rectangular capacitive-like voltage pulses (**Figure 13a**, bottom right) and more generally long pulses of higher voltages, the RGC response spread is minimised. In this representative example, the RGC located at the centre of the

electrode shows a five times higher ML response than the eccentric RGCs. This minimisation of the RGC ML response spread can be attributed to the wider activation of the AC layer. Besides, long or non-rectangular capacitive-like voltage pulses enable the activation of a wider pool of ACs (**Figure 13b**). For paired voltage amplitudes and pulse durations, non-rectangular capacitive-like pulses elicit more sustained membrane depolarisation in ACs than rectangular pulses (**Figure 7**). Also, non-rectangular capacitive-like pulses induce a wider spatial activation of ACs within the gaussian-shaped voltage probability distribution defined around the electrode (**Figure 13b**). This strengthening and widening of the AC response are dependent on the voltage, the duration, and the shape of the pulse, and are favoured by long and non-rectangular capacitive-like pulses. On the other hand, the difference between the AC activation profiles obtained with rectangular and non-rectangular capacitive-like voltage pulses is reduced when the pulse duration is increased to more than 20 ms (**Figure 13b**, right panel), presumably due to the saturation of network response kinetics. At the RGC level, the spatial extent of the activation is also dependent on the voltage, the duration, and the shape of the voltage pulse, but with an inverse relationship. The widest activation of the recorded ACs pool is observed upon 50-ms, 180-mV non-rectangular capacitive-like voltage pulses, in which a 7.5 cells-diameter area is activated around the electrode. This leads up to the most focused RGC response amongst the tested conditions, in which the central RGC indirect (ML) firing rate is 1.8 times higher than its immediate neighbours and 5.7 times higher than the peripheral responding RGCs.

Complementary to the biophysical simulations, we estimated the electrical receptive fields (eRFs) of RGCs *ex-vivo* upon rectangular and capacitive-like voltage pulses (**Figure 14**). *Rd10* retinas were explanted on the custom-made MEA and RGCs were located by recording their spontaneous activity. Each RGC was successively stimulated by using the 25 nearest electrodes with 10- and 50-ms rectangular and non-rectangular capacitive-like voltage pulses (179 mV). The eRFs from individual RGCs upon electrical stimulation were centred on the electrode eliciting the maximal ML activity under 50-ms stimulation and normalised according to the ML firing rate obtained (**Figure 14a**). Direct and indirect firing rates obtained with individual electrodes were spatially averaged over three directions and fitted with a Gaussian function (**Figure 14a,b**). The eRF diameters were calculated from the activity fit as the full width at the median response amplitude, for both direct and indirect activities and labelled as SL-eRF, ML-eRF, or LL-eRF (**Figure 14a**).

The eRFs for 10- and 50-ms capacitive-like and rectangular pulses are shown in **Figure 14c**. SL-eRFs present elongated shapes, showing that electrodes distant more than 300 μm can directly depolarise the RGCs, likely because of axonal stimulation. An action potential generated in a distal axonal segment and antidromically propagated in less than 10 ms would indeed be classified as direct (SL) RGC activation. The diameter of SL-eRFs is respectively of 101 μm for 10-ms rectangular pulses, 226 μm for 50-ms rectangular pulses, 82 μm for 10-ms capacitive-like pulses, and 66 μm for 50-ms capacitive-like pulses ($n = 8$, $N = 8$). Regarding indirect eRFs (ML-eRFs, LL-eRFs), 50-ms capacitive-like stimulation provides the most focused response. This stimulation condition was previously associated with high indirect activity (**Figures 6 and 9**) and with a wide activation of ACs (**Figure 13**). Conversely, the indirect eRFs obtained with rectangular pulses are broader, due to the averaging of idiosyncratic preferred stimulation axis (**Figure 14b-d**). With rectangular pulses, the diameter of ML-eRFs and LL-eRFs is respectively of 147 μm and 218 μm for 10-ms pulses ($n = 8$, $N = 8$). Capacitive-like pulses exhibit ML-eRFs and LL-eRFs clustered around the central electrode, with diameters of 93 and 110 μm for 10-ms pulses ($n = 8$, $N = 8$). With longer (50-ms) capacitive-like pulses, a more clustered indirect eRF is observed; the diameter of ML-eRFs and LL-eRFs is reduced respectively to 76 μm and 86 μm ($n = 8$, $N = 8$). For rectangular pulses, the increase in duration also helps, to a lesser extent, to reduce the diameter of the indirect eRFs, which becomes respectively of 111 μm and 220 μm for 50-ms pulses ML-eRFs and LL-eRFs.

Thereby, lengthening the stimulation pulse and/or substituting the rectangular waveform into a capacitive-like one allows not only to increase the RGC network-mediated activity, but also to cluster it. The reduction in indirect eRFs under stimulation conditions favouring high ML and LL activities (50-ms and/or non-rectangular capacitive-like pulse) precisely originates in the strong and sustained recruitment of the non-spiking retinal network, including the inhibitory surround of the targeted RGC.



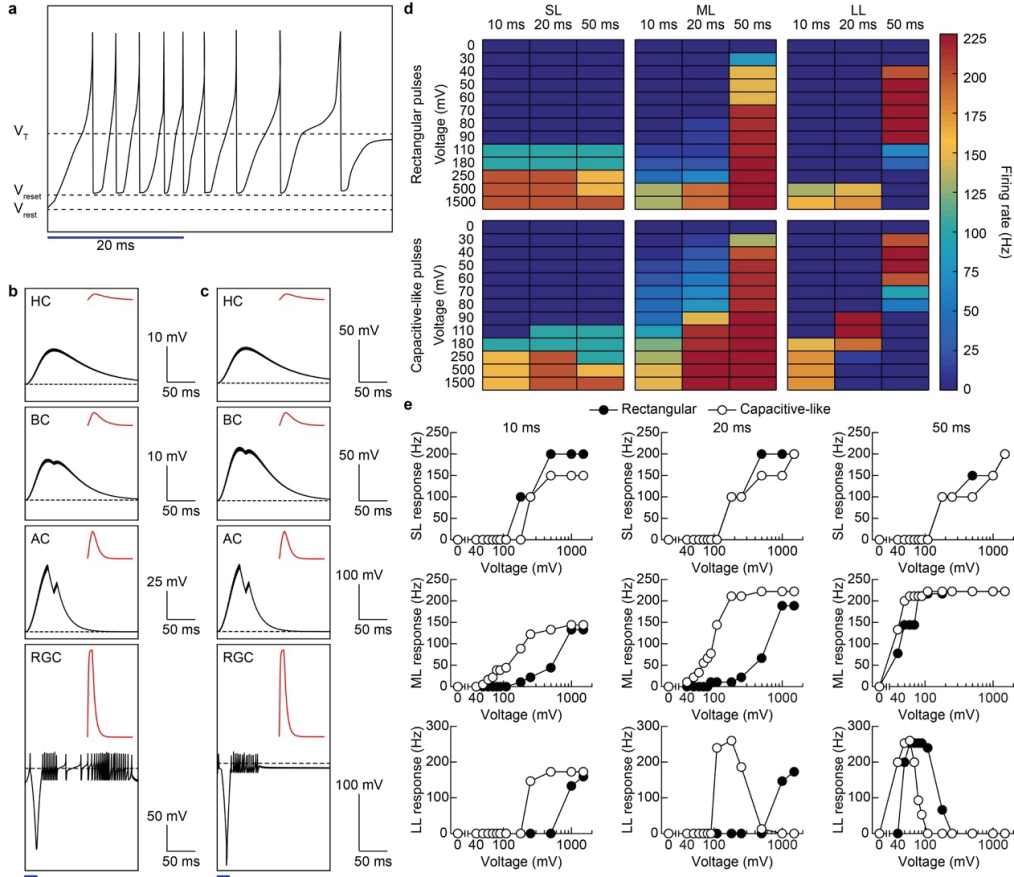
Ch.3 Figure 14 - Electrical receptive fields of RGCs upon rectangular and non-rectangular capacitive-like stimulation
a, Sketch of the stimulating and recording setup. The approximated location of the recorded cell's soma is indicated by the red circle below the pipette's tip. Voltage pulses were delivered alternatively from each of 25 nearest electrodes of the MEA. The red crosses represent experimental points obtained for successive RGC stimulation with each of the 25 electrodes and the green mesh the 2D Gaussian fit of those points from which was calculated the eRF diameter, itself represented by the black arrow. **b**, Fit of the grand average SL (green), ML (red), and LL (blue) response amplitudes. Experimental measures obtained with individual electrode stimulation have been averaged over the horizontal, the diagonal, and the vertical axes and fitted with a Gaussian function ($n = 8, N = 8$). For each RGC, ten consecutive sweeps have been averaged. **c**, Representative heatmaps of normalised SL, ML, and LL activities recorded with 10-ms and 50-ms rectangular or non-rectangular capacitive-like voltage pulses, both with a peak voltage of 179 mV ($n = 1$, ten sweeps have been averaged). **d**, Mean heatmaps of normalised SL, ML, and LL activities recorded with 10-ms and 50-ms rectangular or non-rectangular capacitive-like voltage pulses, with a peak voltage of 179 mV ($n = 8, N = 8$). For each RGC, ten consecutive sweeps have been averaged. Heatmaps in (c) and (d) have been generated from linear interpolation of experimental SL, ML, and LL values recorded from individual electrode stimulations. The scale bars in (c) and (d) display the electrode pitch (150 μm).

3.4.6 Modelling sustained α -RGCs

In order to reproduce LL indirect activity *in-silico*, sustained RGCs were modeled by modifying the intrinsic membrane properties to introduce spike-triggered post-spike facilitation and spike-frequency adaptation using an adaptive exponential integrate-and-fire neuron model^{392,420}. A post-spike reset membrane potential (V_{reset}) 2.5 mV higher than the resting potential (V_{rest}) was notably introduced to maintain post-spike RGC in a high excitability state after the spiking event (Figure 15a). Such nonlinear model is able to reproduce repetitive firing and tonic response to current and voltage stimulation (Figure 15a)^{392,420}. Upon epiretinal stimulation, sustained RGCs exhibited SL spikes, inhibition period, and ML response, similarly to transient cells described above (Figure 15b,c). SL and ML responses developed along the same trend as transient RGC ones (Figure 15d right and middle, and (e) top and middle, respectively for SL and ML activities). But conversely to the transient model, within sufficient pulse amplitudes, LL responses can be induced, following ML spikes and a second inhibitory period (Figure 15b, 20-ms capacitive-like stimulation, 180 mV). The start of LL activity indeed appears to be synchronous with the closure of ACs rise in activity. In this perspective, LL activity is a chain consequence of ML activity, which maintained the sustained cell in an excitable state for several tens of milliseconds, and of the consecutive RGC disinhibition. Indeed, as for ML response, LL response occurs only under the condition of sufficient initial input from BCs, and the LL activity depends on the pulse duration, amplitude, and shape. Accordingly, the voltage threshold for LL activity is lower for non-rectangular capacitive like voltage pulses (Figures 15d right and 15e bottom). Therefore, LL responses are as well favored by increasing the pulse duration and by using non-rectangular capacitive-like voltage pulses.

It is worth to notice that for strong stimulation (high amplitudes and long durations) LL response showed an upper voltage threshold above which the firing rate decrease with the increase of voltage amplitude. This upper voltage threshold is lowered by increasing the pulse duration and by using non-rectangular capacitive-like voltage pulses (Figure 15 bottom, visible for 20- and 50-ms non-rectangular capacitive-like voltage pulses). The presence of an LL upper threshold in RGCs exhibiting ML and LL responses is also supported by our data *ex-vivo* (Figure 6b). The model output suggests that once the upper threshold is reached, the two indirect

responses (ML and LL) are fused together, because the large input from BCs cannot be balanced anymore by the inhibitory input from ACs (Figure 15c).



Ch.3 Figure 15 - Sustained RGC modelling

a, Exponential integrate-and-fire model membrane potential behaviour under voltage stimulation exhibits spike facilitation and tonic response. The sampled neuron had no synaptic connection and was stimulated with capacitive-like 20-ms pulse at 150 mV. Its resting potential (V_{rest}) was set to -70 mV, its threshold potential (V_T) to -55 mV and its reset potential (V_{reset}) to -67.5 mV. **b**, **c**, Membrane potentials of an HC, BC, AC, and RGC located at the centre of the electrode, upon 20-ms non-rectangular capacitive-like stimulation at 180 mV (**b**) and 1 V (**c**). The red traces show the filtered voltage pulse effective at each layer. **d**, Heatmaps of SL (left), ML (middle) and LL (right) mean firing rates upon 10-, 20-, and 50-ms rectangular (top) and non-rectangular capacitive-like (bottom) voltage pulses. The voltage amplitudes are indicated on the left of each row. **e**, SL (top), ML (middle) and LL (bottom) spiking activity generated in the RGC located at the centre of the electrode by 10-, 20-, and 50-ms stimuli for both rectangular and non-rectangular capacitive-like voltage pulses.

3.5 Discussion

In this work, we used the POLYRETINA photovoltaic prosthesis, whose 80- μm pixels generate cathodic capacitive-like voltage pulses under green light stimulation, to generate network-mediated indirect activation of RGCs from dystrophic *Rd10* retinas. In our experiments, we have observed that the non-rectangular capacitive-like waveforms generated by the photovoltaic interface induce higher indirect responses than rectangular pulses of paired pulse duration and amplitude. Photovoltaic stimulations, electrical stimulations, and *in-silico* simulations consistently demonstrate that indirect activity of RGCs could be enhanced by irradiance or voltage increase, pulse lengthening, and substitution of rectangular pulses into non-rectangular capacitive-like pulses, all resulting in higher activation of inner retinal interneurons. In the present set of experiments, we intentionally evaluated a wide range of pulse amplitudes leading to charge densities up to 20 mC cm^{-2} per phase. In real applications, though, the safe charge injection limit of the electrode should be considered while designing the stimulation protocol. In this respect, the use of non-rectangular capacitive-like pulses allows to elicit maximal indirect activity at voltages one order of magnitude lower than rectangular pulses, thus reducing the total charge delivered by the electrode.

Both the sustained voltage delivery (pulses longer than 10 ms) and the gradual voltage decrease (as in capacitive-like pulses) showed the ability to maintain non-spiking BCs and ACs active for tenths of milliseconds after the stimulus onset. This sustained activation leads to the characteristic RGC activation pattern consisting of one or two direct spikes generated by the local membrane depolarisation (SL), an inhibition period, and a second burst of activity (ML). In addition to SL and ML activities, a third indirect and further delayed burst of activity (LL) is reported in this work and others^{337,382}. The identification of sustained-RGCs as generators of persistent activation bursts under electrical stimulation³⁸² suggests that the LL wave might have an origin related to the functional type of RGCs. It has also been proposed that LL activity may originate from the photoreceptors layer³³⁷. However, in retinal degeneration models, whereas the connectivity patterns between BCs and RGCs is preserved¹⁰², early PRs death and BCs' dendrites retraction¹⁰¹ makes it very unlikely to have a straight vertical excitation from the outer nuclear layer at late stages of degeneration (> P120).

We demonstrated that the photovoltaic approach, despite its apparent loss of temporal sharpness due to the capacitive-like voltage transients generated at the pixel interface, triggers a realistic indirect activity in degenerated retinas upon epiretinal stimulation. In particular, the slow voltage decay generated at the photovoltaic pixel-electrolyte interface allows both to enhance the indirect response and to lower its voltage threshold. Indeed, it has been previously shown that a slow decreasing ramp is more efficient than a slow increasing ramp to minimise the threshold charge for neuronal activation while maximising the injectable charge from the electrodes⁴¹⁶. These findings are in line with recent reports about the efficiency of non-rectangular pulses to trigger indirect activity³⁸⁶ and the sensitivity to low-frequency stimuli of inner retinal neurons. Fast responding spike-encoding RGCs might indeed show preferential sensitivity to rectangular stimuli, while the activation of voltage-encoding interneurons can be modulated by slower voltage changes³⁸⁷. This evidence corroborates the increase in INL-mediated responses observed with non-rectangular capacitive-like pulses.

However, it is still not consensual whether non-rectangular stimuli may favour or not the generation of SL direct activity. Some evidence suggests that the high-pass filtering behaviour of RGC is presumably related to their sodium- and potassium-driven dynamics³⁸⁷. On the other hand, models of single neuron stimulation suggest that rectangular stimuli are not an optimum choice to match the membrane dynamics of spiking cells^{416,417}: slower ascending ramps might allow a better match with the ionic channel kinetics⁴¹⁶. In the absence of fine compartmentalised modelling taking into account the quantitative ionic channel kinetic properties and their distribution along the RGC soma and axon hillock, no direct (SL) stimulation efficiency difference can be found between rectangular and non-rectangular stimuli⁴¹⁸. The biophysical origin of the frequency shift observed between RGC and inner retinal neurons remains then unclear. However, the reduction of the indirect activity delay that we observe when displacing the electrode in the subretinal space, as previously observed *ex-vivo*³³⁷, suggests that the input filters are not – or not only – intrinsic electrophysiological properties of the cell types, but rather consequences of the layered structure of the retina and its electrical resistivity. Reports of direct response within a timescale of several milliseconds in subretinal configuration, twice as long as delays reported in epiretinal configuration direct stimulation, also supports this hypothesis^{337,421}. Because non-rectangular capacitive-like pulses also facilitate the temporal summation of sub-threshold stimuli, thanks to their ability to sustainably depolarise retinal interneurons, it is conceptually feasible to abolish any direct depolarisation of RGCs, using sub-threshold pulses promoting the formation of an indirect summed activity, as previously suggested³⁷⁹. Such stimulation design can allow an almost exclusive epiretinal indirect stimulation of RGCs.

The use of capacitive-like pulses in epiretinal stimulation not only allows to enhance the indirect activity compared to direct RGC depolarisation but it can improve the stimulation resolution. The indirect excitation of the RGC layer enables a more focal population response owing to the recruitment of lateral inhibition within the retina. Our results suggest a crucial role of ACs in the generation of indirect activity. Simulations *in-silico* and *ex-vivo* experiments suggest that non-rectangular capacitive-like voltage pulses, in contrast to rectangular pulses, induce a wider and more sustained activation of the inhibitory AC layer, thus a more clustered indirect activation of RGC layer. The clustering effect at the RGC level is reinforced by the conjoint use of long and capacitive-like pulses since long pulse durations appear to be more sensitive to the pulse shape for optimal neurons excitation⁴²². Our computational-

experimental approach suggests that the RGC indirect activity is necessarily associated with the activation of the AC layer and backwards inhibition of the eRF surround.

In epiretinal stimulation, the focusing of the RGC eRF can be impaired by several factors: (i) the local depolarisation of the RGC axon by a peripheral electrode, (ii) the electrode size, for example an 80- μm electrode can activate BCs leading to secondary activation of 15 to 20 RGCs in an intact mouse retina, but up to 160 RGCs in the human fovea^{423,424}, and (iii) the extra potential generated around the electrode which can cover 10 additional RGCs. Furthermore, gap junctions between RGCs and eventually aberrant connection or other miswired partners could alter the spatial focusing of the response from individual RGCs. All those factors can be attenuated by decoupling the eRFs of individual RGCs thanks to their respective inhibitory surround. The sustained stimulation of the inner retina and the lateral inhibitory network, via long non-rectangular capacitive-like pulses, contributes to the focusing of the indirect eRF. This evidence clarifies the response resolution refinement previously demonstrated *ex-vivo* and *in-vivo* with rectangular pulses longer than 25 ms²³⁷. In that study, the calcium imaging readout of the spatial RGC activation *ex-vivo* is narrowed by the lengthening of electrical stimulation. Similarly, the indirect eRFs focusing that we observed with capacitive-like pulses is expected to narrow the spatial extent of the RGC layer activation, as shown by the biophysical model. However, the use of long pulses dramatically limits the affordable stimulation frequency of the prosthesis: an optimal pulse duration of 25 ms would theoretically limit the prosthesis operating range to approximately 20 Hz for biphasic pulses (or less if we consider a safe interval between consecutive pulses). Non-rectangular waveforms such as capacitive-like stimuli allow reaching indirect firing rates comparable to those obtained with 20-ms rectangular pulses, but with pulses two times shorter, thus increasing the theoretical stimulation rate limit of the prosthesis. Along with this, for paired pulse durations, the use of non-rectangular capacitive-like pulses reduces the voltage necessary to activate both excitatory and inhibitory inner retinal cells, which in turn might have a beneficial effect on the stimulation focusing.

3.6 Conclusion

Turning epiretinal stimulation into an indirect stimulation strategy with long non-rectangular capacitive-like pulses offers new perspectives to epiretinal prostheses. The lengthening of the stimulus pulse or the use of pulses with slow voltage changes favour the sustained activation of the inner retinal neurons and induce a focused indirect response in RGCs. However, lengthening the stimulation pulses might excessively reduce the maximal repetition rate of a retinal prosthesis. Therefore, the optimal pulse shape engineering can be a complementary strategy to further promote indirect response without lengthening the stimulation pulses. The various types of indirect response patterns recorded under electrical stimulation^{419,425} suggest that the network-mediation can preserve the diversity of stimulus encoding by the local retinal circuits. If the stimuli encoding is undeniably modified, the network-mediation may allow to preserve a functional specificity through the local wiring, and thus be more likely to reproduce natural responses features, such as inter or intra-burst intervals. Notably, the first latency between direct and medium-latency responses might be critical. The present study demonstrates that, upon the relevant stimulation paradigms, it is possible to indirectly target RGC in a physiologically realistic manner, while benefiting from the implantation convenience of epiretinal devices. In the perspective of axons stimulation avoidance, it seems convenient to design a stimulation protocol favouring an epiretinal indirect stimulation of RGCs thanks to the use of capacitive-like waveforms and long pulse durations. However, how the successive waves of indirect activation would be further processed, integrated, and interpreted by the patient remains to be understood. Moreover, an approach based on epiretinal indirect activation relies on the preservation of the inner nuclear layer connectivity. Nevertheless, the appropriate therapeutic window may still have to be clinically determined, although the preservation of ACs and RGCs, together with a relative preservation of the inner nuclear layer morphology leaves considerable hope for indirect epiretinal excitation and inhibition of RGCs^{43,68,69,102,104}. Last, the relevance of a strategy based on indirect activity to enhance the resolution of artificial vision still requires to be proven *in-vivo*. Further work may include the simulation of functional diversity in RGCs, together with a more realistic compartmentalised neuron model, in order to provide a deeper sight on the relative roles of retinal stratification and cells specificity.

3.7 Acknowledgements

This work has been supported by École Polytechnique Fédérale de Lausanne, Medtronic, and Fondation Pierre Mercier pour la science. We would like to thank Alban Bornet and Anton Voronov for their help in Python.

Chapter 4 POLYRETINA restores high-resolution responses to single-pixel stimulation in blind retinas

Preprint version of the article submitted to Communications Materials, 2020.

Authors: Naïg A. L. Chenais^a, Marta J. I. Airaghi Leccardi^a, and Diego Ghezzi^a.

^a Medtronic Chair in Neuroengineering, Center for Neuroprosthetics, Institute of Bioengineering, School of Engineering, École Polytechnique Fédérale de Lausanne, Switzerland

Authors contribution: N.A.L.C. designed, performed and analysed spatial selectivity measurements and electrophysiological experiments, and wrote the manuscript. M.J.I.A.L. designed, fabricated, and characterised the prosthesis, and performed mechanical and thermal simulations. D.G. designed and led the study, and wrote the manuscript. All the authors read and accepted the manuscript.

4.1 Abstract

Retinal prostheses hold the promise of restoring vision in totally blind people. However, a decade of clinical trials highlighted quantitative limitations hampering the possibility to reach this goal. A key challenge in retinal stimulation is to independently activate retinal neurons over a large portion of the subject's visual field. Reaching such a goal would significantly improve the perception accuracy in retinal implants' users, along with their spatial cognition, attention, ambient mapping and interaction with the environment. To address this issue, here we show a wide-field, high-density and high-resolution photovoltaic epiretinal prosthesis for artificial vision (POLYRETINA). The prosthesis embeds 10,498 physically and functionally independent photovoltaic pixels allowing for wide retinal coverage and high-resolution stimulation. Single-pixel illumination reproducibly induced network-mediated responses from retinal ganglion cells at safe irradiance levels. Furthermore, POLYRETINA allowed response discrimination with a high spatial resolution equivalent to the pixel pitch (120 μm) thanks to the network-mediated stimulation mechanism. This approach could allow mid-peripheral artificial vision in patients with *Retinitis Pigmentosa*.

4.2 Introduction

Visual prostheses provide artificial vision through electrical stimulation of the preserved neurons in the visual system^{426,99,427}. Over the years, several devices were proposed, including retinal, optic nerve and cortical implants^{428,143,429,183,158,147}. Still, so far, only retinal prostheses have reached large testing in patients together with tremendous improvements from the technological perspective^{237,320,369,430}.

Retinal implants have been predominantly tested in blind patients affected by *Retinitis Pigmentosa*, a set of inherited retinal dystrophies causing the progressive loss of retinal photoreceptors, the visual field's constriction and eventually blindness¹⁹. *Retinitis Pigmentosa* has a prevalence of about 1:4,000 individuals, although totally blind people are rare (*i.e.* with no remaining light perception). *Retinitis Pigmentosa* patients implanted with either epiretinal or subretinal prostheses could localise and identify letters or objects, and perform orientation tasks^{186,280,431}. Nevertheless, despite the research community's effort and the patients' enthusiasm, most of the latter ceased using their implant in the first to the third year following their surgery²⁷⁰. Furthermore, one-third of the users of the Argus® II epiretinal prosthesis (the most implanted so far) declared that the device had a neutral impact on their quality of life after three years²⁷².

This discouragement can be attributed to quantitative limitations in the artificial vision provided by retinal implants²⁷⁰. Retinal prostheses approved by regulatory agencies provide at best a visual angle of 20 degrees (Argus® II¹⁵⁸) and despite already being an incredible achievement in medical technology, such angle does not allow for safe and independent navigation in open spaces with obstacles and moving objects^{345,432}. Independent mobility is of primary importance to increase the quality of life in profoundly blind patients with *Retinitis Pigmentosa*¹³. Additionally, the coarse visual resolution offered by the device (*i.e.* for the Argus® II⁴³³, 6 x 10 electrodes with a 525- μ m pitch), combined with the small visual angle, provides little help in daily tasks involving object identification and recognition. Last, patients reported that retinal prostheses are cognitively exhausting due to the constant need of space decomposition²⁷⁰: because of the limited visual angle, the users are instructed to move their head and body to scan the environment. Scanning implies a constant visual decomposition and mental reconstruction of the visual scene, often guided by a complex pairing of the coarse visual information with audio-tactile cues²⁷⁰. Studies under simulated prosthetic vision identified a visual angle of 30 degrees as the minimal requirement to efficiently complete everyday mobility and manipulation tasks^{277,279-281,434}. This number might even underestimate the real needs of implanted patients, which exhibit poor performance in those tasks, due to the perceptual and behavioural learning required to adapt to the spatially fractioned artificial vision^{435,436}. Thus, the small visual angle is a significant bottleneck preventing patients affected by *Retinitis Pigmentosa* from efficiently performing daily activities. New retinal prostheses should overcome this challenge and restore a large enough visual angle fitting the natural scanning via eye movements to provide a helpful and valuable visual aid to patients with *Retinitis Pigmentosa*. Wide-field retinal prostheses enabling theoretical visual angles larger than 30 degrees were recently proposed and tested in preclinical studies to meet these requirements^{168,369}.

Nevertheless, the visual angle is not the only barrier. Object identification and recognition require devices able to provide enough resolution. Wide-field arrays were so far designed for epiretinal placement only since large subretinal implants might encounter considerable difficulty in the surgical placement and represent a high risk of retinal detachment^{136,285,437}. However, clinical trials showed that the best visual resolution was achieved using subretinal prostheses. The highest visual acuities reported to date, as measured with Landolt-C test, were 20/460 (logMAR 1.37) with the subretinal implant PRIMA⁴³⁸ and 20/546 (logMAR 1.43) with the subretinal implant Alpha-AMS¹⁸¹. Grating acuities reported in the literature range from 20/1260 with the epiretinal Argus® II implant²⁸⁴ to 20/364 with the subretinal Alpha-AMS implant²⁷⁵. The inadequate performance of epiretinal prostheses like the Argus® II can be attributed to two factors: on the one hand, the implantable pulse generator, the transscleral cable and the feedlines in the array strongly limit the number and density of the electrodes, despite the large retinal coverage allowed by the epiretinal placement. On the other hand, the direct activation of the nerve fibers distorts the retinotopic map by stimulating cells far from the electrode.

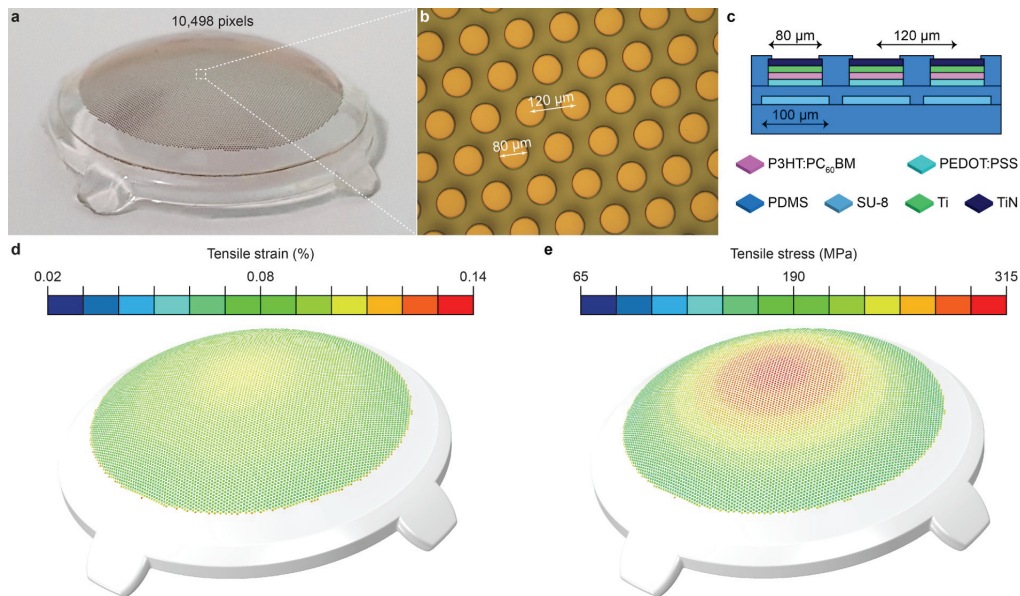
In this work we propose a wide-field curved organic photovoltaic epiretinal prosthesis with a high pixel density to address the aforementioned limitations. The high-density POLYRETINA implant was conceived to offer a large visual angle requiring minimal head scanning and a high resolution through epiretinal network-mediated stimulation, thus overcoming the nerve fibers direct activation. However, a high pixel density in the prosthesis does not necessarily correlate with high visual discrimination, since the response resolution at the retinal ganglion cell (RGC) level might be altered by the high spatial interconnectivity of the retinal network^{136,348,439}. Therefore, we investigated *ex-vivo* the response resolution provided by this high-density retinal prosthesis. Our results demonstrated that POLYRETINA could achieve a high spatial resolution in epiretinal stimulation, which is a substantial step forward for artificial vision.

4.3 Results

4.3.1 High-density retinal prosthesis

POLYRETINA is a wide-field high-density epiretinal prosthesis which contains 10,498 photovoltaic pixels (80- μm diameter, 120- μm pitch) distributed with a density of 79.1 pixels mm^{-2} over an active area of 13 mm in diameter (**Figure 1a,b**). Once bonded to its curved flexible support, the active area is slightly stretched to 13.4 mm, and the prosthesis covers a visual angle of about 43 degrees (750 mrad). Compared to the first POLYRETINA design³⁶⁹, the number of pixels and their density were increased, together with two other technical improvements. First, titanium (Ti) electrodes were coated with a layer of titanium nitride (TiN) to enhance the stimulation efficiency while keeping a safe capacitive stimulation. Second, the polymer-based layers below each cathode were patterned to generate physically independent photovoltaic pixels (**Figure 1c**) and to avoid having cracks between rigid platforms made out of SU-8 (**Figure 1b**).

The fabrication of a high-density array brings on several challenges. First, the higher the pixel density, the higher the risk that the pixels would crack during the hemispherical shaping of the device. We performed finite element analysis simulations to estimate the level of tensile stress and strain occurring onto the cathodes during hemispherical shaping (**Figure 1d,e**). The TiN coating reduced the tensile strain from -0.55 % (Ti pixels) to -0.13 % (TiN-coated pixels) and the tensile stress from 574.8 MPa (Ti) to 310.9 MPa (TiN). The reduction of tensile stress during hemispherical shaping further protects the metal cathodes (**Figure 1b**).

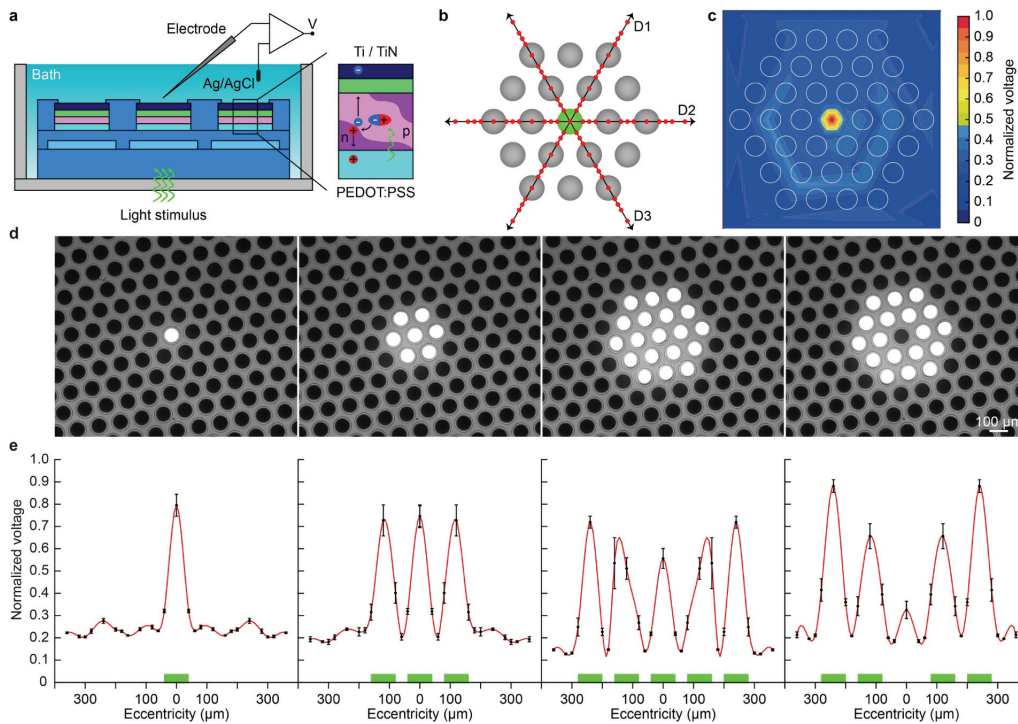


Ch.4 Figure 1 - High-density POLYRETINA device

a, Picture of a fabricated high-density POLYRETINA prosthesis with 10,498 photovoltaic pixels. **b**, Magnified view of the photovoltaic pixels having a diameter of 80 μm and a pitch of 120 μm . **c**, Sketch of the cross-section structure of the POLYRETINA photovoltaic interface before bonding to the hemispherical dome. The layer thicknesses are as follow: base PDMS layer: 50 μm ; SU-8 platforms: 6 μm ; second PDMS layer embedding SU-8 platforms: 15 μm ; PEDOT:PSS: 50 nm, P3HT:PCBM: 100 nm, Ti-TiN: 80-60 nm, final PDMS layer: 4 μm . PDMS: polydimethylsiloxane; PEDOT: poly(3,4-ethylenedioxythiophene); PSS: poly(styrenesulfonate); P3HT: regioregular poly(3-hexylthiophene-2,5-diyl); PC₆₀BM: [6,6]-phenyl-C61-butyric acid methyl ester; Ti: titanium; TiN: titanium nitride. **d**, Tensile strain simulated at the level of TiN. **e**, Tensile stress simulated at the level of TiN.

Second, a higher pixel density might induce cross-talk during stimulation with neighbouring pixels. To rule out this possibility, we measured the radial voltage spreading (**Figure 2a**) in three directions (D1, D2 and D3 in **Figure 2b**) using a glass microelectrode upon pulsed illumination of a single-pixel (560 nm, 10 ms). The minimum irradiance level required to activate RGCs *ex-vivo* is about one hundred of $\mu\text{W mm}^{-2}$ for large-field illumination³⁶⁹; yet, to exclude cross-talk even at very high irradiance levels, we performed the experiment at 22.65 mW mm^{-2} , the maximal irradiance attainable by the illumination system. For each direction, the voltage generated from the pixel was measured in several points at increasing distance from the illuminated pixel (red points in **Figure 2b**) and interpolated in a two-dimensional colour map (**Figure 2c**). The voltage generated by single-pixel illumination remained localised above the pixel. In order to ensure that neighbouring pixels do not induce cross-talk, we repeated the experiment activating one pixel (**Figure 2d**, left), one pixel with one surrounding corona of pixels (seven pixels; **Figure 2d**, middle left), one pixel with two surrounding coronas of pixels (nineteen pixels; **Figure 2d**, middle right), or the two surrounding coronas of pixels with the central pixel off (eighteen pixels; **Figure 2d**, right). For each condition, the normalised voltage profiles in the three principal directions were

averaged. The average plot of the voltage profile showed that the voltage generated by each pixel is sharply discriminated from the one of neighbouring pixels and does not show a voltage summation effect, in all the configurations tested (**Figure 2e**). Even in the extreme case where the central pixel is off while the surrounding eighteen pixels are on, there is very high contrast in the voltage drop between the central pixel and the neighbouring ones (**Figure 2e**, right), although a small residual potential is present also onto the central pixel. These results show that the pixels are electrically independent (*i.e.* no cross-talk). However, it must be noted that the voltage measures were taken close to the device's surface (2-5 μm distance). Such a sharp discrimination of the voltage profile might be reduced at larger distances from the array, where RGCs and bipolar cells (BCs) are located.

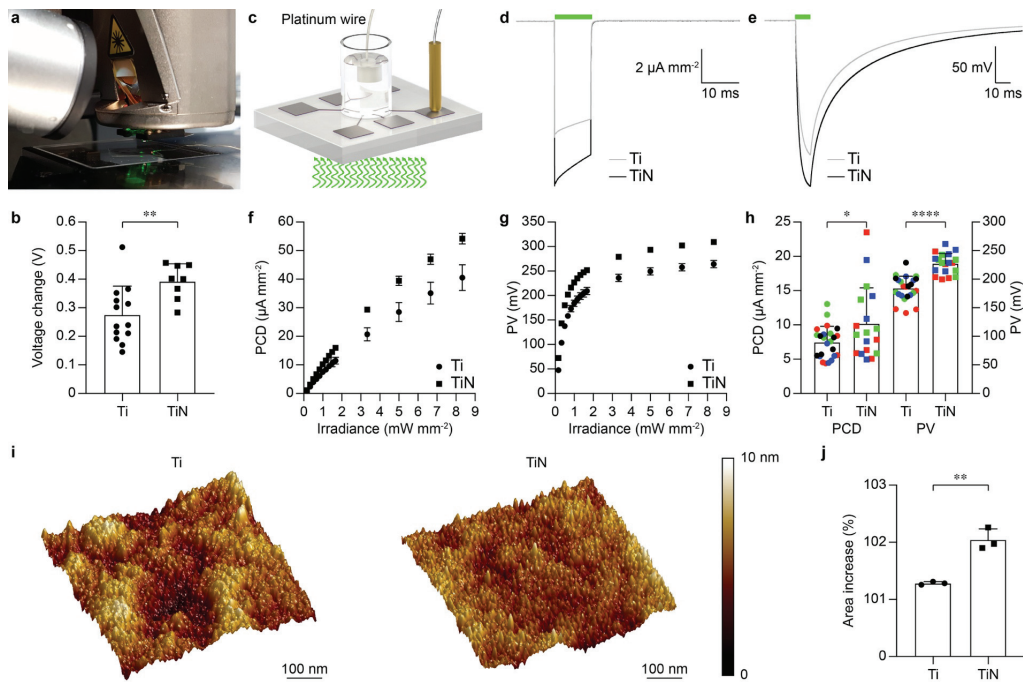


Ch.4 Figure 2 - Stimulation selectivity of the photovoltaic pixel

a, Sketch of the experimental set-up to measure the voltage spreading. The insert shows the photovoltaic transduction mechanism. A photon is absorbed by the P3HT (p-type semiconductor, electron donor) and an exciton is formed. The exciton travels until it reaches the interface between P3HT and PCBM (n-type semiconductor, electron acceptor) and dissociates. The electron is attracted towards the cathode (Ti/TiN), and the hole is attracted towards the anode (PEDOT:PSS) because of their work function levels. **b**, Sketch of the experimental methodology. The green dot corresponds to the illuminated pixel (560 nm, 10 ms, 22 mW mm^{-2}). The grey ones represent the surrounding pixels. The voltage was measured in 25 positions (red dots) for each direction (D1, D2, and D3). **c**, Voltage spreading colour map generated by interpolating the experimental measures with a triangulation-based linear interpolation. For each data point, 10 consecutive recordings were averaged and the voltage peaks were normalised to the maximal value obtained in the whole experiment. **d**, Pictures of the four stimulation patterns: central on (left), central on and one corona on (middle left), central on and two coronas on (middle right), and central off and two coronas on (right). The light spots are visible (brighter area). **e**, Normalised voltage profiles obtained for the four illumination patterns (mean \pm s.e.m.; $n = 4$ prostheses). For each prosthesis, the normalised data from the 3 directions were averaged. The red line shows a Gaussian fitting, and the green bars beneath corresponds to the active pixels.

Third, high-density retinal prostheses would represent a useful advancement only if stimulation of RGCs can be achieved by single-pixel illumination. Thus, TiN was coated on top of the pixels to increase their stimulation efficiency. Using Kelvin Probe Force Microscopy (KPFM), we evaluated the changes in the surface potential generated at the cathode upon illumination (560 nm, 60 s, 0.9 mW mm^{-2}) with and without the TiN coating (**Figure 3a**). The irradiance level was set to 0.9 mW mm^{-2} since our previous results showed a saturation of the RGC response beyond this value³⁶⁹. TiN-coated pixels showed a statistically significant higher change in the surface potential compared to Ti pixels (**Figure 3b**; $p = 0.0083$, two-tailed unpaired t-test). Next, we measured the photo-current (PC) and the photo-voltage (PV) generated by the pixels upon illumination (565 nm, 10 ms) at increasing irradiance levels. We fabricated chips embedding 6 pixels, each of them connected to a contact pad to measure the signal at the cathode against a platinum reference electrode immersed in saline solution (**Figure 3c**). The mean PC density (PCD) and PV were both higher for TiN-coated pixels upon illumination at increasing irradiance levels (**Figure 3f,g**). We further evaluated the PCD and the PV at the representative irradiance level of 0.9 mW mm^{-2} (**Figure 3h**): a statistically significant difference between Ti and TiN-coated pixels was found for both

the PCD ($p = 0.0288$, two-tailed unpaired t-test) and the PV ($p < 0.0001$, two-tailed unpaired t-test). The surface area of the cathodes was measured with an atomic force microscope (AFM) over an area of $500 \times 500 \text{ nm}^2$ (**Figure 3i,j**). On average ($n = 3$ pixels), TiN-coated pixels showed a statistically higher surface area compared to Ti pixels ($p = 0.0024$, two-tailed unpaired t-test). These results confirmed that the photovoltaic pixels are physically and functionally independent. The coating with TiN reduced the mechanical stress of the pixels and increased their photovoltaic performance by likely reducing the electrode-electrolyte impedance, increasing the interface capacitance and reducing the parasitic resistances of the photovoltaic pixel. In fact, the TiN coating produces a more homogeneous film than Ti alone, with a better contact and likely decreasing the series resistance. In turns, a lower series resistance reduced the current flowing into the shunt resistance of the device, especially at the light onset, hence increasing the PCD peak. It is worth to mention that the additional fabrication steps needed to process the TiN layer might also influence the polymer layer underneath and lead to higher PCD. These results open up the possibility of high-resolution single-pixel stimulation of RGCs.



Ch.4 Figure 3 - Optoelectronic characterisation of the photovoltaic pixel

a, Picture of the KPFM set-up. **b**, Surface voltage changes obtained with Ti (circles) and TiN-coated (squares) cathodes. Each bar is the mean (\pm s.d.) of the measures from $n = 13$ Ti pixels and $n = 8$ TiN-coated pixels. **c**, Drawing of the experimental set-up for the measure of the PC and PV; the light pulse comes from the bottom. **d,e**, Mean PCD (**d**) and PV (**e**) measures obtained from Ti (grey) and TiN-coated (black) pixels upon illumination (565 nm, 10 ms, 0.9 mW mm^{-2}). For Ti, $n = 24$ pixels from 4 chips were averaged; for TiN, $n = 18$ pixels from 3 chips were averaged. **f,g**, Mean (\pm s.e.m) PCD (**f**) and PV (**g**) amplitudes quantified at increasing irradiance levels (565 nm, 10 ms) for Ti pixels (circles; $n = 24$ pixels from 4 chips) and TiN-coated pixels (squares; $n = 18$ pixels from 3 chips). **h**, Mean (\pm s.e.m) PCD and PV amplitudes quantified at 0.9 mW mm^{-2} for Ti ($n = 24$ pixels from 4 chips) and TiN-coated ($n = 18$ pixels from 3 chips) pixels. **i**, AFM images of the Ti and Ti/TiN surfaces. The colour bar shows the surface roughness. **j**, Mean (\pm s.d.) percental increase of the surface area compared to the nominal flat area ($500 \times 500 \text{ nm}^2$).

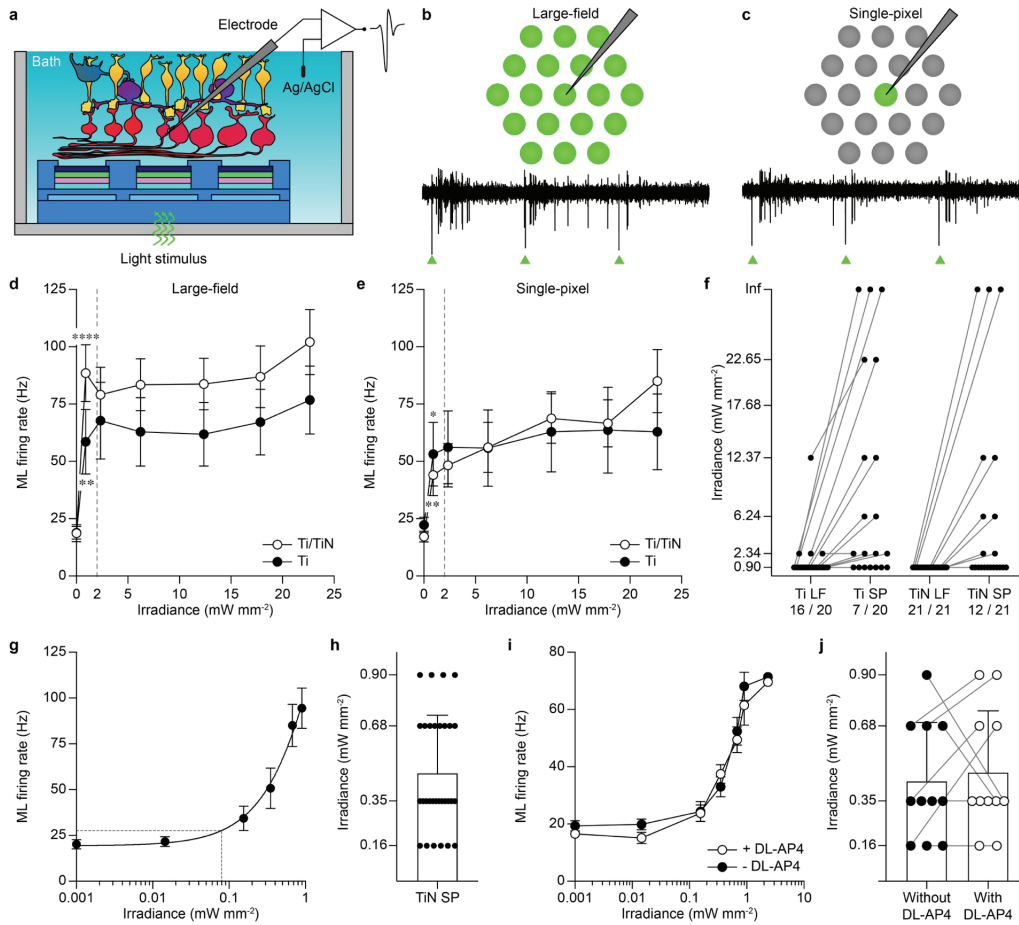
4.3.2 Single-pixel stimulation efficiency of titanium nitride photovoltaic pixels

We subsequently evaluated whether the increased photovoltaic performances of TiN-coated pixels translated into a higher stimulation efficiency of RGCs. For this study, we used explanted retinas from the *Retinal degeneration 10 (Rd10)* mouse model, which is an established model for *Retinitis Pigmentosa*^{101,121,413}. According to our previous study⁴⁴⁰ and studies performed by other laboratories^{335,414}, *Rd10* retinas beyond post-natal day (P) 60 can be considered light-insensitive. In order to ensure a proper exclusion of intrinsic light responses due to spared photoreceptors, the experiments in this work were performed in *Rd10* retinas at a very late stage of degeneration (mean age \pm s.d.: 127.2 ± 14.9). Both male and female mice were used to exclude any effect related to sex-related differences in the degeneration onset and progression in *Rd10* retinas (**Table 3**). Explanted retinas were layered in epiretinal configuration, and the prosthetic-evoked activity of RGCs was recorded via single-electrode extracellular recordings (**Figure 4a**). Light pulses (560 nm, 10 ms) were delivered in a broad range of irradiance levels (0.9, 2.34, 6.24, 12.37, 17.68 and 22.65 mW mm⁻²) and the network-mediated medium-latency (ML) responses of RGCs to large-field (covering approximately 70 pixels) illumination (**Figure 4b**) and single-pixel illumination (**Figure 4c**) were compared. The quantification of the ML spiking activity upon large-field illumination revealed that TiN-coated pixels elicited on average higher ML spiking activity than Ti pixels (**Figure 4d**). Moreover, in both conditions, the first irradiance tested (0.9 mW mm⁻²) elicited a statistically significant ML spiking activity higher than the basal activity computed without light (Ti: $p = 0.0088$; TiN: $p < 0.0001$; two-tailed unpaired t-test). When the illumination was switched to single-pixel (**Figure 4e**), both Ti and TiN-coated pixels also evoked a statistically significant ML spiking activity at the first irradiance tested (0.9 mW mm⁻²; Ti: $p = 0.0378$; TiN: $p = 0.0062$; two-tailed unpaired t-test). This result revealed that both Ti and TiN-coated photovoltaic pixels induced RGC activity upon single-pixel illumination.

Next, we quantified the fraction of RGCs that could be activated with 10-ms pulses at 0.9 mW mm⁻² under both large-field and single-pixel stimulation. For Ti pixels and large-field stimulation, 16 out of 20 RGCs showed ML responses at 0.9 mW mm⁻², or in other words, exhibited an activation threshold lower or equal to 0.9 mW mm⁻². 3 out of 20 RGCs showed activation at 2.34 mW mm⁻², and 1 out of 20 RGCs showed activation at 12.37 mW mm⁻². Switching to single-pixel illumination, only one-third of the RGCs (7 out of 20) preserved ML activity upon illumination at 0.9 mW mm⁻². For TiN-coated pixels, all RGCs (21 out of 21) showed ML activity upon large-field illumination at 0.9 mW mm⁻², and still more than half RGCs (12 out of 21) when the illumination was switched to single-pixel. This result shows the higher efficiency in single-pixel retinal stimulation of TiN-coated photovoltaic pixels compared to Ti pixels. Noteworthy, this increase in efficiency cannot be attributed to sex-related differences. For Ti pixels, nine animals were used (129.4 ± 15.6 , mean age \pm s.d.), of which 7 males (77.8 %) and 2 females (22.2 %). For TiN-coated pixels, six animals were used (126.5 ± 22.0 , mean age \pm s.d.), of which 4 males (66.7 %) and 2 females (33.3 %). Also, the mice's age was not statistically different among the two groups ($p = 0.77$, two-tailed unpaired t-test). With TiN-coated pixels and single-pixel illumination, 57 % (12 out of 21) of the recorded cells could be activated at 0.9 mW mm⁻² while the others required higher irradiance: a result coherent with those obtained by another photovoltaic retinal prosthesis⁴⁴¹. The variation in the irradiance threshold can be related to the location of the RGCs and their pre-synaptic networks compared to the position of the illuminated pixel, which cannot be precisely located due to the recording method. Therefore, RGCs having their pre-synaptic network centred over a pixel might have a lower threshold than those RGCs eccentric to the pixel because of the very limited lateral spreading of the photovoltaic stimulus.

In a second set of cells ($n = 30$ RGCs) exhibiting ML response upon single-pixel illumination of TiN-coated pixels at 0.9 mW mm⁻², we determined the threshold for activation using lower irradiance levels (0.014, 0.16, 0.35, 0.68, and 0.9 mW mm⁻²). The average ML firing rates upon single-pixel illumination increased as a function of the irradiance (**Figure 4g**) with an activation threshold of about 79 μ W mm⁻², obtained as the irradiance level providing 10 % of the maximal ML firing rate measured at 0.9 mW mm⁻². This result shows that the responsivity of the RGCs can be modulated as a function of the irradiance level. However, we observed that the single-pixel activation threshold for individual RGCs is variable among the irradiance levels tested (**Figure 4h**), and more than half (18 out of 30) of the RGCs exhibited a ML response threshold lower or equal to 0.35 mW mm⁻². While the population threshold was estimated to be 79 μ W mm⁻², only 6 out of 30 cells showed ML responses at 160 μ W mm⁻². As before, the disparity of the network-mediated ML activation thresholds can be related to the location of the cell and its pre-synaptic network compared to the position of the illuminated pixel. Last, we evaluated in a subset of RGCs ($n = 11$, TiN-coated pixels) the ML responsivity with and without the application of a broad spectrum glutamatergic synaptic antagonist (DL-AP4, 250 μ M I⁻¹; No. 0101, Tocris Bioscience), which blocks the synaptic input of ON BCs⁴⁴² (**Figure 4i**). The ML response curve was not altered by the introduction of the antagonist. This excludes any contribution from potential spared photoreceptors to the ML responses recorded upon photovoltaic stimulation. Also, the single-pixel activation threshold measured in individual RGCs was not statistically different after DL-AP4 application (**Figure 4j**; $p = 0.68$, two-tailed paired t-test).

These results confirmed that the network-mediated stimulation of RGCs in epiretinal configuration is achieved with single-pixel illumination at irradiance levels largely below the maximum permissible exposure (MPE) limit for retinal safety, which for POLYRETINA varies between 8.32 and 2.08 mW mm⁻² respectively for 5 and 20 Hz illumination rate and 10-ms pulse duration.



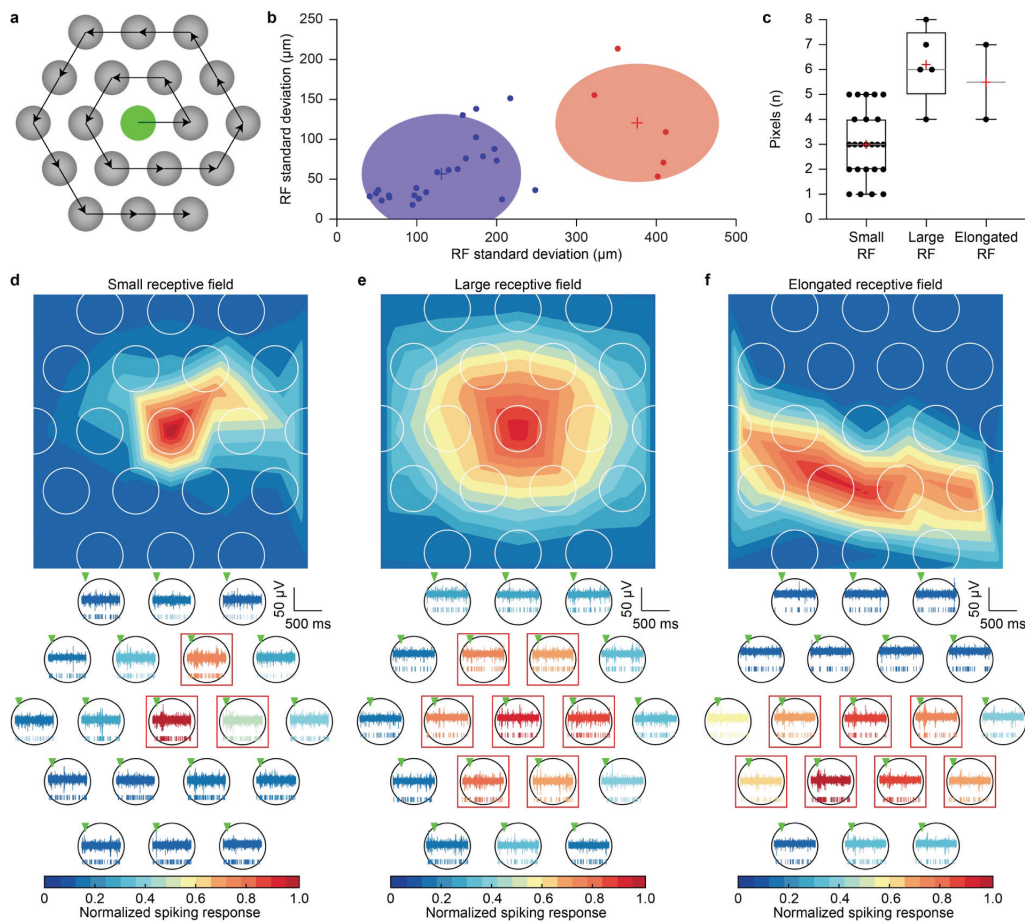
Ch.4 Figure 4 - Single-pixel stimulation of retinal ganglion cells

a, Sketch of the recording set-up. **b,c**, Representative responses from a retinal ganglion cell upon 3 consecutive light pulses (560 nm, 10 ms, 0.9 mW mm⁻²) with large-field illumination (**b**) and single-pixel illumination (**c**). **d,e**, Comparison of the stimulation efficacy during large-field (**d**) and single-pixel (**e**) illumination under increasing irradiances with Ti-based ($n = 20$ RGCs, mean \pm s.e.m.) and TiN-based pixels ($n = 21$ RGCs, mean \pm s.e.m.). **f**, Change in the activation threshold from large-field to single-pixel illumination for both Ti pixels ($n = 20$ RGCs) and TiN-coated pixels ($n = 21$ RGCs). The numbers for each column are the fraction of RGCs activated by a 10-ms light pulse of 0.9 mW mm⁻². Inf means that the RGC does not show ML activity at any of the irradiance level tested. LF: large-field, SP: single-pixel. **g**, ML firing rate ($n = 30$ RGCs, mean \pm s.e.m.) at low irradiance levels for TiN-coated pixels and single-pixel illumination. The black line is the second-order polynomial interpolation (R squared = 0.29). The grey dashed lines show the activation threshold computed as the irradiance eliciting 10 % of the maximal ML firing rate at 0.9 mW mm⁻². **h**, Activation threshold for each RGCs with single-pixel illumination and TiN-coated pixels (mean \pm s.d.). **i**, ML firing rate ($n = 11$ RGCs, mean \pm s.e.m.) at low irradiance levels for TiN-coated pixels and single-pixel illumination before and after the application of DL-AP4. **j**, Activation threshold for each individual RGC with single-pixel illumination and TiN-coated pixels before (black circles) and after (white circles) the application of DL-AP4 (mean \pm s.d.).

4.3.3 Photovoltaic receptive fields

Using TiN-coated pixels and single-pixel illumination at 0.9 mW mm⁻², we quantified the number of pixels eliciting a network-mediated ML response in a given RGC (**Figure 5**). The 19 neighbouring pixels around the recording electrode were successively illuminated (560 nm, 10 ms, 0.9 mW mm⁻²) according to a counter-clockwise pattern (**Figure 5a**). The network-mediated ML activities elicited by the illumination of each pixel were mapped to the pixel coordinates, and the photovoltaic receptive fields (RFs) of the RGCs were fitted with a two-dimensional gaussian model. Each photovoltaic RF diameter was then calculated as the average between the horizontal and vertical standard deviation of its two-dimensional activation map. The majority of the recorded RGCs (24 out of 31 cells) exhibited small photovoltaic RFs with a radius ranging from 34.5 to 142.5 μ m (**Figure 5d**). 5 out of 31 RGCs exhibited large photovoltaic RFs whose radius varied between 184.3 and 282.7 μ m (**Figure 5e**). 2 out of 31 RGCs exhibited elongated photovoltaic RFs, showing high responses to several aligned pixels (**Figure 5f**). The activation maps of the RGCs could be clustered (Gaussian mixture model) into two populations (**Figure 5b**), namely those exhibiting small or large photovoltaic RFs (RGCs with elongated RFs were excluded from the analysis). For clustering, the RFs were rotated so that the horizontal direction (x-axis)

corresponds to the axis of maximal dispersion and the vertical direction (y-axis) corresponds to the dispersion in the orthogonal direction. The average photovoltaic RF diameter for each population was respectively $153.7 \pm 26.1 \mu\text{m}$ and $335.5 \pm 49.3 \mu\text{m}$ (mean \pm s.e.m). In both the healthy and the *Rd10* mouse retinas, most of the RGCs exhibit functional RFs of a size similar to the small photovoltaic RFs (with a median cluster diameter between 119 and $280 \mu\text{m}$)^{79,102,443}. Also, populations of large α -RGCs with larger dendritic trees (up to $395 \mu\text{m}$ diameter) were reported in the mouse retina^{79,444}, with RFs sizes similar to large photovoltaic RFs recorded in the present study. Statistical analysis revealed that RGCs with small photovoltaic RFs are indirectly stimulated through an average of three photovoltaic pixels (Figure 5c). A pixel was considered to induce statistically significant activation of the RGC if the mean ML response, evaluated over ten repetitions, was statistically significantly higher than the cell background activity ($p < 0.05$, two-tailed unpaired t-test), which was calculated as the activity in the 100-ms pre-stimulus period averaged across all the illuminated pixels. Cells with very small photovoltaic RFs could be activated by one pixel only. The larger the photovoltaic RF size, the higher the number of pixels stimulating the RGC. However, the number of pixels activating one RGC might also be affected by the actual centring of the cell and its pre-synaptic network compared to the photovoltaic pixels: a single RGC can be activated by multiple neighbouring pixels when it is centred in between the pixels.

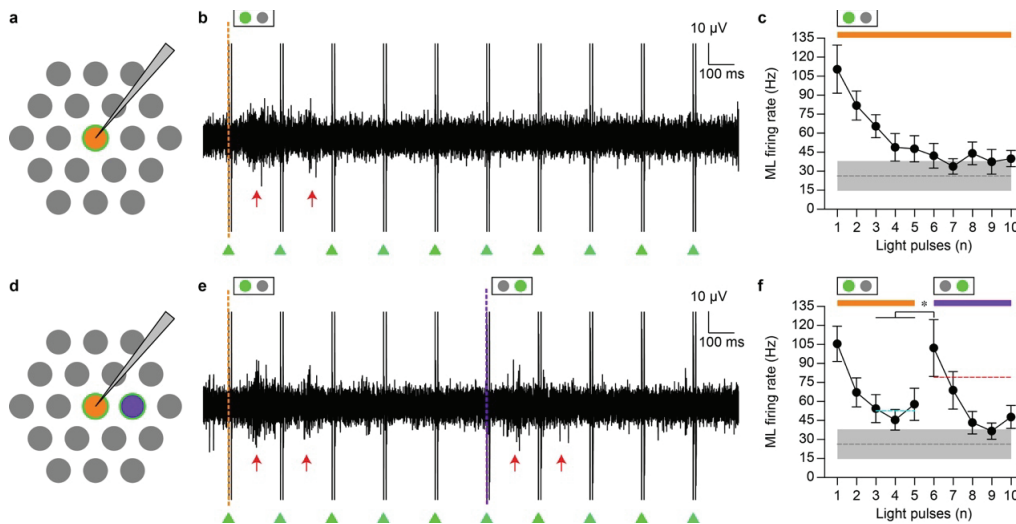


Ch.4 Figure 5 - Photovoltaic receptive fields

a, Sketch of the temporal pattern used for stimulation. Each of the 19 pixels centred around the recording location was successively illuminated following a counter-clockwise pattern (560 nm , 10 ms , 0.9 mW mm^{-2}). The total illumination sequence was repeated for 10 consecutive sweeps. The receptive fields or activation maps were obtained by two-dimensional Gaussian approximation of the network-mediated ML responses elicited by single-pixel, averaged over sweeps, and normalized to the maximal responding pixel. **b**, Gaussian mixture model of the RF sizes over the small ($n = 24$ RGCs) and large RFs RGC populations ($n = 5$ RGCs). The average RF diameter of the small and large types are respectively of $153.7 \pm 26.1 \mu\text{m}$ and $335.5 \pm 49.3 \mu\text{m}$ (mean \pm s.e.m.). **c**, Quantification of the number of pixels able to induce statistically significant ($p < 0.05$) ML activation in the recorded RGC. The horizontal grey line is the median, the red cross is the average and the the boxes extend from the 25th to 75th percentiles. **d,e,f**, Photovoltaic RFs from three individual RGCs classified as small RF cell (**d**), large RF cell (**e**), and elongated RF cell (**f**). The bottom panels show raw electrophysiological recordings and raster plots from the same cells for each single-pixel illumination (560 nm , 10 ms , 0.9 mW mm^{-2} , first sweep). The red boxes show the pixels inducing a statistically significant activation of the recorded RGC.

4.3.4 Spatial resolution of single-pixel stimulation

The retina desensitises upon repetitive and static network-mediated stimulation, and the RGC spiking response decays proportionally to the stimulation frequency^{252,253,445}. Taking advantage of this desensitisation process (*i.e.* to the adaptation to static electrical stimulation), we investigated the stimulation response resolution using a two-point discrimination pattern reversal paradigm (referred as pixel switch). In a fourth set of cells ($n = 12$ RGCs), RGCs were either statically stimulated with the most responsive pixel of their RF or alternatively from the two most responding pixels of their RF. Upon repetitive stimulation from the same pixel at 5 Hz (560 nm, 10 ms, 0.9 mW mm⁻², 10 pulses), the response desensitisation could be observed already at the second light pulse, and it reached a steady-state close to the average resting activity, calculated as the activity in the 100-ms pre-stimulus period averaged across all the RGCs (**Figure 6a-c**). When stimulating the RGCs with the two most responding pixels of their RF (**Figure 6d**), the ML activity was recovered by the switch of the stimulation pixel. Upon repetitive stimulation from the first pixel at 5 Hz (560 nm, 10 ms, 0.9 mW mm⁻², 5 pulses) the desensitisation could also be observed from the second light pulse (**Figure 6e,f**) with a $27.3 \pm 11.2\%$ drop in the ML firing rate (mean \pm s.e.m.) compared to the first pulse response ($p = 0.0105$, two-tailed paired t-test) and a $\tau = 0.93 \pm 0.14$ s decay constant (mean \pm s.e.m.) over the five consecutive pulses. However, the ML response was fully recovered when the stimulation pattern was reversed (*i.e.* when the stimulation was switched to the adjacent pixel). To evaluate the response recovery, we computed a recovery threshold (red dashed line in **Figure 6f**) defined as the central value between the naïve ML response (*i.e.*, to the first pulse in the sequence) and the average desensitised ML response (average over pulses 3, 4 and 5; cyan dashed line in **Figure 6f**). The ML response at the pixel reversal exceeded the threshold and it was statistically significantly higher than the desensitised response ($p = 0.0226$, one-tailed paired t-test). Moreover, the ML response at the pixel reversal was not statistically different from the naïve response to the first pulse ($p = 0.9054$, two-tailed paired t-test). A strong ML response to the first pulse from each pixel but not during the steady stimulation with the same pixel indicates that RGCs stimulated with POLYRETINA were able to resolve the spatial difference between the two pixels, allowing a two-point discrimination of 120 μ m (equivalent to the pixel pitch).

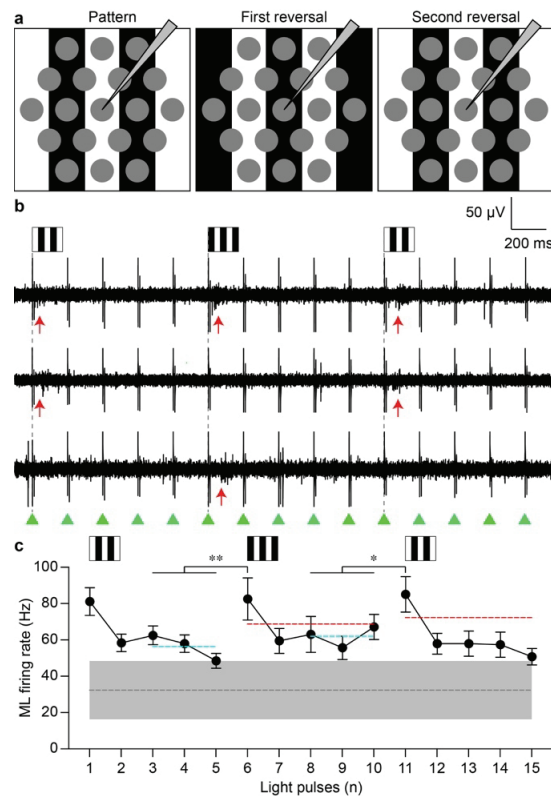


Ch.4 Figure 6 - Two-points discrimination pattern reversal test with single-pixel stimulation

a, Sketch of the single-pixel repeated stimulation paradigm. One pixel was repeatedly illuminated at 5 Hz (560 nm, 10 ms, 0.9 mW mm⁻²) for 2 s. **b**, Raw electrophysiological recordings of a single RGC under 5 Hz continuous stimulation from a single pixel. The green triangles correspond to the onset of each light pulse. The red arrows highlight the ML activity. **c**, Quantification of the ML firing rate (mean \pm s.e.m.) under continuous stimulation from a single pixel ($n = 12$ RGCs). The grey dashed line shows the average resting firing rate with its s.d. represented by the grey area. **d**, Sketch of the two-point discrimination pattern reversal paradigm. The central (orange) pixel was repeatedly illuminated for 1 s at 5 Hz (560 nm, 10 ms, 0.9 mW mm⁻²), then the illumination was switched to the adjacent pixel (purple) for 1 s at 5 Hz (560 nm, 10 ms, 0.9 mW mm⁻²). **e**, Raw electrophysiological recordings of a single RGC under 5 Hz two-point discrimination pattern reversal paradigm. The green triangles correspond to the onset of each light pulse. The pixel switch is highlighted by the purple dashed line. The red arrows highlight ML activity. **f**, Quantification of the ML firing rate (mean \pm s.e.m.) under two-point discrimination pattern reversal paradigm ($n = 12$ RGCs). The cyan dashed line is the average desensitized ML firing rate and the red dashed line is the recovery threshold. The grey dashed line and grey area show the average resting firing rate (\pm s.d.).

Next, in a fifth set of cells ($n = 26$ RGCs), we tested spatial resolution with a high-contrast grating pattern reversal paradigm, with a fixed bar width of 120 μ m (**Figure 7a**). Among the cells, we found three main behaviours presumably due to a variable alignment of the RGC presynaptic network with the illuminated bar: RGCs responding to the first pattern and the two reversals (**Figure 7b**, top row), RGCs responding to the first pattern and the second reversal (**Figure 7b**, middle row) and RGCs responding only to the first reversal (**Figure 7b**, bottom row). As observed in the two-points discrimination experiment, the ML response was reduced upon

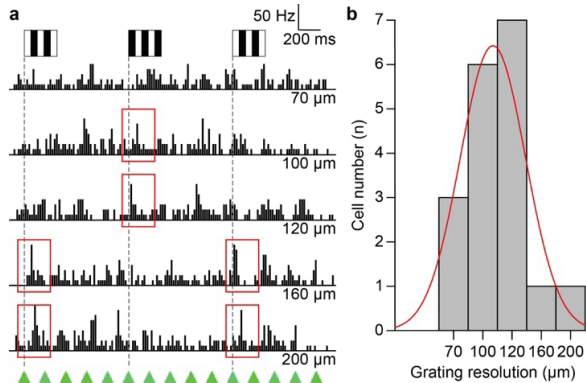
5-Hz repetitive stimulation with a steady grating pattern (**Figure 7c**), but the ML response was recovered at the two reversals of the gratings pattern (pulses 6 and 11). As previously, we defined a recovery threshold for each reversal (red dashed lines in **Figure 7c**) as the central values between the ML firing rate in response to the first pulse delivered with the previous pattern (pulse 1 and pulse 6 respectively for the first and the second reversal) and the average desensitised ML firing rate before the reversal (averaged over the ML responses to pulses 3, 4 and 5 for the first reversal and pulses 8, 9 and 10 for the second reversal; cyan dashed lines in **Figure 7b**). The ML response to the first and second pattern reversals (pulse 6 and 11) exceeded their respective recovery thresholds (red dashed lines in **Figure 7c**), and they were statistically significantly higher than the corresponding desensitised firing rate ($p = 0.0081$ and $p = 0.0140$ respectively for the first and the second reversal, one-tailed paired t-test). Moreover, the ML responses to the grating reversals were not statistically different from the response to the first naïve pulse in the sequence ($p = 0.8971$ and $F = 0.0893$, repeated measure one-way ANOVA among responses to pulses 1, 6 and 11). These results demonstrated that RGCs stimulated with POLYRETINA could resolve 120- μm wide gratings.



Ch.4 Figure 7 - Grating pattern reversal with a fixed bar width

a, Sketch of the grating pattern reversal stimulation paradigm with a fixed bar width. A grating pattern with black and green 120- μm wide vertical bars (560 nm, 10 ms, 0.9 mW mm^{-2}) was projected onto the array with a 5-Hz illumination rate for 3 s and reverted every 5 pulses. **b**, Raw electrophysiological recordings of three RGCs under grating pattern reversal with a fixed bar width. The green triangles correspond to the onset of each light pulse. The first pattern and the reversals are highlighted by the grey dashed lines. The red arrows highlight ML activity. **c**, Quantification of the ML firing rate (mean \pm s.e.m.) under grating pattern reversal with 120- μm bar width ($n = 26$ RGCs). The cyan dashed lines are the average desensitized ML firing rates and the red dashed lines are the recovery thresholds. The grey dashed line and grey area show the average resting firing rate (\pm s.d.).

To determine the spatial resolution limit, the grating pattern reversal paradigm was repeated with variable bar widths (200, 160, 120, 100 and 70 μm) in a sub-set of cells ($n = 18$ RGCs). The grating resolution of individual RGCs was assessed as the smallest grating size whose at least one reversal elicits a ML response at least two-third higher than the corresponding average desensitized ML firing rate (**Figure 8a**). When varying the grating size, the alignment of the cell's presynaptic network and the illuminated bar varied, and ML responses were observed either at the first pattern and the two reversals, at the first pattern and the second reversal or at the first reversal only (**Figure 8a**). The majority of the recorded cells RGCs shows a response resolution matching the pixel pitch (120 μm , 7 out of 18) or slightly higher (100 μm , 6 out of 18). In rarer case, ganglion cells show a response resolution lower than the pixel pitch (160, 1 out of 18; 200 μm , 1 out of 18) or higher than the pixel pitch (70 μm , 3 out of 18) (**Figure 8b**). Response resolutions higher than the pixel pitch could be explained by non-linear integration in RF's subunits, as previously reported¹⁹⁴.

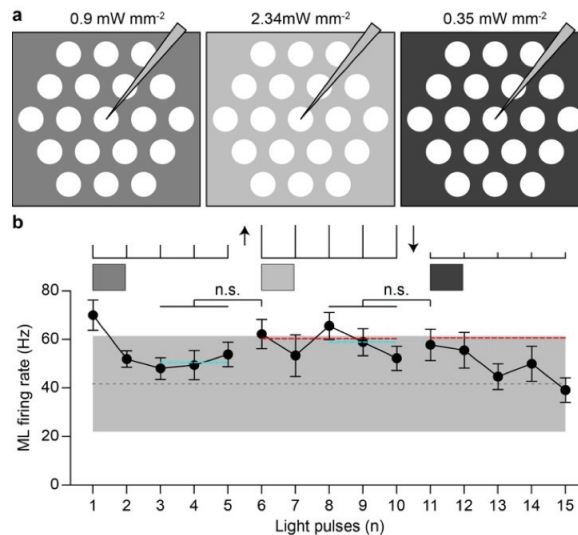


Ch.4 Figure 8 - Spatial resolution limit

a, Peri-stimulus time histograms (bins of 10 ms) for one RGC upon grating pattern reversal stimulation with decreasing bar widths (200, 160, 120, 100 and 70 μm). A grating pattern with black and green vertical bars (560 nm, 10 ms, 0.9 mW mm^{-2}) was projected onto the array with a 5-Hz illumination rate for 3 s and reverted every 5 pulses. The first pattern and the reversals are highlighted by the grey dashed lines. The green triangles correspond to the onset of each light pulse. The red rectangles highlight ML activity.
b, Distribution of grating resolutions obtained in 18 RGCs.

Last, in a sixth set of cells ($n = 12$ RGCs), we verified that the responses obtained at the pixel switch or the pattern reversals were not induced by a change in the stimulus contrast. Thus, we evaluated RGC's responses to irradiance steps without spatial content. RGCs were successively stimulated with large-field illumination (covering approximately 70 pixels) at three irradiance levels (0.9, 2.34 and 0.35 mW mm^{-2}) at 5-Hz illumination rate; 5 consecutive pulses were delivered for each irradiance level (**Figure 9a**). No ML response recovery was observed for both the positive (from 0.9 to 2.34 mW mm^{-2}) and the negative (from 2.34 to 0.35 mW mm^{-2}) irradiance steps (**Figure 9b**). The ML firing rates at the two irradiance steps (pulses 6 and 11) were not statistically significantly different than the corresponding desensitised responses ($p = 0.1224$ and $p = 0.8546$ respectively for the first and the second irradiance step, two-tailed paired t-test). This result prevents the responses to pattern reversals to be attributed to changes in the stimulus irradiance - due to the shift of illumination in the RGC presynaptic network. Yet, a small increase in the overall ML firing rate was observed during the positive irradiance step (pulses from 6 to 10), but this can be related to the irradiance dependence of ML activity (**Figure 4**).

In summary, this set of experiments confirmed a spatial resolution of the high-density POLYRETINA at least equivalent to its pixel pitch (120 μm).

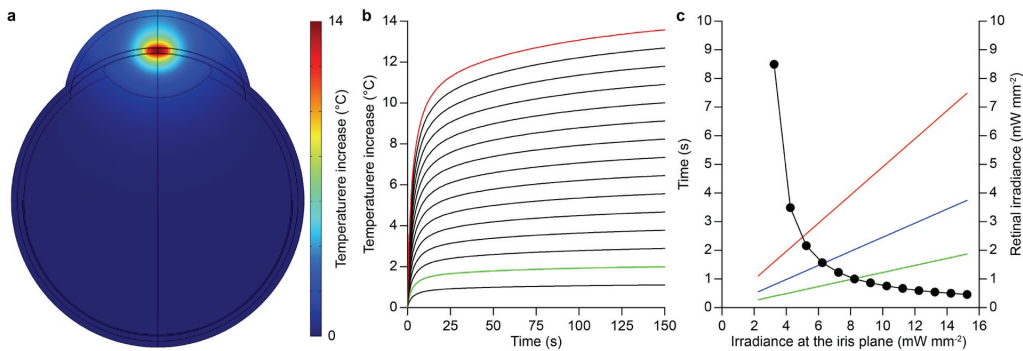


Ch.4 Figure 9 - Modulation of stimulus contrast without spatial content

a, Sketch of the stimulus contrast modulation paradigm. Pixels were repeatedly illuminated with large-field illumination at 5 Hz (560 nm, 10 ms) for 3 s, and the irradiance level was changed every 5 pulses (0.9, 2.34 and 0.35 mW mm^{-2}), the first irradiance step was positive while the second was negative. **b**, Quantification of the ML firing rate (mean \pm s.e.m.) under modulation of the stimulus contrast without spatial content ($n = 12$ RGCs). The cyan dashed lines are the average desensitised ML firing rates and the red dashed lines are the recovery thresholds. The grey dashed line and grey area show the average resting firing rate (\pm s.d.).

4.3.5 Design constraints for thermal safety

POLYRETINA achieved network-mediated stimulation of RGCs with single-pixel illumination at irradiance levels below the MPE limit for retinal safety. However, retinal damage is not the only element to be considered. During photovoltaic stimulation, a light beam is projected into the pupil, which might be transiently focused on the iris during involuntary large eye movements. In such a case, the temperature of the iris should not increase more than 2 °C (ISO 14708-1:2014 / EN 45502-1:1997). We performed a finite element analysis simulation, based on the worst-case scenario in which the full beam at the retinal MPE was stationarily projected onto the iris for a prolonged period. According to the calculated MPE for retinal safety, 47.90 mW at 565 nm could enter the pupil for chronic exposure for an illuminated retinal area of 127.97 mm² (43 degrees). Given a constricted pupil of about 3 mm (as considered in the safety standard²⁹¹) and a light beam reduced to a spot of 2 mm in diameter (to avoid beam clipping), the resulting irradiance at the iris plane is 15.25 mW mm⁻². Due to the axial symmetry of the thermal simulation, we modelled the iris as a continuous tissue without pupil (**Figure 7a**). The temperature in the iris increased by 13.58 °C after 150 s of continuous illumination at the MPE (**Figure 7b**, red line), which is largely above the safety limit of 2 °C. In order to keep the chronic thermal increase in the iris below 2 °C, the irradiance should be reduced to 2.25 mW mm⁻² (**Figure 7b**, green line), corresponding to a total of 7.07 mW chronically entering from the pupil. At the retinal level, this irradiance would correspond to a maximum of 1.1 mW mm⁻² for 10-ms pulses, 5 Hz repetition rate, and an illuminated area of 127.97 mm², which is still above the irradiance threshold for single-pixel stimulation of RGCs.



Ch.4 Figure 10 - Thermal simulations at the iris plane

a, Temperature increase at the iris plane in the modelled eye after 150 s of continuous illumination at the MPE (565 nm, 15.25 mW mm⁻²). **b**, Quantification of the temperature increase at the iris plane during 150 s of continuous illumination for various irradiance levels: 1.25, 2.25, 3.25, 4.25, 5.25, 6.25, 7.25, 8.25, 9.25, 10.25, 11.25, 12.25, 13.25, 14.24 and 15.25 mW mm⁻². The red line corresponds to 15.25 mW mm⁻² and the green line to 2.25 mW mm⁻². **c**, Quantification of the time to reach a thermal increase of 2 °C (left axis) as a function of the irradiance at the iris plane for continuous illumination at 565 nm (black circles and line). The colored lines show the irradiance obtained at the retinal level (right axis) for 10-pulses repeated at 5 Hz (red line), 10 Hz (blue line) and 20 Hz (green line) as a function of the irradiance at the iris plane for continuous illumination.

However, it is unlikely that the beam remains statically focused on the same area of the iris for 150 s, as the continuous eye movements would spread the light beam over a larger area and reduce its thermal impact²⁹¹. Therefore, we quantified the time needed to reach 2 °C with a stable beam (**Figure 7c**, black line and circles). At 15.25 mW mm⁻², an increase of 2 °C is reached after 460 ms, and the time increases by decreasing the irradiance at the iris plane: at 3.25 mW mm⁻², an increase of 2 °C is reached after 8.5 s. It is reasonable to consider that eye movements will reduce the thermal impact. Therefore, the maximal irradiance entering the pupil can be further increased well above the irradiance threshold for single-pixel stimulation of RGCs compared to the worst-case scenario. Moreover, eye-tracking sensors embedded in modern virtual reality glasses provide tracking at 120 Hz, thus allowing real-time adjustment of the beam based on the eye gaze. Under a working hypothesis of 10-ms pulses repeated at 5 Hz to 20 Hz, the eye tracker will have enough time to correct the projection system by using a steering mirror or, in the worst case, to close the beam to preserve the iris. Therefore, the obtained retinal irradiance can be further increased (**Figure 7c**, coloured lines), thus allowing higher pulse rates.

4.4 Discussion

So far, the maximum number of electrodes embedded in retinal prostheses, as well as their overall density were limited by the use of implantable pulse generators, transcleral connections and feedlines in the array¹³⁶. The introduction of the photovoltaic technique in the field of retinal prostheses has overcome all the problems mentioned above in a single step¹⁹⁶. However, despite this advancement, the small size, high stiffness and low conformability of many devices limit the overall retinal coverage to few millimetres, and so the restored visual angle to about 6 degrees^{194,320}. The retinal coverage could be slightly increased by tiling small rigid implants, as shown in rabbits up to approximately a 3.5-mm diameter area (approximately 11 degrees)³¹², but such visual angle is still below estimated patient's needs for practical uses.

Conjugated polymers combined with stretchable substrates, such as in the POLYRETINA prosthesis, allows for photovoltaic retinal stimulation together with a wide coverage of the retinal surface. Conjugated polymers were first introduced in retinal stimulation as continuous films directly interfaced with the retina^{319,446}, and already proved to be effective *in-vivo* to restore visual acuity in blind rats³²⁰. In principle, a continuous film might be advantageous compared to discrete electrodes, since a fixed arrangement of the electrodes limits the spatial resolution of the stimulation. However, focused stimulation with continuous films is possible only with materials having low carrier mobility and lifetime, such as conjugated polymers³⁶⁹. A similar continuous approach is now proposed with other materials like TiO₂ nanotubes³⁷⁰ and Au-TiO₂ nanowires⁴³⁰. However, while continuous films are interesting for small implants, they become more challenging for wide-field implants aiming at restoring a large visual angle. Inorganic materials might not be easily fabricated on conformable materials since they often require high-temperature processes. Polymers can be deposited on a large area, but they would immediately crack and eventually delaminate once stretched over a spherical surface. Therefore, pixels must be fabricated and protected to preserve the mechanical integrity of the polymers. The microscale patterning of conjugated polymers is an essential element to fabricate a high-density wide-field organic photovoltaic prosthesis: it allows the high-density POLYRETINA to embed 10,498 physically and electrically independent pixels with a 120- μm pitch. The device's mechanical integrity is preserved thanks to the SU-8 platforms, the patterning of the conjugated polymers and the TiN coating, which reduces the tensile stress on the pixels. The device's mechanical compliance allows the bonding of the high-density array over a large and soft hemispherical dome to maintain close contact between the pixels and the retinal tissue over the central and peripheral retina. The TiN coating enhances the stimulation efficiency, improves the mechanical stability and eases the fabrication process. Such pixels can be independently activated with a focused light pattern; the photovoltage generated largely remains localised within the pixel lateral boundaries, even at high irradiance levels, thus ensuring the absence of electrical cross-talk between the pixels.

The POLYRETINA interface delivers a capacitive-like photovoltage optimal for network-mediated activation of the RGCs from the epiretinal¹⁴⁰, provided that long (*e.g.* 10-ms) light pulses are used. The increase in the pixels' number and density resulted into epiretinal network-mediated stimulation with high spatial resolution. In this study, we demonstrated a response resolution of the POLYRETINA device equivalent to at least its pixel pitch (120 μm), using both a two-point discrimination test and a grating pattern reversal paradigm. Such resolution would theoretical corresponds to a visual acuity of 20/480¹⁹³, what places POLYRETINA in the upper intermediate level close to the PRIMA and Alpha-AMS devices: a borderline resolution range for faces and emotions recognition⁴⁴⁷. Nevertheless, such a form of artificial vision may be valuable for a more reliable obstacle recognition and ambulation^{280,448}. The primary difference between POLYRETINA and the aforementioned implants is its large visual angle, which impacts both the perceived visual field and the visual space scanning strategies. The combination of visual acuity and visual angle is recognised as a crucial need to map and interact with one's environment, having consequences on the layout space understanding, walking distance evaluation, identify-and-reach tasks, spatial cognition, and attention^{449,450}. Our study was conducted with degenerated mouse retinas. Compared to the human one, the mouse retina's peculiarity is to have RGCs with large and relatively homogeneous RFs despite their eccentricities. The RGC's topography is organised in a dorsoventral axis, without any region devoted to high visual acuity^{79,451}. In the perspective of clinical applications, it should be noted that the RGCs' dendritic fields in the human fovea are substantially smaller: 5 to 12 μm for midget cells and 30 to 40 μm for parasol cells^{84,452}. The pixel pitch would thus determine the theoretical resolution limit in the fovea and parafovea. However, in humans, the size of RFs and the arborisation of both midget and parasol cells increases with eccentricity^{84,452,453}. POLYRETINA covers 43 degrees, about 11 to 13 % of the retinal surface^{454,455}, *i.e.* the fovea, the parafovea, the perifovea, and up to 6-7 mm away from the fovea in the mid-peripheral retina. The dendritic tree varies between 150 and 270 μm for parasol cells and between 25 and 70 μm for midget cells in the perifovea. In the mid-peripheral retina, it varies between 175 and 310 μm for parasol cells and between 50 and 120 μm for midget cells⁴⁵². Outside of the fovea, both cell types have RF diameters equal to or larger than the pixel pitch in POLYRETINA. Based on our results in mice retinas, nearly 40 % of the human RGCs, mostly parafoveal and mid-peripheral parasol cells but also mid-peripheral midget cells, could be stimulated with a resolution higher than their physiological RFs.

The legal definition of blindness in the United States of America and most European countries does not only take into account the foveal acuity (worse than 20/200) but also the visual angle (smaller than 20 degrees), because of its critical role in the naturalistic perception of complex scenes, movements and objects. Indeed, self-orienting task and free mobility in a moving environment require the rapid detection of movements and luminance changes from the entire visual field. The restoration of a large visual field with appropriate resolution represents a leap forward for artificial vision. However, some steps are still required before considering POLYRETINA for a clinical trial. One open question is the distortion of phosphenes experienced by patients during epiretinal

stimulation because of the direct activation of the axons of passage, which might have a negative impact on the perceived resolution. Previous results in patients implanted with the Argus® II device showed that phosphene's distortion could be reduced if not avoided by lengthening duration of the stimulation pulse²³⁷. Results in explanted retinas^{337,386,440} and computational models⁴⁴⁰ suggested that the implementation of both long pulses and non-rectangular waveform (as it is the case for POLYRETINA) allows a preferential activation of RGCs via the network-mediated mechanism. Despite the direct activation of RGCs cannot be totally avoided, the probability to elicit short-latency direct spikes upon POLYRETINA stimulation was previously evaluated to be about 20 % per light pulse³⁶⁹, what corresponds to 0.2 spikes per light pulse: a very low spike rate, about 25 times lower than network-mediated ML spikes (about 5 spikes per pulse). It still remains unclear if those low probability short-latency direct spikes would be meaningful for the patients from a perceptual standpoint. Only human trials could provide an answer to this question.

Another limit of photovoltaic retinal prostheses based on conjugated polymers is the use of semiconducting materials absorbing light in the visible spectrum (e.g. P3HT). Visible light for prosthetic activation is not optimal due to the possible activation of remaining photoreceptors in patients with some residual vision. Moreover, the high irradiance levels required to activate POLYRETINA might be perceived even in blind patients without residual vision. Novel conjugated polymers with shifted sensitivity in the far-red and near-infrared could be exploited to overcome this problem^{456,457}. Recent results reported the possibility to use a red-shifted polymer in neural interfaces⁴⁵⁸ and retinal prostheses⁴⁵⁹.

A third limit is set by the constraints imposed by the maximal irradiance, such as the maximal illumination rate. So far, *Retinitis Pigmentosa* patients implanted with retinal prostheses preferred low stimulation rates (e.g. 5-10 Hz)^{183,201,460}, which are within the safety limits for POLYRETINA. However, higher stimulation rates might be desirable to avoid flickering and achieve flicker fusion (i.e. above 30 Hz), as shown in a study with implanted patients affected by age-related macular degeneration⁴³⁸. It is unclear at this stage, which is the optimal stimulation frequency for a device like POLYRETINA : psychophysical studies will be required to characterise it. In order to achieve higher illumination rates, the thermal impact should be minimised: both near-infrared sensitive polymers and beam compensation strategies might be helpful. A reduction in the visual angle could also contribute to reduce the thermal impact. Although a wide-visual angle (i.e. above 30 degrees) is highly desirable in profoundly and totally blind patients, only psychophysical tests can determine the exact minimum angle required. POLYRETINA covers 43 degrees, but a reduction to 35 degrees will increase the maximal irradiance at the iris plane by 50 %. Last, POLYRETINA's safety and efficacy should be validated in preclinical trials *in-vivo*.

4.5 Methods

4.5.1 Mechanical simulations

Finite element analysis simulations were performed in Abaqus/CAE 6.14, using a three-dimensional deformable shell (photovoltaic interface) moving against a static spherical solid (hemispherical dome) to create a full hard contact. The edges of the shell were clamped to move only in the vertical direction toward the solid dome. The surface roughness and intrinsic thin-film stresses arising from deposition techniques were not considered in the simulation. The shell was constructed using the parameters listed in **Table 1**.

Material	Young's modulus (MPa)	Poisson's ratio	Density (kg m ⁻³)
PDMS (Neo-Hookean)	C ₁₀ =0.662, D ₁ =0.255	0.5	970
SU-8	2,920	0.22	-
PEDOT:PSS	1,900	0.34	-
P3HT:PC ₆₀ BM	1,970	0.35	-
Ti	90,000	0.34	-
TiN	220,000	0.25	-

Ch.4 Table 1 – Mechanical simulations.

List of parameters used for the construction of the deformable shell. Apart from PDMS, the behaviours of the other materials were considered isotropic elastic. PDMS: polydimethylsiloxane; PEDOT: poly(3,4-ethylenedioxythiophene); PSS: poly(styrenesulfonate); P3HT: regioregular poly(3-hexylthiophene-2,5-diyl); PC₆₀BM: [6,6]-phenyl-C₆₁-butyric acid methyl ester; Ti: titanium; TiN: titanium nitride. The values for the Young's modulus and Poisson's ratio of the used materials and the hyperelastic coefficients for PDMS were taken from the following references^{461–467}.

4.5.2 Thermal model

COMSOL Multiphysics 5.3 was used with the Bioheat module and the General PDE module for the heat transfer and Beer-Lambert light propagation. A uniform beam with a diameter of 2 mm (565 nm) was used as the illumination source. The eye model was built with several spheres representing each component (cornea, aqueous humour, lens, iris anterior border layer, iris stroma, iris pigmented epithelium, vitreous humour, retina, retinal pigmented epithelium, choroid, and sclera). The iris was simulated as a continuous film completely covering the pupil, while the light beam was projected on the iris, centred to the pupil location. All the parameters used in the model are listed in **Table 2**.

Material	Thickness	Heat Capacity	Thermal Conductivity	Density	Absorption (565 nm)	Perfusion rate	Self-Heat
	μm	J kg ⁻¹ K ⁻¹	W m ⁻¹ K ⁻¹	Kg m ⁻³	m ⁻¹	s ⁻¹	W m ⁻³
Aqueous humour	3100	3997	0.58	1000	0.025	0	0
Choroid	430	3840	0.53	1050	15000	0.0091	10000
Cornea	500	4178	0.58	1050	51	0	0
Lens	3600	3000	0.4	1050	2.5	0	0
Retina	100	3680	0.565	1000	400	0	0
Retinal pigment epithelium	10	4178	0.603	1050	110000	0	0
Sclera	500	4178	0.58	1000	590	0	0
Vitreous humour	/	3997	0.6	1000	0.025	0	0
Iris anterior border layer	50	4178	0.58	1050	5470	0	0
Iris stroma	400	3840	0.53	1050	2750	0.0091	10000
Iris pigment epithelium	70	4178	0.603	1050	100000	0	0

Ch.4 Table 2 – Eye parameters used for the eye model

The parameters were obtained from references^{354–356,358–361}. The heat capacity, thermal conductivity, density, perfusion rate and self-heat of the iris anterior border layer, stroma, and pigment epithelium were taken respectively from the cornea, choroid and retinal pigment epithelium, due to their biological similarity.

4.5.3 Chips micro-fabrication

Samples were fabricated on 20 x 24 mm² glass substrates (2947-75X50, Corning Incorporated) cleaned by ultrasonication in acetone, isopropyl alcohol, and deionised water for 15 min each and then dried with a nitrogen gun. PEDOT:PSS (PH1000, Clevis Heraeus) was mixed to 0.1 v/v% (3-glycidyloxypropyl)trimethoxysilane (440167, Sigma Aldrich), filtered (1 μm PTFE filters), and then spin-coated at 3000 rpm for 40 seconds on each chip. Subsequent annealing at 115 °C for 30 minutes was performed. The preparation

of the bulk heterojunction was performed in a glove box under nitrogen atmosphere. 20 mg of P3HT (M1011, Ossila) and 20 mg of PC₆₀BM (M111, Ossila) were dissolved in 1 mL of anhydrous chlorobenzene each and let stirring overnight (16 hr) at 70 °C. The solutions were then filtered (0.45 µm PTFE filters) and blended (1:1 v:v). The P3HT:PC₆₀BM blend was spin-coated at 1000 rpm for 45 seconds. Subsequent annealing at 115 °C for 30 min was performed. Titanium and titanium nitride cathodes were deposited by direct-current (Ti) and radio frequency (TiN) magnetron sputtering using a shadow mask. The polymer patterning step was obtained by exposing the chips to oxygen plasma. A plastic reservoir was then attached to the sample using PDMS as an adhesive.

4.5.4 Measure of photo-voltage and photo-current

Samples were placed on a holder, and each electrode was sequentially contacted. A platinum wire immersed in physiological saline solution (NaCl 0.9 %) was used as a counter electrode. 10-ms light pulses were delivered by a 565-nm LED (M565L3, Thorlabs) focused at the sample level. Photo-voltage and photo-current were measured using respectively a voltage amplifier (1201, band DC-3000 Hz, DL-Instruments) and a current amplifier (1212, DL-Instruments). Data sampling (40 kHz) and instrument synchronisation were obtained via a DAQ board (PCIe-6321, National Instruments) and custom-made software. Data analysis was performed in MATLAB (MathWorks). When evaluating the photo-current density generated by the interface, the area of the connecting line exposed to light was also considered.

4.5.5 POLYRETINA micro-fabrication

Photovoltaic interfaces were fabricated on silicon wafers. A thin sacrificial layer of poly(4-styrenesulfonic acid) solution (561223, Sigma-Aldrich) was spin-coated on the wafers (1500 rpm, 40 s) and baked (120 °C, 15 min). Degassed PDMS pre-polymer (10:1 ratio base-to-curing agent, Sylgard 184, Dow-Corning) was then spin-coated (1000 rpm, 60 s) and cured in the oven (80 °C, 2 hr). After surface treatment with oxygen plasma (30 W, 30 s), a 6-µm thick SU-8 (GM1060, Gersteltec) layer was spin-coated (3800 rpm, 45 s), soft-baked (130 °C, 300 s), exposed (140 mJ cm⁻², 365 nm), post-baked (90 °C, 1800 s; 60 °C, 2700 s), developed in propylene glycol monomethyl ether acetate (48443, Sigma-Aldrich) for 2 min, rinsed in isopropyl alcohol and dried with nitrogen. After surface treatment with oxygen plasma (30 W, 30 s), a second layer of degassed PDMS pre-polymer (10:1) was spin-coated (3700 rpm, 60 s) and cured in the oven (80 °C, 2 hr). PEDOT:PSS and P3HT:PC₆₀BM were prepared and deposited as described before. Titanium and titanium nitride cathodes were deposited by direct-current (Ti) and radio frequency (TiN) magnetron sputtering using a shadow mask aligned with the SU-8 pattern. After the patterning of polymers by oxygen plasma, the encapsulation layer of degassed PDMS pre-polymer (5:1 ratio) was spin-coated (4000 rpm, 60 s) and cured in the oven (80 °C, 2 hr). Photolithography and PDMS dry etching were performed to expose the cathodes. The wafers were then placed in deionised water to allow for the dissolution of the sacrificial layer and the release of the photovoltaic interfaces. The floating membranes were finally collected and dried in air. The hemispherical PDMS domes were fabricated using a milled PMMA mould, filled with PDMS pre-polymer (10:1), which was then degassed and cured in the oven (80 °C, 2 hr). The supports were released from the moulding parts and perforated with a hole-puncher (330-µm in diameter) at the locations dedicated to the insertion of retinal tacks. The released photovoltaic interfaces were clamped between two O-rings and, together with the hemispherical domes, were exposed to oxygen plasma (30 W, 30 s). The activated PDMS surfaces were put in contact and allowed to uniformly bond thanks to radial stretching of the fixed membrane. The excessive PDMS used to clamp the array was removed by laser cutting.

4.5.6 Atomic force microscopy

AFM images and roughness measurements were obtained with a Bruker Dimension icon microscope and scanasyst-air Si tips. Images (500 nm x 500 nm) were plotted and the surface area was calculated with NanoScope analysis 1.9 software.

4.5.7 Kelvin Probe Force Microscopy

KPFM characterisation was performed in ambient air conditions with a dimension icon atomic force microscope (Bruker Corporation) using n-doped silicon tips (SCM-PIT-V2, Bruker Corporation) in surface potential, amplitude-modulated imaging mode. KPFM images were collected by repetitively scanning a single 100-nm line under dark and light conditions to measure the surface potential variation. The green LED of a Spectra X illumination system (Emission filter 560/32, Lumencor) was used to illuminate the pixel using an optical fiber and focused onto the pixel (Photo-Conductive accessory, Bruker Corporation). The samples were grounded using a silver paste; however, individual pixels could not be connected to the paste and were therefore floating. The voltage bias was sent to the AFM tip. KPFM images were analysed using Gwyddion 2.36 software. For each image, the average surface potential variation value was obtained by subtracting the surface potential in the dark to the one under illumination (voltage in light – voltage in dark).

4.5.8 Spatial selectivity measures

Measures of the voltage spread were performed in Ames' medium (A1420, Sigma-Aldrich) at 32 °C with a glass micropipette (tip diameter about 10 µm) located approximately 2-5 µm from the implant surface. Data were amplified (Model 3000, A-M System), filtered (DC – 1,000 Hz), and digitalised at 30 kHz (Micro1401-3, CED Ltd.). Illumination was carried out on a Nikon Ti-E inverted microscope (Nikon Instruments) using a Spectra X illumination system (Emission filter 560/32, Lumencor). The microscope was equipped with a dichroic filter (FF875-Di01-25x36, Semrock) and a 10x (CFI Plan Apochromat Lambda) objective. The patterning of the light stimulus was carried out using a light patterning system (Polygon 400, Mightex). The light pattern sequences were adjusted in real-time to align the light patterns to the prosthesis pixels (PolyScan, Mightex). After alignment of the illumination pattern onto the POLYRETINA pixels, 10 pulses of 10 ms were delivered at 1 Hz with an irradiance of 22.65 mW mm⁻². Data analysis was conducted in MATLAB. Voltage peaks above noise level were detected, and their amplitude normalised respect to the central pixel value.

4.5.9 Electrophysiology

Animal experiments were conducted according to the animal authorizations GE3717 issued by the Département de l'Emploi, des Affaires sociales et de la Santé (DEAS), Direction Générale de la Santé of the République et Canton de Genève (Switzerland). Both male and female *Rd10* mice were used (Table 3). Mice were kept in a 12 h day/night cycle with access to food and water ad libitum. White light (300 ± 50 lux) was present from 7 AM to 7 PM and red light (650-720 nm, 80-100 lux) from 7 PM to 7 AM.

Ti vs TIN comparison Figure 4b-f			TIN irradiance threshold Figure 4g,h		Photovoltaic RF Figure 5		Pixel switch Figure 6		Pattern reversal Figures 7, 8		Contrast sensitivity Figure 9	
Sex	Age	Material	Sex	Age	Sex	Age	Sex	Age	Sex	Age	Sex	Age
male	133	Ti	male	115	female	137	male	108	male	122	male	133
male	141	Ti	male	123	male	117	male	130	male	103	male	131
male	108	Ti	female	127	male	119	male	108	male	132		
female	116	Ti	female	134	male	148	male	108	male	136		
female	114	Ti	Pharmacology		male	123			male	152		
male	117	Ti	Figure 4g,h,i,j		female	127						
male	142	Ti	male	115	female	134						
male	146	Ti	male	107	male	135						
male	148	Ti	male	108	male	138						
female	142	TiN	female	147	male	139						
male	108	TiN	female	143								
female	96	TiN										
male	119	TiN										
male	146	TiN										
male	148	TiN										

Ch.4 Table 3 - Animal groups

Sex and age of the *Rd10* mice used in the study.

Retinas from inbred *Rd10* mice colony were explanted in normal light conditions after the animals were sacrificed by injection of Sodium Pentobarbital (150 mg kg⁻¹). After eye enucleation, retinas were dissected in carboxygenated (95 % O₂ and 5 % CO₂) Ames' medium (A1420, Sigma-Aldrich) and transferred to the microscope stage for stimulation and recording. Retinas were placed with the retinal ganglion cells facing down on the prosthesis. Recordings were performed in dim light at 32 °C with a sharp metal electrode (PTM23B05KT, World Precision Instruments), amplified (Model 3000, A-M System), filtered (300-3000 Hz), and digitalized at 30 kHz (Micro1401-3, CED Ltd.). Illumination was carried out on a Nikon Ti-E inverted microscope (Nikon Instruments) using a Spectra X illumination system (Emission filter 560/32, Lumencor). The microscope was equipped with a dichroic filter (FF875-Di01-25x36, Semrock) and a 10x (CFI Plan Apochromat Lambda) objective. The patterning of the light stimulus was carried out using a light patterning system (Polygon 400, Mightex). The light pattern sequences were real-time adjusted to align the light patterns to the prosthesis pixels (PolyScan, Mightex). After alignment of the illumination pattern onto the POLYRETINA pixels, for each retinal ganglion cell, 10 pulses of 10 ms were delivered at 1 Hz for each illumination condition. Spike detection and sorting were performed by threshold detection using the Matlab-based algorithm Wave_clus³⁵² and further data processed in MATLAB. An exclusion period of ± 1 ms around light onset and offset was applied to avoid artefact misclassification. The time window for the quantification of the network-mediated medium-latency response was selected according to previous results with the POLYRETINA device, which evokes a 30 to 50-ms long network-mediated medium-latency response^{369,440,445}. For each stimulation pulse, the network-mediated medium-latency response was calculated as the average firing rate elicited in a 50-ms window around the highest bin of the peri-stimulus time histogram (5 bins of 10 ms each). The highest bin was screened from 40 to 120 ms after the stimulus onset.

4.5.10 Optical safety

Retinal damage upon light exposure can occur because of three main factors: photo-thermal damage, photo-chemical damage, and thermo-acoustic damage²⁹¹. In ophthalmic devices, Maxwellian illumination is used where the incident illumination occupies a fraction of the pupil (no overfilling). For continuous illumination, the MPE could be controlled by the photo-thermal (MPE_T) or photo-chemical damage (MPE_C), calculated in W according to **Equations 1** and **2**, respectively.

$$MPE_T = 6.93 \cdot 10^{-5} C_E C_T \frac{1}{P}$$

Ch.4 Equation 1

$$MPE_C = 5.56 \cdot 10^{-10} C_B \alpha^2$$

Ch.4 Equation 2

For POLYRETINA, the visual angle α is calculated according to **Equation 3**, and the exposed area according to **Equation 4**, in which $d = 13.4$ mm is the diameter covered by the active area and $f = 17$ mm is the eye's focal length.

$$\alpha = 2 \tan^{-1} \frac{d}{2f} = 750.85 \text{ mrad}$$

Ch.4 Equation 3

$$A \approx \frac{\pi}{4} (\alpha f)^2 = 127.97 \text{ mm}^2$$

Ch.4 Equation 4

For $\lambda = 565$ nm, both limits apply and $C_E = 6.67 \cdot 10^{-3} \alpha^2$; $C_T = 1$; $P = 5.44$; $C_B = 10^{0.02(\lambda-450)}$. The limits are $MPE_T = 47.90$ mW and $MPE_C = 62.54$ mW. Therefore, the limiting factor is MPE_T which results in 47.90 mW entering the pupil, and corresponds to 374.3 $\mu\text{W mm}^{-2}$ for an exposed area of 127.97 mm^2 . However, POLYRETINA operates with pulsed illumination. With pulses of 10 ms and duty cycle of 20, 10, or 5 % (respectively for 20, 10, or 5 Hz), the MPE is increased to 1.87, 3.74, or 7.48 mW mm^{-2} respectively⁴⁵⁹. In addition, a previous thermal model showed that at 565 nm and over the broad range of irradiance levels the temperature increase in the retina is reduced by 11 % with POLYRETINA³⁶⁹. Therefore, the MPE could be increased to 2.08, 4.16, or 8.32 mW mm^{-2} respectively for 20, 10, or 5 Hz.

4.5.11 Statistical analysis and graphical representation

Statistical analysis and graphical representation were performed with Prism (GraphPad Software Inc.) and MATLAB. The normality test (D'Agostino & Pearson omnibus normality test) was performed in each dataset to justify the use of a parametric or non-parametric test. In each figure p-values were represented as: * $p < 0.05$, ** $p < 0.01$, *** $p < 0.001$, and **** $p < 0.0001$.

4.6 Acknowledgment

We would like to acknowledge the Center of Micronanotechnology at École polytechnique fédérale de Lausanne and The Neural Microsystems Platform at the Wyss Center for Bio and Neuroengineering for their support. We would like to acknowledge Jacob Thorn (at École polytechnique fédérale de Lausanne) for English editing. This work was supported by École polytechnique fédérale de Lausanne, Medtronic, Fondation Pierre Mercier pour la Science, Velux Stiftung (Project 1102), Fondation Pro Visu and Gebert R uf Stiftung (Project GRS-035/17).

Chapter 5 Naturalistic spatiotemporal modulation of epiretinal stimulation increases the response persistence of retinal ganglion cell

Postprint version of the article published in Journal of Neural Engineering, 2020 (DOI: 10.1088/1741-2552/abcd6f)

Authors: Naïg A. L. Chenais^a, Marta J. I. Airaghi Leccardi^a, and Diego Ghezzi^a.

^a Medtronic Chair in Neuroengineering, Center for Neuroprosthetics, Institute of Bioengineering, School of Engineering, École Polytechnique Fédérale de Lausanne, Switzerland

Authors contribution: N.A.L.C performed the experiments, analysed data and wrote the manuscript. M.J.I.A.L. fabricated the prosthesis. D.G. designed and led the study, and wrote the manuscript. All the authors read and accepted the manuscript.

5.1 Abstract

Retinal stimulation in blind patients evokes the sensation of discrete points of light called phosphenes, which allows them to perform visually guided tasks, such as orientation, navigation, object recognition, object manipulation and reading. However, the clinical benefit of artificial vision in profoundly blind patients is still tenuous, as several engineering and biophysical obstacles keep it far away from natural perception. The relative preservation of the inner retinal neurons in hereditary degenerative retinal diseases, such as *Retinitis Pigmentosa*, supports artificial vision through the network-mediated stimulation of retinal ganglion cells. However, the response of retinal ganglion cells to repeated electrical stimulation rapidly declines, primarily because of the intrinsic desensitisation of their excitatory network. In patients, upon repetitive stimulation, phosphenes fade out in less than half of a second, which drastically limits the understanding of the percept.

A more naturalistic stimulation strategy, based on spatiotemporal modulation of electric pulses, could overcome the desensitisation of retinal ganglion cells. To investigate this hypothesis, we performed network-mediated epiretinal stimulations paired to electrophysiological recordings in retinas explanted from both male and female *Retinal degeneration* 10 mice.

The results showed that the spatial and temporal modulation of the network-mediated epiretinal stimulation prolonged the persistence of the retinal ganglion cell's response from 400 ms up to 4.2 s.

A time-varied, non-stationary and interrupted stimulation of the retinal network, mimicking involuntary microsaccades, might reduce the fading of the visual percept and improve the clinical efficacy of retinal implants.

5.2 Introduction

The first notion of electrically-evoked visual percept came in 1755 when Charles Le Roy's patient had reported seeing flashes of light while receiving an electric current across the head⁴⁶⁸. Almost three centuries later, three retinal stimulation systems (Argus® II, Second Sight Medical Products Inc; Alpha-IMS and Alpha-AMS, Retinal Implant AG) received marketing approval in Europe or in the United States of America for *Retinitis Pigmentosa*, a set of inherited retinal dystrophies, causing the progressive loss of retinal photoreceptors, the constriction of the visual field and eventually blindness¹⁹.

The relative preservation of the inner retinal neurons in *Retinitis Pigmentosa*^{20,68,469} supports artificial vision through the network-mediated stimulation of retinal ganglion cells (RGCs) either from the subretinal or the epiretinal side^{470,337}. In epiretinal stimulation, RGCs can be stimulated either through direct activation of their axons and somas^{235,471,472} or through network-mediated stimulation of their presynaptic neurons^{337,473}. The latter strategy offers two advantages: it avoids the uncontrolled activation of distal axons leading to streak-like elongated phosphenes^{237,440} and it provides spiking patterns resembling the natural response to visual stimuli^{383,470}. However, the rapid desensitisation of the RGC response under repeated indirect stimulation is a significant limitation of this approach, as it is assumed to be the principal neural correlate of the image fading in artificial vision^{253,269,474–477}.

In animal models, the response of RGCs to network-mediated electrical stimulation rapidly decreases with repeated pulsed stimulation^{252,253}. This decrease is likely caused by the intrinsic desensitisation of bipolar cells (BCs)²⁵¹, although an active contribution from the inhibitory network also has to be considered^{251,253}. Moreover, the reduction of responsivity in RGCs might be associated with the phosphene fading reported by implanted patients during the clinical trials of the Argus® II and the Alpha-IMS retinal prostheses^{183,186,283}. The RGC response reduction is characterised by a rapid decay immediately after the first electric stimulus, followed by a slower response decay lasting up to several seconds for prolonged stimulation. This time course remarkably matches the two-phase decay in phosphene brightness reported by implanted patients under stationary vision^{253,268,478}. In artificial vision, the sensory adaptation observed at the perceptual level in patients might be caused by several mechanisms all throughout the visual process, as in natural vision⁴⁷⁹. At the retina level, two mechanisms lead to adaptation in RGCs: the intrinsic desensitisation of sodium channels in the RGC membrane⁴⁸⁰ and the activation of the excitatory-inhibitory presynaptic microcircuit²⁵³. During higher visual processes other adjustments (e.g. dynamic altering of the tuning of the primary visual cortex and the middle temporal area neurons or more complex after-effects) are likely to occur during artificial stimulation of the retina^{479,481}. Due to the stationary nature of most retinal stimulation systems and the matching timescales of RGC desensitisation and phosphenes fading, it is assumed that the early synaptic adaptation stages are predominant in artificial vision^{253,269,474–477}.

During visual stimulation of the retina, static images cannot generate continuous firing of RGCs either. However, in sighted humans, a variety of ocular micromovements refresh the image: drifts and microsaccades cause frequent changes in the retinal image allowing to counteract the fading of the neural response^{482,483}. Microsaccades particularly are thought to be crucial in this process^{484,258,485}. Similarly, we hypothesised that in retinal prostheses, a temporal and spatial modulation of the electric pulses might counteract the desensitisation process at the microcircuit level. Electric stimuli with randomised inter-pulse intervals elicited in-vivo electrically evoked potentials stronger than regularly spaced pulses⁴⁸⁶, suggesting the ability of temporal modulation to reduce the fading process. Additionally, in a study with high-density epiretinal network-mediated stimulation, we showed that alternating the stimulation among two neighbouring pixels allowed for the recovery of the RGC response at the pixel switch⁴⁸⁷. This result suggests that a RGC could be activated successively but independently through a different portions of its inner retinal network. This last property offers excellent potential to mimic the effect of microsaccades artificially, and it indicates the use of spatial modulation to reduce the fading process. Therefore, we investigated whether a more naturalistic stimulation with spatiotemporal modulations, including time-varied, non-stationary and interrupted features could increase the persistence of the prosthetic responses at the RGC level.

5.3 Materials and methods

5.3.1 POLYRETINA micro-fabrication

Photovoltaic interfaces were fabricated on silicon wafers. A thin sacrificial layer of poly(4-styrenesulfonic acid) solution (561223, Sigma-Aldrich) was spin-coated on the wafers (1500 rpm, 40 s) and baked (135 °C, 10 min). Degassed PDMS pre-polymer (10:1 ratio base-to-curing agent, Sylgard 184, Dow-Corning) was then spin-coated (500 rpm, 60 s) and cured in the oven (80 °C, 2 hr). PEDOT:PSS (PH1000, Clevis Heraeus) was mixed to 0.1 v/v% (3-glycidyoxypropyl)trimethoxysilane (440167, Sigma Aldrich), ultrasonicated for 20 min, filtered (0.2 µm PES filters), and then spin-coated at 3000 rpm for 40 seconds. Subsequent annealing at 115 °C for 30 min was performed. The preparation of the bulk heterojunction was performed in a glove box under nitrogen atmosphere. 20 mg of P3HT (M1011, Ossila) and 20 mg of PC₆₀BM (M111, Ossila) were dissolved in 1 mL of anhydrous chlorobenzene each and let stirring overnight (16 hr) at 70 °C. The solutions were then filtered (0.45 µm PTFE filters) and blended (1:1 v:v). The P3HT:PC₆₀BM blend was spin-coated at 1000 rpm for 45 seconds. Subsequent annealing at 115 °C for 30 min was performed. Titanium and titanium nitride were deposited respectively by direct-current and radio frequency magnetron sputtering using a shadow mask. Polymers were patterned by oxygen plasma. The wafers were then placed in deionised water to allow for the dissolution of the sacrificial layer and the release of the photovoltaic interfaces. The floating membranes were finally collected and dried in air.

5.3.2 Preparation of retinal explants

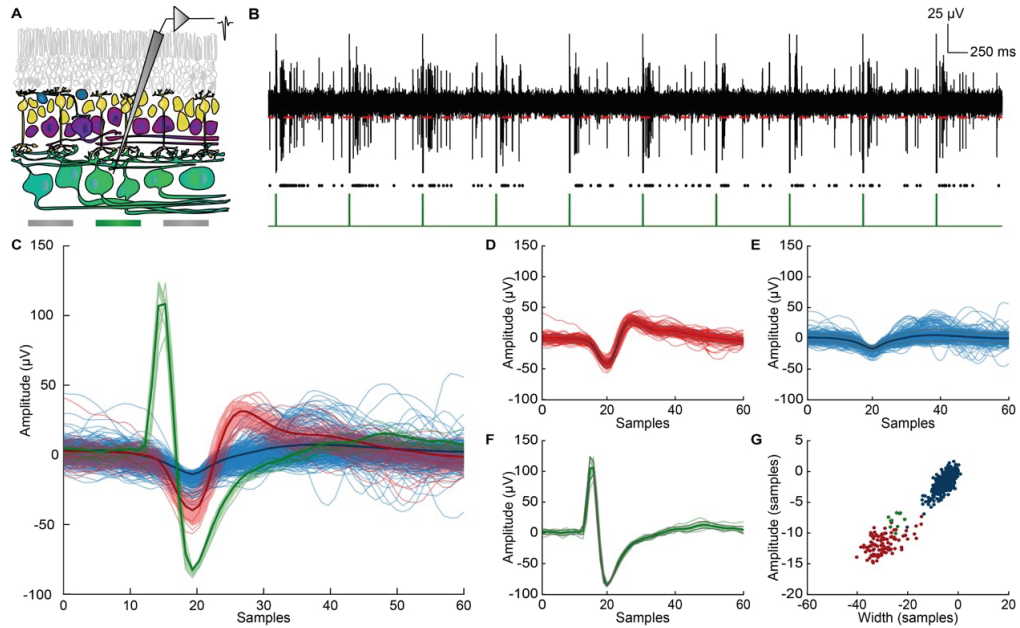
Animal experiments were conducted according to the animal authorisation GE3717 issued by the Département de l'Emploi, des Affaires sociales et de la Santé (DEAS), Direction Générale de la Santé of the République et Canton de Genève (Switzerland). *Retinal degeneration 10 (Rd10)* mice (aged 121.5 ± 13.8 days; mean \pm s.d.) were sacrificed under normal light conditions by injection of sodium pentobarbital (150 mg/kg), and eyes were immediately collected and dissected in carboxygenated (95 % O₂ and 5 % CO₂) Ames' medium (A1420, Sigma-Aldrich). Whole-mount retinas were placed ganglion cell down onto the stimulation pixels and transferred to the microscope stage for stimulation and recording. During the entire preparation and recording procedures, the retinas were maintained under dim red light and perfused with carboxygenated Ames' medium at 32 °C.

5.3.3 Electrophysiological recordings

Extracellular recordings (**Figure 1A**) were performed with a sharp metal electrode (PTM23B05KT, WPI), amplified (Model 3000, A-M System), filtered (300-3,000 Hz) and digitalized at 30 kHz (Micro1401-3, CED). RGCs were identified by their spontaneous spiking activity. Spike detection and spike sorting were performed offline by threshold detection using `wave_clus` algorithm (**Figure 1B,C**)³⁵². Should multiple units be recorded, the single unit with the highest signal to noise ratio was selected for further analysis. Out of the 73 cells recorded, 52 cells (71 %) resulted in only two clusters (one single-unit cell and the electric artefact), while only 21 cells (29 %) resulted in three clusters (two single-unit cells and the electric artefact). In the latter case, only the single-unit with the highest signal to noise ratio was selected for further analysis (**Figure 1D-G**). Data processing was performed in MATLAB (MathWorks).

5.3.4 Retina stimulation

Retinal explants were stimulated with the POLYRETINA photovoltaic interface. 80-µm photovoltaic pixels separated by a 120-µm pitch were individually illuminated from a Nikon Ti-E inverted microscope (Nikon Instruments) using a Spectra X illumination system (Emission filter 560/32, Lumencor). The microscope was equipped with a dichroic filter (FF875-Di01-25x36, Semrock) and a 10x (CFI Plan Apochromat Lambda) objective. The timing, spatial patterning and alternation of the light stimuli were carried out with a light patterning system (Polygon 400, Mightex). Each light pattern was aligned to the pixels in real-time. Green light (560-nm) was projected with a 0.9 mW/mm² irradiance for all the stimuli. According to our previous results with single-pixel stimulation⁴⁸⁷, 10-ms 0.9 mW/mm² pulses induce a robust activation of RGCs. Each pixel of the POLYRETINA prosthesis delivers, upon pulsed illumination, a capacitive stimulation characterised by a monophasic cathodic non-rectangular voltage pulse⁴⁴⁰.


Ch.5 Figure 1 - Detection and sorting of RGC network-mediated activity

A, Sketch of the stimulation and recording set-up. A single pixel (in green) of the POLYRETINA device was illuminated with 10-ms pulses (560 nm, 0.9 mW/mm²). Solid and empty cells represent respectively preserved (RGCs, ACs, BPs and horizontal cells) and degenerated (photoreceptors) cells in the *Rd10* mice model. **B**, Representative recordings of a RGC response to single-pixel illumination at 1 Hz for 10 s. The photovoltaic light pulses are shown in green. The red dotted line indicates the threshold for spike detection. The raster plot shows the identified spikes after spike sorting. **C**, Spike waveforms clustering from the recording shown in **A**. The bold lines represent the average waveform of each cluster. **D-F**, Panels shows the waveforms for the selected unit (**D**), the discarded unit (**E**) and the artefacts (**F**). The bold lines represent the average waveform of each cluster and the grey lines their standard deviation. **G**, Characteristics of the clusters identified from **A**. recording. The artefact waveforms are shown in green, the waveforms from the selected unit in red, and the waveforms from the discarded unit in blue.

5.3.5 Experimental Design and statistical analyses

The experimental design is shown in **Table 1**. Statistical analysis and graphical representation were performed in MATLAB. For each stimulation pulse, the network-mediated medium-latency (ML) response was calculated as the average firing rate elicited in a ± 20 -ms window around the highest bin of the peri-stimulus time histogram (PSTH). The highest bin was screened for from 40 to 120 ms after the stimulus onset. The time windows for the quantification of the network-mediated ML response were selected based on our previous results with the POLYRETINA device, which evokes a 30 to 50-ms long network-mediated ML response with a latency of approximately 65 ms⁴⁴⁰. The D'Agostino & Pearson omnibus normality test was performed to justify the use of a parametric or non-parametric test. The Tukey's honestly significant difference post-hoc test was used to verify the use of multiple comparison tests.

Experimental group	Number of animals	Number of RGCs	Post-natal days (mean \pm s.d.)	Females / Males	Stimulation protocols
A	4	16	121.7 \pm 10.6	2/2	Figure 2 and Figure 3
B	3	22	113.0 \pm 8.7	0/3	Figure 4
C	3	12	115.3 \pm 12.7	0/4	Figure 5 and Figure 6
D	4	23	132.2 \pm 17.1	2/2	Figures 7, 8 and 9

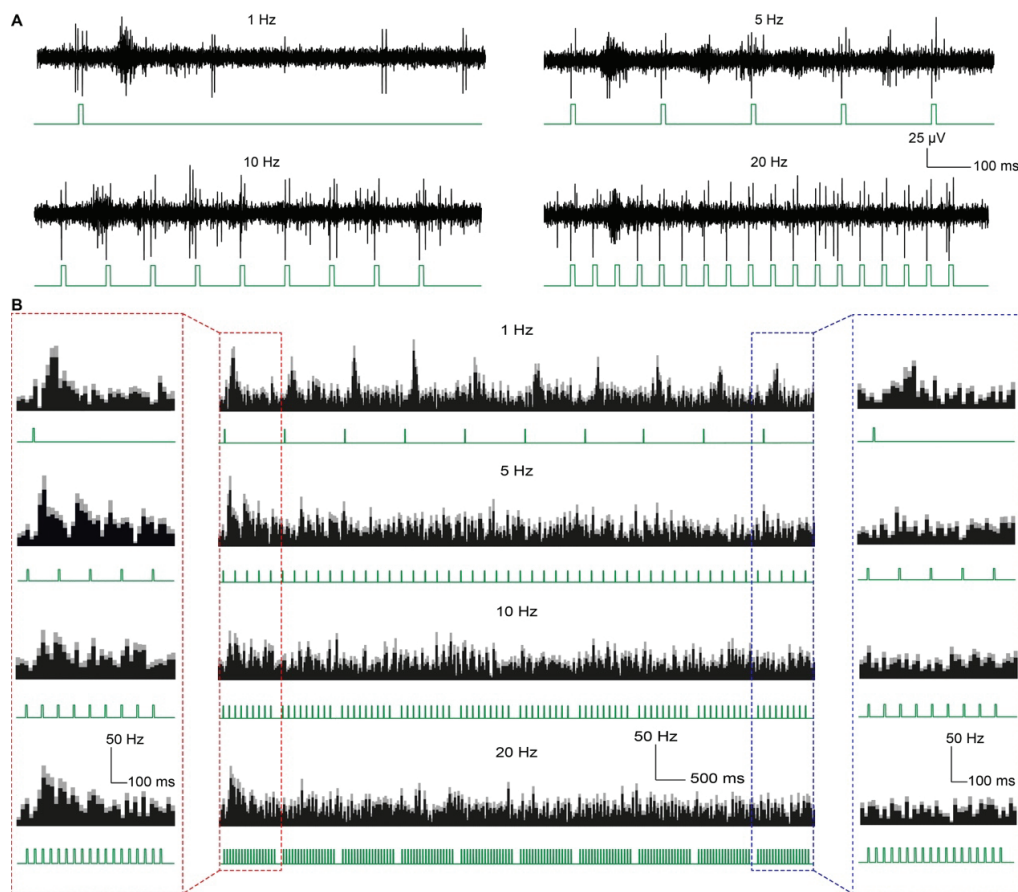
Ch.5 Table 1 - Animals and experimental conditions

5.4 Results

5.4.1 Frequency dependent desensitisations of RGCs

Epiretinal network-mediated activation of RGCs is subjected to strong desensitisation under repeated electrical stimulation, partially as the result of the intrinsic desensitisation of BCs²⁵¹. Therefore, we characterised the response decay of RGCs from explanted *Rd10* retinas (group A in **Table 1**) elicited by 10-ms photovoltaic stimulation from a selected pixel (stationary) repeated at 1 Hz, 5 Hz, 10 Hz and 20 Hz for 10 s using the POLYRETINA epiretinal prosthesis.

First, we evaluated whether and for how long the network-mediated ML response was significantly higher than spontaneous activity. In agreement with previous studies^{252,421,253,268}, we found that RGCs showed a strong naïve spiking response to the first pulse in the train (**Figure 2B,C**), whose firing rate reaches up to 230 Hz. This response was significantly higher than the corresponding resting activity for each of the stimulation rates tested ($p < 0.0001$, $p = 0.0001$, $p = 0.0069$ and $p = 0.0016$ respectively for 1, 5, 10 and 20 Hz stimulation rate, two-tailed paired t-test). After 10 s of stimulation (**Figure 2C**), only the 1-Hz stimulation rate evoked network-mediated ML responses significantly higher than the corresponding resting activity ($p = 0.0030$, two-tailed paired t-test). For higher stimulation rates, the response was not significantly higher than the corresponding resting activity anymore after 1.8, 0.4 and 0.25 s respectively for 5, 10 and 20 Hz stimulation rates ($p = 0.4488$, $p = 0.0642$ and $p = 0.1831$ respectively, two-tailed paired t-test).

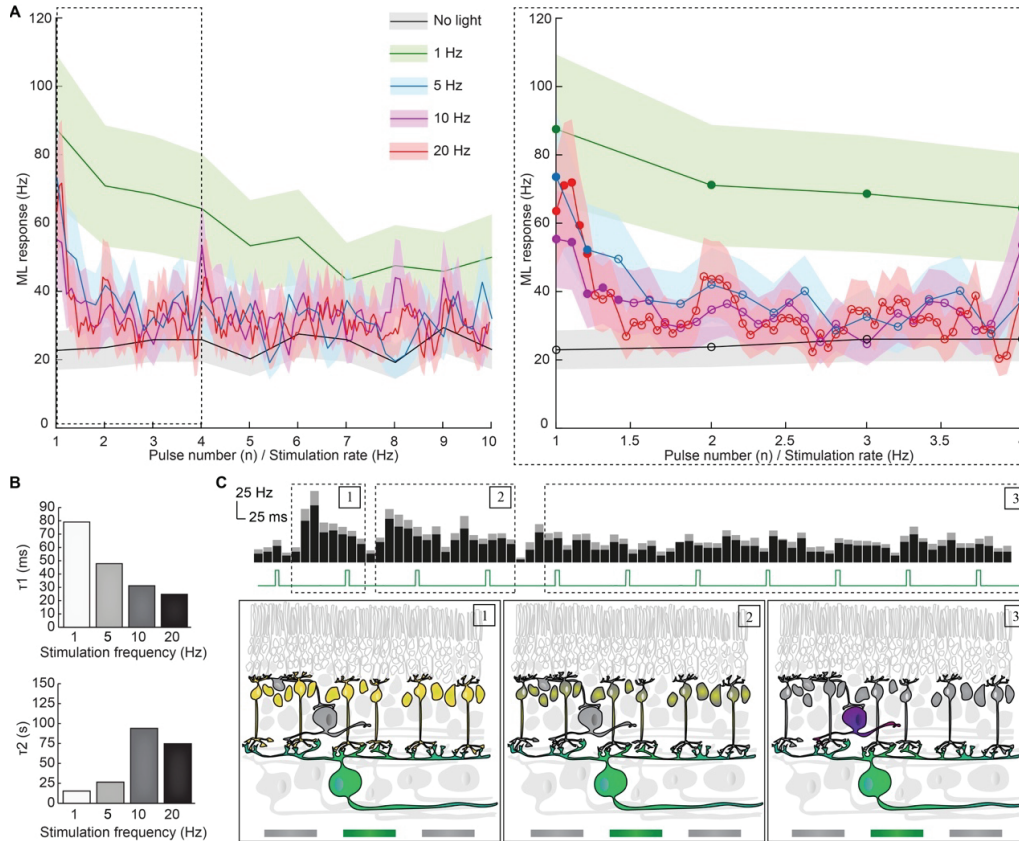


Ch.5 Figure 2 - RGC responses to repeated indirect photovoltaic stimulation

A, Representative recordings of a RGC response to single-pixel illumination at 1, 5, 10 and 20 Hz for 1 s. The photovoltaic light pulses are shown in green. **B**, Mean PSTHs upon 10 consecutive sweeps of 1 s (10 s in total) at 1, 5, 10 and 20 Hz (mean \pm s.e.m., group A, $n = 16$ RGCs). The filled area indicates the mean value, while the grey area shows the s.e.m. The first and tenth sweeps are highlighted respectively in red and blue. The corresponding light pulses are shown in green.

Even if the network-mediated ML response exceeds the resting activity, upon repetitive electrical stimulation, it rapidly decayed already from the second pulse of the sequence (**Figure 3A**). Therefore, we evaluated whether and for how long the network-mediated ML response was significantly as strong as the naïve response to the first pulse (*i.e.* the response persistence). We computed the response persistence as the time between the first pulse of the train and the first pulse evoking a network-mediated ML response

statistically significantly lower (at least $p < 0.05$) than the naïve response (*i.e.* the response to the first pulse). With 1-Hz stimulation rate (**Figure 3A**, green), the network-mediated ML response became statistically significantly lower than the naïve response after 3 s (fourth pulse in the sequence; $p = 0.038$, two-tailed paired t-test). The response persistence shortens as the stimulation rate increased: with 5-Hz stimulation rate (**Figure 3A**, blue) the response persisted for 0.4 s (third pulse in the sequence; $p = 0.0278$, two-tailed paired t-test), at 10-Hz stimulation rate (**Figure 3A**, red) for 0.5 s (sixth pulse in the sequence; $p = 0.0183$, two-tailed paired t-test) and at 20-Hz (**Figure 3A**, orange) for 0.25 s (sixth pulse in the sequence; $p = 0.0329$, two-tailed paired t-test).



Ch.5 Figure 3 - Double exponential decay of network-mediated ML RGC activity

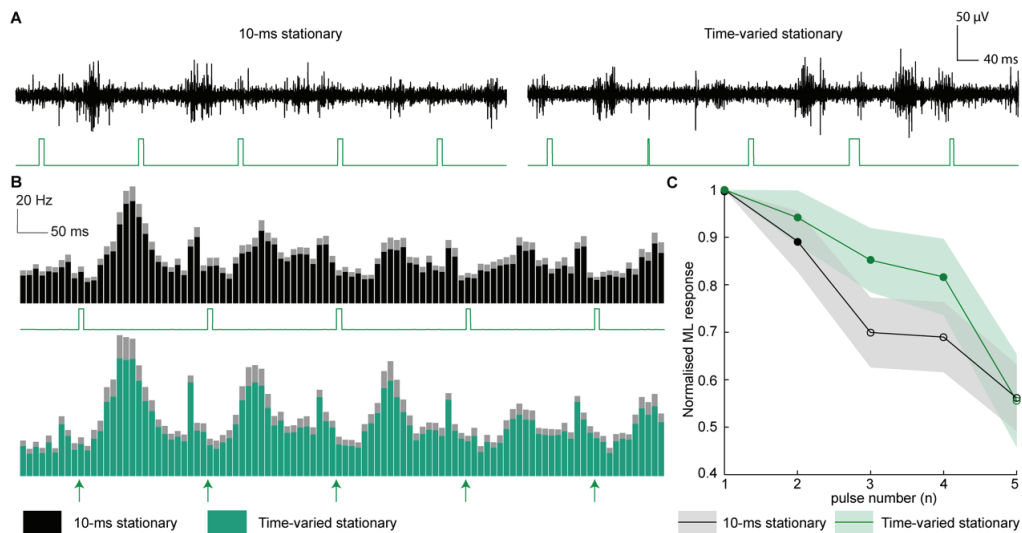
A, Quantification of the network-mediated ML RGC response over 10 s of repetitive stimulation at 1, 5, 10 and 20 Hz and without light stimulation (mean \pm s.e.m., group A, $n = 16$ RGCs). The right panel highlights the early desensitisation up to 2 s from the start of the pulse train. The shaded area shows the s.e.m. Filled circles represent pulses inducing a network-mediated ML activity not statistically significantly different than the naïve response to the first pulse. Empty circles represent pulses inducing a network-mediated ML activity statistically significantly reduced compared to the naïve response to the first pulse. **B**, Time constants of the fast (τ_1) and slow (τ_2) desensitisation components, extracted from the double exponential model for 1, 5, 10 and 20 Hz stimulation rates. **C**, Theoretical framework of excitation- then inhibition-mediated synaptic adaptation in RGC. Solid and empty cells represent respectively preserved and degenerated cells in the *Rd10* mice model. The highlighted cells show the recorded RGC and its presynaptic neurons, among which resting cells are shown in grey, and depolarised cells are coloured. Panels illustrate the naïve network response (1), the early desensitisation phase (2) and the later desensitised state (3) respectively. The illustrative PSTH corresponds to a 5-Hz stimulation rate (2.5 s; mean \pm s.e.m., group A, $n = 16$ RGCs). The filled area indicates the mean value, while the grey area shows the s.e.m.

Last, we evaluated the decay time constant (τ) of the network-mediated ML response. The quantification of the network-mediated ML response decay revealed that it was inversely proportional to the stimulation frequency (**Figure 3A,B**). In agreement with previous hypotheses describing a two-phases process behind RGCs desensitisation²⁵³, the decay curves were fitted with a double exponential model. For all the stimulation rates tested, we found a first rapid phase occurring immediately after the first stimulation pulse, and a slower phase dominating the decay during prolonged stimulations. The decay time constant of the rapid phase (τ_{fast}) ranged from 25.6 ms to 79.0 ms (for 1 Hz and 20 Hz respectively), and it exponentially decreased with the increase of the stimulation frequency ($R^2 = 0.99$; $\text{SSE} = 3.45 \cdot 10^{-6}$). The decay time constant of the slow phase (τ_{slow}) ranged from 19.7 ms to 93.7 ms, but it did not correlate to the stimulation frequency (**Figure 3B**).

It was previously proposed that the rapid decay reflected the intrinsic desensitisation of the excitatory network^{253,268} since the BCs in the *Rd10* retina were strongly desensitised upon electrical stimulation with frequencies above 4-6 Hz. Also, for stimulation rates exceeding 14 Hz, a repolarisation period with a time constant of 39.49 ms per pulse was reported to be necessary for repeated BC activation²⁵¹. Nevertheless, the involvement of the inhibitory network in the RGC desensitisation process could not be formally excluded^{251,253}. Amacrine cells (ACs) are likely to play an active role in the RGC response during epiretinal stimulation⁴⁴⁰, as well as to be the source of the slow desensitisation phase^{253,268}. Indeed, network-mediated electrical stimulation of the retina engages the inner retinal mechanisms mediating visual adaptation, including feedback and feedforward inhibition^{269,488}. In this perspective, the two-phases RGC desensitisation would reflect the excitatory-inhibitory activity balance of the retinal network (Fig 2C): at the first pulse, the naïve BCs strongly depolarise and generate a high-frequency burst in the targeted RGCs (1); since BCs rapidly lose their intrinsic excitability, their input to RGCs in response to the next pulses is continuously decreased (2), and the inhibition from ACs might become predominant (3).

5.4.2 Temporal modulation of epiretinal stimulation with irregular pulse trains

The inverse relation between the fast decay time constant and the stimulation frequency underlies the relevance of a recovery period between electric pulses. Increasing the inter-pulse interval could allow the recovery of excitability in BCs and reduce the desensitisation process. However, an increase in the inter-pulse interval does not necessarily imply to lower the stimulation frequency, since it can be achieved using a time-varying stimulation train in which each stimulation pulse has a different pulse width. During natural vision, the light sequence reaching a steady location on the retina exhibits a highly irregular temporal profile, due to both eye and object movements. This continuous dynamic change contributes to counteract the desensitisation of BCs to natural stimuli^{489,490}. Likewise, the use of time-varied and amplitude-varied pulse trains was shown to reduce fading of electrically evoked potentials recorded in the superior colliculus of healthy rats⁴⁸⁶.



Ch.5 Figure 4 - Randomised time-varied stationary pulse trains reduced RGC desensitisation

A, Representative recordings from a RGC upon 5-Hz single-pixel photovoltaic stimulation (5 light pulses for 1 s) with 10-ms stationary pulses (left) and randomised time-varying stationary pulses (right). The light pulses are shown in green. **B**, Mean PSTHs (mean \pm s.e.m., group B, $n = 22$ RGCs) upon 5-Hz single-pixel photovoltaic stimulation (5 light pulses for 1 s) with 10-ms stationary pulses (top) and randomised time-varying stationary pulses (bottom). The filled area indicates the mean value, while the contoured area shows the s.e.m. Because of the randomly varying duration of each pulse over sequences, only the onset of the light pulses is indicated by the green arrows. **C**, Quantification of the normalised network-mediated ML RGC response over 1 s of repetitive stimulation at 5 Hz (mean \pm s.e.m., group B, $n = 22$ RGCs) with 10-ms stationary pulses (black) and randomised time-varying stationary pulses (green). The firing rates were normalised to the naïve response to the first pulse. The shaded area shows the s.e.m. Filled circles represent pulses inducing a network-mediated ML activity not statistically significantly different than the naïve response to the first pulse. Empty circles represent pulses inducing a network-mediated ML activity statistically significantly reduced compared to the naïve response to the first pulse.

We tested randomised time-varying pulses (temporal modulation) in explanted *Rd10* retinas (group B in **Table 1**) upon photovoltaic single-pixel illumination at 5-Hz repetition rate (**Figure 4**). The stimulation rate was set to 5 Hz as it was shown to be a comfortable stimulation rate for most patients^{180,268}, while it is low enough to allow the temporal modulation of the electric pulses. The pulse width was varied between 5 ms and 25 ms, and random sequences were delivered for 10 s. Each RGC was tested with a different random sequence, whose cumulative exposure time was kept equal to 50 ms every 5 pulses for a total of 500 ms for the whole 10-s

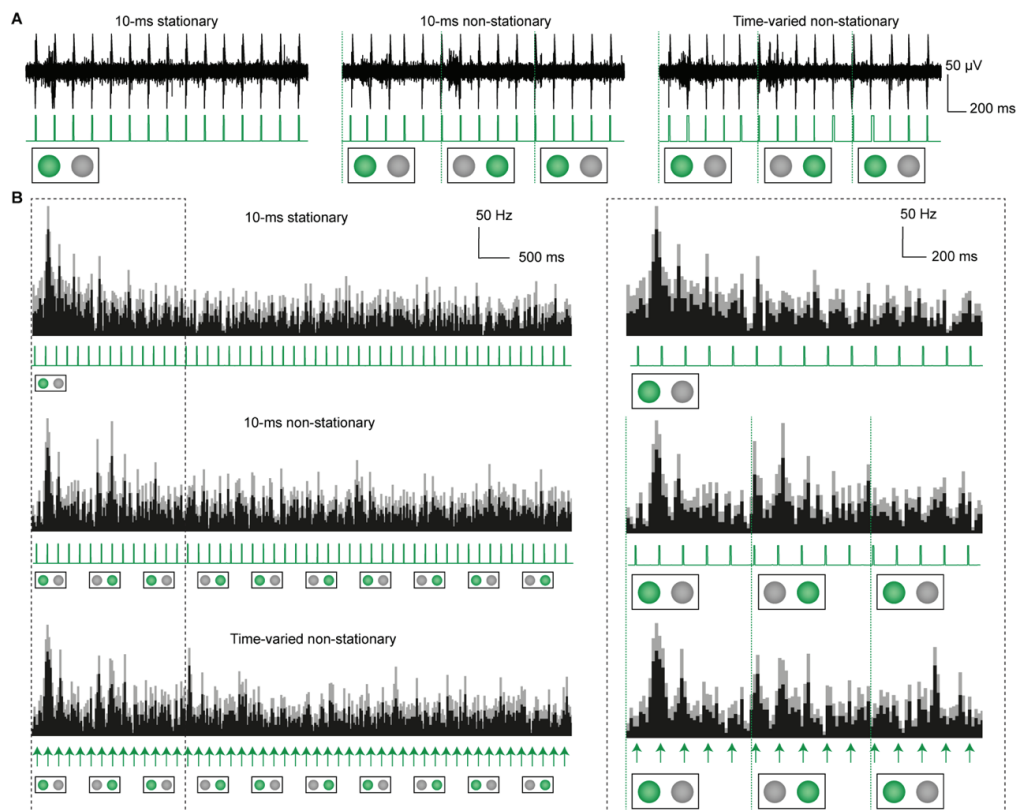
protocol, as for the 10-ms stationary stimulation. The fast response decay was slowed down by randomised time-varying stationary pulses (Figure 4A,B), which allowed a network-mediated ML response persistence up to 0.8 s (Figure 4C); the network-mediated ML response becoming statistically significantly lower than the naïve response from the fifth pulse in the sequence ($p = 0.0154$, two-tailed paired t-test). On the other hand, the response to 10-ms stationary pulses persisted only for 0.4 s (third pulse in the sequence; $p = 0.0255$, two-tailed paired t-test), as in the previous experiment.

In summary, pulse trains with irregular pulse widths showed a transient ability to reduce the RGC desensitisation upon repeated electrical stimulation, lengthening the RGC response persistence from 0.4 s to 0.8 s.

5.4.3 Spatial modulation of epiretinal stimulation with non-stationary pulse trains

Another strategy exploited in natural vision to reduce fading is performing a variety of eye movements during visual tasks. Saccades, eye drifts and microsaccades allow focus on a specific object, while slightly shifting it to create a non-stationary image projection on the retina^{257,258,491}. A previous experiment with single-pixel photovoltaic stimulation in *Rd10* retinas using the high-density POLYRETINA device suggested that non-stationary stimulation of the retina can be achieved by alternating the stimulation via neighbouring pixels, provided that the electrode density is high enough for more than one pixel to activate the same RGC⁴⁸⁷. The POLYRETINA prosthesis can indeed generate highly focused stimuli from each of its independent pixels, and because of its high resolution, a single RGC can be stimulated through two adjacent pixels.

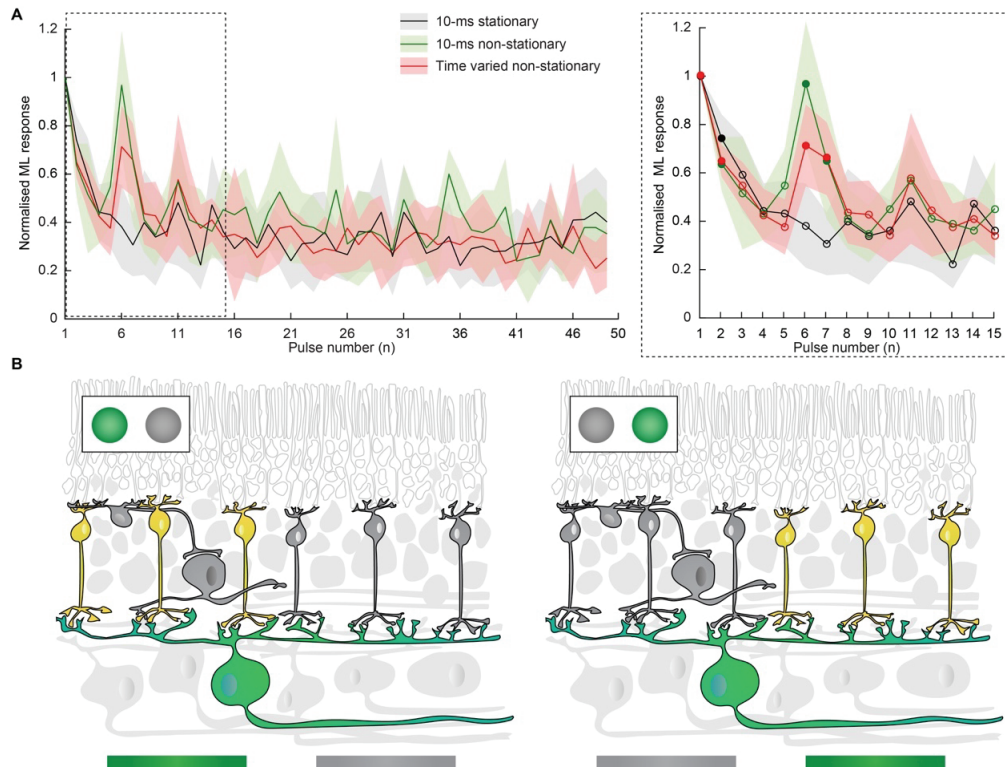
Thus, we tested whether mimicking microsaccades with an alternating stimulation pattern (spatial modulation) in which the stimulation is switched between two adjacent pixels (10-ms non-stationary pulses) could reduce the RGC response desensitisation (Figure 5).



Ch.5 Figure 5 - Non-stationary pulse trains reduced RGC desensitisation

A, Representative recordings from a RGC upon 5-Hz single-pixel photovoltaic stimulation (15 light pulses for 3 s) with 10-ms stationary pulses (left), 10-ms non-stationary pulses (middle) and randomised time-varying non-stationary pulses (right). The light pulses are shown in green. For non-stationary stimulation, the stimulating pixels were switched at 1 Hz. **B**, Mean PSTHs (mean \pm s.e.m., group C, $n = 12$ RGCs) upon 5-Hz single-pixel photovoltaic stimulation (15 light pulses for 3 s) with 10-ms stationary pulses (top), 10-ms non-stationary pulses (middle) and randomised time-varying non-stationary pulses (bottom). The black area shows the mean value, while the grey area shows the s.e.m. The right panels highlight the first 3 s of the recordings. The light stimuli are indicated in green (top and middle), while the onset of the light pulses is indicated with green arrows for the randomised time-varying pulses (bottom).

After the identification of a RGC and its electrical receptive field (group C in **Table 1**), the illumination spot was switched at a 1-Hz rate between the two most responding pixels of its electrical receptive field (10-ms pulses, 5-Hz stimulation rate).



Ch.5 Figure 6 - Quantification of the RGC response preservation with non-stationary pulse trains

A, Quantification of the normalised medium-latency network-mediated RGC response over 10 s 5-Hz stimulation with 10-ms stationary pulses, 10-ms non-stationary pulses and randomised time-varying non-stationary pulses (mean \pm s.e.m., group C, $n = 12$ RGCs). The firing rates were normalised to the naïve response. The right panel highlights the first 3 s of the recordings. The shaded area shows the s.e.m. Filled circles represent pulses inducing a network-mediated ML activity not statistically significantly different than the naïve response to the first pulse. Empty circles represent pulses inducing a network-mediated ML activity statistically significantly reduced compared to the naïve response to the first pulse. **B**, Sub-receptive field stimulation of spatially distinct pools of BCs during non-stationary stimulation. Solid and empty cells represent respectively preserved and degenerated cells in the *Rd10* mice model. The highlighted cells show the recorded RGC and its presynaptic neurons, among which resting cells are shown in grey, and depolarised cells are coloured.

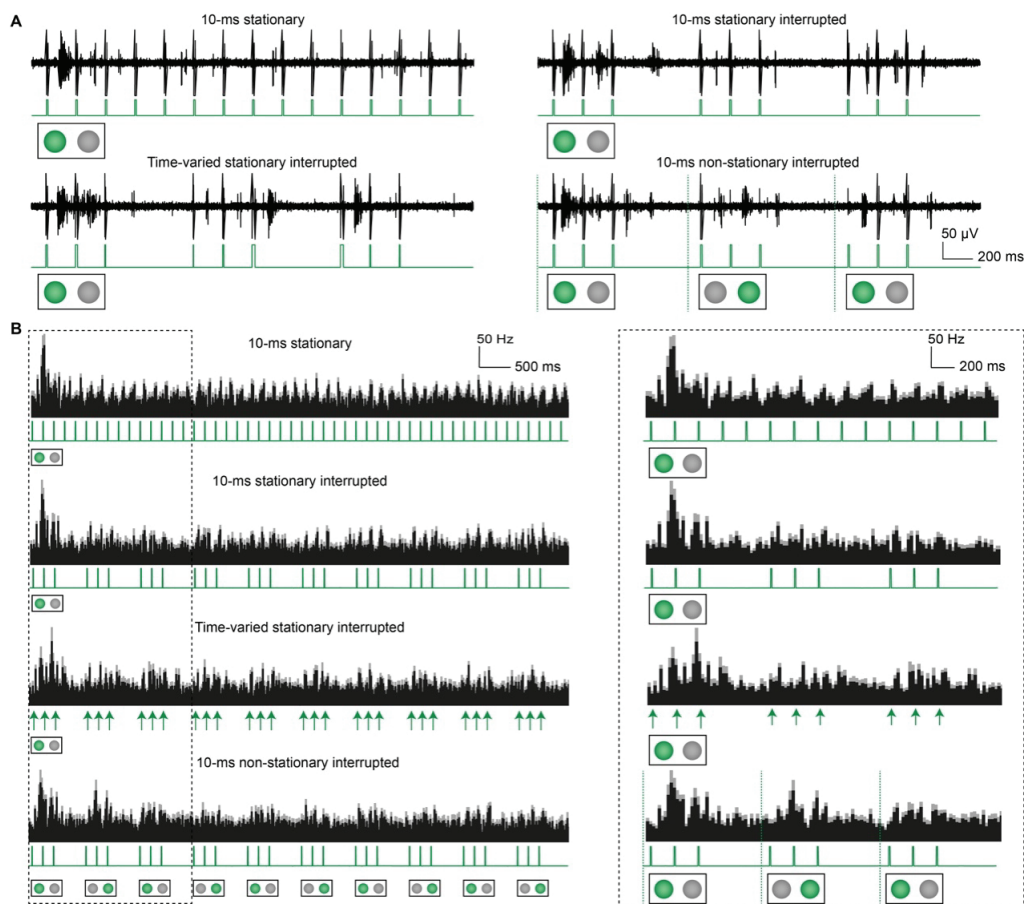
With 10-ms stationary stimulation, the network-mediated ML activity is reduced due to the desensitisation process (**Figure 5A** left and **5B** top), and the response persisted only up to 0.4 s, as before (**Figure 6A**, black). When the stimulation is switched to the neighbouring pixel (**Figure 5A** middle and **5B** middle), the network-mediated ML activity is transiently recovered (**Figure 6A** green), and it is not statistically significantly lower than the naïve response to the first pulse for two consecutive pulses (pulse 6: $p = 0.9003$, two-tailed paired t-test; pulse 7: $p = 0.0835$, two-tailed paired t-test). The stimulation from each of the two alternating pixels evoked persisting responses, lengthening the total RGC response duration up to 1.4 s (**Figure 6A**). The pixel switch experiment was repeated with randomised time-varying non-stationary pulses, and identical results were obtained (**Figure 5A** right, **5B** bottom and **6A** orange). However, when the stimulation was switched back to the first pixel (second switch, pulse number 11), the network-mediated ML activity was statistically significantly reduced compared to the naïve response for both 10-ms non-stationary ($p = 0.0271$, two-tailed paired t-test) and randomised time-varying non-stationary pulses ($p = 0.0267$, two-tailed paired t-test).

Non-stationary pulses (both 10-ms and randomised time-varying) lengthened the duration of the RGC response from 0.4 to 1.4 seconds, by reducing the fast RGC desensitisation. According to these findings and previous results⁴⁸⁷, we hypothesised that the response recovery at the pixel switch arose from another pool of BCs that were not desensitised by the first stimulation pattern (**Figure 6B**): that is to say that switching the stimulation pixels allows stimulating a RGC alternatively from different portions of its receptive field.

5.4.4 Temporal modulation of epiretinal stimulation with interrupted pulse trains

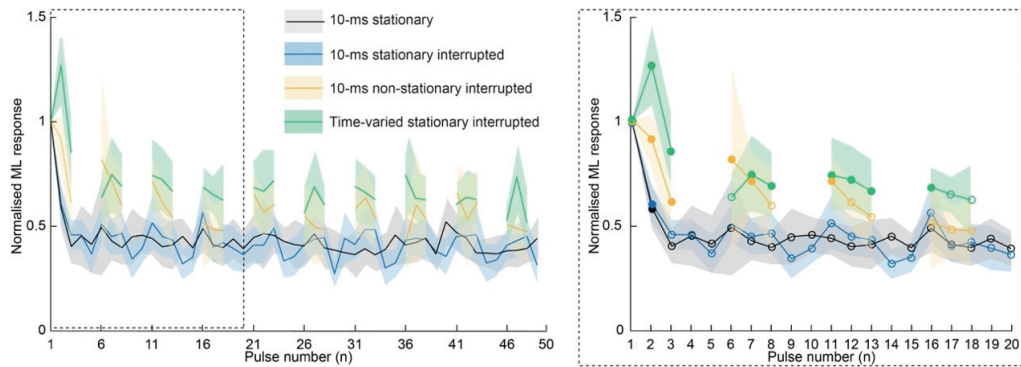
In the previous experiment, non-stationary pulses prolonged the response persistence. However, when the illumination spot was switched back to the original pixel, the response was statistically significantly reduced compared to the naïve response. Thus, we introduced another temporal modulation in the stimulation sequence. For each stimulation block (5 pulses at 5 Hz), the last two pulses were removed (interrupted sequence, **Figure 7**) since the network-mediated ML response to these pulses were always statistically significantly reduced compared to the naïve response. Instead, the interrupted sequence leaves a longer gap to each pool of BCs to repolarise. The interrupted sequence design was tested on *Rd10* explanted retinas (group D in **Table 1**) in combination with 10-ms stationary pulses, randomised time-varying stationary pulses and 10-ms non-stationary pulses (**Figure 7A,B**). The interruption of the 10-ms stationary pulse train had no effect since the evoked network-mediated response persisted only for 0.4 (**Figure 8**, blue), similar to 10-ms stationary pulses (**Figure 8**, black). However, the combination of the interrupted sequence with randomised time-varying stationary pulses allowed the persistence of the response up to the third switch (pulse number 16), which corresponds to a response persistence of 3.2 s (**Figure 8**, green). In contrast, the combination of interrupted sequence and 10-ms non-stationary stimulation allowed a response persistence to only 2.2 s (**Figure 8**, yellow).

In summary, randomised time-varying stationary interrupted pulses allows an eightfold lengthening of the RGC response persistence from 0.4 to 3.2 seconds, by strongly reducing the fast RGC desensitisation.



Ch.5 Figure 7 - Interrupted pulse trains reduced RGC desensitisation

A, Representative recordings from a RGC upon 5-Hz single-pixel photovoltaic stimulation (3 s) with 10-ms stationary pulses (top left), 10-ms stationary interrupted pulses (top right), randomised time-varying stationary interrupted pulses (bottom left) and non-stationary interrupted pulses (bottom right). The light pulses are shown in green. For non-stationary stimulation, the stimulating pixels were switched at 1 Hz. **B**, Mean PSTHs (mean \pm s.e.m., group D, $n = 23$ RGCs) upon 5-Hz single-pixel photovoltaic stimulation (10 s) with 10-ms stationary pulses (first row), 10-ms stationary interrupted pulses (second row), randomised time-varying stationary interrupted pulses (third row) and 10-ms non-stationary interrupted pulses (fourth row). The black area shows the mean value, while the grey area shows the s.e.m. The right panels highlight the first 3 s of the histograms. The light stimuli are indicated in green for 10-ms pulses, while the onset of the light pulses is indicated with green arrows for the randomised time-varying pulses.



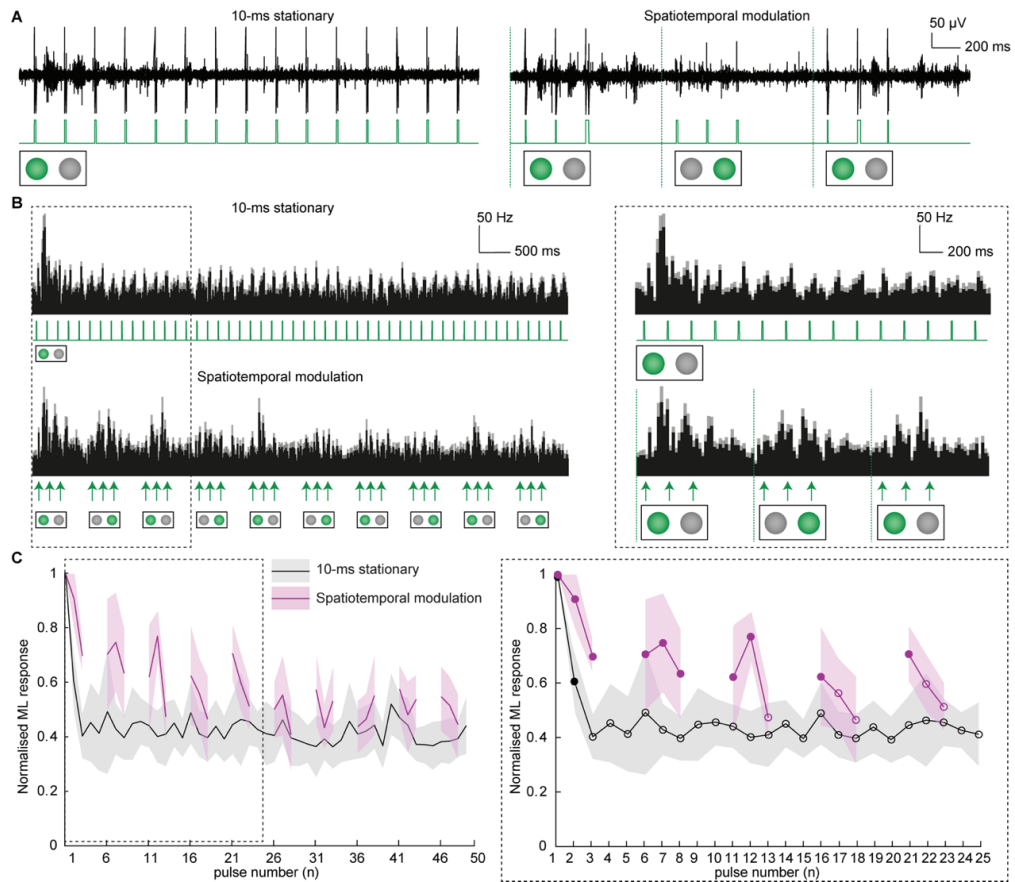
Ch.5 Figure 8 - Quantification of the RGC response preservation with interrupted pulses

Quantification of the normalised network-mediated ML RGC response over 10 s 5-Hz stimulation with 10-ms stationary pulses, 10-ms stationary interrupted pulses, randomised time-varying stationary interrupted pulses and non-stationary interrupted pulses (mean \pm s.e.m., group D, $n = 23$ RGCs). The firing rates were normalised to the response to the naïve pulse. The right panel highlights the first 3 s of the recordings. The shaded area shows the s.e.m. Filled circles represent pulses inducing a network-mediated ML activity not statistically significantly different than the naïve response to the first pulse. Empty circles represent pulses inducing a network-mediated ML activity statistically significantly reduced compared to the naïve response to the first pulse.

5.4.5 Spatiotemporal modulation of epiretinal stimulation

Last, we tested on *Rd10* explanted retinas (group D in **Table 1**) a complex stimulation sequence associating the three modulations described so far (**Figure 9A,B**). The combination of non-stationary stimulation together with randomised time-varying pulses and interrupted stimulation sequence theoretically maximise the recovery time between consecutive stimulations of each of the two pools of BCs. Such a sequence can reproducibly evoke network-mediated ML responses not statistically different than the first naïve response up to four pixel switches (pulse number 21), corresponding to a response persistence of 4.4 seconds (**Figure 7C**).

When used in conjunction to maximize the recovery time of the excitatory cells, temporal and spatial modulations of the stimulation exhibited great synergy. A stimulation sequence, whose design included time-varied, non-stationary and interrupted pulse trains, efficiently counteracts the desensitisation process since it offers to each pool of BCs a long recovery period of about 1.8 s to repolarise between consecutive stimulations. Though, the slow RGC desensitisation, likely imputable to inhibitory interneurons, is not affected by those modulations.



Ch.5 Figure 9 - Combined spatiotemporal modulation reduced RGC desensitisation

A, Representative recordings from a RGC upon 5-Hz single-pixel photovoltaic stimulation (3 s) with 10-ms stationary pulses (left) and non-stationary randomised time-varying interrupted pulses (right). The light pulses are shown in green. For non-stationary stimulation, the stimulating pixels were switched at 1 Hz. **B**, Mean PSTHs (mean \pm s.e.m., group D, n = 23 RGCs) upon 5-Hz single-pixel photovoltaic stimulation (10 s) with 10-ms stationary pulses (left) and non-stationary randomised time-varying interrupted pulses (right). The black area shows the mean values, while the grey area shows the s.e.m. The right panels highlight the first 3 s of the histograms. The light stimuli are indicated in green for 10-ms pulses, while the onset of the light pulses is indicated with green arrows for the randomised time-varying pulses. **C**, Quantification of the normalised network-mediated ML RGC response over 10 s of repetitive stimulation at 5 Hz (mean \pm s.e.m., group D, n = 23 RGCs) with 10-ms stationary pulses (back) and non-stationary randomised time-varying interrupted pulses (pink). The firing rates were normalised to the naïve response. The shaded area shows the s.e.m. Filled circles represent pulses inducing a network-mediated ML activity not statistically significantly different than the naïve response to the first pulse. Empty circles represent pulses inducing a network-mediated ML activity statistically significantly reduced compared to the naïve response to the first pulse.

5.5 Discussion

5.5.1 The cognitive burden of transient percepts

The artificial vision provided by retinal implants allows profoundly blind patients to perform visual guided tasks, such as orientation, navigation, object recognition, object manipulation and reading^{163,275}. However, the unnaturalistic vision provided by the current retinal prostheses poses a significant issue to implanted patients in daily life^{98,270,283}; only a very small fraction of users keeps using their prosthesis at the end of the clinical trial due to the high cognitive load of its use^{126,270}. This fate matches the abandonment rate in cochlear implant or upper-limb prosthesis users which, if not abandoned, become an intermittent aid due to both their physiological and cognitive burden^{492–495}. Similarly, artificial vision is a highly specific cognitive task, that implies long associative learning but also a permanent multisensory adjustment of the perception^{126,270}.

In retinal stimulation, electric stimuli are translated into phosphenes organised in a reduced two-dimensional space. The fading of those phosphenes, the absence of depth information and the fragmentation of the visual space make it necessary to adopt multisensorial strategies to localise and recognise the visual cues. Users of retinal prostheses are taught to perform body and head movements to scan the visual scene while performing active viewing through their implant²⁸³. These movements serve two purposes: to scan a portion of the visual field larger than the one allowed by a small-size implant and to counteract the fading of the phosphenes. Several groups worldwide are developing wide-field implants that could address the first issue from an engineering perspective^{323,369,168}. However, the rapid fading of the percept still forces the users to voluntarily refresh the stimulation pattern on their retina, performing large body and head movements²⁶⁸.

Artificial vision requires the subject to fixate a visual target in order to identify it; therefore, it accounts on the retinal response to one or several stationary electrodes at a time, leaving open the likelihood of response fading. It was suggested that when stimulating the retina repetitively and synchronously, a minimal delay of 155 ms (6.5 Hz) was required between stimuli to avoid fading⁴⁷⁸. However, RGC desensitisation was also observed at lower stimulation frequencies²⁵³: already from 1 Hz in the present study. Another study also argued that repeated stimulation of distant stimulation sites (at least 790 μm) could avoid fading, suggesting that counteracting fading goes through large spatial variations of RGCs targets during fixation⁴⁷⁸. With a high-resolution photovoltaic approach, we showed that two adjacent pixels, separated by 120 μm only, could stimulate the same RGC from different subsections of its receptive field and maintain response up to 4.2 seconds. The ability to maintain a sustained and localised RGC response may drastically reduce the need for active body or head movements and the constant attention required from varying the RGC target for a static object.

5.5.2 Spatial and temporal modulations reduce the rapid desensitisation

The stability of the percept evoked by retinal stimulation depends on several factors, among which the electrode location, the stimulation frequency but also the integrity of the retinal network. In *Rd10* mice retinas, the RGC, the inner nuclear and the plexiform layers are largely preserved even at advanced stage of degeneration^{101,102,496}, and the time course of RGC desensitisation is not affected by the degeneration process²⁵¹. The integrity of the excitatory and inhibitory pathways is crucial in the synaptic desensitisation process. According to the theoretical framework proposed by Freeman & Fried²⁵³, the involvement of both pathways in RGC desensitisation might explain the two temporal components of fading reported by patients. Indeed they often describe a fast fading phase (hundreds of milliseconds) followed by a slow fading phase (tens of seconds)^{268,283}. The nonlinearity we observed in the temporal relationship between desensitisation and stimulation rate corroborates the coexistence of more than one mechanism. Both excitatory and inhibitory interneurons can be activated during electrical stimulation, independently of the electrode location^{385,440}. The kinetics of BCs voltage-gated Na^+ -channels and the recruitment of the inhibitory network (both involved in synaptic adaptation during natural vision⁴⁸⁹) are two valid candidates to explain the decay of the RGC responsivity during epiretinal network-mediated stimulation^{251,497,498}. Growing evidence suggests that AC to BC synapses may be essential players in the slow desensitisation process, and inhibitory postsynaptic potentials were recorded in BCs after depolarising responses to electrical stimulation²⁵¹. As a consequence of the joint presence of inhibitory postsynaptic potentials and Na^+ -channels closure time-course, BCs require from 0.2 to 2 seconds to fully repolarise after a depolarising voltage transient²⁵¹. The spatiotemporal modulations of the stimulation explored in this paper showed the ability to counterbalance the rapid phase of the RGCs desensitisation, playing on the BC excitatory pathway. The common thread behind sequence interruption, randomised time-varied pulses and non-stationary stimulation is to allow longer recovery periods for a given BC or pool of BCs.

5.5.3 Artificial microsaccades

The natural fixational microsaccades may help to avoid the fading of phosphenes, however, electric-based prostheses (like the Argus[®] II) bypass eye movements since the image is acquired by an external camera and transmitted to the implanted array in the form of a stimulation pattern. Therefore, fading cannot be counterbalanced either by spontaneous nor by voluntary ocular movements. On the other hand, light-based prostheses use light (natural or artificially projected) entering the pupil and reaching the implanted device as visual information source. In this case, eye micromovements could compensate for the fading process. Yet, two

devices showed opposite clinical results regarding fading. *Retinitis Pigmentosa* patients implanted with the Alpha-IMS/AMS devices reported phosphene fading, but with a high variability of fading rates amongst patients^{183,186}, while age-related macular degeneration patients implanted with the PRIMA device did not⁴³⁸. The origin of these opposite results is still unclear, and it might be associated with two factors. First, the higher stimulation resolution of the PRIMA device could allow for an efficient image shift during eye micromovements. Second, oculomotor reflexes are often impaired in *Retinitis Pigmentosa* and they are highly dependent on the patients' visual history and residual vision^{267,499,500}. *Retinitis Pigmentosa* patients showed large multidirectional involuntary eye movements or nystagmus that could prevent them to perform fine relevant microsaccades across the visual area of interest^{263,265,266}.

In such cases, a non-stationary component within the stimulation strategy itself might be useful to reproduce microsaccades artificially and reduce fading. Eye-tracking systems can operate up to 120 Hz, which can effectively gaze-lock the grid of stimulating elements onto the retina⁵⁰¹. Once gaze-locked, the stimuli can be laterally flickered between two adjacent pixels to mimic microsaccades artificially. Sub-receptive field stimulation allows to do so without affecting the overall pattern of activation of the RGC layer and therefore asking for limited brain adaptation. The 120- μm separating the high-resolution POLYRETINA prosthesis pixels⁴⁸⁷ allows flickering the stimulus within a distance that does not exceed the one of natural microsaccades, estimated from 0.01° to 1° of visual angle^{254,255}. Switching the stimulating pixels at 1 Hz also allows matching the natural fixational saccade occurrence of 1 to 2 per second²⁵⁴.

The non-stationary approach requires high stimulation resolution at the BC level to activate independent excitatory pools within the same receptive field; therefore, it might be limited by two factors. First, the resolution might depend on the strength of the stimulation, since a larger pool of BCs might be desensitized as the stimulation strength increases. In our study, we used an irradiance level of 0.9 mW mm⁻², which was previously demonstrated to be above the activation threshold of RGCs⁴⁸⁷. Second, a single RGC must be activated by at least two neighbouring electrodes; therefore, this approach is limited to RGCs with a receptive field larger than the pixel pitch. In our study, the pixel are 120- μm distant, and most RGC in the mouse retina have dendritic fields exceeding this value⁷⁹: at least two pixels can activate a RGC. However, both the irradiance level and the response resolution must be validated *in-vivo* with animal models and patients to verify the translation of this approach.

In conclusion, providing a naturalistic type of stimulation, where the changes in the RGC activity pattern matches the natural spatiotemporal features, might improve the chances of successful adoption of prosthetic stimulation. At first, increasing the persistence of RGC response up to 4.2 seconds may allow reaching the critical phosphene duration for a sound understanding of the percept. Evidence suggests an active role of non-stationary retina stimulation into shaping and enlarging the cortical receptive fields, which in turn allows targeted saccades and proper allocation of attention during faces recognition or visual exploration tasks^{502,503}.

5.6 Acknowledgement

This work was supported by École polytechnique fédérale de Lausanne, Medtronic and Fondation Pierre Mercier pour la Science.

Chapter 6 Conclusion

6.1 Achieved results

The present work introduces a hybrid epiretinal photostimulation approach, that gathers the advantages of photovoltaic subretinal implants and large epiretinal arrays, while circumventing the major drawbacks of each of them.

Organic semiconductors allow to fabricate flexible miniaturized *p-n* junctions that only relies on a light beam as power and command sources. In this perspective, the POLYRETINA approach could be compared to optogenetic stimulation: both are entirely withstanding but require a high-power light beam to induce retinal cell depolarization. A prosthetic approach with discrete stimulation sites can hardly compete with optogenetic cellular resolution. Yet, a high and dense array of stimulating pixels may allow to stimulate the larger mid-peripheral and peripheral ganglion cells with their native resolution. Indeed, the pitch only limits the theoretical acuity restored in the macula. If the array can cover the retina beyond 10 to 20° of eccentricity, a 120- μm spacing can guarantee a native resolution for most of the RGCs beyond the fovea^{452,453}.

The restoration of a large visual field is made possible by two joined elements: the flexibility of the substrate and the active materials, and the epiretinal placement of the implant. It allows the implant to be rolled, inserted through a 6.5 mm scleral incision and to self-open facing the retina over a 13.4 mm diameter area, what corresponds to roughly 45° of visual angle.

The use of 10-ms long light pulses allows to stimulate the RGCs through their presynaptic network, despite the epiretinal placement. Long light pulses generate long and capacitive-like photovoltage at the pixel-tissue interface. Both features have been isolated as potent candidates to activate the inner retinal cells rather than the RGCs directly^{237,416,386,440}. This work also demonstrated that their conjoint use allowed to recruit both excitatory and inhibitory inner retinal networks. The network-mediated stimulation of RGCs has benefits and drawbacks, as previously observed in subretinal stimulation paradigms^{268,337,419,381}. The first advantage is to circumvent axonal stimulation issue. The second and major advantage, though the extent of its benefit on the actual perception is not measured, is the preservation of the inner retinal processing. The present work suggests that one measurable consequence of this preservation is the focusing of the response on the GCL. The modulation of excitatory input or the direct RGC inhibition from ACs allows to spatially segregate the RGCs response when single cell resolution is not possible, *i.e.* in the macula.

In this way, POLYRETINA allows to conciliate visual field and visual acuity restoration.

The second Chapter of this work introduces the first concept and design of the POLYRETINA implant, which embeds 2215 stimulating pixels, in a number and density already remarkably higher than most implants proposed to date (**Appendix Supplementary Table 1**). The spacing of stimulating pixels in such design (150 μm) could theoretically have provided a restored visual acuity of 20/600. Though better than Argus® II subjects' performances, this acuity would not allow blind patients to rely on their visual sense in daily activities, and they would be prone to orientate towards substitution strategies⁵⁰. Patients would besides still be considered legally blind. However, the visual field offered exceeds the thresholds defined for both legal blindness (20°) and adequate mobility skills (30° to 40°^{281,282,322}). But, importantly, without high visual acuity, this large visual field would be of little help in localizing and manipulating activities^{277,279}.

Further improvements on POLYRETINA resolution have thus been conducted along two complementary lines: downscaling the pixel array, and dissecting the retinal circuit activation under epiretinal photovoltaic stimulation to avoid neural cross-talk.

A second design of the implant could embed 10'498 photovoltaic pixels, spaced out with a 120- μm pitch. This tremendous increase in pixel density has been made possible mostly thanks to the patterning of the organic polymer film into physically independent and mechanically stable stimulating units. Such design allows for a theoretical visual acuity of 20/480^{193,487}.

However, increasing the electrode density does not necessarily translate into increasing the prosthetic resolution. Among the obstacles that limit spatial resolution, five major issues can be isolated. First, the impedance of electrodes increases when their area is reduced⁴³⁹. Second, the reduction of electrode spacing induces a risk of lateral cross-talk. This may have a major impact when combined with the third issue, which is the frequently noted gap between the epiretinal array and the retinal surface⁵⁰⁴. The lateral spreading of the electric field might be enhanced by the presence of the vitreous humour, resulting in a loss of spatial confinement. Fourth, epiretinal implants' risk of stimulating axon bundles, which dramatically impairs the resolution of the RGC response^{372,348}, both in diameter and in lateral displacement, and consequently the perceived phosphenes. Last, in implants relying on network-

mediated activation, neural cross-talk can also limit the resolution. The intrication of the neural connections – either due to the natural convergence and inhibition schemes of the healthy circuit, or due to aberrant rewiring – is a biological parameter that may defeat any effort to solve the technical resolution issues. It is then necessary to integrate it too into the design of a stimulation strategy.

Regarding the technical limiting factors, we verified in Chapter 4 that the second high-resolution POLYRETINA electrodes had an impedance low enough to stimulate RGCs under safe exposure ($79 \mu\text{W}\cdot\text{mm}^{-2}$ activation threshold, 10-ms pulses, TiN coating), and that the electric cross-talk between adjacent electrodes was minimal. Also, the hemispherical shape of the PDMS substrate must guarantee a tight contact between the photovoltaic pixels and the retinal tissue all over the implant's surface. Its realization by injection molding also opens the possibility to fabricate highly conformable personalized domes.

The uncontrolled axonal stimulation issue can be solved by turning the POLYRETINA epiretinal implant into a network-mediated stimulation implant. In actual fact, this is what is done when the Argus® II implant is used with long pulses (> 10 ms), or when the Epi-Ret group investigates the potentiality of sinusoidal and non-rectangular waveforms^{384,387}. While the stimulation is conducted from the epiretinal side, the spiking profiles reported in the latter studies are network-mediated. We indeed showed in Chapter 3 that long (≥ 10 ms), capacitive-like pulses, or both combined, had the ability to polarize the inner retinal interneurons with greater efficiency than shorter rectangular pulses. The recruitment and role of the outer retinal cells in such process is controversial, and further anatomical and electrophysiological studies may be needed to determine whether degenerating light-insensitive photoreceptors having lost their outer terminals can be stimulated from the epiretinal side (as it has been shown from the subretinal side⁵⁰⁵), and whether horizontal cells can contribute to the response inhibition, despite the retraction of most bipolar cells dendrites. The recruitment of the inner retinal cells from the epiretinal side has three major consequences: to partially avoid uncontrolled direct RGC depolarization; to preserve the spatio-temporal characteristics of the sighted RGC response; and to benefit from lateral inhibition from the amacrine cells. This latter point may be more prominent in epiretinal network-mediated stimulation than in subretinal stimulation, due to the vicinity of amacrine cell bodies with – and within – the GCL⁵⁰⁶.

These findings are in line with the major reports on the topic: different epiretinal pulse durations involve the contribution of different cell types³⁴⁸. Short pulses (60 μs pulses to 0.15 ms) generate action potentials at the AIS and distal axon level^{372,235}, which leads to laterally offset RGC responses³⁴⁸, and wide areas of activation²³⁷. On the other hand, long pulses (1 ms to 25 ms) generate focused RGC response over the electrode³⁴⁸, and better spatial confinement of the activation and of the percept²³⁷. One can assume that the prolonged voltage exposition leads to cumulative transmembrane change in graded voltage cells – *i.e.* ACs and BCs – and thus in their sustained postsynaptic activity⁴⁸⁸. The same chronaxy mechanism can be exploited using non-rectangular pulses³⁸⁷ (*c.f.* Chapter 3). This explains the strong ability of POLYRETINA pixels, that generates a capacitive-like photovoltage with a 6 ms discharge rate, to activate the inner retina. In further developments of POLYRETINA implant, the adjuvants to photovoltaic materials have been tuned in order to preserve this capacitive photovoltage⁴⁵⁹.

The conjoint use of non-rectangular long pulses and a high-density pixel array allows to stimulate RGCs through their presynaptic network and in most cases through subportions of their large presynaptic network (*c.f.* Chapter 4). Indeed, the RGCs' photovoltaic receptive fields measured in the mouse retina are no less than 154 μm wide and a RGC can be activated through on average three different adjacent pixels. This is a symptomatic example in which the high resolution of stimulation provided by POLYRETINA is fraught with biological limitation – the spatial extend of RGCs presynaptic network.

The over-resolution of POLYRETINA array compared to natural receptive field size in the mouse retina leads to two interesting results. First, it makes it possible to stimulate a given RGC in a non-stationary fashion by vibrating the light pattern from one pixel to another. Second, it means that POLYRETINA resolution also exceeds natural spatial resolution in the human peripheral retina whose RGCs have large presynaptic network. Consequently, in the fovea, the theoretically restored visual acuity is 20/480¹⁹³ (as limited by the 120- μm pitch); but from respectively ~ 2.5 and 5 mm of eccentricity parasol and midget cells can be stimulated with their natural arborization as the only limit^{452,84,487}.

Restoring peripheral vision with a natural spatial resolution can be critical for motion perception, self-orientation and ambulation, especially in late blind patients relying on allocentric spatial processing^{282,14,11,279}. Moreover, the visual acuity restored in patients, if not impaired by axonal stimulation, is expected to exceed the theoretical value from spatial RGC resolution. The single features parallelly encoded by the various RGC types are spatially and temporally integrated back into V1^{507,508}. The V1 non-linear spatial integration processes, such as contour integration, collinear facilitation, or attention facilitation play a prominent role in the clinical visual acuity, that are hardly predictable from retinal studies^{509–513}. Perceptual learning is also expected to improve clinical visual acuity^{514,515}.

Be that as it may, the quantitative performances of retinal implants are not the only factors predicting the benefits patients could gain from it. The qualitative impact of the epiretinal photovoltaic stimulation paradigm presented in this work can take three forms. First, the delivery of long non-rectangular voltage pulse may allow to avoid stimulation of RGCs axonal bundle, as they preferentially target inner retinal graded cells. Long sub-threshold pulses could eventually allow exclusive epiretinal indirect stimulation³⁷⁹, and prevent the blurring and distortion of complex percepts. Second, the restoration of a large visual field with natural

spatial resolution can limit the need for head and body scanning to seek for the relevant objects and features. This is expected to make patients able to rely on their peripheral vision for near-normal orientation and mobility performances⁵⁰.

Third, the network-mediated stimulation strategy preserves some of the spatio-temporal characteristics of the sighted RGC response, which can be at the same time a drawback. The preserved latency between light onset and RGC spiking response, as well as the preservation of rate coding are considered as an advantage for the activity integration in the LGN and V1^{516–518}. Yet, the asynchronicity of the RGC response and thus temporal order coding is not reproduced in prosthetic approaches, which could represent a significant loss of information⁵¹⁷. Additionally, network-mediated activation of RGCs preserves their adaptation mechanism and desensitisation upon repeated stationary stimulation (*c.f.* Chapter 5). POLYRETINA photovoltaic electrodes can sustain up to 20 Hz of stimulation rate, but the frequency dependant desensitisation of RGCs limits its operating rate to 5 Hz, similarly to other epiretinal (*e.g.* Argus® II) and subretinal (*e.g.* Alpha-IMS) prostheses. Yet, the over-resolution of POLYRETINA can be of substantial help in dealing with adaptation issues, as it allows to introduce a non-stationary stimulation pattern within the same receptive field. Implemented together with time-variation and interruption of the light stimuli – in a naturalistic stimulation sequence closer to natural stimuli asynchronicity and mobility – it could extend RGC responsivity by a factor of 10.

Altogether, this work is thus intended to provide technical and network-oriented solutions to the main obstacles encountered by retinal implants users. The high-resolution POLYRETINA implant stimulated with naturalistic sequence of 10-ms long pulses of 1 mW mm⁻² 560 nm light (*i.e.* below the irradiance safety limit) showed the ability to stimulate RGCs with sub-receptive field resolution for 4.2 seconds. At the macroscopic level, the implant and stimulation paradigm are expected to cover approximately 45° visual field, with 20/480 foveal resolution and native spatial resolution from the mid-peripheral visual field; and to evoke distinct seconds-lasting phosphenes, without requiring head scanning, for a minimum lifetime of 2 years.

6.2 Future development

6.2.1 Foveal resolution and selectivity

The ability to restore a wide visual field, wider than 40°, is a tremendous improvement regarding existing and developing retinal implants (**Appendix Supplementary Table 1**) and might offer great daily benefits in *Retinitis Pigmentosa* patients. Yet, the visual acuity theoretically restored with POLYRETINA, if it can be very satisfying in the mid-to-far periphery thanks to the retinal coverage and receptive field increase with eccentricity, does not exceed performances reported in patients implanted with Alpha or PRIMA implants. With such acuity (20/480), *Retinitis Pigmentosa* patients with highly reduced tunnel vision or no light sensitivity will still be severely visually impaired, and are not expected to perform high acuity tasks in their daily life such as reading, identifying emotions on faces or perform fine visually guided movements. The management of patients' expectations has been underlined as an important part of the surgical surveillance^{519,126}. An implant with an electrode density similar to native foveal midget receptive fields^{452,84} should possess a 5 µm distance from an approximately 12 µm pitch. An approaching resolution could have been tested in the primate retina and evoked direct activity in RGCs with cellular resolution⁵²⁰. However, such a native foveal resolution approach raises several concerns. The design of an implant with such high density requires totally wireless technology. In addition, the extremely high impedance of such microelectrodes condemns them to be used for direct stimulation of the RGCs, if placed in an epiretinal position. And, more importantly, the stimulation of RGCs at an individual level must recreate the visual encoding capacity of the retina: the very high spatial resolution of stimulation creates the need for cell type selectivity. The risk to stimulate multiple parallel processing channels sending contradictory signals is present regardless of the resolution, but the increase in spatial targeting must necessarily go with the knowledge of the relevant cells to be stimulated. Such biologically smart stimulation would be incredibly complex, as the retinal visual encoding is still a black box: models can reproduce its main functional outputs^{521–524}, some relevant image processing has been enhanced for artificial and computer vision^{512,525,526}, and various RGCs' functional properties identified^{82,79}, but the relationship between cell types, location and visual encoding is hardly linear. Further insights on the retinal processing that could provide a sufficiently approaching model relating cell types and complex features processing would be necessary in order to efficiently downscale retinal implants resolution.

Such downscaling also pushes forward the limits of existing technology and manufacturing techniques. Regarding POLYRETINA, the standardized microfabrication techniques allow to fabricate photovoltaic pixels down to 40 µm and 60 µm pitch. However, such small pixels do not allow to generate a confined enough electrical current, nor can one single 40-µm pixel elicit network-mediated RGC activation. Alternative designs of the photovoltaic pixels must be implemented to further enhance the stimulation resolution. In addition, this very high resolution design will require experiments in the primate retina, as such resolution would exceed that of the mouse retina smallest dendritic fields.

Chapter 5 highlighted the excitatory and inhibitory components of contrast adaptation involved in RGC desensitisation under repeated electrical or photovoltaic stimulation. Stimulating the inhibitory network and especially the amacrine cells present in the GCL and inner part of the INL is, on one side, a drawback for the temporal resolution of the response; but on the other side, it helps in its spatial segregation, especially in the foveal retina with high RGC density. In sighted contrast adaptation, RGC membrane potential drop is caused by multiple mechanisms: intrinsic membrane and channel properties, ceasing of excitation, feedback

inhibition, and feedforward inhibition^{243,245,246}. RGC sensitivity can be prolonged, but adaptation – to light or to electrical stimuli – can naturally not be suppressed, only due to the intrinsic RGC electrical properties⁵²⁷. Identifying the role of amacrine cells in RGC desensitisation, and defining a balance between favorable and noxious inhibition are exciting steps to dig deeper in a network-oriented stimulation strategy.

Finally, the risk to stimulate multiple parallel processing channels must be acknowledged. The non-selective activation of different visual pathway from joined stimulation of antagonistic spatial areas compromises the formation of a relevant information signal. Besides the above-mentioned pharmacoprostheses or light response individual cell testing, ON and OFF cells cannot be classified and separately stimulated. In natural vision, ON and OFF RGCs stimulation in a local retinal area are mutually exclusive. The consequence of their joined stimulation is still unclear: large phosphene perception could suggest that both signals do not cancel but that ON signal override OFF one. One should mention though that in retinal degeneration models, OFF pathway integrity seem less affected than ON one, at the least in early stages of the disease⁵²⁸, but the functionally mutual exclusion of ON and OFF pathways is supported by an ON to OFF inhibitory circuit, that could argue for an ON dominated response in network-mediated strategies^{529,530}, provided a sufficient asymmetry between the ON to OFF and OFF to ON synaptic input can be demonstrated^{529,531}.

In addition to the ON-OFF cell opponency, there are more than 30 types of functionally distinct mammalian RGCs, responsible for specific feature encoding, such as brightness, movement, color, etc^{89,82,79}. Their overlapping receptive fields allows the visual information to be decomposed into highly specific features later integrated back together in V1^{508,82}. Contrary to ON-OFF cells, the joined stimulation of these spatially overlapping but functionally different RGCs' presynaptic networks might rather be an advantage than an issue, both in terms of cognition and outcomes. It participates to provide a sighted input decomposition to the LGN and V1, what should facilitate the information processing in the late blind brain; and it allows for high-level nonlinear integration of the parallel visual information, what might further enhance the clinically restored visual acuity^{508-511,513}.

6.2.2 Assessing the functional usefulness of network-based strategies

It is critical to not separate the *in-vitro* cellular and network-based stimulation strategies from their *in-vivo* consequences. The evaluation of preclinical animal models should allow to test whether the confined stimulation of the RGCs we observed *ex-vivo* can lead to spatially segregated V1 response (VEPs) and eventually to complex phosphene perception. Preclinical testing of the surgical implantation procedure has been conducted, and preliminary results showed that wide-field flashes of light could evoke VEPs in blind minipigs⁵³². Further *in-vivo* studies should also allow to confirm the mechanical stability of the materials, of the implant fixation, and address the spatial discrimination achievable.

Another critical aspect addressed at this stage is the potential usefulness of the POLYRETINA implant and stimulation strategies. The recent past of retinal implants has proven that the dialogue with patients is essential: to understand their needs, their experience, to manage their expectation, to judge of the pertinence of the restored vision and to design back retinal stimulation approaches. The qualitative performance must necessarily be included in device evaluation processes. Self-reports and home environment investigations are the first available tools for doing so. However, there is no standardization in the evaluation of a prosthesis' functional outcomes. Quantitative and reliable measures can be provided by psychophysical, direction of motion, localization, or orientation tasks, but they have limited translatability out of a controlled laboratory environment. On the other hand, real world functional assessment and self-reports are highly subjective.

A solution can be brought by the development of Virtual Reality (VR) and Augmented Reality (AR) interfaces. VR allows to create virtually controlled but highly complex environments, in the spirit of the Pedestrian Accessibility and Movement Environment Laboratory⁵³³. Simulation of prosthetic vision in such environments can give precious standardized insights on what would be the real-world performance of implanted patients. Additionally, AR simulating prosthetic vision over a real-world environment can be used to compare the accuracy of the simulated vision prediction with respect to real patient performance.

Considering scanning and cognition efforts are key to build standardized usefulness evaluation. Mapping of body movement, of head scans but also of eye movements can easily be included in a VR or AR experimental paradigm. Decision time and pupillary measures can also be envisaged for cognitive effort measure⁵³⁴⁻⁵³⁶.

In that regard, it would be important to collect more knowledge on the presence and the role of natural eye movements of patients implanted with subretinal or suprachoroidal prosthesis. The high variability of preferred stimulation frequencies and the variability of the verbal fading reports^{268,283,180,184} could to some extent be explained by various oculomotor strategies or impairments in *Retinitis Pigmentosa* patients. The present work showed that non-stationary stimulation with a 120- μ m amplitude can lengthen the RGC responsivity to photovoltaic stimulation. The question remains whether this strategy can be unconsciously used or taught to implants users, or whether it should be implemented as an image preprocessing, together with its transformation into binary image.

A pioneering study in Alpha-IMS patients indeed confirms the hypothesis that the quality of a percept and its duration depends on the subjects' oculomotor behavior. Eye tracking of patients' gaze showed the presence of square waves, small amplitude drifts and microsaccades during phosphene visibility phases; but it also revealed the versatility of these movements, leading to a sudden

reversal of visibility⁵³⁷. It is interesting to mention that the frequency of microsaccades was found to adapt to the flickering (or stimulating) frequency of the image. Authors identified 5 Hz stimulation as the rate eliciting the longest percepts' duration, and a saccade frequency close to sighted patients average (*i.e.* an inter-saccadic interval of 200 to 250 ms). Fixational microsaccades thus clearly have the potential to limit fading *in-vivo*, and relatively low stimulation rates that favors natural microsaccades might be more efficient than higher stimulation rates (> 15-20 Hz) aiming at flicker fusion.

Yet, the same study also showed that microsaccades theoretical potential might not be exploited by all patients. Various evidence suggest that the experience of blindness impairs the voluntary and the involuntary oculomotor control. A reduced visual field can notably lead to saccadic movements of reduced amplitude^{267,266,500}. Also, *Retinitis Pigmentosa* patients with narrow residual vision exhibit a common voluntary saccade strategy consisting of large aberrant saccades out of the visual field^{538,499}. This strategy was associated with poor percept visibility in Alpha-IMS patients⁵³⁷. A patient exhibiting nystagmus – a frequent impairment in severe forms of *Retinitis Pigmentosa*²⁶⁴ – also showed increased difficulties in maintaining visibility, as it resulted in large corrective eye movements⁵³⁷. For such patients, implementation of artificial saccades might be necessary. The relative effects of artificial and natural microsaccades could be tested in locked and freely moving gaze VR environments. Understanding the systematicity and the reversibility of oculomotor disfunctions – or acquired counterproductive oculomotor strategies – could also help in deciding which training or artificial saccade implementation is the best solution, for most patients, and as individual rehabilitation strategy.

6.2.3 Interaction of prosthetic stimulation with the plastic visual system

The great variety of *Retinitis Pigmentosa* genotypes makes it extremely difficult to draw out systematic phenotypes regarding the oculomotor behavior, the cellular preservation of the retina, and its plasticity. In addition, each patient's history of blindness has a direct impact on its vision strategies: the motor strategies but also the mental representations and associative perceptions, that can be affected by visual field loss^{267,539}. A deeper knowledge on the variety of these phenotypes is required to provide adequate stimulation and rehabilitation strategies. Notably, given the current state of knowledge, the risk arising from retinal remodeling may as well be over- or underestimated.

The various types of network-mediated response patterns^{382,383}, together with their temporal characteristic, and their ability to be modulated suggests that network-mediated stimulation can preserve the diversity of stimulus encoding by the local retinal circuits, and thus even in retinas at advanced levels of degeneration. The network-mediation also allows to modulate the natural lateral inhibition to spatially segregate the RGC response, and to modulate the local excitation source to delay desensitisation. However, the integrity of the connectivity between vertical and inhibitory pathways is crucial to these benefits. From the *in-vitro* results gathered in the above chapters, the advanced stage of retinal degeneration does not seem to represent a threat in the mouse *Rd10* model, although synaptic remodeling has been reported since early disease stages⁵⁴⁰. As previously highlighted, the integrity of the RGC layer and of the INL to RGL synaptic projection in *Rd* mouse model corroborates this finding^{101,102,496}. It could be speculated that the inconsistency between advocates for preserved retina and advocates for remodeling could be solved in the statistical understanding of retinal reorganization. Knowledge on the systematicity of retinal remodeling and the genetic factors associated with it are necessary to solve this perennial question. More, the knowledge of remodeling systematicity, associated factors, and therapeutical windows must necessarily be extended to the primate retina and eventually human patients. For instance, the presence of RGCs' spontaneous activity in the *Rd* mouse model is well documented, and relatable to the triadic connection of RGC, BC, and AC, thus potentially of aberrant synaptic strengthening^{540,121,414,415}. On the other hand, little is known on the presence of spontaneous activity in human *Retinitis Pigmentosa*, nor in AMD patients. The presence of microneuromas in histological samples cannot at this stage be correlated with any functional changes. Also, the spontaneous activity is likely to be reduced by the electrical stimulation of one or several of the RGC-BC-AC triad protagonists, suggesting focal electrical activation could dominate aberrant activity, as observed in other neural networks^{541,542}. The impact of electrical stimulation on the miswired retina, both in short-term stimulation and long-term stimulation, is well worth discovering. Studies for now focused on the impact of retinal degeneration on the electrical stimulation at an empirical level, and led to variable results regarding the elevation of activation threshold in *Rd* retinas, either directly or indirectly stimulated^{470,543–546}. In a network-mediated epiretinal or subretinal approach, both empirical and precise physiological knowledge are needed to understand the joined effect of stimulation and synaptic reorganization – if systematic. In addition, the mechanical effect of a prosthesis implantation induces histological changes in the retina, especially for subretinal implants⁵⁴⁷, whose impact on functional response are overlooked.

The high plasticity of the retinal network following deafferentation, although qualified as negative and leading to aberrant activities, can be a silver lining. Remodeling may constrain therapeutical intervals, equally for molecular optogenetic or prosthetic therapies, but suggests an incredibly high adaptability of the retinal neurons to form output-oriented circuits. Chronic electrical or photovoltaic stimulation could potentially help in several regards. The electrical stimulation alone is suspected to have neuroprotective effects^{548–550}, if not neurotrophic effects²²⁹. Axonal growth was indeed reported under long-term electrical stimulation of retinal cells⁵⁵¹. One can also hypothesize that the framing of the deafferented circuit towards a meaningful output might nullify the need of alternative synapses formation and phantom visual inputs.

The interaction between chronic electrical stimulation and the visual system of implanted patients is a major question. As above-mentioned, this question first expresses at the cellular level in the retina: cells in retinal degenerative retinas might have higher

stimulation threshold, cells might form aberrant synapses, that could presumably be silenced or modified by chronic network-mediated stimulation. However, one should also consider the interaction of prosthetic stimulation with the intact portions of the retina, and thus the higher interaction of prosthetic vision with remaining vision.

The presence of multiple bursts of indirect activity (LL activity) has been proposed to originate from remaining photoreceptors' stimulation³³⁷, either from cells locally preserved from degeneration or from cells having lost their outer segment but still exhibiting electrical excitability. While this may be possible in healthy retinas with subretinal electrode placement, the presence of multiple bursts in *Rd* retinas under epiretinal stimulation can rather be associated with the sustained functional characteristics of RGCs³⁸². Indeed, on the *Rd* retina, only a few isolated photosensitive areas – likely consisting of surviving cones – can be found, with extremely low statistical incidence and not beyond intermediate stages of degeneration⁵⁵² (*c.f.* Chapter 3). However, in the degenerating primate retina that has a fovea, the photoreceptors loss is spatially dependant. Most cones are preserved in the macula of *Retinitis Pigmentosa* patients; and peripheral rods as local cones clusters can be almost untouched in AMD patients, besides rare patients with no residual light sensitivity^{44,20,22,31}. With a wide-field implant covering a 13.4 mm wide area of retinal surface, the macula, the mid-peripheral and the proximal far-peripheral retina are unselectively stimulated, and so risk to be surviving photoreceptors. In the case of photovoltaic stimulation, preserved photoreceptors can be stimulated both by the photocurrent delivered by the photovoltaic pixels, or by the incident light projected onto the pixels. While the epiretinal placement of POLYRETINA may limit the photovoltaic stimulation of the photoreceptor layer (*c.f.* Chapter 3), the use of visible light to activate conjugated polymers favors light-induced depolarization of the photoreceptors.

The only available study on the interaction of prosthetic and residual vision was conducted with the PRIMA implant, *i.e.* an implant that only covers the macula¹². It showed a very promising reproduction of center-periphery crowding effects – while the central retina was stimulated through the implant and the periphery through preserved photoreceptors. Yet, this does not allow to predict the cortical integration of prosthetic and natural vision when both spatially overlap at the retinal level. The timing of both types of responses are comparable: 50 to 300 ms for the RGCs' light response⁵⁵³ and 40 to 120 ms for the network-mediated response (ML); but the prosthetic response latency is slightly lower, as it does not require phototransduction. One can thus assume that the photoreceptor light response might reach already depolarized BCs, if not already desensitized BCs, and be of only minor effect with regards of the prosthetic response. Another difference lies in the light offset response: photovoltaic pixels stimulate both ON and OFF circuits at the light onset, but none at light offset; while incident light activates ON circuit at light onset and OFF circuit at light offset. The almost constant stimulation of the OFF circuit with such paradigm could lead to strong adaptation and OFF circuit neglect for the benefit of ON selective activation. Insights on the RGCs behavior but also on the cortical response under joined photovoltaic and light stimulation are needed to understand the functional risks of spatially overlapping stimulation.

In parallel, the requirement for light stimulation in the visible spectrum can be addressed through semiconducting materials refinement. The P3HT:PCBM polymeric blend used in the present studies absorbs light preferentially between 450 and 590 nm, but recent work showed that POLYRETINA sensitivity can be shifted towards near-infrared wavelengths, conjugating PCBM with another organic polymer (PCPDTBT)⁴⁵⁹. PCPDTBT:PCBM absorption peak is comprised between 660 and 760 nm, *i.e.* outside of rods, M-cones, L-cones and S-cones spectral sensitivities. Such near-infrared shifted POLYRETINA demonstrated the ability to stimulate the inner retina network from the subretinal side⁴⁵⁹. PDPP3T p-type polymer has also been proposed to form organic photodiode for prosthetic applications⁵⁵⁴. Inorganic silicon photodiodes have shown their efficiency in stimulating the retinal tissue¹⁹⁶; but their stiffness remains a biocompatibility constraint. One of the main challenges in developing these new materials is to reach a photoefficiency comparable to that of high-energy light, in order to be able to stimulate the inner retinal network from the epiretinal side. The use of organic photodiodes in tandem circuits has been proposed as an interesting approach⁵⁵⁴.

Finally, cortical plasticity and perceptual learning are certain to play a role in the success of the new generation of high-resolution implants. It is very likely that the discrepancies in retinal circuit stimulation (non-selective ON-OFF stimulation, synchronous light-mediated and photovoltaic stimulation, synchronous direct and network-mediated RGC stimulation) will be solved during the cortical processing of the information. The brain is constantly solving inference and incongruence problems⁵⁵⁵, the question remains to determine whether relevant spatial and temporal information can arise from its solutions. The high visual acuity (20/460) reported with the PRIMA implant, and the integration of the prosthetic and light-mediated stimuli together are a leap that suggest so^{12,438}. But despite this encouraging preliminary results *in-vivo*, perceptual learning and plastic cortical reorganization in retinal implants' users are still unknown.

In the adult mammalian brain, the plasticity in the early visual areas (LGN, V1) is reduced, especially compared to tactile or auditory cortices⁵⁵⁶⁻⁵⁵⁸. Nevertheless, it has been shown that the V1 regions corresponding to damaged retinal areas undergo dramatic pruning and sprouting from the regions responsive to intact surrounding retinal areas⁵⁵⁹⁻⁵⁶². In humans, shifts of the retinotopic organization have been reported following visual field loss⁵⁶³, but this reorganization appears to be limited^{564,565}. This suggests that, in the absence of afferent reorganization, higher-order visual areas might compensate for the missing, distorted or multiple synchronous inputs sent by the retina⁴³⁶. Indeed, neurons in V4 or in the inferiotemporal cortex – the highest-order area of the ventral visual stream – can efficiently be tuned to respond to specific features, contrarily to V1^{566,567}.

The consequence of the varying plasticity across visual hierarchy is that, in human patients, the processing of basic features such as discrimination tasks and simple shape recognition is tremendously impaired by altered vision (both in the case of retinal degeneration

and when a coarse form of prosthetic vision is restored); but higher-level visual functions are more malleable and have a greater potential to be restored. Notably, tasks involving cross-modal integration of vision can rapidly be tuned in function of the sensory input. Ambulation and proprioception – involving visuomotor integration – are typically modified in short-term prism experiments⁵⁶⁸. Also, visual dominance over audition is rapidly observed in both congenitally blind and late blind people after sight restoration^{569,570}. In patients implanted with Argus® II, the basic recognition performances can be significantly improved with adequate training, but the positive effects of perceptual learning are even wider on visuomotor tasks such as spatial orientation, reaching or grasping^{431,571,283,280}. This underlies the need for real-life evaluation of retinal prosthesis, but more importantly it emphasizes the relevance of multisensory rehabilitation training after prosthesis implantation. In spite of the relative rigidity of the connectivity pattern from the retina until the first cortical layers, these results suggest that the high plasticity observed in high-level visual areas can have a direct impact on a patient's functional outcomes. Pharmacological enhancement of synaptic plasticity in the adult brain – through serotonin uptake inhibitors administration, *e.g.* fluoxetine, donepezil^{572–574} – has also been envisaged to improve perceptual learning, *i.e.* the capacity of patients to adapt and make functional use of their devices. Yet, learning depends on the relevance of the provided input, and has shown its limitations when the spatio-temporal characteristic of phosphenes were too far from sighted sensory inputs²⁷⁰. The further the provided inputs are from the expected sighted retinal, the higher the perceptual learning and the cognitive load are for patients.

In summary, granted retinal prosthesis can offer minimal spatial and temporal resolution, the plasticity of higher-level and cross-modal sensory areas, together with their early shaping with visual experience in late blind patients, represents a formidable opening for useful functional sight restoration. Naturalistic stimulation paradigms designed to match and take advantage of the intrinsic retinal processing can only favor the offered spatial resolution and facilitate its integration in the poorly plastic early visual pathway. Cortical and behavioral responses of wide-field retinal stimulation should provide precious insights on how the brain can resolve the interaction of prosthetic and natural vision, as well as the inevitable deficiencies of artificial vision.

References

1. Wong *et al.* Global prevalence of age-related macular degeneration and disease burden projection for 2020 and 2040: a systematic review and meta-analysis *Lancet Glob. Health (N. Y.)* **2**, 106–16 (2014).
2. Burton, H. Visual Cortex Activity in Early and Late Blind People. *J. Neurosci.* **23**, 4005–4011 (2003).
3. Qin, W., Liu, Y., Jiang, T. & Yu, C. The Development of Visual Areas Depends Differently on Visual Experience. *PLoS ONE* **8**, e53784 (2013).
4. Spence, C., Nicholls, M. E., Gillespie, N. & Driver, J. Cross-modal links in exogenous covert spatial orienting between touch, audition, and vision. *Percept. Psychophys.* **60**, 544–557 (1998).
5. Greene, A. J., Easton, R. D. & LaShell, L. S. Visual–auditory events: cross-modal perceptual priming and recognition memory. *Conscious. Cogn.* **10**, 425–435 (2001).
6. Spence, C., Parise, C. & Chen, Y.-C. The Colavita visual dominance effect. in *The neural bases of multisensory processes* (CRC Press/Taylor & Francis, 2012).
7. Cattaneo, Z., Vecchi, T., Monegato, M., Pece, A. & Cornoldi, C. Effects of late visual impairment on mental representations activated by visual and tactile stimuli. *Brain Res.* **1148**, 170–176 (2007).
8. Heller, M. A. Picture and Pattern Perception in the Sighted and the Blind: The Advantage of the Late Blind. *Perception* **18**, 379–389 (1989).
9. Iverson, J. M., Tencer, H. L., Lany, J. & Goldin-Meadow, S. The Relation Between Gesture and Speech in Congenitally Blind and Sighted Language-Learners. *J. Nonverbal Behav.* **24**, 105–130 (2000).
10. Bedny, M., Pascual-Leone, A., Dravida, S. & Saxe, R. A sensitive period for language in the visual cortex: Distinct patterns of plasticity in congenitally versus late blind adults. *Brain Lang.* **122**, 162–170 (2012).
11. Pasqualotto, A., Spiller, M. J., Jansari, A. S. & Proulx, M. J. Visual experience facilitates allocentric spatial representation. *Behav. Brain Res.* **236**, 175–179 (2013).
12. Lorach, H. *et al.* Interactions of Prosthetic and Natural Vision in Animals With Local Retinal Degeneration. *Investig. Ophthalmology Vis. Sci.* **56**, 7444 (2015).
13. Hahm, B.-J. *et al.* Depression and the vision-related quality of life in patients with retinitis pigmentosa. *Br. J. Ophthalmol.* **92**, 650–654 (2008).
14. Sugawara, T. *et al.* Relationship between peripheral visual field loss and vision-related quality of life in patients with retinitis pigmentosa. *Eye* **24**, 535–539 (2010).
15. Zeeshan, M. & Aslam, N. Resilience and psychological well-being among congenitally blind, late blind and sighted individuals. *J. Educ. Res. Stud.* **1**, 1–7 (2013).
16. World Health Organization. ICD-11. in *The 11th Revision of the International Classification of Diseases 11* doi:<http://www.who.int/classifications/icd/en/>.
17. Lee, R., Wong, T. Y. & Sabanayagam, C. Epidemiology of diabetic retinopathy, diabetic macular edema and related vision loss. *Eye Vis.* **2**, 17 (2015).
18. Cho, N. H. *et al.* IDF Diabetes Atlas: Global estimates of diabetes prevalence for 2017 and projections for 2045. *Diabetes Res. Clin. Pract.* **138**, 271–281 (2018).
19. Hamel, C. Retinitis pigmentosa. *Orphanet J. Rare Dis.* **1**, 40 (2006).
20. Hartong, D. T., Berson, E. L. & Dryja, T. P. Retinitis pigmentosa. *The Lancet* **368**, 1795–1809 (2006).
21. Daiger, S. P. Perspective on Genes and Mutations Causing Retinitis Pigmentosa. *Arch. Ophthalmol.* **125**, 151 (2007).
22. Parmeggiani, F. *et al.* Retinitis Pigmentosa: Genes and Disease Mechanisms. *Curr. Genomics* **12**, 238–249 (2011).
23. Stefánsson, E. *et al.* Screening and prevention of diabetic blindness. *Acta Ophthalmol. Scand.* **78**, 374–385 (2000).
24. Einarsdóttir, A. B. & Stefánsson, E. Prevention of diabetic retinopathy. *The Lancet* **373**, 1316–1318 (2009).
25. Borrie, S. C., Duggan, J. & Cordeiro, M. F. Retinal cell apoptosis. *Expert Rev. Ophthalmol.* **4**, 27–45 (2009).
26. Doonan, F., Groeger, G. & Cotter, T. G. Preventing retinal apoptosis — Is there a common therapeutic theme? *Exp. Cell Res.* **318**, 1278–1284 (2012).
27. Murakami, Y. *et al.* Programmed necrosis, not apoptosis, is a key mediator of cell loss and DAMP-mediated inflammation in dsRNA-induced retinal degeneration. *Cell Death Differ.* **21**, 270–277 (2014).
28. Dennis, J., Baggaley, H. C., Brown, G. M., Rubin, G. S. & Astle, A. T. Properties of Visual Field Defects Around the Monocular Preferred Retinal Locus in Age-Related Macular Degeneration. *Investig. Ophthalmology Vis. Sci.* **58**, 2652 (2017).
29. Goetz, G. & Palanker, D. Electronic approaches to restoration of sight. *Rep. Prog. Phys.* **79**, 096701 (2016).
30. Tarita-Nistor, L., González, E. G., Markowitz, S. N., Lillakas, L. & Steinbach, M. J. Increased Role of Peripheral Vision in Self-Induced Motion in Patients with Age-Related Macular Degeneration. *Investig. Ophthalmology Vis. Sci.* **49**, 3253 (2008).
31. Mathenge, W. Age-related macular degeneration. *Community Eye Health J.* **27**, 49 (2014).
32. Fine, E. M. & Rubin, G. S. Effects of cataract and scotoma on visual acuity: a simulation study. *Optom. Vis. Sci. Off. Publ. Am. Acad. Optom.* **76**, 468–473 (1999).
33. Ergun, E. *et al.* Scotoma size and reading speed in patients with subfoveal occult choroidal neovascularization in age-related macular degeneration. *Ophthalmology* **110**, 65–69 (2003).
34. Rovamo, J. & Virsu, V. An estimation and application of the human cortical magnification factor. *Exp. Brain Res.* **37**, 495–510 (1979).
35. Schmolesky, M. The Primary Visual Cortex by Matthew Schmolesky. *Webvision, Moran Eye Center* (2020).
36. Grover, S., Fishman, G. A., Anderson, R. J., Alexander, K. R. & Derlacki, D. J. Rate of Visual Field Loss in Retinitis Pigmentosa. *Ophthalmology* **104**, 460–465 (1997).
37. Vámos, R. *et al.* The Structure and Function of the Macula in Patients with Advanced Retinitis Pigmentosa. *Investig. Ophthalmology Vis. Sci.* **52**, 8425 (2011).
38. Massof, R. W. & Finkelstein, D. Two forms of autosomal dominant primary retinitis pigmentosa. *Doc. Ophthalmol.* **51**, 289–346 (1981).

39. Daiger, S. P., Sullivan, L. S. & Bowne, S. J. RetNet. *RetNet* <https://sph.uth.edu/retnet/home.htm>.
40. Phelan, J. K. & Bok, D. A brief review of retinitis pigmentosa and the identified retinitis pigmentosa genes. *Mol Vis* **6**, 24 (2000).
41. Grover, S., Fishman, G. A. & Brown Jr, J. Patterns of visual field progression in patients with retinitis pigmentosa. *Ophthalmology* **105**, 1069–1075 (1998).
42. Birch, D. G., Anderson, J. L. & Fish, G. E. Yearly rates of rod and cone functional loss in retinitis pigmentosa and cone-rod dystrophy. The authors have no financial interest in any aspect of this study. *Ophthalmology* **106**, 258–268 (1999).
43. Jones B. W. *et al.* Retinal remodeling in human retinitis pigmentosa. *Exp. Eye Res.* **150**, 149–165 (2016).
44. Grover, S. *et al.* Visual acuity impairment in patients with retinitis pigmentosa at age 45 years or older. *Ophthalmology* **106**, 1780–1785 (1999).
45. Acton, J. H., Gibson, J. M. & Cubbidge, R. P. Quantification of Visual Field Loss in Age-Related Macular Degeneration. *PLoS ONE* **7**, e39944 (2012).
46. Syndicat national des Ophthalmologistes de France. Malvoyance et Handicap Visuel. *SNOF (Syndicat National des Ophthalmologistes de France)* www.snof.org/public/conseiller/malvoyance-et-handicaps-visuels (2020).
47. Eyecare Trust. Registering As Blind or Partially Sighted. *Eyecare Trust UK* <https://www.eyecaretrust.org.uk>.
48. Brasse, P. The Situation of the Blind and Visually Impaired in Germany — An Overview. *American Council of the Blind (ACB)* <https://acb.org/situation-blind-and-visually-impaired-germany>.
49. Lee, S. Y. & Mesfin, F. B. Blindness. *National Health* | www.ncbi.nlm.nih.gov/books/NBK448182/.
50. Colenbrander, A. Visual standards: Aspects and ranges of vision loss. in *Report prepared for the 29th International Congress of the International Council of Ophthalmology, Sydney, Australia* (2002).
51. Horton, S. & Guly, C. Prevention and treatment of age-related macular degeneration. *Prescriber* www.prescriber.co.uk (2017).
52. Han, Sang Beom, Kwon, Ji Won, & Han, Young Keun. Clinical aspect of low vision patients due to macular degeneration. *J. Korean Ophthalmol. Soc.* **50**, 280–284 (2009).
53. Donnell J. Creel. The Electroretinogram and Electro-oculogram: Clinical Applications. *Webvision, Moran Eye Center* webvision.med.utah.edu.
54. Weleber, R. G. & Gregory-Evans, K. Retinitis Pigmentosa and Allied Disorders. in *Retina* 395–498 (Elsevier, 2006). doi:10.1016/B978-0-323-02598-0.50023-9.
55. Lambertus, S. *et al.* Highly sensitive measurements of disease progression in rare disorders: Developing and validating a multimodal model of retinal degeneration in Stargardt disease. *PLOS ONE* **12**, e0174020 (2017).
56. Li, Y. *et al.* Long-term Safety and Efficacy of Human-Induced Pluripotent Stem Cell (iPS) Grafts in a Preclinical Model of Retinitis Pigmentosa. *Mol. Med.* **18**, 1312–1319 (2012).
57. Bassuk, A. G., Zheng, A., Li, Y., Tsang, S. H. & Mahajan, V. B. Precision Medicine: Genetic Repair of Retinitis Pigmentosa in Patient-Derived Stem Cells. *Sci. Rep.* **6**, 19969 (2016).
58. Latella, M. C. *et al.* In vivo Editing of the Human Mutant Rhodopsin Gene by Electroporation of Plasmid-based CRISPR/Cas9 in the Mouse Retina. *Mol. Ther. - Nucleic Acids* **5**, e389 (2016).
59. Yu, W. *et al.* Nrl knockdown by AAV-delivered CRISPR/Cas9 prevents retinal degeneration in mice. *Nat. Commun.* **8**, 14716 (2017).
60. Moreno, A. M. *et al.* In Situ Gene Therapy via AAV-CRISPR-Cas9-Mediated Targeted Gene Regulation. *Mol. Ther.* **26**, 1818–1827 (2018).
61. Vagni, P. *et al.* Gene Editing Preserves Visual Functions in a Mouse Model of Retinal Degeneration. *Front. Neurosci.* **13**, 945 (2019).
62. Smalley, E. First AAV gene therapy poised for landmark approval. *Nat. Biotechnol.* **35**, 998–999 (2017).
63. Pennesi, M. E. *et al.* Results at 5 Years After Gene Therapy for RPE65-Deficient Retinal Dystrophy. *Hum. Gene Ther.* **29**, 1428–1437 (2018).
64. Roska, B. & Sahel, J.-A. Restoring vision. *Nature* **557**, 359–367 (2018).
65. The Eyetech Study Group. Anti-vascular endothelial growth factor therapy for subfoveal choroidal neovascularization secondary to age-related macular degeneration: Phase II study results. *Ophthalmology* **110**, 979–986 (2003).
66. Ventrice, P. *et al.* Anti-vascular endothelial growth factor drugs safety and efficacy in ophthalmic diseases. *J. Pharmacol. Pharmacother.* **4**, S38–S42 (2013).
67. Tranos, P. *et al.* Resistance to antivascular endothelial growth factor treatment in age-related macular degeneration. *Drug Des. Devel. Ther.* **7**, 485–490 (2013).
68. Santos, A. *et al.* Preservation of the inner retina in retinitis pigmentosa. A morphometric analysis. *Arch Ophthalmol Chic Ill* **115** 511–5 (1997).
69. Medeiros, N. E. & Curcio, C. A. Preservation of Ganglion Cell Layer Neurons in Age-Related Macular Degeneration. *Invest. Ophthalmol. Vis. Sci.* **42**, 9 (2001).
70. Liu, H., Agam, Y., Madsen, J. R. & Kreiman, G. Timing, Timing, Timing: Fast Decoding of Object Information from Intracranial Field Potentials in Human Visual Cortex. *Neuron* **62**, 281–290 (2009).
71. Potter, M. C., Wyble, B., Hagmann, C. E. & McCourt, E. S. Detecting meaning in RSVP at 13 ms per picture. *Atten. Percept. Psychophys.* **76**, 270–279 (2014).
72. Purves, D. *et al.* Phototransduction. *Neurosci. 2nd Ed.* (2001).
73. Terakita, A. The opsins. *Genome Biol.* **6**, 213 (2005).
74. Büchel, C., Price, C. & Friston, K. A multimodal language region in the ventral visual pathway. *Nature* **394**, 274–277 (1998).
75. Amedi, A., Malach, R., Hendler, T., Peled, S. & Zohary, E. Visuo-haptic object-related activation in the ventral visual pathway. *Nat. Neurosci.* **4**, 324–330 (2001).
76. Kravitz, D. J., Saleem, K. S., Baker, C. I. & Mishkin, M. A new neural framework for visuospatial processing. *Nat. Rev. Neurosci.* **12**, 217 (2011).
77. Sheth, B. R. & Young, R. Two Visual Pathways in Primates Based on Sampling of Space: Exploitation and Exploration of Visual Information. *Front. Integr. Neurosci.* **10**, (2016).
78. Graubard, K. Synaptic transmission without action potentials: input-output properties of a nonspiking presynaptic neuron. *J. Neurophysiol.* **41**, 1014–1025 (1978).
79. Baden, T. *et al.* The functional diversity of retinal ganglion cells in the mouse. *Nature* **529**, 345–350 (2016).
80. MacNeil, M. A. & Masland, R. H. Extreme Diversity among Amacrine Cells: Implications for Function. *Neuron* **20**, 971–982 (1998).
81. Cherry, T. J., Trimarchi, J. M., Stadler, M. B. & Cepko, C. L. Development and diversification of retinal amacrine interneurons at single cell resolution. *Proc. Natl. Acad. Sci.* **106**, 9495–9500 (2009).
82. Dacey, D. Origins of perception : retinal ganglion cell diversity and the creation of parallel visual pathways. *Cogn. Neurosci.* **3**, 281-301. (2004).
83. Glezer, V. D. The receptive fields of the retina. *Vision Res.* **5**, 497–525 (1965).
84. Dacey, D. M. The mosaic of midget ganglion cells in the human retina. *J. Neurosci.* **13**, 5334–5355 (1993).

85. Lee, B. B. Receptive field structure in the primate retina. *Vision Res.* **36**, 631–644 (1996).
86. Devries, S. H. & Baylor, D. A. Mosaic Arrangement of Ganglion Cell Receptive Fields in Rabbit Retina. *J. Neurophysiol.* **78**, 2048–2060 (1997).
87. Vardi, N., Morigiwa, K., Wang, T.-L., Shi, Y.-J. & Sterling, P. Neurochemistry of the mammalian cone 'synaptic complex'. *Vision Res.* **38**, 1359–1369 (1998).
88. Deniz, S. *et al.* Mammalian retinal horizontal cells are unconventional GABAergic neurons. *J. Neurochem.* **116**, 350–362 (2011).
89. Wässle, H. Parallel processing in the mammalian retina. *Nat. Rev. Neurosci.* **5**, 747–757 (2004).
90. Diamond, J. S. Inhibitory Interneurons in the Retina: Types, Circuitry, and Function. *Annu. Rev. Vis. Sci.* **3**, 1–24 (2017).
91. Yang, X. L. & Wu, S. M. Feedforward lateral inhibition in retinal bipolar cells: input-output relation of the horizontal cell-depolarizing bipolar cell synapse. *Proc. Natl. Acad. Sci.* **88**, 3310–3313 (1991).
92. Cook, P. B. & McReynolds, J. S. Lateral inhibition in the inner retina is important for spatial tuning of ganglion cells. *Nat. Neurosci.* **1**, 714–719 (1998).
93. Ichinose, T. & Lukasiewicz, P. D. Inner and outer retinal pathways both contribute to surround inhibition of salamander ganglion cells. *J. Physiol.* **565**, 517–535 (2005).
94. Mirochnik, R. M. & Pezaris, J. S. Contemporary approaches to visual prostheses. *Mil. Med. Res.* **6**, 19 (2019).
95. Humayun, M. S. *et al.* Morphometric analysis of the extramacular retina from postmortem eyes with retinitis pigmentosa. *Invest. Ophthalmol. Vis. Sci.* **40**, 143–148 (1999).
96. Kim, S. Y. *et al.* Morphometric analysis of the macula in eyes with geographic atrophy due to age-related macular degeneration. *Retina Phila. Pa* **22**, 464–470 (2002).
97. Kim, S. Y. *et al.* Morphometric analysis of the macula in eyes with disciform age-related macular degeneration. *Retina Phila. Pa* **22**, 471–477 (2002).
98. Weiland, J. D. & Humayun, M. S. Retinal Prosthesis. *IEEE Trans. Biomed. Eng.* **61**, 1412–1424 (2014).
99. Ghezzi, D. Retinal prostheses: progress toward the next generation implants. *Front. Neurosci.* **9**, (2015).
100. Bloch, E., Luo, Y. & da Cruz, L. Advances in retinal prosthesis systems. *Ther. Adv. Ophthalmol.* **11**, 2515841418817501 (2019).
101. Gargini, C., Terzibasi, E., Mazzoni, F. & Strettoi, E. Retinal organization in the retinal degeneration 10 (rd10) mutant mouse: A morphological and ERG study. *J. Comp. Neurol.* **500**, (2007).
102. Mazzoni, F., Novelli, E. & Strettoi, E. Retinal ganglion cells survive and maintain normal dendritic morphology in a mouse model of inherited photoreceptor degeneration. *J. Neurosci.* **28**, 14282–14292 (2008).
103. Jones, B. W. *et al.* Retinal remodeling. *Jpn. J. Ophthalmol.* **56**, 289–306 (2012).
104. Sullivan R.K. P., WoldeMussie E, & Pow D. V. Dendritic and Synaptic Plasticity of Neurons in the Human Age-Related Macular Degeneration Retina. *Invest. Ophthalmol. Vis. Sci.* **48**, 2782 (2007).
105. Jones, B. W. *et al.* Retinal Remodeling and Metabolic Alterations in Human AMD. *Front. Cell. Neurosci.* **10**, (2016).
106. Jones, B. W. *et al.* Retinal remodeling triggered by photoreceptor degenerations. *J. Comp. Neurol.* **464**, 1–16 (2003).
107. Marc, R. E. & Jones, B. W. Retinal remodeling in inherited photoreceptor degenerations. *Mol. Neurobiol.* **28**, 139–147 (2003).
108. Sullivan, R., Penfold, P. & Pow, D. V. Neuronal migration and glial remodeling in degenerating retinas of aged rats and in nonneovascular AMD. *Invest. Ophthalmol. Vis. Sci.* **44**, 856–865 (2003).
109. Yee, C. W., Toychiev, A. H., Ivanova, E. & Sagdullaev, B. T. Aberrant synaptic input to retinal ganglion cells varies with morphology in a mouse model of retinal degeneration. *J. Comp. Neurol.* **522**, 4085–4099 (2014).
110. Cotman, C. W. & Sampedro, M. N. Brain Function, Synapse Renewal, and Plasticity. *Annu. Rev. Psychol.* **33**, 371–401 (1982).
111. Chen, S. & Hillman, D. E. Robust synaptic plasticity of striatal cells following partial deafferentation. *Brain Res.* **520**, 103–114 (1990).
112. Deller, T. *et al.* Lesion-Induced Axonal Sprouting in the Central Nervous System. in *Brain Repair* (ed. Bähr, M.) vol. 557 101–121 (Springer US, 2006).
113. Li, Z., Klijavin, I. & Milam, A. Rod photoreceptor neurite sprouting in retinitis pigmentosa. *J. Neurosci.* **15**, 5429–5438 (1995).
114. Strettoi, E. & Pignatelli, V. Modifications of retinal neurons in a mouse model of retinitis pigmentosa. *Proc. Natl. Acad. Sci. U. S. A.* **97**, 11020–11025 (2000).
115. Jones, B. W. & Marc, R. E. Retinal remodeling during retinal degeneration. *Retin. Remodel. Retin. Degener.* **81**, 123–137 (2005).
116. Cuenca, N., Pinilla, I., Sauvé, Y. & Lund, R. Early changes in synaptic connectivity following progressive photoreceptor degeneration in RCS rats. *Eur. J. Neurosci.* **22**, 1057–1072 (2005).
117. Yang, J., Nan, C., Ripps, H. & Shen, W. Destructive Changes in the Neuronal Structure of the FVB/N Mouse Retina. *PLoS One* **10**, e0129719 (2015).
118. Jones, B. W., Watt, C. B. & Marc, R. E. Retinal remodelling. *Clin. Exp. Optom.* **88**, 282–291 (2005).
119. Watt, C. B., Jones, B. W., Yang, J.-H., Marc, R. E. & LaVail, M. M. Complex Rewiring In Retinal Remodeling. *Invest. Ophthalmol. Vis. Sci.* **45**, 777–777 (2004).
120. Jones, B. W. *et al.* Structure and Function of Microneuromas in Retinal Remodeling. *Invest. Ophthalmol. Vis. Sci.* **48**, 2487–2487 (2007).
121. Margolis, D. J. & Detwiler, P. B. Cellular Origin of Spontaneous Ganglion Cell Spike Activity in Animal Models of Retinitis Pigmentosa. *J. Ophthalmol.* **2011**, (2011).
122. Strettoi, E., Porciatti, V., Falsini, B., Pignatelli, V. & Rossi, C. Morphological and Functional Abnormalities in the Inner Retina of the rd/rd Mouse. *J. Neurosci.* **22**, 5492–5504 (2002).
123. MARC, R. E., Jones, B. W. & Anderson, J. R. Neural reprogramming in retinal degenerations. *Invest. Ophthalmol. Vis. Sci.* **48**, 3364–3371. (2007).
124. Yanai, D. *et al.* The value of preoperative tests in the selection of blind patients for a permanent microelectronic implant. *Trans. Am. Ophthalmol. Soc.* **101**, 223–228; discussion 228–230 (2003).
125. Naycheva, L. *et al.* Phosphene thresholds elicited by transcorneal electrical stimulation in healthy subjects and patients with retinal diseases. *Invest. Ophthalmol. Vis. Sci.* **53**, 7440–7448 (2012).
126. Finn, A. P., Grewal, D. S. & Vajzovic, L. Argus II retinal prosthesis system: a review of patient selection criteria, surgical considerations, and post-operative outcomes. *Clin. Ophthalmol. Auckl. NZ* **12**, 1089 (2018).
127. Shepherd, R. K. & Javel, E. Electrical stimulation of the auditory nerve. I. Correlation of physiological responses with cochlear status. *Hear. Res.* **108**, 112–144 (1997).
128. Grill, W. M., Craggs, M. D., Foreman, R. D., Ludlow, C. L. & Buller, J. L. Emerging clinical applications of electrical stimulation: Opportunities for restoration of function. **38**, 14 (2001).

129. Shinkman, P. G. Electrical Stimulation of the Brain. in *International Encyclopedia of the Social & Behavioral Sciences* (eds. Smelser, N. J. & Baltes, P. B.) 4382–4385 (Pergamon, 2001). doi:10.1016/B0-08-043076-7/03418-5.
130. Creasey, G. H. *et al.* Clinical Applications of Electrical Stimulation After Spinal Cord Injury. *J. Spinal Cord Med.* **27**, 365–375 (2004).
131. McIntyre, C. C. & Thakor, N. V. Uncovering the Mechanisms of Deep Brain Stimulation for Parkinson's Disease through Functional Imaging, Neural Recording, and Neural Modeling. *Crit. Rev. Trade Biomed. Eng.* **30**, (2002).
132. Gordon, B. & Ledoux, K. CHAPTER 10 - Direct Electrical Stimulation of Language Cortex. in *Handbook of the Neuroscience of Language* (eds. Stemmer, B. & Whitaker, H. A.) 105–113 (Elsevier, 2008). doi:10.1016/B978-0-08-045352-1.00010-0.
133. Tyler, R. S. *et al.* Electrical Stimulation of the Cochlea to Reduce Tinnitus. *Semin. Hear.* **29**, 326–332 (2008).
134. Bordi, F., Cametti, C. & Naglieri, A. Ionic Transport in Lipid Bilayer Membranes. *Biophys. J.* **74**, 1358–1370 (1998).
135. Schoen, I. & Fromherz, P. The Mechanism of Extracellular Stimulation of Nerve Cells on an Electrolyte-Oxide-Semiconductor Capacitor. *Biophys. J.* **92**, 1096–1111 (2007).
136. Yue, L., Weiland, J. D., Roska, B. & Humayun, M. S. Retinal stimulation strategies to restore vision: Fundamentals and systems. *Prog. Retin. Eye Res.* **53**, 21–47 (2016).
137. Löwenstein, K. & Borchardt, M. Symptomatologie und elektrische Reizung bei einer Schußverletzung des Hinterhauptlappens. *Dtsch. Z. Für Nervenheilkd.* **58**, 264–292 (1918).
138. Krause, F. Die Sehbahn in chirurgischer Beziehung und die faradische Reizung des Sehzentrums. *Klin. Wochenschr.* **3**, 1260–1265 (1924).
139. Foerster, O. Beiträge zur Pathophysiologie der Sehbahn und der Sehsphäre. *J. Psychol. Neurol.* 39:463 (1929).
140. Hodgkin, A. L. & Huxley, A. F. A quantitative description of membrane current and its application to conduction and excitation in nerve. *J. Physiol.* **117**, 500–544 (1952).
141. Tassicker, G. E. Retinal stimulator. (1956).
142. Button, J. & Putnam, T. Visual responses to cortical stimulation in the blind. *J. Iowa Med. Soc.* **52**, 17–21 (1962).
143. Veraart, C. *et al.* Visual sensations produced by optic nerve stimulation using an implanted self-sizing spiral cuff electrode. *Brain Res.* **813**, 181–186 (1998).
144. Delbeke, J., Oozeer, M. & Veraart, C. Position, size and luminosity of phosphenes generated by direct optic nerve stimulation. *Vision Res.* **43**, 1091–1102 (2003).
145. Sakaguchi, H. *et al.* Artificial vision by direct optic nerve electrode (AV-DONE) implantation in a blind patient with retinitis pigmentosa. *J. Artif. Organs* **12**, 206–209 (2009).
146. Lu, Y. *et al.* Electrical stimulation with a penetrating optic nerve electrode array elicits visuotopic cortical responses in cats. *J. Neural Eng.* **10**, 036022 (2013).
147. Gaillet, V. *et al.* Spatially selective activation of the visual cortex via intraneural stimulation of the optic nerve. *Nat. Biomed. Eng.* **4**, 181–194 (2020).
148. Maroon, J. C. & Kennerdell, J. S. Surgical approaches to the orbit: Indications and techniques. *J. Neurosurg.* **60**, 1226–1235 (1984).
149. Veraart, C., Wanet-Defalque, M.-C., Gérard, B., Vanlierde, A. & Delbeke, J. Pattern Recognition with the Optic Nerve Visual Prosthesis. *Artif. Organs* **27**, 996–1004 (2003).
150. Zeng, F.-G. Trends in Cochlear Implants. *Trends Amplif.* **8**, 1–34 (2004).
151. Rosahl, S. K. Vanishing senses—restoration of sensory functions by electronic implants. *Poiesis Prax.* **2**, 285–295 (2004).
152. Flores, T. *et al.* Optimization of pillar electrodes in subretinal prosthesis for enhanced proximity to target neurons. *J. Neural Eng.* **15**, 036011 (2018).
153. Clements, M. *et al.* An implantable power and data receiver and neuro-stimulus chip for a retinal prosthesis system. in *ISCAS'99. Proceedings of the 1999 IEEE International Symposium on Circuits and Systems VLSI (Cat. No.99CH36349)* vol. 1 194–197 (IEEE, 1999).
154. Clements, M. *et al.* An implantable neuro-stimulator device for a retinal prosthesis. in *1999 IEEE International Solid-State Circuits Conference. Digest of Technical Papers. ISSCC. First Edition (Cat. No.99CH36278)* 216–217 (IEEE, 1999). doi:10.1109/ISSCC.1999.759200.
155. Liu, W. *et al.* Retinal prosthesis to aid the visually impaired. in *IEEE SMC'99 Conference Proceedings. 1999 IEEE International Conference on Systems, Man, and Cybernetics (Cat. No.99CH37028)* vol. 4 364–369 (IEEE, 1999).
156. Margalit, E. *et al.* Retinal prosthesis for the blind. *Surv. Ophthalmol.* **47**, 335–356 (2002).
157. Humayun, M. S. *et al.* Visual perception in a blind subject with a chronic microelectronic retinal prosthesis. *Vision Res.* **43**, 2573–2581 (2003).
158. Luo, Y. H.-L. & Da Cruz, L. The Argus® II retinal prosthesis system. *Prog. Retin. Eye Res.* **50**, 89–107 (2016).
159. Second Sight Medical Products, Inc. Argus® II Retinal Prosthesis System Surgeon Manual 090001-004.
160. Olmos de Koo, L. C. & Gregori, N. Z. Step-by-Step Guide to Retinal Implant Surgery. *Retina Today* (2015).
161. Stanga, P. E. *et al.* Initial word recognition results with the Argus™ II retinal prosthesis. *Invest. Ophthalmol. Vis. Sci.* **51**, 426–426 (2010).
162. Stanga, P. E. *et al.* Patients blinded by outer retinal dystrophies are able to perceive simultaneous colors using the Argus® II retinal prosthesis system. *Invest. Ophthalmol. Vis. Sci.* **53**, 6952–6952 (2012).
163. Da Cruz, L. *et al.* The Argus II epiretinal prosthesis system allows letter and word reading and long-term function in patients with profound vision loss. *Br. J. Ophthalmol.* **97**, 632–636 (2013).
164. Stanga, P. *et al.* Face detection using the Argus® II retinal prosthesis system. *Invest. Ophthalmol. Vis. Sci.* **54**, 1766–1766 (2013).
165. Stieglitz, T., Beutel, H. & Keller, R. A flexible retina implant for people suffering from retinitis pigmentosa. *Proc. Int. Funct. Electr. Stimul. Soc.* 61–64 (1999).
166. Koch, C., Mokwa, W., Goertz, M. & Walter, P. First results of a study on a completely implanted retinal prosthesis in blind humans. in *2008 IEEE SENSORS 1237–1240* (2008). doi:10.1109/ICSENS.2008.4716667.
167. Waschkowski, F. *et al.* Development of very large electrode arrays for epiretinal stimulation (VLARS). *Biomed. Eng. OnLine* **13**, 11 (2014).
168. Lohmann, T. K. *et al.* The very large electrode array for retinal stimulation (VLARS)—A concept study. *J. Neural Eng.* **16**, 066031 (2019).
169. Hesse, L., Schanze, T., Wilms, M. & Eger, M. Implantation of retina stimulation electrodes and recording of electrical stimulation responses in the visual cortex of the cat. *Graefes Arch. Clin. Exp. Ophthalmol.* **238**, 840–845 (2000).
170. Keserü, M. *et al.* Acute electrical stimulation of the human retina with an epiretinal electrode array. *Acta Ophthalmol. (Copenh.)* **90**, e1–e8 (2012).
171. Richard, G. *et al.* Multicenter Study on Acute Electrical Stimulation of the Human Retina With an Epiretinal Implant: Clinical Results in 20 Patients. *Invest. Ophthalmol. Vis. Sci.* **46**, 1143–1143 (2005).

172. Richard, G., Keserue, M., Feucht, M., Post, N. & Hornig, R. Visual Perception After Long-Term Implantation of a Retinal Implant. *Invest. Ophthalmol. Vis. Sci.* **49**, 1786–1786 (2008).
173. Zhou, M., Yuce, M. R. & Liu, W. A non-coherent DPSK data receiver with interference cancellation for dual-band transcutaneous telemetries. *IEEE J. Solid-State Circuits* **43**, 2003–2012 (2008).
174. Hornig, R. *et al.* Pixium vision: first clinical results and innovative developments. in *Artificial Vision* 99–113 (Springer, 2017).
175. Eckmiller, R., Becker, M. & Hunermann, R. Dialog concepts for learning retina encoders. in *Proceedings of International Conference on Neural Networks (ICNN'97)* vol. 4 2315–2320 (IEEE, 1997).
176. Eckmiller, R. Learning Retina Implants with Epiretinal Contacts. *Ophthalmic Res.* **29**, 281–289 (1997).
177. Eckmiller, R., Neumann, D. & Baruth, O. Tunable retina encoders for retina implants: why and how. *J. Neural Eng.* **2**, S91–S104 (2005).
178. Muqit, M. M. K. *et al.* Six-Month Safety and Efficacy of the Intelligent Retinal Implant System II Device in Retinitis Pigmentosa. *Ophthalmology* **126**, 637–639 (2019).
179. Hemami, P. & Jacobs, M. *Pixium seeks to address short Iris II lifespan.* London: Edison Investment Research.
180. Mills, J. O., Jallil, A. & Stanga, P. E. Electronic retinal implants and artificial vision: journey and present. *Eye* **31**, 1383–1398 (2017).
181. Zrenner, E. *et al.* The subretinal implant ALPHA: implantation and functional results. in *Artificial Vision* 65–83 (Springer, 2017).
182. Prévot, P.-H. *et al.* Behavioural responses to a photovoltaic subretinal prosthesis implanted in non-human primates. *Nat. Biomed. Eng.* **1**–9 (2019).
183. Stingl, K. *et al.* Artificial vision with wirelessly powered subretinal electronic implant alpha-IMS. *Proc. R. Soc. B Biol. Sci.* **280**, 20130077 (2013).
184. Daschner, R., Rothermel, A., Rudolf, R., Rudolf, S. & Stett, A. Functionality and performance of the subretinal implant chip Alpha AMS. *Sens Mater* **30**, 179–192 (2018).
185. Koitschev, A. *et al.* Extraocular surgical approach for placement of subretinal implants in blind patients: lessons from cochlear-implants. *J. Ophthalmol.* **2015**, (2015).
186. Stingl, K. *et al.* Subretinal visual implant alpha IMS—clinical trial interim report. *Vision Res.* **111**, 149–160 (2015).
187. Gekeler, F. *et al.* Re-alignment and explantation of subretinal prostheses: surgical aspects and proteomic analyses. *Invest. Ophthalmol. Vis. Sci.* **54**, 1036–1036 (2013).
188. Daschner, R. *et al.* Laboratory and clinical reliability of conformally coated subretinal implants. *Biomed. Microdevices* **19**, (2017).
189. Stingl, K. *et al.* Interim results of a multicenter trial with the new electronic subretinal implant alpha AMS in 15 patients blind from inherited retinal degenerations. *Front. Neurosci.* **11**, 445 (2017).
190. Rizzo, J. F., Wyatt, J., Loewenstein, J., Kelly, S. & Shire, D. Methods and perceptual thresholds for short-term electrical stimulation of human retina with microelectrode arrays. *Invest. Ophthalmol. Vis. Sci.* **44**, 5355–5361 (2003).
191. Rizzo, J. F. *et al.* Development of the boston retinal prosthesis. in *2011 Annual International Conference of the IEEE Engineering in Medicine and Biology Society* 3135–3138 (2011). doi:10.1109/IEMBS.2011.6090855.
192. Kelly, S. K. *et al.* Developments on the Boston 256-channel retinal implant. in *2013 IEEE International Conference on Multimedia and Expo Workshops (ICMEW)* 1–6 (IEEE, 2013).
193. Palanker, D., Vankov, A., Huie, P. & Baccus, S. Design of a high-resolution optoelectronic retinal prosthesis. *J. Neural Eng.* **2**, 105 (2005).
194. Lorach, H. *et al.* Photovoltaic restoration of sight with high visual acuity. *Nat. Med.* **21**, (2015).
195. Wang, L. *et al.* Photovoltaic retinal prosthesis: implant fabrication and performance. *J. Neural Eng.* **9**, 046014 (2012).
196. Mathieson, K. *et al.* Photovoltaic retinal prosthesis with high pixel density. *Nat. Photonics* **6**, (2012).
197. Ho, E. *et al.* Characteristics of prosthetic vision in rats with subretinal flat and pillar electrode arrays. *J. Neural Eng.* **16**, 066027 (2019).
198. Pixium Vision SA. *Feasibility Study of Compensation for Blindness With the PRIMA System in Patients With Dry Age Related Macular Degeneration.* clinicaltrials.gov/ct2/show/NCT03333954 (2019).
199. Pixium Vision SA. *PRIMA US-Feasibility Study in Atrophic Dry AMD.* clinicaltrials.gov/ct2/show/NCT03392324 (2020).
200. Pixium Vision SA. Dry AMD and PRIMA feasibility studies indication. *Pixium Vision* www.pixium-vision.com.
201. Zrenner, E. *et al.* Subretinal electronic chips allow blind patients to read letters and combine them to words. *Proc. R. Soc. B Biol. Sci.* **278**, 1489–1497 (2011).
202. Rizzo, J. F. Update on Retinal Prosthetic Research: The Boston Retinal Implant Project. *J. Neuroophthalmol.* **31**, 160–168 (2011).
203. Suaning, G. J., Lovell, N. H. & Lehmann, T. Neuromodulation of the retina from the suprachoroidal space: The Phoenix 99 implant. in *2014 IEEE Biomedical Circuits and Systems Conference (BioCAS) Proceedings* 256–259 (2014). doi:10.1109/BioCAS.2014.6981711.
204. Ayton, L. N. *et al.* First-in-human trial of a novel suprachoroidal retinal prosthesis. *PLoS One* **9**, e115239 (2014).
205. Petoe, M. A. *et al.* Determining the contribution of retinotopic discrimination to localization performance with a suprachoroidal retinal prosthesis. *Invest. Ophthalmol. Vis. Sci.* **58**, 3231–3239 (2017).
206. Shivdasani, M. N. *et al.* Identification of characters and localization of images using direct multiple-electrode stimulation with a suprachoroidal retinal prosthesis. *Invest. Ophthalmol. Vis. Sci.* **58**, 3962–3974 (2017).
207. Fujikado, T. *et al.* One-Year Outcome of 49-Channel Suprachoroidal–Transretinal Stimulation Prosthesis in Patients With Advanced Retinitis Pigmentosa. *Invest. Ophthalmol. Vis. Sci.* **57**, 6147–6157 (2016).
208. Endo, T. *et al.* Light localization with low-contrast targets in a patient implanted with a suprachoroidal–transretinal stimulation retinal prosthesis. *Graefes Arch. Clin. Exp. Ophthalmol.* **256**, 1723–1729 (2018).
209. Gupta, P. R. & Huckfeldt, R. M. Gene therapy for inherited retinal degenerations: initial successes and future challenges. *J. Neural Eng.* **14**, 051002 (2017).
210. Nagel, G. Channelrhodopsin-1: A Light-Gated Proton Channel in Green Algae. *Science* **296**, 2395–2398 (2002).
211. Nagel, G. *et al.* Channelrhodopsin-2, a directly light-gated cation-selective membrane channel. *Proc. Natl. Acad. Sci.* **100**, 13940–13945 (2003).
212. Boyden, E. S., Zhang, F., Bamberg, E., Nagel, G. & Deisseroth, K. Millisecond-timescale, genetically targeted optical control of neural activity. *Nat. Neurosci.* **8**, 1263–1268 (2005).
213. Bi, A. *et al.* Ectopic expression of a microbial-type rhodopsin restores visual responses in mice with photoreceptor degeneration. *Neuron* **50**, 23–33 (2006).
214. Lagali, P. S. *et al.* Light-activated channels targeted to ON bipolar cells restore visual function in retinal degeneration. *Nat. Neurosci.* **11**, 667–675 (2008).
215. Tomita, H. *et al.* Channelrhodopsin-2 gene transduced into retinal ganglion cells restores functional vision in genetically blind rats. *Exp. Eye Res.*

- 90, 429–436 (2010).
216. Taylor, W. R. & Smith, R. G. Transmission of scotopic signals from the rod to rod-bipolar cell in the mammalian retina. *Vision Res.* **44**, 3269–3276 (2004).
 217. Strettoi, E., Novelli, E., Mazzoni, F., Barone, I. & Damiani, D. Complexity of retinal cone bipolar cells. *Prog. Retin. Eye Res.* **29**, 272–283 (2010).
 218. Aggarwal, P., Nag, T. C. & Wadhwa, S. Age-related decrease in rod bipolar cell density of the human retina: an immunohistochemical study. *J. Biosci.* **32**, 293–298 (2007).
 219. Sjöstrand, J., Olsson, V., Popovic, Z. & Conradi, N. Quantitative estimations of foveal and extra-foveal retinal circuitry in humans. *Vision Res.* **39**, 2987–2998 (1999).
 220. Sengupta, A. *et al.* Red-shifted channelrhodopsin stimulation restores light responses in blind mice, macaque retina, and human retina. *EMBO Mol. Med.* **8**, 1248–1264 (2016).
 221. Yan, B. & Nirenberg, S. An embedded real-time processing platform for optogenetic neuroprosthetic applications. *IEEE Trans. Neural Syst. Rehabil. Eng.* **26**, 233–243 (2017).
 222. GenSight Biologics. *A Phase 1/2a, Open-Label, Non-Randomized, Dose-Escalation Study to Evaluate the Safety and Tolerability of GS030 in Subjects With Retinitis Pigmentosa*. <https://clinicaltrials.gov/ct2/show/NCT03326336> (2020).
 223. Dalkara, D. *et al.* In vivo-directed evolution of a new adeno-associated virus for therapeutic outer retinal gene delivery from the vitreous. *Sci. Transl. Med.* **5**, 189ra76–189ra76 (2013).
 224. Lu, Q. *et al.* AAV-mediated transduction and targeting of retinal bipolar cells with improved mGluR6 promoters in rodents and primates. *Gene Ther.* **23**, 680–689 (2016).
 225. Peterman, M. C. *et al.* The artificial synapse chip: a flexible retinal interface based on directed retinal cell growth and neurotransmitter stimulation. *Artif. Organs* **27**, 975–985 (2003).
 226. Corey M Rountree, Ashwin Raghunathan, John B Troy, & Laxman Saggere. Prototype chemical synapse chip for spatially patterned neurotransmitter stimulation of the retina ex vivo. *Microsyst. Nanoeng.* **3**, (2017).
 227. Nelson, R. & Connaughton, V. Bipolar cell pathways in the vertebrate retina. in *Webvision: The Organization of the Retina and Visual System [Internet]* (University of Utah Health Sciences Center, 2012).
 228. Ferrari, U. *et al.* Towards optogenetic vision restoration with high resolution. *PLOS Comput. Biol.* **16**, e1007857 (2020).
 229. Chow, A. Y., Bittner, A. K. & Pardue, M. T. The artificial silicon retina in retinitis pigmentosa patients (an American Ophthalmological Association thesis). *Trans. Am. Ophthalmol. Soc.* **108**, 120 (2010).
 230. Musienko, P., van den Brand, R., Maerzendorfer, O., Larmagnac, A. & Courtine, G. Combinatory Electrical and Pharmacological Neuroprosthetic Interfaces to Regain Motor Function After Spinal Cord Injury. *IEEE Trans. Biomed. Eng.* **56**, 2707–2711 (2009).
 231. Luo, Y. H.-L., Zhong, J. J., Clemo, M. & da Cruz, L. Long-term Repeatability and Reproducibility of Phosphene Characteristics in Chronically Implanted Argus II Retinal Prosthesis Subjects. *Am. J. Ophthalmol.* **170**, 100–109 (2016).
 232. Nanduri, D., Humayun, G. R. J., J. M. M. & D, W. J. Retinal Prosthesis Phosphene Shape Analysis. *2008 30th Annu. Int. Conf. IEEE Eng. Med. Biol. Soc.* 1785–8 (2008).
 233. Tsai, D. *et al.* Responses of Retinal Ganglion Cells to Extracellular Electrical Stimulation, from Single Cell to Population: Model-Based Analysis. *PLoS ONE* **7**, e53357 (2012).
 234. Beyeler, M. *et al.* A model of ganglion axon pathways accounts for percepts elicited by retinal implants. *Sci. Rep.* **9**, 9199 (2019).
 235. Grosberg, L. E. *et al.* Activation of ganglion cells and axon bundles using epiretinal electrical stimulation. *J. Neurophysiol.* (2017) doi:10.1152/jn.00750.2016.
 236. De Lahunta, A. & Glass, E. Visual System. in *Veterinary Neuroanatomy and Clinical Neurology* 389–432 (Elsevier, 2009). doi:10.1016/B978-0-7216-6706-5.00014-7.
 237. Weitz, A. C. *et al.* Improving the spatial resolution of epiretinal implants by increasing stimulus pulse duration. *Sci. Transl. Med.* **7**, (2015).
 238. Sinclair, N. C. *et al.* The Appearance of Phosphenes Elicited Using a Suprachoroidal Retinal Prosthesis. *Invest. Ophthalmol. Vis. Sci.* **57**, 4948–4961 (2016).
 239. Hartline, H. K. The Nerve Messages in the Fibers of the Visual Pathway. *JOSA* **30**, 239–247 (1940).
 240. Kuffler, S. W. Neurons in the retina: organization, inhibition and excitation problems. in *Cold Spring Harbor Symposia on Quantitative Biology* vol. 17 281–292 (Cold Spring Harbor Laboratory Press, 1952).
 241. Adrian, E. D. The basis of sensation. (1928).
 242. Wong, W. A Universal Law of Sensory Adaptation. *bioRxiv* 2020.02.17.953448 (2020) doi:10.1101/2020.02.17.953448.
 243. Tachibana, M. & Kaneko, A. Retinal bipolar cells receive negative feedback input from GABAergic amacrine cells. *Vis. Neurosci.* **1**, 297–305 (1988).
 244. Brown, S. P. & Masland, R. H. Spatial scale and cellular substrate of contrast adaptation by retinal ganglion cells. *Nat. Neurosci.* **4**, 44–51 (2001).
 245. Wark, B., Lundstrom, B. N. & Fairhall, A. Sensory adaptation. *Curr. Opin. Neurobiol.* **17**, 423–429 (2007).
 246. Demb, J. B. Functional circuitry of visual adaptation in the retina. *J. Physiol.* **586**, 4377–4384 (2008).
 247. Baccus, S. A. & Meister, M. Fast and Slow Contrast Adaptation in Retinal Circuitry. *Neuron* **36**, 909–919 (2002).
 248. Clarke, F. J. J. A study of Troxler's effect. *Opt. Acta Int. J. Opt.* **7**, 219–236 (1960).
 249. Pritchard, R. M. Stabilized images on the retina. *Sci. Am.* **204**, 72–79 (1961).
 250. Coppola, D. & Purves, D. The extraordinarily rapid disappearance of entopic images. *Proc. Natl. Acad. Sci.* **93**, 8001–8004 (1996).
 251. Walston, S. T., Chow, R. H. & Weiland, J. D. Direct measurement of bipolar cell responses to electrical stimulation in wholemount mouse retina. *J. Neural Eng.* **15**, 046003 (2018).
 252. Jensen, R. J. & Rizzo, J. F. Responses of ganglion cells to repetitive electrical stimulation of the retina. *J. Neural Eng.* **4**, S1 (2007).
 253. Freeman, D. K. & Fried, S. I. Multiple components of ganglion cell desensitization in response to prosthetic stimulation. *J. Neural Eng.* **8**, 016008 (2011).
 254. Engbert, R. & Mergenthaler, K. Microsaccades are triggered by low retinal image slip. *Proc. Natl. Acad. Sci.* **103**, 7192–7197 (2006).
 255. Rolfs, M., Laubrock, J. & Kliegl, R. Microsaccade-induced prolongation of saccade latencies depends on microsaccade amplitude. *J. Eye Mov. Res.* **1**, (2009).
 256. Sparks, D. L. The brainstem control of saccadic eye movements. *Nat. Rev. Neurosci.* **3**, 952–964 (2002).
 257. Ahissar, E., Arieli, A., Fried, M. & Bonneh, Y. On the possible roles of microsaccades and drifts in visual perception. *Vision Res.* **118**, 25–30 (2016).

258. Randl, K. R. Active dynamic vision based on micro-saccades. (2017).
259. Gerrits, H. J. M. & Vendrik, A. J. H. The influence of stimulus movements on perception in parafoveal stabilized vision. *Vision Res.* **14**, 175-181 (1974).
260. Ditchburn, R. W. The function of small saccades. *Vision Res.* (1980).
261. Hafed, Z. M. & Clark, J. J. Microsaccades as an overt measure of covert attention shifts. *Vision Res.* **42**, 2533-2545 (2002).
262. Engbert, R. & Kliegl, R. Microsaccades uncover the orientation of covert attention. *Vision Res.* **43**, 1035-1045 (2003).
263. Cohen, E. D. Prosthetic interfaces with the visual system: biological issues. *J. Neural Eng.* **4**, R14 (2007).
264. Wester, S. T., Rizzo, J. F., Balkwill, M. D. & Wall, C. Optokinetic Nystagmus as a Measure of Visual Function in Severely Visually Impaired Patients. *Invest. Ophthalmol. Vis. Sci.* **48**, 4542-4548 (2007).
265. Schiller, P. H. & Tehovnik, E. J. Visual prosthesis. *Perception* **37**, 1529-1559 (2008).
266. Paraskevoudi, N. & Pezaris, J. S. Eye Movement Compensation and Spatial Updating in Visual Prosthetics: Mechanisms, Limitations and Future Directions. *Front. Syst. Neurosci.* **12**, 73 (2019).
267. Vargas-Martín, F. & Peli, E. Eye Movements of Patients with Tunnel Vision While Walking. *Invest. Ophthalmol. Vis. Sci.* **47**, 5295-5302 (2006).
268. Pérez Fornos, A. *et al.* Temporal Properties of Visual Perception on Electrical Stimulation of the Retina. *Investig. Ophthalmology Vis. Sci.* **53**, 2720 (2012).
269. Fried, S., Hsueh, H. & Werblin, F. A Method for Generating Precise Temporal Patterns of Retinal Spiking Using Prosthetic Stimulation. *J. Neurophysiol.* **95**, (2006).
270. Erickson-Davis, C. & Korzybska, H. *What do blind people "see" with retinal prostheses? Observations and qualitative reports of epiretinal implant users.* <http://biorxiv.org/lookup/doi/10.1101/2020.02.03.932905> (2020) doi:10.1101/2020.02.03.932905.
271. Fine, I. & Boynton, G. M. Pulse trains to percepts: the challenge of creating a perceptually intelligible world with sight recovery technologies. *Philos. Trans. R. Soc. B Biol. Sci.* **370**, 20140208 (2015).
272. Ho, A. C. *et al.* Long-Term Results from an Epiretinal Prosthesis to Restore Sight to the Blind. *Ophthalmology* **122**, 1547-1554 (2015).
273. Fujikado, T. *et al.* Testing of Semicronically Implanted Retinal Prosthesis by Suprachoroidal-Transretinal Stimulation in Patients with Retinitis Pigmentosa. *Invest. Ophthalmol. Vis. Sci.* **52**, 4726-4733 (2011).
274. Geruschat, D. R. *et al.* FLORA™: Phase I development of a functional vision assessment for prosthetic vision users. *Clin. Exp. Optom.* **98**, 342-347 (2015).
275. Edwards, T. L. *et al.* Assessment of the Electronic Retinal Implant Alpha AMS in Restoring Vision to Blind Patients with End-Stage Retinitis Pigmentosa. *Ophthalmology* **125**, 432-443 (2018).
276. Hayes, J. S. *et al.* Visually Guided Performance of Simple Tasks Using Simulated Prosthetic Vision. *Artif. Organs* **27**, 1016-1028 (2003).
277. Pérez Fornos, A., Sommerhalder, J., Pittard, A., Safran, A. B. & Pelizzone, M. Simulation of artificial vision: IV. Visual information required to achieve simple pointing and manipulation tasks. *Vision Res.* **48**, 1705-1718 (2008).
278. Chader, G. J., Weiland, J. & Humayun, M. S. Artificial vision: needs, functioning, and testing of a retinal electronic prosthesis. *Prog. Brain Res.* **175**, 317-332 (2009).
279. Thorn, J. T., Migliorini, E. & Ghezzi, D. Virtual reality simulation of epiretinal stimulation highlights the relevance of the visual angle in prosthetic vision. *J. Neural Eng.* (2020) doi:10.1088/1741-2552/abb5bc.
280. Dagnelie, G. *et al.* Performance of real-world functional vision tasks by blind subjects improves after implantation with the Argus® II retinal prosthesis system. *Clin. Experiment. Ophthalmol.* **45**, 152-159 (2017).
281. Cha, K., Horch, K. W. & Normann, R. A. Mobility performance with a pixelized vision system. *Vision Res.* **32**, 1367-1372 (1992).
282. Sommerhalder, J. R. *et al.* Minimum requirements for mobility in unpredictable environments. *Invest. Ophthalmol. Vis. Sci.* **47**, 3204-3204 (2006).
283. Stronks, H. C. & Dagnelie, G. The functional performance of the Argus II retinal prosthesis. *Expert Rev. Med. Devices* **11**, 23-30 (2014).
284. Humayun, M. S. *et al.* Interim results from the international trial of Second Sight's visual prosthesis. *Ophthalmology* **119**, 779-788 (2012).
285. Ktiratschky, V. B. *et al.* Safety evaluation of retina implant alpha IMS—a prospective clinical trial. *Graefes Arch. Clin. Exp. Ophthalmol.* **253**, 381-387 (2015).
286. Cohen, E. *et al.* Optical coherence tomography imaging of retinal damage in real time under a stimulus electrode. *J. Neural Eng.* **8**, 056017 (2011).
287. Youssed, P. N., Sheibani, N. & Albert, D. M. Retinal light toxicity. *Eye* **1-14** (2011) doi:10.1038/eye.2010.149.
288. Henriques, F. C. Studies of thermal injury; the predictability and the significance of thermally induced rate processes leading to irreversible epidermal injury. *Arch. Pathol.* (1947).
289. Birngruber, R., Gabel, V. P. & Hillenkamp, F. Experimental studies of laser thermal retinal injury. *Health Phys.* **44**, 519-531 (1983).
290. Birngruber, R., Hillenkamp, F. & Gabel, V. P. Theoretical investigations of laser thermal retinal injury. (1985).
291. Delori, F. C., Webb, R. H. & Sliney, D. H. Maximum permissible exposures for ocular safety (ANSI 2000), with emphasis on ophthalmic devices. *J. Opt. Soc. Am. A* **24**, 1250 (2007).
292. Foote, C. S. Mechanisms of photooxygenation. *Prog. Clin. Biol. Res.* **170**, 3 (1984).
293. Solley, W. A. & Sternberg Jr, P. Retinal phototoxicity. *Int. Ophthalmol. Clin.* **39**, 1-12 (1999).
294. Verma, L., Venkatesh, P. & Tewari, H. K. Phototoxic retinopathy. *Ophthalmol. Clin. N. Am.* **14**, 601-609 (2001).
295. Glickman, R. D. Phototoxicity to the retina: mechanisms of damage. *Int. J. Toxicol.* **21**, 473-490 (2002).
296. Wenzel, A., Grimm, C., Samardzija, M. & Remé, C. E. Molecular mechanisms of light-induced photoreceptor apoptosis and neuroprotection for retinal degeneration. *Prog. Retin. Eye Res.* **24**, 275-306 (2005).
297. Gawande, A. A., Donovan, W. J., Ginsburg, A. P. & Marmor, M. F. Photoaversion in retinitis pigmentosa. *Br. J. Ophthalmol.* **73**, 115-120 (1989).
298. Digre, K. B. & Brennan, K. C. Shedding Light on Photophobia. *J. Neuroophthalmol.* **32**, 68 (2012).
299. Otsuka, Y. *et al.* Wavelength of light and photophobia in inherited retinal dystrophy. *Sci. Rep.* **10**, 14798 (2020).
300. Aboshiha, J., Dubis, A. M., Carroll, J., Hardcastle, A. J. & Michaelides, M. The cone dysfunction syndromes. *Br. J. Ophthalmol.* **100**, 115-121 (2016).
301. Colombo, L. *et al.* Visual function improvement using photocromic and selective blue-violet light filtering spectacle lenses in patients affected by retinal diseases. *BMC Ophthalmol.* **17**, 1-6 (2017).
302. Schatz, A. *et al.* Transcorneal Electrical Stimulation for Patients with Retinitis Pigmentosa: A Prospective, Randomized, Sham-Controlled

- Exploratory Study. *Investig. Ophthalmology Vis. Sci.* **52**, 4485 (2011).
303. Ito, Y. *et al.* Cultures of neurons on micro-electrode array in hybrid retinal implant. in *1999 IEEE International Conference on Systems, Man, and Cybernetics (Cat. No.99CH37028)* vol. 4 414–417 (IEEE, 1999).
304. Ming, G., Henley, J., Tessier-Lavigne, M., Song, H. & Poo, M. Electrical Activity Modulates Growth Cone Guidance by Diffusible Factors. *Neuron* **29**, 441–452 (2001).
305. Yamashita, M. Electric axon guidance in embryonic retina: Galvanotropism revisited. *Biochem. Biophys. Res. Commun.* **431**, 280–283 (2013).
306. Dagnelie, G. Retinal implants: emergence of a multidisciplinary field. *Curr. Opin. Neurol.* **25**, 67–75 (2012).
307. Krishnamoorthy, V. *et al.* Retinal Remodeling: Concerns, Emerging Remedies and Future Prospects. *Front. Cell. Neurosci.* **10**, (2016).
308. Petersen-Jones, S. M. Animal models of human retinal dystrophies. *Eye* **12**, 566–570 (1998).
309. Volland, S., Esteve-Rudd, J., Hoo, J., Yee, C. & Williams, D. S. A Comparison of Some Organizational Characteristics of the Mouse Central Retina and the Human Macula. *PLoS ONE* **10**, (2015).
310. Ling, T. *et al.* Full-field interferometric imaging of propagating action potentials. *Light Sci. Appl.* **7**, 107 (2018).
311. Laforest, T. *et al.* Transscleral optical phase imaging of the human retina. *Nat. Photonics* **14**, 439–445 (2020).
312. Lee, D. Y., Lorach, H., Huie, P. & Palanker, D. Implantation of Modular Photovoltaic Subretinal Prosthesis. *Ophthalmic Surg Lasers Imaging Retina* **47**, 171–4 (2016).
313. Abdallah, W., Li, W., Weiland, J., Humayun, M. & Ameri, H. Implantation of multiple suprachoroidal electrode arrays in rabbits. *J. Curr. Ophthalmol.* **30**, 68–73 (2018).
314. Szlyk, J. P. *et al.* Relationship between difficulty in performing daily activities and clinical measures of visual function in patients with retinitis pigmentosa. *Arch. Ophthalmol.* **115**, 53–59 (1997).
315. Geruschat, D. R., Turano, K. A. & Stahl, J. W. Traditional measures of mobility performance and retinitis pigmentosa. *Optom. Vis. Sci.* **75**, 525–537 (1998).
316. Haymes, S. A., Johnston, A. W. & Heyes, A. D. Relationship between vision impairment and ability to perform activities of daily living. *Ophthalmic Physiol. Opt.* **22**, 79–91 (2002).
317. Subhi, H., Latham, K., Myint, J. & Crossland, M. D. Functional visual fields: relationship of visual field areas to self-reported function. *Ophthalmic Physiol. Opt.* **37**, 399–408 (2017).
318. Nanduri, D. *et al.* Frequency and Amplitude Modulation Have Different Effects on the Percepts Elicited by Retinal Stimulation. *Invest. Ophthalmol. Vis. Sci.* **53**, 205–14 (2012).
319. Ghezzi, D. *et al.* A polymer optoelectronic interface restores light sensitivity in blind rat retinas. *Nat. Photonics* **7**, 400–406 (2013).
320. Maya-Vetencourt, J. F. *et al.* A fully organic retinal prosthesis restores vision in a rat model of degenerative blindness. *Nat. Mater.* **16**, 681–689 (2017).
321. Bourne, R. R. Causes of vision loss worldwide, 1990–2010: a systematic analysis. *Lancet Glob Health* **1**, 339–49 (2013).
322. Dagnelie, G. *et al.* Real and virtual mobility performance in simulated prosthetic vision. *J. Neural Eng.* **4**, S92–S101 (2007).
323. Ameri, H. *et al.* Toward a wide-field retinal prosthesis. *J. Neural Eng.* **6**, 035002 (2009).
324. The Lasker/IRRF Initiative for Innovation in Vision Science & Rathbun, D. Restoring Vision to the Blind: The New Age of Implanted Visual Prostheses. *Transl. Vis. Sci. Technol.* **3**, 3–3 (2014).
325. Pérez Fornos, A., Safran, A. & Pelizzone, M. Simulation of artificial vision, III: do the spatial or temporal characteristics of stimulus pixelization really matter? *Invest Ophthalmol Vis Sci* **46**, 3906–12 (2005).
326. Jung, J.-H. H., Aloni, D., Yitzhaky, Y. & Peli, E. Active confocal imaging for visual prostheses. *Vis. Res* **111**, 182–96 (2015).
327. Ghezzi, D. *et al.* A hybrid bioorganic interface for neuronal photoactivation. *Nat. Commun.* **2**, (2011).
328. Antognazza, M. *et al.* Characterization of a Polymer-Based, Fully Organic Prosthesis for Implantation into the Subretinal Space of the Rat. *Adv. Heal. Mater.* **5**, 2271–82 (2016).
329. Antognazza, M. Characterization of a Polymer-Based, Fully Organic Prosthesis for Implantation into the Subretinal Space of the Rat. *Adv. Heal. Mater.* **5**, 2271–2282 (2016).
330. Mineev, I. Biomaterials. Electronic dura mater for long-term multimodal neural interfaces. *Science* **347**, 159–63 (2015).
331. Bareket, L. Semiconductor nanorod-carbon nanotube biomimetic films for wire-free photostimulation of blind retinas. *Nano Lett* **14**, 6685–92 (2014).
332. Cogan, S. Neural Stimulation and Recording Electrodes. *Annu Rev Biomed Eng* **10**, 275–309 (2008).
333. Merrill, D. R., Bikson, M. & Jefferys, J. G. Electrical stimulation of excitable tissue: design of efficacious and safe protocols. *J Neurosci Methods* **141**, 171–98 (2005).
334. Boinagrov, D. Photovoltaic Pixels for Neural Stimulation: Circuit Models and Performance. *IEEE Trans Biomed Circuits Syst* **10**, 85–97 (2016).
335. Chang, B. *et al.* Two mouse retinal degenerations caused by missense mutations in the β -subunit of rod cGMP phosphodiesterase gene. *Vision Res.* **47**, 624–633 (2007).
336. Chang. Retinal degeneration mutants in the mouse. *Vis. Res* **42**, 517–25 (2002).
337. Boinagrov, D., Pangratz-Fuehrer, S., Goetz, G. & Palanker, D. Selectivity of direct and network-mediated stimulation of the retinal ganglion cells with epi-, sub- and intraretinal electrodes. *J. Neural Eng.* **11**, 026008 (2014).
338. Stett, A., Barth, W., Weiss, S., Haemmerle, H. & Zrenner, E. Electrical multisite stimulation of the isolated chicken retina. *Vision Res.* **40**, 1785–1795 (2000).
339. Romeo, A., Liu, Q., Suo, Z. & Lacour, S. Elastomeric substrates with embedded stiff platforms for stretchable electronics. *Appl Phys Lett* **102**, 131904 (2013).
340. Lorach, H. Retinal safety of near infrared radiation in photovoltaic restoration of sight. *Biomed Opt Express* **7**, 13–21 (2016).
341. Norren & Vos. Light damage to the retina: an historical approach. *Eye* **30**, 169–172 (2015).
342. Ahnood, A. Diamond Devices for High Acuity Prosthetic Vision. *Adv Biosyst* **1**, 1600003 (2017).
343. Tumbleston, K., Samulski, & Lopez. Analyzing local exciton generation profiles as a means to extract transport lengths in organic solar cells. *Phys Rev B* **82**, 205325 (2010).
344. Gupta, D., Bag, M., & Narayan. Area dependent efficiency of organic solar cells. *Appl Phys Lett* **93**, 384 (2008).
345. Dorn, J. D. *et al.* The detection of motion by blind subjects with the epiretinal 60-electrode (Argus II) retinal prosthesis. *JAMA Ophthalmol.* **131**, 183–189 (2013).

346. Yue, L. Ten-Year Follow-up of a Blind Patient Chronically Implanted with Epiretinal Prosthesis Argus I. *Ophthalmology* **122**, 2545-2552 1 (2015).
347. Jensen, R. & Rizzo, J. Thresholds for activation of rabbit retinal ganglion cells with a subretinal electrode. *Exp Eye Res* **83**, 367-373 (2006).
348. Behrend, M. R., Ahuja, A. K., Humayun, M. S., Chow, R. H. & Weiland, J. D. Resolution of the Epiretinal Prosthesis is not Limited by Electrode Size. *IEEE Trans. Neural Syst. Rehabil. Eng.* **19**, 436-442 (2011).
349. Kuo, A. Posterior Eye Shape Measurement With Retinal OCT Compared to MRI Posterior Eye Shape Measurement With Retinal OCT. *Invest Ophthalmol Vis Sci* **57**, 196-203 (2016).
350. Lei, X. SiC protective coating for photovoltaic retinal prosthesis. *J Neural Eng* **13**, 046016 (2016).
351. Hukins, D. W. L., Mahomed & Kukureka, S. N. Accelerated aging for testing polymeric biomaterials and medical devices. *Med Eng Phys* **30**, 1270-1274 (2008).
352. Quiroga, Q., Nadasdy, & Ben-Shaul. Unsupervised Spike Detection and Sorting with Wavelets and Superparamagnetic Clustering. *Neural Comput* **16**, 1661-1687 (2006).
353. Johnson, P. *et al.* Optical constants of transition metals. *Phys. Rev. B* **9**, 5056-5070 (1974).
354. Hammer, M., Roggan, A., Schweitzer, D. & Müller, G. Optical properties of ocular fundus tissues—an in vitro study using the double-integrating-sphere technique and inverse Monte Carlo simulation. *Phys Med Biol* **40**, 963-978 (1995).
355. Gosalia, K., Weiland, J., Humayun, M. & Lazzi, G. Thermal Elevation in the Human Eye and Head Due to the Operation of a Retinal Prosthesis. *IEEE Trans Biomed Eng* **51**, 1469-1477 (2004).
356. Brown, J. S. *et al.* In Vivo Human Choroidal Thickness Measurements: Evidence for Diurnal Fluctuations. *Invest. Ophthalmol. Vis. Sci.* **50**, 5-12 (2009).
357. Mark, J. E. *Polymer Data Handbook*. (Oxford University Press, 2009).
358. Sardar, D. K., Yust, B. G., Barrera, F. J., Mimun, L. C. & Tsin, A. T. Optical absorption and scattering of bovine cornea, lens and retina in the visible region. *Lasers Med. Sci.* **24**, 839-847 (2009).
359. Narasimhan, A. & Jha, K. K. Bio-heat transfer simulation of square and circular array of retinal laser irradiation. *Front. Heat Mass Transf. FHMT* **2**, (2011).
360. Wang, J. *et al.* Retinal safety of near-infrared lasers in cataract surgery. *J. Biomed. Opt.* **17**, 0950011-09500112 (2012).
361. Mirnezami, S. A., Rajaei Jafarabadi, M. & Abrishami, M. Temperature distribution simulation of the human eye exposed to laser radiation. *J Lasers Med Sci* **4**, 175-181 (2013).
362. Sarnaik, R., Chen, H., Liu, X. & Cang, J. Genetic disruption of the On visual pathway affects cortical orientation selectivity and contrast sensitivity in mice. *J. Neurophysiol.* **111**, 2276-2286 (2014).
363. Liu, J. *et al.* Thermal conductivity and elastic constants of PEDOT: PSS with high electrical conductivity. *Macromolecules* **48**, 585-591 (2015).
364. Martino, N. Photothermal cellular stimulation in functional bio-polymer interfaces. *Sci. Rep.* **5**, 8911 (2015).
365. Müllerová, J., Kaiser, M., Nádaždy, V., Šíffalovič, P. & Majková, E. Optical absorption study of P3HT: PCBM blend photo-oxidation for bulk heterojunction solar cells. *Sol. Energy* **134**, 294-301 (2016).
366. Stankova, N. E. *et al.* Optical properties of polydimethylsiloxane (PDMS) during nanosecond laser processing. *Appl. Surf. Sci.* **374**, 96-103 (2016).
367. Weiland, J. D., Cho A. K. & Humayun M. Retinal prostheses: current clinical results and future needs. *Ophthalmology* **118**, 2227-37 (2011).
368. Antognazza, M. Shedding Light on Living Cells. *Adv. Mater.* **27**, 7662-7669 (2015).
369. Ferlauto, L. *et al.* Design and validation of a foldable and photovoltaic wide-field epiretinal prosthesis. *Nat. Commun.* **9**, 992 (2018).
370. Ronzani, C. *et al.* High-Frequency Stimulation of Normal and Blind Mouse Retinas Using TiO₂ Nanotubes. *Adv. Funct. Mater.* (2018) doi:1804639.
371. Esler, T. B. *et al.* Minimizing activation of overlying axons with epiretinal stimulation: The role of fiber orientation and electrode configuration. *PLOS ONE* **13**, (2018).
372. Fried, S., Lasker A.C., W., Desai, N. J., Eddington, D. K. & Rizzo, J. Axonal sodium-channel bands shape the response to electric stimulation in retinal ganglion cells. *J. Neurophysiol.* **101**, 1972-87 (2009).
373. Spencer, T. C., Fallon, J. B., Thien, P. C. & Shivdasani, M. N. Spatial Restriction of Neural Activation Using Focused Multipolar Stimulation With a Retinal Prosthesis. *Invest. Ophthalmol. Vis. Sci.* **57**, 3181-3191 (2016).
374. Kang-Wook Lee *et al.* Pillar-shaped stimulus electrode array for high-efficiency stimulation of fully implantable epiretinal prosthesis. *J. Micromechanics Microengineering* **22**, 105015 (2012).
375. Leccardi, M. J. I. A., Vagni, P. & Ghezzi, D. Multilayer 3D electrodes for neural implants. *J. Neural Eng.* **16**, 026013 (2018).
376. Samba, R., T, H. & Zeck, G. PEDOT-CNT coated electrodes stimulate retinal neurons at low voltage amplitudes and low charge densities. *J. Neural Eng.* **12**, 016014 (2015).
377. Biswas, S., Sikdar, D., Das, D., M, M. & Das, S. PDMS based multielectrode arrays for superior in-vitro retinal stimulation and recording. *Biomed. Microdevices* (2017).
378. Tsai, D., Morley J. W, Suaning G. J, & Lovell N. H. Direct Activation and Temporal Response Properties of Rabbit Retinal Ganglion Cells Following Subretinal Stimulation. *J. Neurophysiol.* **102**, 2982-93 (2009).
379. Sekhar, S., Jalligampala, A., Zrenner, E. & Rathbun, D. Ticking the retina: integration of subthreshold electrical pulses can activate retinal neurons. *J. Neural Eng.* **13**, (2016).
380. Ho, E. *et al.* Temporal structure in spiking patterns of ganglion cells defines perceptual thresholds in rodents with subretinal prosthesis. *Sci. Rep.* **8**, 3145 (2018).
381. Ho, E. *et al.* Spatio-temporal characteristics of retinal response to network-mediated photovoltaic stimulation. *J. Neurophysiol.* (2017) doi:10.1152/jn.00872.2016.
382. Im, M., Werginz, P. & Fried, S. I. Electric stimulus duration alters network-mediated responses depending on retinal ganglion cell type. *J. Neural Eng.* **15**, 036010 (2018).
383. Im, M. & Fried, S. I. Indirect activation elicits strong correlations between light and electrical responses in ON but not OFF retinal ganglion cells. *J. Physiol.* **593**, 3577-3596 (2015).
384. Freeman, D. K., Eddington, D. K., Rizzo III, J. F. & Fried, S. I. Selective activation of neuronal targets with sinusoidal electric stimulation. *J. Neurophysiol.* **104**, 2778-2791 (2010).
385. Jensen, R. J., Ziv, O. R. & Rizzo, J. F. Responses of rabbit retinal ganglion cells to electrical stimulation with an epiretinal electrode. *J. Neural Eng.* **2**, S16 (2005).
386. Lee, J.-I. & Im, M. Non-rectangular waveforms are more charge-efficient than rectangular one in eliciting network-mediated responses of ON

- type retinal ganglion cells. *J. Neural Eng.* (2018) doi:10.1088/1741-2552/aad416.
387. Rathbun, D. L., Ghorbani, N., Shabani, H., Zrenner, E. & Hosseinzadeh, Z. Spike-triggered average electrical stimuli as input filters for bionic vision—a perspective. *J. Neural Eng.* **15**, 063002 (2018).
 388. Peyser, A. *et al.* *NEST*. (2017).
 389. Greenberg, R. J., Velte, T. J., Humayun, M. S., Scarlatis, G. N. & Juan, E. D. A computational model of electrical stimulation of the retinal ganglion cell. *IEEE Trans. Biomed. Eng.* **46**, 505–514 (1999).
 390. Cho, A. K., Sampath, A. P. & Weiland, J. D. Physiological Response of Mouse Retinal Ganglion Cells to Electrical Stimulation: Effect of Soma Size. *IEEE Eng. Med. Biol. Soc. Annu. Conf.* **2011**, 1081–1084 (2011).
 391. Hahne, J. *et al.* A unified framework for spiking and gap-junction interactions in distributed neuronal network simulations. *Front. Neuroinformatics* **9**, (2015).
 392. Brette, R. & Gerstner, W. Adaptive Exponential Integrate-and-Fire Model as an Effective Description of Neuronal Activity. *J. Neurophysiol.* **94**, 3637–42 (2005).
 393. Gerstner, W., M, K. W., R, N. & Paninski, L. *Neuronal Dynamics: From Single Neurons to Networks and Models of Cognition*. (Cambridge University Press, 2014).
 394. Gerstner, W. Spike-response model. *Scholarpedia* **3**, 1343 (2008).
 395. Sterling, P., Freed, M. A. & Smith, R. G. Architecture of rod and cone circuits to the on-beta ganglion cell. *J. Neurosci.* **8**, 623–642 (1988).
 396. Jeon, C.-J., Strettoi, E. & Masland, R. H. The Major Cell Populations of the Mouse Retina. *J. Neurosci.* **18**, 8936–8946 (1998).
 397. Ferguson, L. R., Grover, S., Li, J. M. D., Balaiya, S. & Chalam, K. V. Retinal Thickness Measurement Obtained with Spectral Domain Optical Coherence Tomography Assisted Optical Biopsy Accurately Correlates with Ex Vivo Histology. *PLOS ONE* **9**, e11203 (2014).
 398. Helmstaedter, M. Connectomics: The dense reconstruction of neuronal circuits using volume electron microscopy. *Microsc. Microanal.* **19**, 400–1 (2013).
 399. Dowling J., E. *The retina: An approachable part of the brain*. (Belknap Press, 2012).
 400. Stuart, G. & Spruston, N. Determinants of voltage attenuation in neocortical pyramidal neuron dendrites. *J. Neurosci. Off. J. Soc. Neurosci.* **18**, 3501–3510 (1998).
 401. Gleixner, R. & Fromherz, P. The Extracellular Electrical Resistivity in Cell Adhesion. *Biophys. J.* **90**, 2600–2611 (2006).
 402. Niebur, E. Electrical properties of cell membranes. *Scholarpedia* **3**, 7166 (2008).
 403. Bear, M., Connors B. W, & Paradiso M. A. *Neuroscience: Exploring the Brain*. (Lippincott Williams & Wilkins, 2006).
 404. Masland, R. H. The neuronal organization of the retina. *Neuron* (2012) doi:10.1016/j.neuron.2012.10.002.
 405. N. Arshi *et al.* Thickness effect on properties of titanium film deposited by d.c. magnetron sputtering and electron beam evaporation techniques. *Bull. Mater. Sci.* **36**, 807–12 (2013).
 406. Girtan, M. On the stability of the electrical and photoelectrical properties of P3HT and P3HT:PCBM blends thin films. *Org. Electron.* **14**, 200–5 (2013).
 407. Black, D., I, S. & Paul, S. Route to enhance the efficiency of organic photovoltaic solar cells - by adding ferroelectric nanoparticles to P3HT/PCBM admixture. *EPJ Photovolt.* **5**, (2014).
 408. Lin, Y.-J., J-Y, L. & Chen, S.-M. Changing electrical properties of PEDOT:PSS by incorporating with dimethyl sulfoxide. *Chem. Phys. Lett.* **664**, 213–8 (2016).
 409. Aleksandrova, M. P., Dobrikov, G. H. & Kolev, G. D. Electrical characterisation of PEDOT:PSS based flexible organic optoelectronic devices. *Int. J. Technical Phys. Probl. Eng.* **8**, 71–76 (2016).
 410. Sauerheber R & Heinz B. Temperature Effects on Conductivity of Seawater and Physiologic Saline, Mechanism and Significance. *Chem. Sci. J.* (2015).
 411. Gavish N & Promislow K. Dependence of the dielectric constant of electrolyte solutions on ionic concentration: A microfield approach. *Phys. Rev. E* **94**, 012611 (2016).
 412. Gabriel, S., W, L. R. & Gabriel, C. The dielectric properties of biological tissues: III. Parametric models for the dielectric spectrum of tissues. *Phys. Med. Biol.* **41**, 2271–93 (1996).
 413. Pennesi, M. E. *et al.* Long-Term Characterization of Retinal Degeneration in rd1 and rd10 Mice Using Spectral Domain Optical Coherence TomographySD-OCT Imaging of rd1 and rd10 Mice. *Investig. Ophthalmology Vis. Sci.* **53**, (2012).
 414. Stasheff, S. F., Shankar, M. & Andrews, M. P. Developmental time course distinguishes changes in spontaneous and light-evoked retinal ganglion cell activity in rd1 and rd10 mice. *J. Neurophysiol.* **105**, (2011).
 415. Yong Sook Goo, Dae Jin Park, Jung Ryul Ahn, & Solomon S. Senok. Spontaneous Oscillatory Rhythms in the Degenerating Mouse Retina Modulate Retinal Ganglion Cell Responses to Electrical Stimulation. *Front. Cell. Neurosci.* **9**, 512 (2016).
 416. Sahin, M. & Tie, Y. Non-rectangular waveforms for neural stimulation with practical electrodes. *J. Neural Eng.* **4**, 227 (2007).
 417. Wongsarnpigoon, A., P, W. J. & M, G. W. Efficiency Analysis of Waveform Shape for Electrical Excitation of Nerve Fibers. *IEEE Trans. Neural Syst. Rehabil. Eng.* **18**, 319–28 (2010).
 418. Cantrell D. R & Troy J. B. A Time Domain Finite Element Model of Extracellular Neural Stimulation Predicts that Non-Rectangular Stimulus Waveforms May Offer Safety Benefits. *2008 30th Annu. Int. Conf. IEEE Eng. Med. Biol. Soc.* 2768–71 (2008).
 419. Im, M. & Fried, S. I. Temporal properties of network-mediated responses to repetitive stimuli are dependent upon retinal ganglion cell type. *J. Neural Eng.* **13**, 025002 (2016).
 420. Wang, L., Liang, P.-J., P-M, Z. & Qiu, Y.-H. Ionic mechanisms underlying tonic and phasic firing behaviors in retinal ganglion cells: A model study. *Channels* **8**, (2014).
 421. Sekirnjak, C. *et al.* Electrical stimulation of mammalian retinal ganglion cells with multielectrode arrays. *J. Neurophysiol.* **95**, 3311–3327 (2006).
 422. Krouchev, N. I., Danner, S. M., Vinet, A., Rattay, F. & Sawan, M. Energy-optimal electrical-stimulation pulses shaped by the least-action principle. *PLoS One* **9**, e90480 (2014).
 423. Nakazawa, T. *et al.* Tumor Necrosis Factor- α Mediates Oligodendrocyte Death and Delayed Retinal Ganglion Cell Loss in a Mouse Model of Glaucoma. *J. Neurosci.* **26**, 12633–41 (2006).
 424. Watson A., B. A formula for human retinal ganglion cell receptive field density as a function of visual field location. *J. Vis.* **14**, 15–15 (2014).
 425. Twyford, P., C, C. & Fried, S. Differential responses to high-frequency electrical stimulation in ON and OFF retinal ganglion cells. *J. Neural Eng.*

- 11, 025001 (2014).
426. Zrenner, E. Fighting Blindness with Microelectronics. *Sci. Transl. Med.* **5**, 210ps16-210ps16 (2013).
427. Lewis, P. M., Ackland, H. M., Lowery, A. J. & Rosenfeld, J. V. Restoration of vision in blind individuals using bionic devices: a review with a focus on cortical visual prostheses. *Brain Res.* **1595**, 51–73 (2015).
428. Dobbelle, W. H., Mladejovsky, M. G., Evans, J. R., Roberts, T. S. & Girvin, J. P. 'Braille' reading by a blind volunteer by visual cortex stimulation. *Nature* **259**, 111–112 (1976).
429. Normann, R. A., Maynard, E. M., Rousche, P. J. & Warren, D. J. A neural interface for a cortical vision prosthesis. *Vision Res.* **39**, 2577–2587 (1999).
430. Tang, J. *et al.* Nanowire arrays restore vision in blind mice. *Nat. Commun.* **9**, 786 (2018).
431. Ahuja, A. K. *et al.* Blind subjects implanted with the Argus II retinal prosthesis are able to improve performance in a spatial-motor task. *Br. J. Ophthalmol.* **95**, 539–543 (2011).
432. Weiland, J. D. & Humayun, M. S. Retinal Prosthetic Systems for the Treatment of Blindness. *Bridge* **42**, 51–57 (2012).
433. Luo, Y. H.-L. & da Cruz, L. The Argus® II Retinal Prosthesis System. *Prog. Retin. Eye Res.* **50**, 89–107 (2016).
434. Sommerhalder, J. & Pérez Fornos, A. Prospects and Limitations of Spatial Resolution. in *Artificial Vision* (ed. Gabel, V. P.) 29–45 (Springer International Publishing, 2017). doi:10.1007/978-3-319-41876-6_4.
435. Chen, S. C., Suaning, G. J., Morley, J. W. & Lovell, N. H. Simulating prosthetic vision: II. Measuring functional capacity. *Vision Res.* **49**, 2329–2343 (2009).
436. Beyeler, M., Rokem, A., Boynton, G. M. & Fine, I. Learning to see again: biological constraints on cortical plasticity and the implications for sight restoration technologies. *J. Neural Eng.* **14**, 051003 (2017).
437. Abbott, C. J. *et al.* Safety Studies for a 44-Channel Suprachoroidal Retinal Prosthesis: A Chronic Passive Study. *Invest. Ophthalmol. Vis. Sci.* **59**, 1410–1424 (2018).
438. Palanker, D., Le Mer, Y., Mohand-Said, S., Muqit, M. & Sahel, J. A. Photovoltaic Restoration of Central Vision in Atrophic Age-Related Macular Degeneration. *Ophthalmology* (2020) doi:10.1016/j.ophtha.2020.02.024.
439. Tong, W., Meffin, H., Garrett, D. J. & Ibbotson, M. R. Stimulation Strategies for Improving the Resolution of Retinal Prostheses. *Front. Neurosci.* (2020).
440. Chenais, N. A. L., Leccardi, M. J. I. A. & Ghezzi, D. Capacitive-like photovoltaic epiretinal stimulation enhances and narrows the network-mediated activity of retinal ganglion cells by recruiting the lateral inhibitory network. *J. Neural Eng.* **16**, 066009 (2019).
441. Prévot, P.-H. *et al.* Behavioural responses to a photovoltaic subretinal prosthesis implanted in non-human primates. *Nat. Biomed. Eng.* **4**, 172–180 (2020).
442. Green, D. G. & Kapousta-Bruneau, N. V. Evidence that L-AP5 and D,L-AP4 can preferentially block cone signals in the rat retina. *Vis. Neurosci.* **24**, 9–15 (2007).
443. Koehler, C. L., Akimov, N. P. & Rentería, R. C. Receptive field center size decreases and firing properties mature in ON and OFF retinal ganglion cells after eye opening in the mouse. *J. Neurophysiol.* **106**, 895–904 (2011).
444. Krieger, B., Qiao, M., Rousso, D. L., Sanes, J. R. & Meister, M. Four alpha ganglion cell types in mouse retina: Function, structure, and molecular signatures. *PLoS One* **12**, e0180091 (2017).
445. Chenais, N. A. L., Leccardi, M. J. I. A. & Ghezzi, D. Naturalistic spatiotemporal modulation of epiretinal stimulation increases the response persistence of retinal ganglion cell. *J. Neural Eng.* (2020).
446. Gautam, V., Rand, D., Hanein, Y. & Narayan, K. A Polymer Optoelectronic Interface Provides Visual Cues to a Blind Retina. *Adv. Mater.* **26**, 1751–1756 (2014).
447. Bullimore, M. A., Bailey, I. L. & Wacker, R. T. Face recognition in age-related maculopathy. *Invest. Ophthalmol. Vis. Sci.* **32**, 2020–2029 (1991).
448. Bach, M., Wilke, M., Wilhelm, B., Zrenner, E. & Wilke, R. Basic quantitative assessment of visual performance in patients with very low vision. *Invest. Ophthalmol. Vis. Sci.* **51**, 1255–1260 (2010).
449. Smith, A. T. *Visual perception: Physiology, psychology and ecology.* (SAGE Publications Sage UK: London, England, 1997).
450. Parush, A., Parush, D. & Ilan, R. Human Factors in Healthcare: A Field Guide to Continuous Improvement. *Synth. Lect. Assist. Rehabil. Health-Preserv. Technol.* **6**, i–202 (2017).
451. Dräger, U. C. & Olsen, J. F. Ganglion cell distribution in the retina of the mouse. *Invest. Ophthalmol. Vis. Sci.* **20**, 285–293 (1981).
452. Dacey, D. M. & Petersen, M. R. Dendritic field size and morphology of midget and parasol ganglion cells of the human retina. *Proc. Natl. Acad. Sci.* **89**, 9666–9670 (1992).
453. Peterson, B. B. & Dacey, D. Morphology of wide-field, monostratified ganglion cells of the human retina. *Vis. Neurosci.* **16**, 107–120 (1999).
454. Michels, R. G., Wilkinson, C. P. & Rice, T. A. Retinal detachment. p 17. The CV Mosby Company. (1990).
455. Nagra, M., Gilmartin, B., Thai, N. J. & Logan, N. S. Determination of retinal surface area. *J. Anat.* **231**, 319–324 (2017).
456. Grancini, G. *et al.* Hot exciton dissociation in polymer solar cells. *Nat. Mater.* **12**, 29–33 (2012).
457. Simone, G. *et al.* Near-Infrared Tandem Organic Photodiodes for Future Application in Artificial Retinal Implants. *Adv. Mater.* **30**, 1804678 (2018).
458. Feyen, P. *et al.* Light-evoked hyperpolarization and silencing of neurons by conjugated polymers. *Sci. Rep.* **6**, 22718 (2016).
459. Leccardi, M. J. I. A. *et al.* Photovoltaic organic interface for neuronal stimulation in the near-infrared. *Commun. Mater.* **1**, 1–13 (2020).
460. Chuang, A. T., Margo, C. E. & Greenberg, P. B. Retinal implants: a systematic review. *Br. J. Ophthalmol.* **98**, bjophthalmol-2013 (2014).
461. Tsuchiya, T., Hirata, M. & Chiba, N. Young's modulus, fracture strain, and tensile strength of sputtered titanium thin films. *Thin Solid Films* **484**, 245–250 (2005).
462. Lang, U., Naujoks, N. & Dual, J. Mechanical characterization of PEDOT:PSS thin films. *Synth. Met.* **159**, 473–479 (2009).
463. Hasenkamp, W. *et al.* Polyimide/SU-8 catheter-tip MEMS gauge pressure sensor. *Biomed. Microdevices* **14**, 819–828 (2012).
464. Issele, H. *et al.* Determination of the Young's Modulus of a TiN Thin Film by Nanoindentation: Analytical Models and FEM Simulation. *E-J. Surf. Sci. Nanotechnol.* **10**, 624–629 (2012).
465. Chen, Z. & Diebels, S. Nanoindentation of Soft Polymers: Modeling, Experiments and Parameter Identification. *Tech. Mech.* **34** 3-4 166-189 ISSN 2199-9244 3,5 MB (2014) doi:10.24352/UB.OVGU-2017-060.
466. Robin, C. J., Vishnoi, A. & Jonnalagadda, K. N. Mechanical Behavior and Anisotropy of Spin-Coated SU-8 Thin Films for MEMS. *J. Microelectromechanical Syst.* **23**, 168–180 (2014).

467. Savagatrup, S. *et al.* Mechanical degradation and stability of organic solar cells: molecular and microstructural determinants. *Energy Environ. Sci.* **8**, 55–80 (2015).
468. Ghezzi, D. Translation of a photovoltaic retinal prosthesis. *Nat. Biomed. Eng.* **4**, 137–138 (2020).
469. Stone, J. L., Barlow, W. E., Humayun, M. S., Juan, E. de & Milam, A. H. Morphometric Analysis of Macular Photoreceptors and Ganglion Cells in Retinas With Retinitis Pigmentosa. *Arch. Ophthalmol.* **110**, 1634–1639 (1992).
470. Jensen, R. J. & Rizzo, J. F. Activation of retinal ganglion cells in wild-type and rd1 mice through electrical stimulation of the retinal neural network. *Vision Res.* **48**, 1562–1568 (2008).
471. Schiefer, M. A. & Grill, W. M. Sites of Neuronal Excitation by Epiretinal Electrical Stimulation. *IEEE Trans. Neural Syst. Rehabil. Eng.* **14**, 5–13 (2006).
472. Alqahtani, A., Abed, A. A., Guo, T., Lovell, N. H. & Dokos, S. A continuum model of electrical stimulation of multi-compartmental retinal ganglion cells. in *2017 39th Annual International Conference of the IEEE Engineering in Medicine and Biology Society (EMBC) 2716–2719* (IEEE, 2017). doi:10.1109/EMBC.2017.8037418.
473. Im, M. & Fried, S. I. Spatial properties of network-mediated response of retinal ganglion cells to electric stimulation. in *2015 7th International IEEE/EMBS Conference on Neural Engineering (NER) 256–259* (IEEE, 2015).
474. Ahuja, A. K., Behrend, M. R., Kuroda, M., Humayun, M. S. & Weiland, J. D. An in vitro model of a retinal prosthesis. *IEEE Trans. Biomed. Eng.* **55**, 1744–1753 (2008).
475. Jalligampala, A., Zrenner, E. & Rathbun, D. L. Spatial aspects of electrical desensitization in mouse retina. *Invest. Ophthalmol. Vis. Sci.* **57**, 3722–3722 (2016).
476. Chang, Y.-C., Ghaffari, D. H., Chow, R. H. & Weiland, J. D. Stimulation strategies for selective activation of retinal ganglion cell soma and threshold reduction. *J. Neural Eng.* **16**, 026017 (2019).
477. Jalligampala, A. Zapping the Retina-Understanding electrical responsiveness and electrical desensitization in mouse retinal ganglion cells. (Universität Tübingen, 2020).
478. Wilke, R. G., Greppmaier, U., Stingl, K. & Zrenner, E. Fading of perception in retinal implants is a function of time and space between sites of stimulation. *Invest. Ophthalmol. Vis. Sci.* **52**, 458–458 (2011).
479. Kohn, A. Visual Adaptation: Physiology, Mechanisms, and Functional Benefits. *J. Neurophysiol.* **97**, 3155–3164 (2007).
480. Soto-Breceda, A., Kameneva, T., Meffin, H., Maturana, M. & Ibbotson, M. R. Irregularly timed electrical pulses reduce adaptation of retinal ganglion cells. *J. Neural Eng.* **15**, 056017 (2018).
481. Clifford, C. W. & Rhodes, G. *Fitting the mind to the world: Adaptation and after-effects in high-level vision*. vol. 2 (Oxford University Press, 2005).
482. Kagan, I., Gur, M. & Snodderly, D. M. Saccades and drifts differentially modulate neuronal activity in V1: effects of retinal image motion, position, and extraretinal influences. *J. Vis.* **8**, 19–19 (2008).
483. Greschner, M., Bongard, M., Rujan, P. & Ammermüller, J. Retinal ganglion cell synchronization by fixational eye movements improves feature estimation. *Nat. Neurosci.* **5**, 341–347 (2002).
484. Martinez-Conde, S., Macknik, S. L., Troncoso, X. G. & Dyar, T. A. Microsaccades counteract visual fading during fixation. *Neuron* **49**, 297–305 (2006).
485. Intoy, J. & Rucci, M. Finely tuned eye movements enhance visual acuity. *Nat. Commun.* **11**, 1–11 (2020).
486. Davuluri, N. S. & Weiland, J. D. Time-varying pulse trains limit retinal desensitization caused by continuous electrical stimulation. in *2014 36th Annual International Conference of the IEEE Engineering in Medicine and Biology Society 414–417* (IEEE, 2014).
487. Chenais, N., Airaghi Leccardi, M. & Ghezzi, D. *Single-pixel epiretinal stimulation with a wide-field and high-density retinal prosthesis for artificial vision*. <http://biorxiv.org/lookup/doi/10.1101/2020.08.21.261461> (2020) doi:10.1101/2020.08.21.261461.
488. Margalit, E. & Thoreson, W. B. Inner retinal mechanisms engaged by retinal electrical stimulation. *Invest. Ophthalmol. Vis. Sci.* **47**, 2606–2612 (2006).
489. Nikolaev, A., Leung, K.-M., Odermatt, B. & Lagnado, L. Synaptic mechanisms of adaptation and sensitization in the retina. *Nat. Neurosci.* **16**, 934–941 (2013).
490. Euler, T., Haverkamp, S., Schubert, T. & Baden, T. Retinal bipolar cells: elementary building blocks of vision. *Nat. Rev. Neurosci.* **15**, 507–519 (2014).
491. Buettner, R., Baumgartl, H. & Sauter, D. Microsaccades as a Predictor of a User's Level of Concentration. *Information Systems and Neuroscience 173–177* (2019).
492. Biddiss, E. & Chau, T. Upper-limb prosthetics: critical factors in device abandonment. *Am. J. Phys. Med. Rehabil.* **86**, 977–987 (2007).
493. Cajal, M. *Surdités, implants cochléaires et impasses relationnelles*. (Eres, 2013).
494. Gourinat, V. Le corps prothétique: un corps augmenté? *Rev. Déthique Théologie Morale* 75–88 (2015).
495. Lane, F. J., Nitsch, K. P. & Scherer, M. Ethical considerations in the development of neural prostheses. *Neurobiotics Biomed. Eng. Neural Prostheses* 294–318 (2016).
496. Jae, S. A. *et al.* Electrophysiological and Histologic Evaluation of the Time Course of Retinal Degeneration in the rd10 Mouse Model of Retinitis Pigmentosa. *Korean J. Physiol. Pharmacol.* **17**, (2013).
497. Hadjinicolaou, A. E. *et al.* Optimizing the electrical stimulation of retinal ganglion cells. *IEEE Trans. Neural Syst. Rehabil. Eng.* **23**, 169–178 (2014).
498. Hadjinicolaou, A. E., Meffin, H., Maturana, M. I., Cloherty, S. L. & Ibbotson, M. R. Prosthetic vision: devices, patient outcomes and retinal research: A review of prosthetic vision research. *Clin. Exp. Optom.* **98**, 395–410 (2015).
499. Ivanov, I. V. *et al.* Eye Movement Training and Suggested Gaze Strategies in Tunnel Vision - A Randomized and Controlled Pilot Study. *PLOS ONE* **11**, e0157825 (2016).
500. Titchener, S. A. *et al.* Head and Gaze Behavior in Retinitis Pigmentosa. *Investig. Ophthalmology Vis. Sci.* **60**, 2263 (2019).
501. Wang, L., Yang, L. & Dagnelie, G. Virtual Wayfinding Using Simulated Prosthetic Vision in Gaze-locked Viewing. *Optom. Vis. Sci.* **85**, E1057–E1063 (2008).
502. Tolia, A. S. *et al.* Eye Movements Modulate Visual Receptive Fields of V4 Neurons. *Neuron* **29**, 757–767 (2001).
503. Martinez-Conde, S., Otero-Millan, J. & Macknik, S. L. The impact of microsaccades on vision: towards a unified theory of saccadic function. *Nat. Rev. Neurosci.* **14**, 83–96 (2013).
504. Gregori, N. Z. *et al.* Retinal Anatomy and Electrode Array Position in Retinitis Pigmentosa Patients After Argus II Implantation: An International Study. *Am. J. Ophthalmol.* **193**, 87–99 (2018).

505. Haq, W., Dietter, J. & Zrenner, E. Electrical activation of degenerated photoreceptors in blind mouse retina elicited network-mediated responses in different types of ganglion cells. *Sci. Rep.* **8**, 1–11 (2018).
506. Balasubramanian, R. & Gan, L. Development of Retinal Amacrine Cells and Their Dendritic Stratification. *Curr. Ophthalmol. Rep.* **2**, 100–106 (2014).
507. Singer, W. & Gray, C. M. Visual Feature Integration and the Temporal Correlation Hypothesis. 32.
508. Quinlan, P. T. Visual feature integration theory: Past, present, and future. *Psychol. Bull.* **129**, 643–673 (2003).
509. Treisman, A. Perceptual grouping and attention in visual search for features and for objects. *J. Exp. Psychol. Hum. Percept. Perform.* **8**, 194 (1982).
510. Wilson, H. R. Nonlinear processes in visual pattern discrimination. *Proc. Natl. Acad. Sci.* **90**, 9785–9790 (1993).
511. Bonnef, Y. & Polat, U. Collinear interactions and contour integration. *Spat. Vis.* **13**, 393–401 (2000).
512. Fang, Y. *et al.* Visual acuity inspired saliency detection by using sparse features. *Inf. Sci.* **309**, 1–10 (2015).
513. Keane, B. P., Kastner, S., Paterno, D. & Silverstein, S. M. Is 20/20 vision good enough? Visual acuity differences within the normal range predict contour element detection and integration. *Psychon. Bull. Rev.* **22**, 121–127 (2015).
514. Polat, U. Making perceptual learning practical to improve visual functions. *Vision Res.* **49**, 2566–2573 (2009).
515. Barollo, M., Contemori, G., Battaglini, L., Pavan, A. & Casco, C. Perceptual learning improves contrast sensitivity, visual acuity, and foveal crowding in amblyopia. *Restor. Neurol. Neurosci.* **35**, 483–496 (2017).
516. Warland, D. K., Reinagel, P. & Meister, M. Decoding Visual Information From a Population of Retinal Ganglion Cells. *J. Neurophysiol.* **78**, 2336–2350 (1997).
517. Gautrais, J. & Thorpe, S. Rate coding versus temporal order coding: a theoretical approach. *Biosystems* **48**, 57–65 (1998).
518. Lesica, N. A. & Stanley, G. B. Encoding of Natural Scene Movies by Tonic and Burst Spikes in the Lateral Geniculate Nucleus. *J. Neurosci.* **24**, 10731–10740 (2004).
519. Ghodasra, D. H. *et al.* Worldwide Argus II implantation: recommendations to optimize patient outcomes. *BMC Ophthalmol.* **16**, 52 (2016).
520. Sekirnjak, C. *et al.* High-Resolution Electrical Stimulation of Primate Retina for Epiretinal Implant Design. *J. Neurosci.* **28**, 4446–4456 (2008).
521. Herscher, M. B. & Kelley, T. P. Functional Electronic Model of the Frog Retina. *IEEE Trans. Mil. Electron.* **MIL-7**, 98–103 (1963).
522. Bálya, D., Roska, B., Roska, T. & Werblin, F. S. A CNN framework for modeling parallel processing in a mammalian retina. *Int. J. Circuit Theory Appl.* **30**, 363–393 (2002).
523. Morillas, C. A. *et al.* A design framework to model retinas. *Biosystems* **87**, 156–163 (2007).
524. Martínez-Cañada, P., Morillas, C., Pino, B., Ros, E. & Pelayo, F. A Computational Framework for Realistic Retina Modeling. *Comput. Framew. Realistic Retina Model.* **26**, (2016).
525. Zhang, X.-S., Gao, S.-B., Li, C.-Y. & Li, Y.-J. A Retina Inspired Model for Enhancing Visibility of Hazy Images. *Front. Comput. Neurosci.* **9**, (2015).
526. Melanitis, N. & Nikita, K. S. Biologically-inspired image processing in computational retina models. *Comput. Biol. Med.* **113**, 103399 (2019).
527. Soto-Breceda, A., Kameneva, T., Meffin, H., Maturana, M. & Ibbotson, M. R. Irregularly timed electrical pulses reduce adaptation of retinal ganglion cells. *J. Neural Eng.* **15**, 056017 (2018).
528. Stasheff, S. F. Emergence of Sustained Spontaneous Hyperactivity and Temporary Preservation of off Responses in Ganglion Cells of the Retinal Degeneration (rd1) Mouse. *J. Neurophysiol.* **99**, (2008).
529. Zaghoul, K. A., Boahen, K. & Demb, J. B. Different Circuits for ON and OFF Retinal Ganglion Cells Cause Different Contrast Sensitivities. *J. Neurosci.* **23**, 2645–2654 (2003).
530. Popova, E. ON-OFF Interactions in the Retina: Role of Glycine and GABA. *Curr. Neuropharmacol.* **12**, 509–526 (2014).
531. Liang, Z. & Freed, M. A. Cross inhibition from ON to OFF pathway improves the efficiency of contrast encoding in the mammalian retina. *J. Neurophysiol.* **108**, 2679–2688 (2012).
532. Vagni, P. In vivo evaluation of gene editing and prosthetic strategies to restore vision in small and large animal models of retinal degeneration. (EPFL, 2020).
533. Childs, C. R., Fujiyama, T., Brown, I. E. W. & Tyler, N. Pedestrian accessibility and movement environment laboratory. in (Walk21, 2005).
534. Cooper-Martin, E. Measures of cognitive effort. *Mark. Lett.* **5**, 43–56 (1994).
535. López-Ornat, S., Karousou, A., Gallego, C., Martín, L. & Camero, R. Pupillary Measures of the Cognitive Effort in Auditory Novel Word Processing and Short-Term Retention. *Front. Psychol.* **9**, (2018).
536. Van der Wel, P. & Van Steenbergen, H. Pupil dilation as an index of effort in cognitive control tasks: A review. *Psychon. Bull. Rev.* **25**, 2005–2015 (2018).
537. Hafed, Z. M., Stingl, K., Bartz-Schmidt, K.-U., Gekeler, F. & Zrenner, E. Oculomotor behavior of blind patients seeing with a subretinal visual implant. *Vision Res.* **118**, 119–131 (2016).
538. Luo, G. & Peli, E. Patients with tunnel vision frequently saccade to outside their visual fields in visual search. *J. Vis.* **6**, 505–505 (2010).
539. Dulin, D., Hatwell, Y., Pylyshyn, Z. & Chokron, S. Effects of peripheral and central visual impairment on mental imagery capacity. *Neurosci. Biobehav. Rev.* **32**, 1396–1408 (2008).
540. Phillips, M. J., Otteson, D. C. & Sherry, D. M. Progression of neuronal and synaptic remodeling in the rd10 mouse model of retinitis pigmentosa. *J. Comp. Neurol.* **518**, 2071–2089 (2010).
541. Durand, D. M. & Bikson, M. Suppression and control of epileptiform activity by electrical stimulation: a review. *Proc. IEEE* **89**, 1065–1082 (2001).
542. Goel, A. & Buonomano, D. V. Chronic electrical stimulation homeostatically decreases spontaneous activity, but paradoxically increases evoked network activity. *J. Neurophysiol.* **109**, 1824–1836 (2013).
543. Goo, Y. S. *et al.* Retinal ganglion cell responses to voltage and current stimulation in wild-type and rd10 mouse retinas. *J. Neural Eng.* **8**, 035003 (2011).
544. Jalligampala, A., Sekhar, S., Zrenner, E. & Rathbun, D. L. Optimal voltage stimulation parameters for network-mediated responses in wild type and rd10 mouse retinal ganglion cells. *J. Neural Eng.* **14**, 026004 (2017).
545. Corna, A., Herrmann, T. & Zeck, G. Electrode-size dependent thresholds in subretinal neuroprosthetic stimulation. *J. Neural Eng.* **15**, 045003 (2018).
546. Cordeiro, M. C. *et al.* Electrical Retina Stimulation in RD10 mice. *Invest. Ophthalmol. Vis. Sci.* **61**, 2213–2213 (2020).
547. Piyathaisere, D. V. *et al.* Heat effects on the retina. *Ophthalmic Surg. Lasers Imaging Retina* **34**, 114–120 (2003).
548. Pardue, M. T. *et al.* Neuroprotective effect of subretinal implants in the RCS rat. *Invest. Ophthalmol. Vis. Sci.* **46**, 674–682 (2005).

549. Schmid, H., Herrmann, T., Kohler, K. & Stett, A. Neuroprotective effect of transretinal electrical stimulation on neurons in the inner nuclear layer of the degenerated retina. *Brain Res. Bull.* **79**, 15–25 (2009).
550. Ni, Y., Gan, D., Xu, H. & Xu, G. Neuroprotective effect of transcorneal electrical stimulation on light-induced photoreceptor degeneration. *Exp. Neurol.* **219**, 439–452 (2009).
551. Palanker, D. V. *et al.* Attracting retinal cells to electrodes for high-resolution stimulation. in vol. 5314 306–314 (International Society for Optics and Photonics, 2004).
552. Piano, I. *et al.* Cone survival and preservation of visual acuity in an animal model of retinal degeneration. *Eur. J. Neurosci.* **37**, 1853–1862 (2013).
553. Tengölics, Á. J. *et al.* Response Latency Tuning by Retinal Circuits Modulates Signal Efficiency. *Sci. Rep.* **9**, 15110 (2019).
554. Simone, G. Near-Infrared Tandem Organic Photodiodes for Future Application in Artificial Retinal Implants. *Adv. Mater.* **30**, e1804678, (2018).
555. Cao, Y., Summerfield, C., Park, H., Giordano, B. L. & Kayser, C. Causal Inference in the Multisensory Brain. *Neuron* **102**, 1076–1087.e8 (2019).
556. Wiesel, T. N. & Hubel, D. H. Extent of recovery from the effects of visual deprivation in kittens. *J. Neurophysiol.* **28**, 1060–1072 (1965).
557. Recanzone, G. H., Merzenich, M. M. & Jenkins, W. M. Frequency discrimination training engaging a restricted skin surface results in an emergence of a cutaneous response zone in cortical area 3a. *J. Neurophysiol.* **67**, 1057–1070 (1992).
558. Recanzone, G. H., Schreiner, C. E. & Merzenich, M. M. Plasticity in the frequency representation of primary auditory cortex following discrimination training in adult owl monkeys. *J. Neurosci.* **13**, 87–103 (1993).
559. Darian-Smith, C. & Gilbert, C. D. Axonal sprouting accompanies functional reorganization in adult cat striate cortex. *Nature* **368**, 737–740 (1994).
560. Darian-Smith, C. & Gilbert, C. D. Topographic reorganization in the striate cortex of the adult cat and monkey is cortically mediated. *J. Neurosci.* **15**, 1631–1647 (1995).
561. Yamahachi, H., Marik, S. A., McManus, J. N., Denk, W. & Gilbert, C. D. Rapid axonal sprouting and pruning accompany functional reorganization in primary visual cortex. *Neuron* **64**, 719–729 (2009).
562. Abe, H. *et al.* Adult cortical plasticity studied with chronically implanted electrode arrays. *J. Neurosci.* **35**, 2778–2790 (2015).
563. Ferreira, S. *et al.* Primary visual cortical remapping in patients with inherited peripheral retinal degeneration. *NeuroImage Clin.* **13**, 428–438 (2017).
564. Masuda, Y., Dumoulin, S. O., Nakadomari, S. & Wandell, B. A. V1 Projection Zone Signals in Human Macular Degeneration Depend on Task, not Stimulus. *Cereb. Cortex* **18**, 2483–2493 (2008).
565. Baseler, H. A. *et al.* Large-scale remapping of visual cortex is absent in adult humans with macular degeneration. *Nat. Neurosci.* **14**, 649–655 (2011).
566. Kobatake, E., Wang, G. & Tanaka, K. Effects of Shape-Discrimination Training on the Selectivity of Inferotemporal Cells in Adult Monkeys. *J. Neurophysiol.* **80**, 324–330 (1998).
567. Yang, T. The Effect of Perceptual Learning on Neuronal Responses in Monkey Visual Area V4. *J. Neurosci.* **24**, 1617–1626 (2004).
568. Sachse, P. *et al.* “The world is upside down” – The Innsbruck Goggle Experiments of Theodor Erismann (1883–1961) and Ivo Kohler (1915–1985). *Cortex* **92**, 222–232 (2017).
569. Guerreiro, M. J. S., Putzar, L. & Röder, B. Persisting Cross-Modal Changes in Sight-Recovery Individuals Modulate Visual Perception. *Curr. Biol.* **26**, 3096–3100 (2016).
570. Stiles, N. R. B., Patel, V. R. & Weiland, J. D. Auditory-Visual Interactions in the Blind with Artificial Vision: Are Multisensory Perceptions Restored After Decades of Blindness? *bioRxiv* 519850 (2019) doi:10.1101/519850.
571. Barry, M. P., Dagnelie, G. & Group, A. I. S. Use of the Argus II Retinal Prosthesis to Improve Visual Guidance of Fine Hand Movements. *Invest. Ophthalmol. Vis. Sci.* **53**, 5095–5101 (2012).
572. Vetencourt, J. F. M. *et al.* The Antidepressant Fluoxetine Restores Plasticity in the Adult Visual Cortex. *Science* **320**, 385–388 (2008).
573. Rokem, A. & Silver, M. A. The benefits of cholinergic enhancement during perceptual learning are long-lasting. *Front. Comput. Neurosci.* **7**, (2013).
574. Chamoun, M. *et al.* Cholinergic Potentiation Improves Perceptual-Cognitive Training of Healthy Young Adults in Three Dimensional Multiple Object Tracking. *Front. Hum. Neurosci.* **11**, (2017).

Appendix

Retinal prostheses	Group	Mode of stimulation			Technical characteristics			Stimulation design			Development stage		Clinical Outcomes		
		Stimulation site	Cellular targets	Image capture	Light transduction	Power supply	Specificities	Number of electrodes	Electrodes characteristics	Visual field	Status	Market approval	Visual acuity	Functional abilities	Adverse effects
Argus II	Second Sight Medical Products, USA	Epiretinal	RGCs	Extrinsic goggles-mounted camera	External processing unit	External-Internal RF coils	Transretinal cable	60 (6 x 10)	200 µm with 575 µm pitch R electrodes	~20 to 22°	CE mark (2011) FDA approval (2013)	20/6324 to 20/800	High-contrast objects recognition and motion, ADLs improvement	Conjunctival erosion, epiphora, retinal detachment	
EPi-RET 3	Aachen University, GE	Epiretinal	RGCs	Extrinsic goggles-mounted camera	External processing unit	External-Internal RF coils	Intracocular receiver coil	25	100 µm diameter 3D RGC electrodes with 500 µm pitch	< 15° (37° for the VLMSS)	Completed acute clinical study	-	Light perception, bar orientation discrimination	-	
His II	Pixium Vision, Paris, F	Epiretinal	RGCs	Extrinsic goggles-mounted camera	External processing unit	External-Internal RF coils	IR data transmission, Transretinal cable	150	R electrodes	40°	Clinical trials (F)	CE mark (2016)	20/2000 to 20/400	High-contrast objects localization, direction of motion	Conjunctival erosion, retinal tear
Nano Retina NRE600	Bioentia, Herzliya, IS	Epiretinal	RGCs/RGCs	Extrinsic goggles-mounted camera	Unknown	Intrinsic photic energy use (NIR beam)	Photovoltaic	26 x 26	3D penetrating macroelectrodes	Unknown	Clinical studies (IS, BE)	-	-	-	
Polyretina	EPFL, Geneva, CH	Epiretinal	RGCs	Extrinsic goggles-mounted camera & eye optics	External processor unit to green/NIR beam & photoconversion by organic pixels	Intrinsic photic energy use	Organic photovoltaic, flexible array	10 498	Organic polymers/TiN electrodes	43°	Preclinical studies	-	-	-	
Alpha IMS	Retina Implant AG, Tübingen, Germany	Subretinal	RGCs	Intrinsic optics of the eye	Direct photoconversion by microphotodiodes	External-Internal RF coils	Light-based	1500	Microphotodiode array complexes (400 µm pitch)	11° x 11°	Commercially available in Europe (2013)	CE mark (2013)	20/2000 to 20/546	Light localization, detection of motion, unknown objects reading, mobility improvement, ADLs improvement	Conjunctival erosion, vascular damage, hypertension, retinal detachment
Alpha AMS	Retina Implant AG, Tübingen, Germany	Subretinal	RGCs	Intrinsic optics of the eye	Direct photoconversion by microphotodiodes	External-Internal RF coils	Light-based	1600	30 µm diameter microphotodiodes/array complexes (400 µm pitch)	~9 to 13° (2.8 x 2.8 mm)	Clinical trials (EU, US Research study)	CE mark (2016)	20/1111 to 20/546	High-contrast objects recognition and localization, navigation improvement	Implant det., conjunctival erosion, retinal detachment
PRIMA	Stanford University, CA USA & Pixium Vision, Paris, F	Subretinal	RGCs	Extrinsic goggles-mounted camera & eye optics	External processing unit to NIR beam & photoconversion by microphotodiodes	Intrinsic photic energy use	Photovoltaic	378	100 µm diameter pixels, microphotodiodes in series	Macula only (2 x 2 mm)	Clinical trials (KOR, FI, US feasibility study)	20/550 to 20/460	Light perception in the macula, high-contrast letters and objects recognition	-	
Boston Retinal Implant Project (BRIP)	Retina Implants Boston, VA, USA	Subretinal	RGCs	Extrinsic goggles-mounted camera	External processing unit	External-Internal RF coils	Transretinal chip platform coil around the cornea	256 (100 in human trials)	400 µm diameter RGC electrodes	14°	Completed acute surgical preclinical studies	-	-	Conjunctival erosion	
Seoul National University Retinal Implant	Seoul National University, KR	Subretinal	RGCs	Extrinsic goggles-mounted camera	External processing unit	External-Internal RF coils	Liquid crystal polymer-based flexible array	Unknown	Liquid crystal polymer electrodes	Unknown	Preclinical studies	-	-	-	
Bionic Vision Australia (BVA)/ NSW, Melbourne, Technologies	University of NSW, Melbourne, AU	Suprachoroidal	RGCs	Extrinsic goggles-mounted camera	External processing unit	External-Internal RF coils	Ease of implantation procedure	99 (24 in human clinical trial)	R electrodes	12.4°x12.2°	Clinical trials (AU)	20/8397	Objects localization, direction of motion	Subretinal and suprachoroidal haemorrhage	
Japan Visual Prostheses Project (JVS)	Osaka University, Gampori, JP	Suprachoroidal	RGCs	Extrinsic goggles-mounted camera	External processing unit	External-Internal RF coils	Promising electrodes	49 (7 x 7)	R electrodes 0.33 mm protruding	~10° (5.8 x 6.3 mm)	Clinical trials (JP)	-	High-contrast objects localization, direction of motion, grasping	-	

Appendix Supplementary Table 1 - Retinal prostheses systems

Comparison of the technical and clinical characteristics of Polyretina implant with the retinal devices having undergone and undergoing clinical trials or preclinical studies. Bold characters indicate the devices that have been tested in human subjects.

Acknowledgement

I would like to thank my advisor Diego Ghezzi for having trusted me and given me the opportunity to complete a PhD. I also express my sincere gratitude to each member of the thesis Committee for their time and interest in this work.

My warm thanks go to Marta Airaghi Leccardi and Laura Ferlauto for their always reliable manufacturing and schedules. This work would not have been possible without their contribution. I also want to acknowledge all my labmates for their ability to manage my social avoidance strategies. I am very grateful to Jake too for the long proofreading.

Finally, I would like to thank my parents for the symbolic capital they passed on to me with sacrifice and openness. And I would like to give a special thanks to Alban for his immutability and his precious mastership in Powerpoint animations.

Curriculum Vitae

CONTACT INFORMATION

Naïg Chenais
naig.chenais@epfl.ch
naig.chenais@gmail.com

PERSONAL INFORMATION

Date of birth: 26/04/1993
Swiss-French citizenship

EMPLOYMENT HISTORY

WORK HISTORY

- Marketing assistant
Feb. 2015 – Oct. 2015
SNI Editions
- Editor
Dec. 2015 – Oct. 2016
SNI Editions

RESEARCH AND TRAINING

- Engineer intern
Jul. 2012 – Sep. 2012
Swiss Tropical and Public Health Institute (Swiss TPH), Ifakara Health Institute & Tanzania Commission for Science and Technology (COSTECH)
Distribution models of cryopreserved PfsPZ Malaria Vaccine
- Research Intern
Sep. 2013 – Dec. 2013
EPFL International Paraplegic Foundation in Spinal Cord Repair - Center for Neuroprosthetics (CNP)
Spontaneous recovery after spinal cord injury in rodents

EDUCATION

- Lycée Xavier Marmier (Pontarlier, F)
2006 – 2009
Major in Sciences - Minor in Mathematics
- CPGE · Lycée du Parc (Lyon, F)
2009 – 2010
Biology – Chemistry – Physics & Engineer Sciences (BCPST)
- BSc · EPFL (Lausanne, CH)
2010 – 2012
Major in Life Sciences & Technologies (SV)
- MSc · EPFL (Lausanne, CH) / Kyoto University (Inuyama, JP)
2012 – 2014
Life Sciences & Technologies (SV)
Major in Neurosciences & Neuroengineering
Master thesis: *Rehabilitative effects of anti-RGMA antibody on manual motor control in non-human primates* · carried out in Kyoto University - Primate Research Institute (PRI) – System Neuroscience laboratory
- PhD · EPFL (Geneva, CH)
Oct. 2016 – Dec. 2020
PhD Program in Neuroscience – EPFL (Geneva, CH)
EPFL Interschool Institute of Bioengineering (IBI-STI) - Center for Neuroprosthetics (CNP) - Neuro-engineering laboratory (LNE)

PUBLICATIONS

FERLAUTO, Laura, LECCARDI, Marta Jole Ildelfonsa Airaghi, CHENAIS, Naïg Aurelia Ludmilla, *et al.* Design and validation of a foldable and photovoltaic wide-field epiretinal prosthesis. *Nature communications*, 2018, vol. 9, no 1, p. 1-15.

CHENAIS, Naïg Aurelia Ludmilla, LECCARDI, Marta Jole Ildelfonsa Airaghi, et GHEZZI, Diego. Capacitive-like photovoltaic epiretinal stimulation enhances and narrows the network-mediated activity of retinal ganglion cells by recruiting the lateral inhibitory network. *Journal of neural engineering*, 2019, vol. 16, no 6, p. 066009.

VAGNI, Paola, PERLINI, Laura E., CHENAIS, Naïg, *et al.* Gene editing preserves visual functions in a mouse model of retinal degeneration. *Frontiers in neuroscience*, 2019, vol. 13, p. 945.

CHENAIS, Naïg Aurelia Ludmilla, LECCARDI, Marta Jole Ildelfonsa Airaghi, et GHEZZI, Diego. High-resolution stimulation of retinal ganglion cells with organic photovoltaic pixels. *Investigative Ophthalmology & Visual Science*, 2019, vol. 60, no 9, p. 4980-4980.

LECCARDI, Marta Jole Ildelfonsa Airaghi, CHENAIS, Naïg Aurelia Ludmilla, FERLAUTO, Laura, *et al.* Photovoltaic organic interface for neuronal stimulation in the near-infrared. *Communications Materials*, 2020, vol. 1, no 1, p. 1-13.

CHENAIS, Naïg Aurelia Ludmilla, LECCARDI, Marta Jole Ildelfonsa Airaghi, et GHEZZI, Diego, Naturalistic spatiotemporal modulation of epiretinal stimulation increases the response persistence of retinal ganglion cell. *Journal of neural engineering*, 2020.

CHENAIS, Naïg Aurelia Ludmilla, LECCARDI, Marta Jole Ildelfonsa Airaghi, et GHEZZI, Diego. POLYRETINA restores high-resolution responses to single-pixel stimulation in blind retinas, 2020.

